

BULGARIAN CHEMICAL COMMUNICATIONS

2018 Volume 50 / Number 3

*Journal of the Chemical Institutes
of the Bulgarian Academy of Sciences
and of the Union of Chemists in Bulgaria*

Synthesis, characterization and antioxidant measurements of selenium (IV) complexes with some amino acids - binuclear complexes

A. M. Naglah^{1,2*}, A. S. Al-Wasidi³, N. M. Al-Jafshar³, J. S. Al-Otifi³, M. S. Refat^{4,5}, R. F. Hassan^{4,6}
W. N. Hozzein^{7,8}

¹ Department of Pharmaceutical Chemistry, Drug Exploration & Development Chair (DEDC), College of Pharmacy, King Saud University, Riyadh 11451, Saudi Arabia

² Peptide Chemistry Department, Chemical Industries Research Division, National Research Centre, 12622-Dokki, Cairo, Egypt

³ Department of Chemistry, College of Science, Princess Nourah Bint Abdulrahman University, Riyadh 11671, Saudi Arabia

⁴ Chemistry Department, Faculty of Science, Taif University, P.O. Box 888, Al-Hawiah, Taif 21974, Saudi Arabia

⁵ Department of Chemistry, Faculty of Science, Port Said, Port Said University, Egypt

⁶ Chemistry Department, Faculty of Science, Helwan University, Cairo, Egypt

⁷ Bioproducts Research Chair, Zoology Department, College of Science, King Saud University, Riyadh 11451, Saudi Arabia

⁸ Botany and Microbiology Department, Faculty of Science, Beni-Suef University, Beni-Suef 62111, Egypt

Received January 9, 2018; Accepted May 17, 2018

A series of selenium(IV) complexes of asparagine (*Asn*), proline (*Pro*), glutamine (*Gln*), methionine (*Met*) and cysteine (*Cys*) amino acids were prepared and well characterized based the (elemental analyses, molar conductance measurement), various spectral studies (IR, Raman, UV-Vis, ¹H-NMR and mass) and thermo gravimetric analyses (TG/DTG). The X-ray diffraction studies were carried out using PANalytical X-ray diffractometer, surface homogeneity of the respected samples was investigated using Quanta FEG 250 scanning electron microscope (SEM) and the chemical compositions of these samples have been studied using energy dispersive X-ray analyses. All the selenium (IV) complexes (**I-V**) are of [Se⁺⁴(AA⁻¹)₂Cl₂] type, where AA = (*Asn*, *Pro*, *Gln*, *Met* and *Cys*) act as monobasic bidentate ligands in the synthesized complexes. Mass fragments of the [Se (*Cys*)₂(Cl)₂] (**V**) suggest monomeric statement. The speculated geometries of the 1:2 complexes were octahedral configuration with two chlorines and two bidentate ligands occupying the corners of the octahedral complexes. In selenium-*Asn*, *Pro*, *Gln*, and *Met* complexes both amino and carboxylate groups are involved in coordination with metal, but, *Cys* coordinates through its sulfhydryl and carboxylate groups. The free radical scavenging activity of newly synthesized selenium (IV) complexes was determined at the concentration of 10, 20 and 30 ppm by means of the interaction with free radical 1,1-diphenyl-2-picrylhydrazyl (DPPH) in stable form. All these complexes have a bullish antioxidant activity.

Keywords: Selenium; Amino acids; Raman; XRD; SEM; Nanorods; DPPH.

INTRODUCTION

Generally, amino acids containing two essential groups (amine and carboxylic acid) attached to the first α -carbon atom, are of particular importance in biochemical field. The chemical formula of α -amino acids is H₂NCHR⁺COOH in most cases where, R is an organic substituent known as a side-chain [1, 2]. Amino acids are the main structural chemical constituents of proteins, which enter into the structure of all living organisms and are the most important factor in biochemical processes that support the preservation of human life [3, 4]. They are highly susceptible to being excellent catalysts and can be chelated with transition metals through their amino or carboxylic groups [5, 6]. Over the past few decades the complexation of transitional metal ions with amino acids has been studied [7, 8].

The amino acid reactions were found to be responsible for the enzymatic activity and stability of protein structures [9, 10]. The complexity of mineral amino acids is an important area of research where they can be used as simulated systems to identify the interaction of mineral protein in biological systems.

Selenium is one of the rarer elements present in low and fundamental concentrations in the human body and is of great importance in nutrition and medicine [11]. Selenium nanoparticles have some unique optical, mechanical, electrical, biological and chemical properties as compared to other chemicals. For example, selenium nanoparticles have been reported to have high biological activity and low toxicity [12], and nanowires of selenium with trigonal geometry have new optical photoconductivity [13]. Thus, selenium

* To whom all correspondence should be sent:

E-mail: amnaglah@gmail.com

nanoparticles attracted considerable interest of researchers and different synthesis methods were exploited [14-17].

Amino acid coordination chemistry is an integral feature of inorganic and bioinorganic chemistry [18-20], with many applications in medicinal design and materials science [21, 22]. Selenium amino acid complexes attract attention of chemists because of their different kinds of applications. In selenium (IV) amino acid complexes syntheses, the amino acid is first reacted with a selenium (IV) ion and gives stable octahedral selenium (IV) complexes. In this paper an overview on structures and coordination chemistry of selenium (IV) amino acid complexes is given. This article describes the synthesis of selenium nanoparticles by *in situ* amino acid chelation. This study presents preliminary results of synthesized bis-chelated complexes of the used five amino acids, shown in Fig. 1.

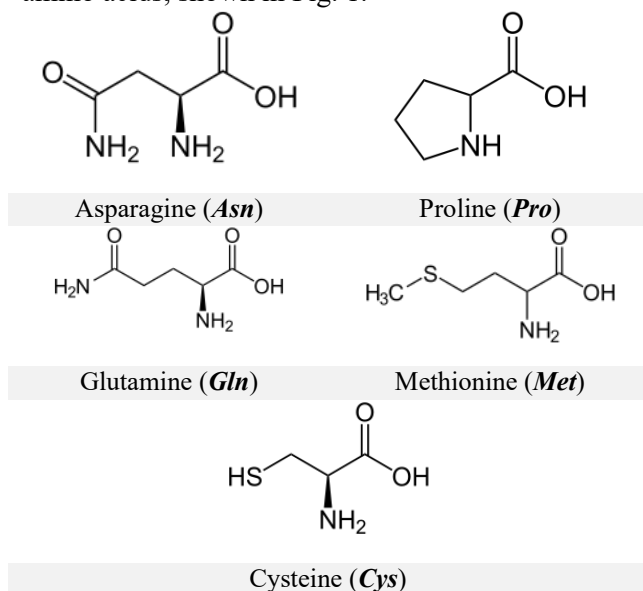


Fig. 1: Chemical structures of the used five amino acids

MATERIALS AND METHODS

Chemicals and reagents

The amino acids (L-configuration) asparagine (*Asn*), proline (*Pro*), glutamine (*Gln*), methionine (*Met*) and cysteine (*Cys*) were purchased from Sigma-Aldrich Chemical Company, all organic solvents and reagents were used in pure form. SeCl₄ was received from Aldrich Company.

Synthesis of selenium (IV) amino acid complexes

The collected compounds were prepared using the same chemical procedures, as follows: adding 25 mL of amino acids in ethanol (4 mmol) to the same volume of selenium (IV) tetrachloride also in ethanol (2 mmol). The solutions were refluxed for 2

h and the resultant brown to black-brown solution was reduced to *ca.* 1/2 of its volume. The solids produced by filtration were collected and washed with petroleum ether (60-80°C) and dried in a vacuum medium over anhydrous CaCl₂.

Instruments

- Elemental analysis (%C, %H and %N) percentage was performed using Perkin Elmer CHN 2400.
- Molar conductivity (10⁻³ mol/cm³) with dimethylsulfoxide (DMSO) solvent was determined using Jenway 4010 conductivity meter.
- Electronic spectra were scanned using UV-3101 PC Shimadzu spectrophotometer.
- FT-IR spectra were scanned on a Bruker FT-IR spectrophotometer.
- Raman laser spectra were collected on a Bruker FT-Raman spectrophotometer equipped with a 50 mW.
- ¹H-NMR spectra were recorded using a Varian Gemini 200 MHz spectrometer.
- Mass spectra were scanned using AEI MS 30 mass spectrometer with 70 eV.
- Thermal study TG/DTG-50H was carried out on a Shimadzu thermogravimetric analyzer under nitrogen atmosphere.
- Scanning electron microscopy (SEM) was performed on Quanta FEG 250 equipment.
- X-ray powder diffraction was measured on X'Pert PRO PANalytical with target Cu with secondary monochromator.

DPPH and Hydroxyl Radical Scavenging assays

The 2, 2-diphenyl-1-picrylhydrazyl (DPPH) assay was performed as described in [23]. Free radical damage imposed on the substrate, deoxyribose, was measured using the thiobarbituric acid test [24, 25]. The inhibition (I) percentage of deoxyribose degradation was experimentally calculated using the following relationship:

$$I (\%) = 100 \times (A_0 - A_1 / A_0)$$

where A₀ is the absorbance of the control sample and A₁ is the absorbance of the tested sample. Statistical analysis: each of the measurements described was conducted in at least three identical trials and the results were reported as mean and standard deviation, significantly different calculated level at p ≤ 0.05.

RESULTS AND DISCUSSION

Microanalysis results

Analytical results for the synthesized selenium (IV) amino acid complexes are listed in Table 1.

Table 1: Elemental analysis and physical data of $[\text{Se}^{+4}(\text{AA}^{-1})_2\text{Cl}_2]$ complexes

Complex/ Empirical formula	M. wt. g/mole	% C % H % N			Mp/ $^{\circ}\text{C}$	Color	Λ_m ($\Omega^{-1}\text{cm}^2\text{mol}^{-1}$)
		(calcd.)/found					
$[\text{Se}(\text{Asn})_2(\text{Cl})_2]$ C₈H₁₄Cl₂N₄O₆Se, I	412.09	(23.32) 23.21	(3.42) 3.39	(13.60) 13.54	179	Brown	27
$[\text{Se}(\text{Pro})_2(\text{Cl})_2]$ C₁₀H₁₆Cl₂N₂O₄Se, II	378.11	(31.77) 31.65	(4.27) 4.23	(7.41) 7.40	185	Brown	25
$[\text{Se}(\text{Gln})_2(\text{Cl})_2]$ C₁₀H₁₈Cl₂N₄O₆Se, III	440.14	(27.29) 27.18	(4.12) 4.10	(12.73) 12.70	210	Red brown	43
$[\text{Se}(\text{Met})_2(\text{Cl})_2]$ C₁₀H₂₀Cl₂N₂O₄S₂Se, IV	446.27	(26.91) 26.88	(4.52) 4.50	(6.28) 6.26	201	Red brown	32
$[\text{Se}(\text{Cys})_2(\text{Cl})_2]$ C₆H₁₂Cl₂N₂O₄S₂Se, V	390.17	(18.47) 18.42	(3.10) 3.07	(7.18) 7.15	245	Black brown	38

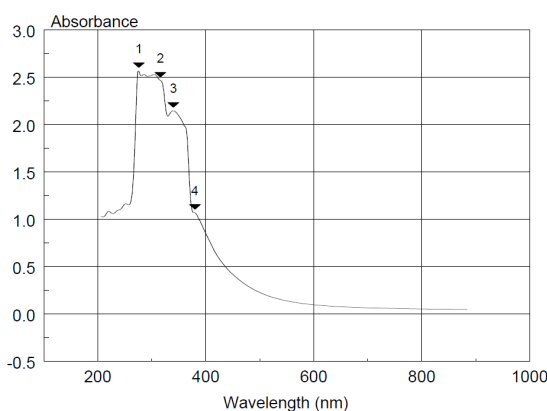
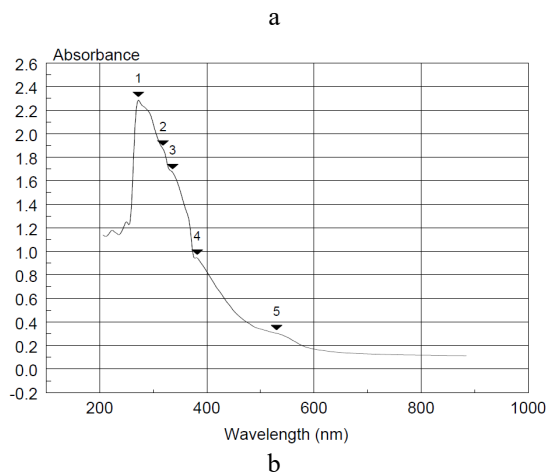
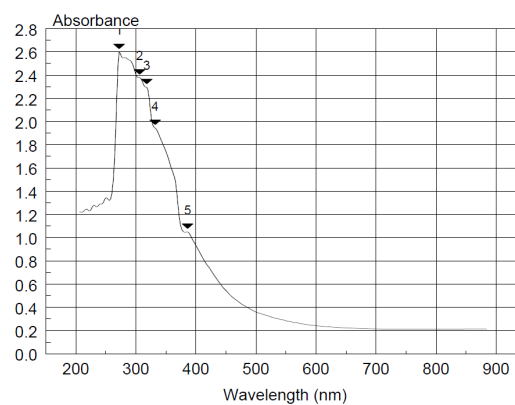
These support the formation of binuclear complexes with chemical composition of 1:2 selenium to amino acid stoichiometry. All complexes are colored, and soluble in DMF and DMSO. The elemental analysis in Table 1 matched well with 1:2 (Se: amino acid) ratio. For selenium complexes, the molar conductivities are in the range of 25-43 $\text{ohm}^{-1}\text{cm}^2\text{mol}^{-1}$. These values deduced that 1:2 complexes are non-electrolytes soluble in DMSO [26, 27]. These results are regarded to be low due to the existence of the two chlorine atoms inside the coordination sphere. These complexes have a melting point within the 179-245 $^{\circ}\text{C}$ range, with yield of 80-88%. The presence of Cl^- ions was checked using AgNO_3 reagent.

Electronic spectra

The shift of $n-\pi^*$ characteristic band in the UV-Vis spectra, attributed to the $\text{C}=\text{O}$ bond (272 nm for *Asn*-Se, 272 nm for *Pro*-Se, 276 nm for *Gln*-Se, 294 nm for *Met*-Se and 264 nm for *Cys*-Se) is due to the involving of the non-bonding electron pairs of the oxygen in the metal-ligand bond formation, Fig. 2. The formation of amino acids SeNPs was confirmed with the help of UV-Vis spectra investigation according to the change in color from colorless (selenium(IV) chloride) to three degrees of brown color (SeNPs), having absorption maximum λ_{max} at 300–400 nm [28].

Infrared spectra

FT-IR spectra of the five investigated complexes are illustrated in Figs. 3a-e. These spectra display very similar spectral bands, so the coordination behavior in all selenium (IV) complexes I-V is similar. The proposed spectral assignments are presented in Table 2.



c

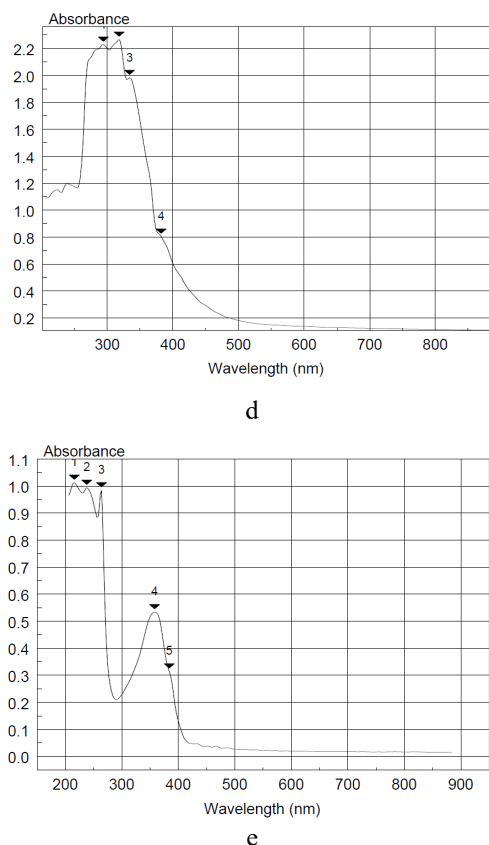


Fig. 2. UV-Vis spectra of $[Se(AA)_2Cl_2]$ complexes: a- *Asn*, b- *Pro*, c- *Gln*, d- *Met*, e- *Cys*.

The assignments were discussed on the basis of literature [29-31] and with the help of some interesting references [32, 33]. The characteristic bands were referred to CH, CH₂ and CH₃ deformational modes, and other skeletal vibrations between 2980-2900 cm⁻¹ with similar energies in all spectra.

- The O-H stretching modes are overlapped with the -NH₂ stretchings around 3000-3200 cm⁻¹.

- The free amino acids exist as zwitterions in the solid state, thus, there are two stretching vibrations for the COO⁻ moiety present in these systems, namely $\nu_s(COO^-)$ and $\nu_{as}(COO^-)$.

- The $\nu_s(COO^-)$ usually has a medium intensity in the IR spectrum, whereas the $\nu_{as}(COO^-)$ has a strong broad band.

- After coordination, one should expect a lowering of the frequency of one of these bands, due to the generation of a Se-O bond and the energy increase of the other, because the C=O double bond is partially reconstructed, as it can be seen from the data presented in Table 2.

- The absence of the characteristic $\nu(NH_3^+)$ and $\delta(NH_3^+)$ bands and the shift in the position of the carboxylate stretching vibrations in the free ligand, clearly confirm its existence in the non zwitterionic form.

In the spectrum of selenium (IV)-*Cys* complex, the infrared frequencies at 1622 and 1407 cm⁻¹ were assigned to antisymmetric and symmetric COO⁻ frequencies, respectively. In free *Cys* the SH frequency appears at 2548 cm⁻¹ but the infrared spectrum of Se(IV)-*Cys* complex shows no SH absorption frequency. The absence of SH frequency in the spectrum of the complex is an evidence of the involvement of S group in complexation with metal. The NH₂ frequencies are found to be at 3027, 1487 and 1125 cm⁻¹. Antisymmetric and symmetric COO⁻ frequencies in Se-*Asn*, Se-*Pro*, Se-*Gln* and Se-*Met* complexes are at (1667 and 1403) cm⁻¹, (1621 and 1403) cm⁻¹, (1593 and 1402) cm⁻¹, and (1617 and 1409) cm⁻¹, respectively. There are no NH₂ bending frequencies in the spectra of these complexes as expected from the symmetry consideration. The complexes exhibit two new frequencies at 600-500 and 500-400 cm⁻¹, respectively, due to Se-O and Se-N stretching [33]. The Se-*Gln* complex has medium strong band at 1682 cm⁻¹ attributed to stretching vibration of the carbonyl of the amido group. From IR data, the energy difference between both $\nu_{as}(COO^-)$ and $\nu_s(COO^-)$ vibrations ($\Delta = 191-264$ cm⁻¹) clearly supports the participation of carboxylate group in monodentate binding [34].

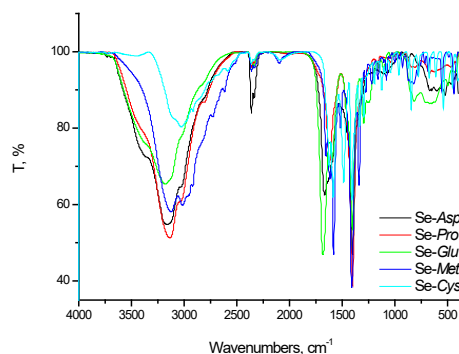


Fig. 3. Infrared spectra of $[Se(AA)_2Cl_2]$ complexes (AA= *Asn*, *Pro*, *Gln*, *Met* and *Cys*).

The infrared spectra of the bi-chelated Se (IV) complexes of the amino acids *Asn*, *Pro*, *Gln*, *Met* and *Cys* were recorded and analyzed in relation to their structure, Fig. 4.

Proton Magnetic Resonance Spectra

The chemical shifts of Se-*Cys* (V) complex are shown in Fig. 6. The spectrum of complex V possesses two characteristic signals. The sharp signal due to the -CH and -a CH₂ proton is observed around 3.31 ppm. The singlet broad signal of the -NH₂ protons is located at 7.01 ppm. The resonance due to the proton of the -OH and -SH groups (11-12 ppm) of the *Cys* chelate disappears in the selenium (IV) complex (V) indicating that coordination has taken place through the

deprotonation of -OH and binding of S atom of -SH group. Finally, the presence of a singlet broad band at 7.01 ppm is due to the faraway of nitrogen atom of -NH₂ from complexation, Fig. 4.

Table 2. IR frequencies (cm⁻¹) of [Se(AA)₂Cl₂] complexes

Compound	ν(O-H) ν(N-H)	ν(COO ⁻)		δ(NH ₂)	ν(M-O)	ν(M-N)
		Asym	Sym			
I	3163	1667	1403	--	524	466
II	3136	1621	1403	--	520	470
III	3180	1593	1402	--	497	428
IV	3124	1617	1409	--	523	439
V	3027	1622	1407	1487	540	455

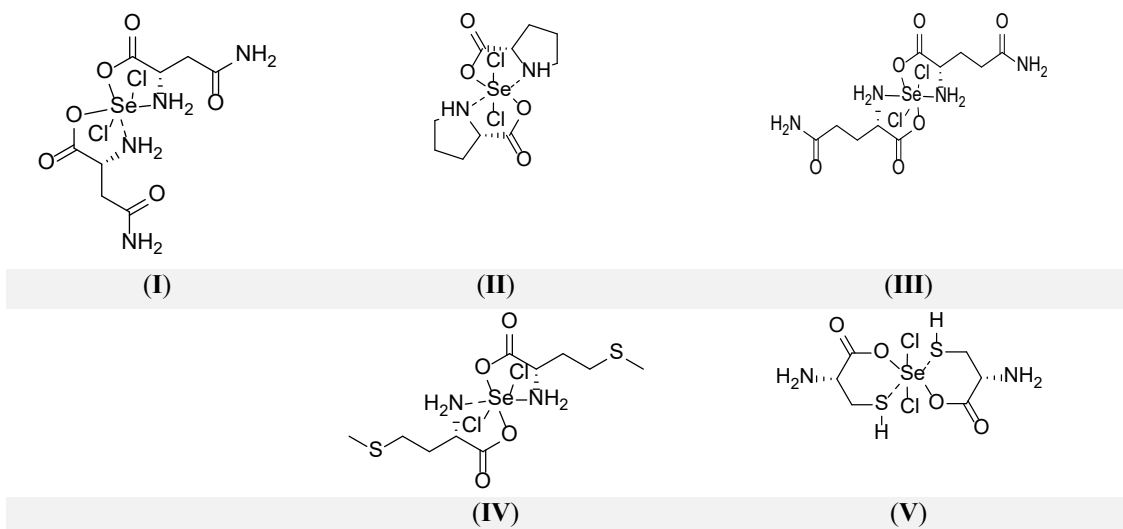


Fig. 4. Speculated structures of [Se(AA)₂Cl₂] complexes (AA= Asp, Pro, Glu, Met and Cys).

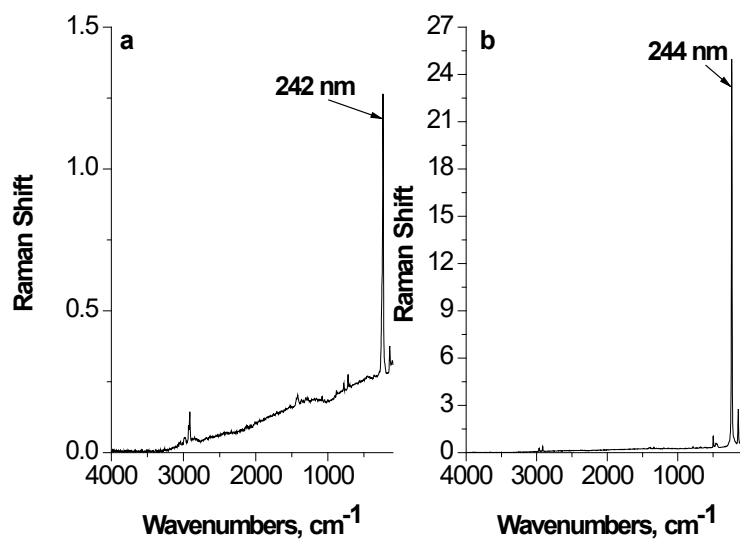


Fig. 5. Raman laser spectrum of a- Se-Met and b- Se-Cys complexes

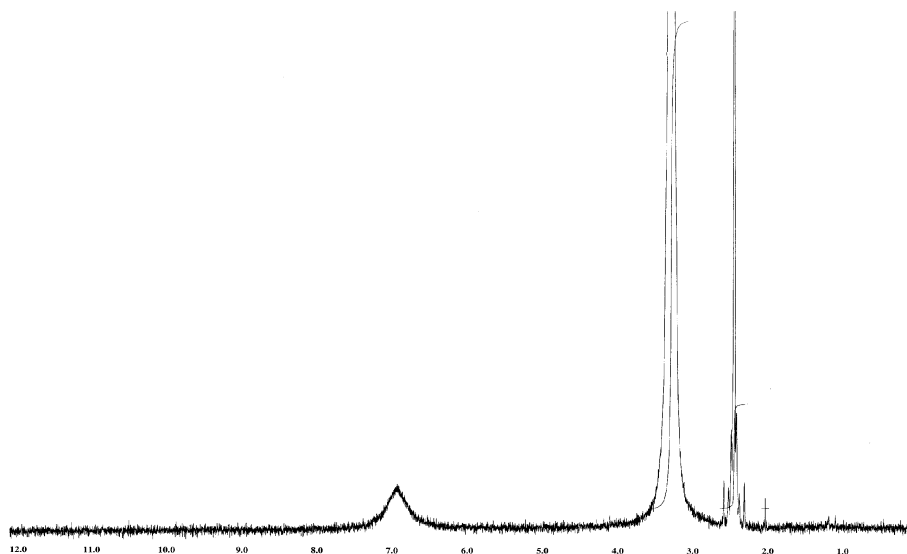


Fig. 6. ¹H-NMR spectrum of the Se-Cys complex.

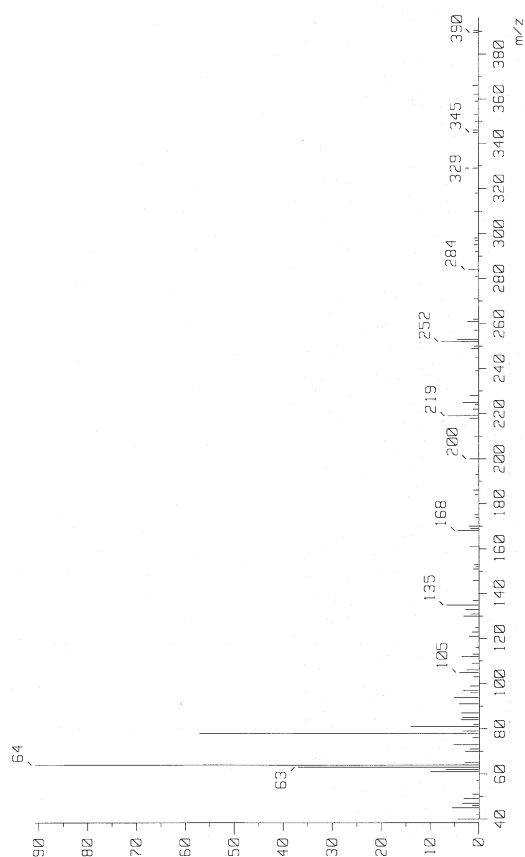


Fig. 7. Mass spectrum of Se-Cys complex.

Mass Spectra

Chemical shifts of the Se-Cys (V) complex: The mass spectral data of the $[\text{Se}(\text{Cys})_2(\text{Cl})_2]$ complex are presented in Fig. 7. The mass spectrum of Se-Cys complex showed a molecular ion peak that is in a good agreement with the expected value. The mass spectrum of Se-Cys shows a peak at 390 m/z,

which was assigned as a [M] peak. The Cys molecule was thought to produce ions at m/z 345, 329, 284, 252, 219, 200, 168, 135, 105, 64, and 63, respectively. The m/z 78 ion, which is a Se-Cys (V) complex, is containing one selenium atom.

XRD Spectra

The X-ray diffraction patterns of the $[\text{Se}(\text{Cys})_2(\text{Cl})_2]$ complex with selenium nanoparticles are shown in Fig. 8. The diffraction peaks present at 2θ (degrees) of 23.42°, 29.57°, 42.05°, 43.75°, 45.47°, 51.43°, 55.70°, 61.46°, 65.09° and 71.59° correspond to (100), (101), (110), (102), (111), (201), (112), (202), (210) and (113) planes of selenium, respectively. The diffraction peaks within the 2θ region due to hexagonal crystal structure of selenium are in agreement with the standard data (JCPDS card No. 01-071-4647), as shown in Fig. 9. The particle size of selenium was estimated using Scherrer's eq. [36]

$$D = \frac{0.94\lambda}{\beta \cos\theta} \quad 1$$

where D = grain size, K = constant equal to 0.94, λ = wavelength of the X-ray radiation, β = full width at half maximum and θ = diffraction angle. The particle size of selenium nanoparticles is found to be ~ 10 nm. The diffraction pattern due to (100), (101), (110), (102), (111) and (201) directions of hexagonal phase of selenium is shown in Fig. 9. The d-spacing values for the diffraction pattern match well with the hexagonal selenium.

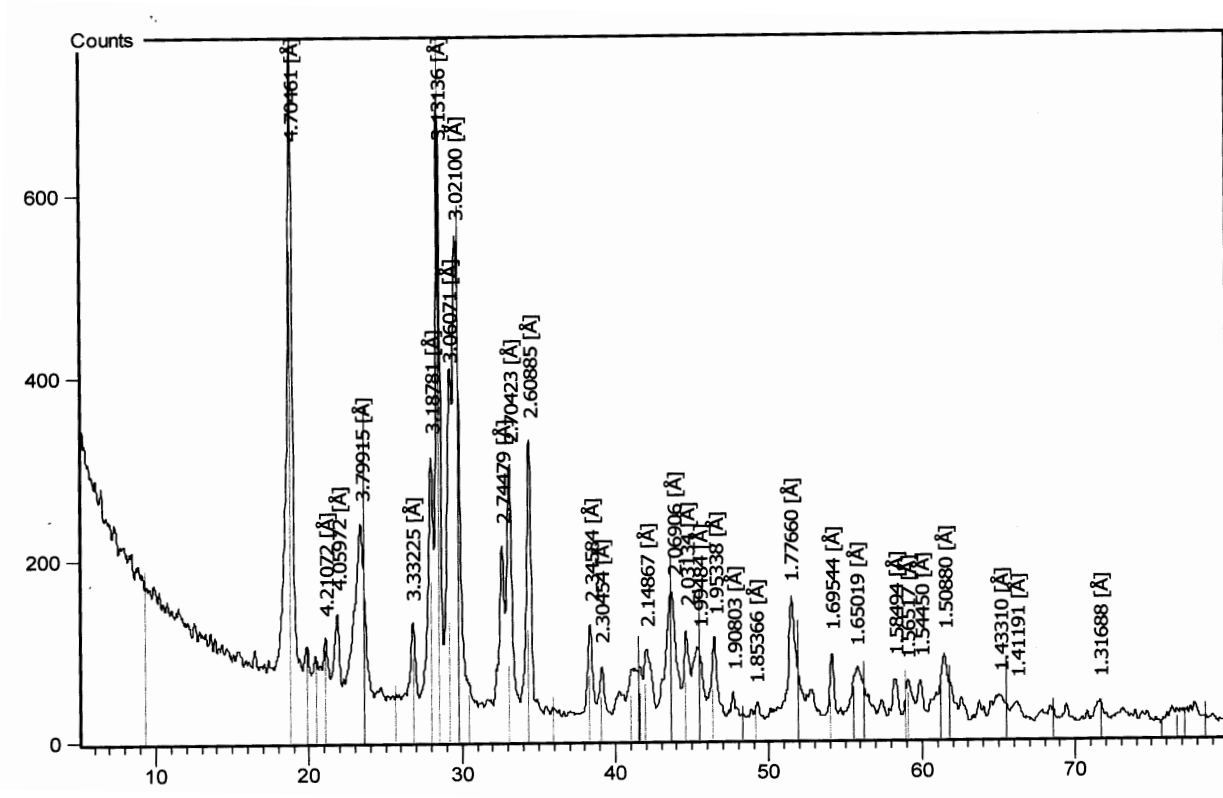


Fig. 8. XRD spectrum of Se-Cys complex.

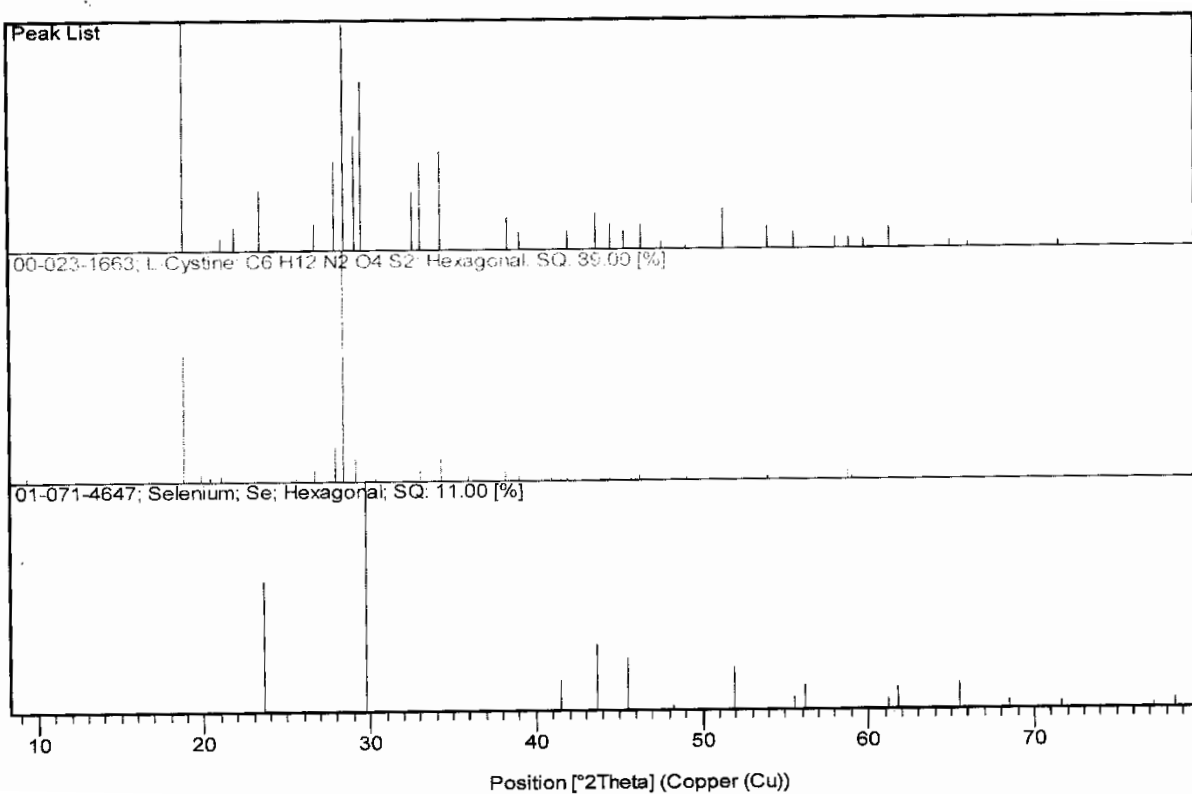


Fig. 9. Standard XRD spectrum of Cys and Se-Cys complex with selenium hexagonal structure.

SEM, TEM and EDX Spectra

The scanning electron microscope (SEM) image of the $[\text{Se}(\text{Cys})_2(\text{Cl})_2]$ complex with selenium nanorods and hexagonal structure is illustrated in Fig. 10. The SEM image reveals that the selenium nanorods are of uniform size with a mean diameter of ~ 10 nm. It can be seen that nanorods are of several micrometers in length with diameter ranging from $10 \mu\text{m}$. Energy dispersive X-ray analysis (EDX) was used to identify and determine the chemical composition of the Se-Cys complex. EDX pattern of the Se-Cys complex is shown in

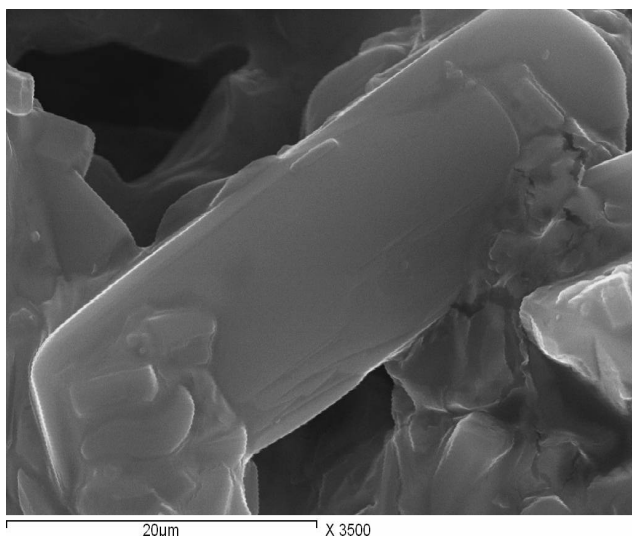


Fig. 10: SEM image of Se-Cys complex.

Fig. 11. Weak signals concerning O atoms have been recorded along with the strong peak due to Se atom. EDX analysis indicates the presence of O, S, C, and Cl with very low intensity, so this analysis supported the purity of the selenium particles.

The transmission electron microscopy images were performed using JEOL 100s microscope. Fig. 12 shows the transmission electron microscope (TEM) image of Se-Cys complex selenium nanorods. The image shows that the nanorods are with an average diameter of ~ 10 nm.

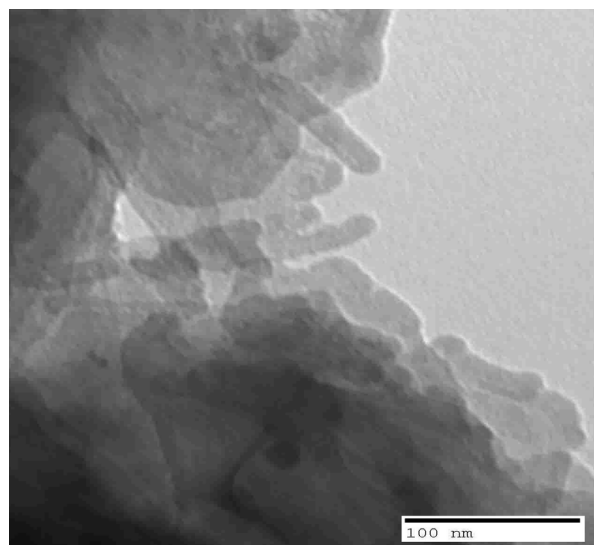


Fig. 12: TEM image of Se-Cys complex

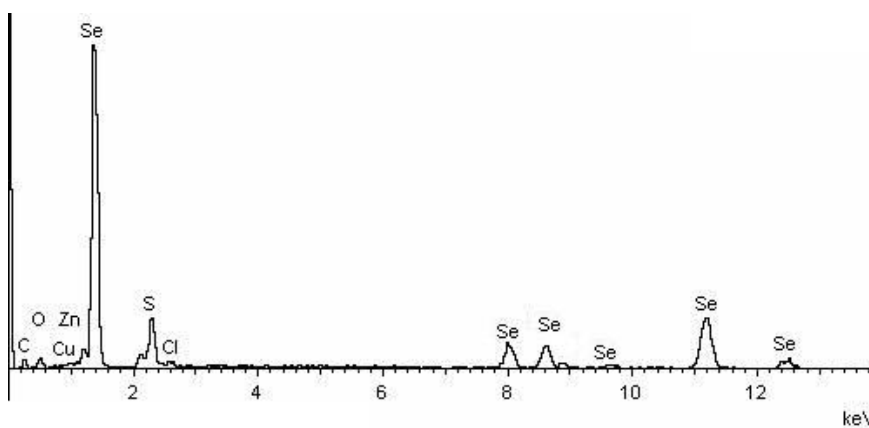


Fig. 11: EDX spectrum of Se-Cys complex.

Thermal analysis

Thermal stability of $[\text{Se}(\text{AA})_2\text{Cl}_2]$ complexes (AA= *Asn*, *Pro*, *Gln*, *Met* and *Cys*) complexes was checked based on thermo gravimetric and its differential analyses started from room temperature till 800°C under N_2 atmosphere. The TG curves were redrawn as mg mass loss versus temperature. The thermal decomposition curves (TG) are given in Fig. 13.

Asn-Se complex: Thermal decomposition of *Asn-Se* complex (I) occurs in four steps. The 1st degradation step takes place in the temperature range of $179\text{--}222^\circ\text{C}$ at $\text{DTG}_{\text{max}} = 196^\circ\text{C}$ (endo) and it correspond to a mass loss of 15.043%. The 2nd step occur within the temperature range of $296\text{--}367^\circ\text{C}$ at $\text{DTG}_{\text{max}} = 317^\circ\text{C}$ (endo) which was assigned to the decomposition of *Asn* molecule with a weight loss of 52.949%. The 3rd step occurs within the

temperature range of 433-475 °C at $DTG_{max} = 452$ °C which is due to loss of organic moiety with a weight loss of 8.835%. The last decomposition step takes place within the temperature range of 573-663 °C with mass loss of 21.464%. The residual carbon atoms (1.709%) in the final product remain stable till 800 °C.

Pro-Se complex: The thermal decomposition of *Pro-Se* complex (II) occurs in three steps. The first degradation step takes place in the temperature range of 121-167 °C at $DTG_{max} = 136$ °C (endo) and it corresponds to the loss of one chlorine atom with mass loss of 7.697%. The second step occurs within the temperature range of 275-383 °C at $DTG_{max} = 325$ °C (endo) which was assigned to the decomposition of two *Pro* and one chlorine molecule with weight loss of 75.077%. The third step occurs within the temperature range of 527-625 °C at $DTG_{max} = 563$ °C (endo) which was assigned to the loss of organic moiety with a weight loss of 12.420%. The few carbon atoms in the final product remain stable till 800 °C with mass loss of 4.806%.

Gln-Se complex: The thermal decomposition of *Gln-Se* complex (III) occurs in four successive steps. The first degradation step takes place in the temperature range of 46-55 °C at $DTG_{max} = 44$ °C and it corresponds to the loss of water molecules with a weight loss of 2.183%. The second step occurs within the temperature range of 156-202 °C at $DTG_{max} = 172$ °C (endo) which was assigned to the loss of one of the chlorine molecules beside the amino terminal groups with a weight loss of 10.069%. The third step occurs within the temperature range of 284-381 °C at $DTG_{max} = 328$ °C (endo) which was assigned to the loss of organic moiety of *Gln* chelate with a weight loss of 54.740%. The fourth step occurs within the temperature range of 432-800 °C at $DTG_{max} = 500$ °C which was assigned to the loss of organic moiety with a weight loss of 8.102%. The few carbon atoms with mass (24.906%) in the final product remain stable till 800 °C.

Met-Se complex: The thermal decomposition of *Met-Se* complex (IV) occurs in three steps. The first degradation step takes place in the temperature range of 128-146 °C at $DTG_{max} = 134$ °C (endo) and it corresponds to the loss of chlorine atoms with a weight loss of 11.363%. The second step occurs within the temperature range of 257-303 °C at $DTG_{max} = 277$ °C (endo) that was assigned to the loss of organic moiety with a weight loss of 56.139%. The third step occurs within the temperature range of 494-535 °C at $DTG_{max} = 511$

°C that was assigned to the loss of organic moiety with a weight loss of 10.147%. The residual carbon with a mass of 2.2351% in the final product remains stable till 800 °C.

Cys-Se complex: The thermal decomposition of *Cys-Se* complex (V) occurs in three successive steps. The first degradation step takes place in the temperature range of 265-305 °C at $DTG_{max} = 284$ °C and it corresponds to the loss of two chlorine atoms and two molecules of *Cys* with weight loss of 70.559%. The second step occurs within the temperature range of 381-436 °C at $DTG_{max} = 397$ °C which was assigned to the loss of organic moiety with a weight loss of 12.665%. The third step occurs within the temperature range of 448-558 °C at $DTG_{max} = 509$ °C (endo) which was assigned to the loss of organic moiety with a weight loss of 11.700%. The residual few carbon atoms with $m(VO_2 + C)$ in the final product remain stable till 800 °C as a final residue.

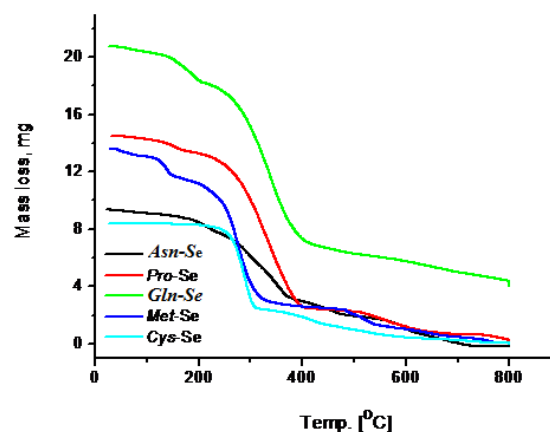


Fig. 13. TG curves of $[Se(AA)_2Cl_2]$ complexes (AA= *Asn*, *Pro*, *Gln*, *Met* and *Cys*).

Antioxidant activity

Bioavailability of selenium from dietary supplements is strongly dependent on its chemical form. Seleno amino acids which possess organically bound selenium are considered to be better absorbed and less toxic than inorganic selenium compounds [37]. Many chemical materials have been evaluated for antioxidant activities using *in vivo* and *in vitro* models and the selenium compounds trial is one of the most successful. The aim of this work was to examine the antioxidant activities of five selenium amino acid complexes. DPPH and hydroxyl radical scavenging methods were applied to *in vitro* models. Resulted data indicated that the radical scavenging activities of the tested compounds depend on the chemical form of selenium. Radical scavenging activity effects of selenium complexes

I-V against DPPH and hydroxyl radicals are shown in Figs. 14 and 15. All concentrations (10, 20 and 30 ppm) of the tested complexes showed significant to moderate radical scavenging activity compared to standard BHA material (70.4, 85.1 and 94.3%), respectively. As shown in Figs. 14 and 15, the radical scavenging activity of all tested compounds gradually increases through all concentrations (10, 20 and 30 ppm) compared with butylated hydroxyanisole (BHA) as positive control.

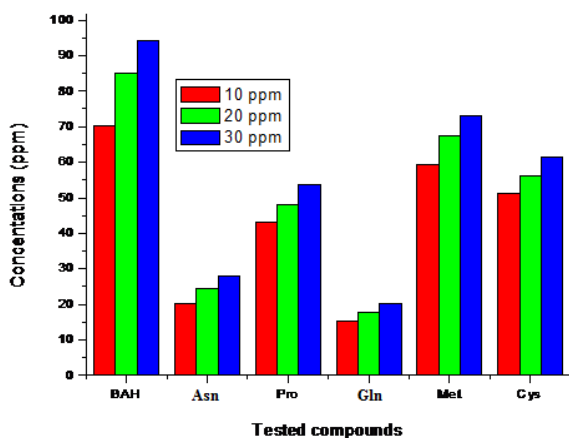


Fig. 14. Diagrams of radical scavenging activity effects of selenium complexes I-V against DPPH.

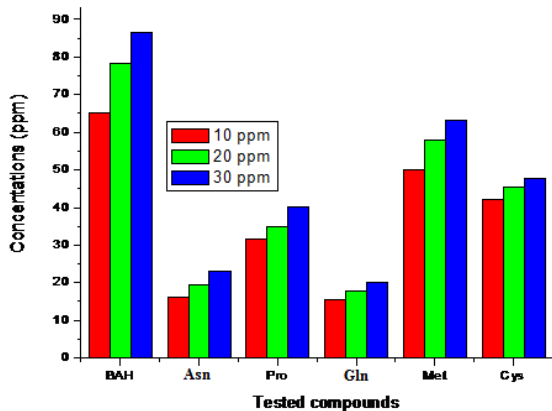


Fig. 15. Diagrams of radical scavenging activity effects of selenium complexes I-V against hydroxyl radicals

The Se-*Met* and Se-*Cys* displayed the highest radical scavenging activity effects against DPPH compared with BHA. In the DPPH free radical scavenging test the stable yellow-colored diphenylpicrylhydrazine (DPPH-H) is formed in the presence of an antioxidant. The scavenging effects of BHA at concentrations 10, 20 and 30 ppm on the hydroxyl radical were 65.2, 78.3 and 86.5%, respectively. When the tested compounds or BHA were incubated with the reaction mixture they were

able to interfere with free radical reaction and could prevent damage to the sugar.

CONCLUSION

Selenium(IV)-amino acids complexes of *Asn*, *Pro*, *Gln*, *Met*, and *Cys* were synthesized and characterized using analytical techniques such as elemental analysis, thermal analyses and (FT-IR, Raman laser, ¹H-NMR, and UV-Vis) spectroscopy. The microanalytical elemental data deduced a 1:2 selenium ions: amino acid ratio of the synthesized complexes. In view of the FT-IR spectroscopy results the selenium (IV) ion was coordinated to the respective amino acids as a bidentate chelate. The geometry of the selenium ions was six-coordinated with those of amino acid complexes. The selenium in nano-structured form was investigated by Raman laser spectroscopy, X-ray powder diffraction, surface morphology, scanning electron microscopy (SEM). The free radical scavenging activity of the newly synthesized selenium (IV) complexes was determined at the concentration of 10, 20 and 30 ppm using stable DPPH free radicals. All complexes displayed a significant antioxidant activity.

Acknowledgements: This work was funded by the Deanship of Scientific Research at Princess Nourah bint Abdulrahman University, through the Research Groups Program Grant no. (RGP-1438-0003).

Author Contributions: Ahmed Naglah, R.F. Hassan and Moamen Refat designed and observed the proposal, contributed to data analysis and interpretation. Wael Hozzien did the biological study and wrote the biological part. Asma S. Al-Wasidi, Nawal M. Al-Jafshar and Jamelah S. Al-Otifi, surveyed data in the database and did the spectral analysis. Ahmed Naglah and Moamen Refat gave conceptual advice and wrote the paper. All authors discussed the results and implications and commented on the manuscript at all stages.

Conflict of Interests: The authors declare no conflict of interests.

REFERENCES

1. Q. Wang, A. R. Parrish, L. Wang. Expanding the genetic code for biological studies, *Chem. Biol.* **16** (3), 323 (2009).
2. P. Newsholme, L. Stenson, M. Sulvucci, R. Sumayao, M. Krause. Amino Acid Metabolism. *Comprehensive Biotechnology* (2nd ed.), **1**, 3 (2011).
3. K. Asemave, S. G. Yiase, S. O. Adejo, B. A. Anhwange, *International Journal of Inorganic and Bioinorganic Chemistry*, **2** (1), 11 (2011).
4. R. H. Garret, C. M. Grisham, *Biochemistry*, Sanders, New York, 1995, p. 216.

5. J. H. Ottawa, D. K. Apps, Biochemistry, ELBS, London, 1984.
6. N. Visfiliumurthy, P. Lingaiah, *Ind. J. Chem. (A)*, **25**, 875 (1986).
7. T. R. Rap, M. Sahay, R. C. Aggarwal, *St. J. Chem. (A)*, **23**, 214 (1984).
8. A. Marcu, A. Stanilaa, O. Cozar, L. David; *Journal of Optoelectronics and Advanced Materials*, **10**(4), 830 (2008).
9. L. R. Dinelli, T. M. Bezerra, J. J. Sene, *Curr. Res. Chem.*, **2**, 18 (2010).
10. S. S. Dara, A Textbook of Environmental Chemistry and Pollution Control, S. Chand and Company Ltd, India, 2005, p. 67.
11. B. H. Xu, K.Y. Huang, Chemistry, Biochemistry of Selenium and its Application in Life Science, Hua East University of Science & Technology Press (Ch). 1994.
12. X. Y. Gao, J. S. Zhang, L. D. Zhang, M. X. Zhu, *China Public Health*, **16**, 421 (2000).
13. B. Gates, B. Mayers, B. Cattle, Y. N. Xia, *Adv. Funct. Mater.*, **12**, 219 (2002).
14. V. V. Kopeikin, S.V. Valueva, A. I. Kipper, L. N. Borovikova, A. P. Filippov, *Polymer Science, Series A*, **45** (4), 374 (2003).
15. X. Y. Gao, J. S. Zhang, L. D. Zhang, *Adv. Mater.*, **14**, 290 (2002).
16. X. Zhang, Y. Xie, F. Xu, X. H. Liu, *Chin. J. Inorg. Chem.*, **19**, 77 (2003).
17. B. Gates, B. Mayers, A. Grossman, Y. N. Xia, *Adv. Mater.*, **14**, 1749 (2002).
18. E. R. dos Santos, R. S. Corrêa, L. V. Pozzi, A. E. Graminha, H. S. Selistre-de-Araújo, F. R. Pavan, A. A. Batista, *Inorg. Chim. Acta*, **463**, 1, (2017).
19. M. Taha, I. Khan, J. A. P. Coutinho, *Journal of Inorganic Biochemistry*, **157**, 25 (2016).
20. S. Choksakulporn, A. Punkvang, Y. Sritana-anant, *Journal of Molecular Structure*, **1082**, 97 (2015).
21. S. Ghasemi, A. H. Khoshgoftarmanesh, M. Afyuni, H. Hadadzadeh, R. Schulin, *Soil Biology and Biochemistry*, **63**, 73 (2013).
22. P. Ramakrishnan, S. Shanmugam, *Journal of Power Sources*, **316**, 60 (2016).
23. W. Brand-Williams, M. E. Cuvelier, C. Berset, Use of a free radical method to evaluate antioxidant activity, *LWT Food Sci. Technol.*, **28**, 25 (1995).
24. H. Ohkawa, N. Ohishi, K. Yagi, Assay for lipid peroxides in animal tissues by thiobarbituric acid reaction, *Anal. Biochem.*, **95**, 351 (1979).
25. K. Shimoda, K. Fujikawa, K. Yahara, T. Nakamura, Antioxidative properties of xanthan on the autoxidation of soybean oil in cyclodextrin emulsion, *J. Agric. Food Chem.*, **40**, 945 (1992).
26. W. J. Geary, *Coord. Chem. Rev.*, **7**, 81 (1971).
27. M. S. Refat, *J. Mol. Struct.*, **842** (1–3), 24 (2007).
28. C. H. Ramamurthy, K. S. Sampath, P. Arunkumar, M. S. Kumar, V. Sujatha, K. Premkumar, C. Thirunavukkarasu, *Bioprocess and Biosystems Engineering*, **36**, 1131 (2013).
29. E.J. Baran, I. Viera, M.H. Torre, *Spectrochim. Acta*, **66A**, 114 (2007).
30. T.J. Lane, J.A. Durkin, R.J. Hooper, *Spectrochim. Acta*, **20**, 1013 (1964).
31. J.F. Jackovitz, J.L. Walter, *Spectrochim. Acta*, **22**, 1393 (1966).
32. B. Smith, Infrared Spectral Interpretation, CRC Press, Boca Raton, 1999.
33. K. Nakamoto, Infrared and Raman Spectra of Inorganic and Coordination Compounds: Part B, 5th ed., Wiley, New York, 1997.
34. G.B. Deacon, R.J. Phillips, *Coord. Chem. Rev.*, **33**, 227(1980).
35. M.S. Refat and Kh. M. Elsabawy, *Bulletin of Material Sciences*, **34**(4), 873 (2011).
36. B.D. Cullity, Elements of X-ray Diffraction, Addison-Wesley Publication Company, Massachusetts, 1978.
37. M. P Rayman, The importance of selenium to human health, *The Lancet*, **356**, 233 (2000).

СИНТЕЗ, ОХАРАКТЕРИЗИРАНЕ И АНТИОКСИДАНТНА АКТИВНОСТ НА КОМПЛЕКСИ НА СЕЛЕН (IV) С НЯКОИ АМИНОКИСЕЛИНИ – БИНУКЛЕАРНИ КОМПЛЕКСИ

А. М. Наглах^{1,2*}, А. С. Ал-Васиди³, Н. М. Ал-Джафшар³, Дж. С. Ал-Отифи³, М. С. Рефат^{4,5}, У. Н. Хоцеин^{6,7}

¹ Департамент по фармацевтична химия, Катедра по разработване и изследване на лекарства, Колеж по фармация, Университет „Крал Сауд“, Рияд 11451, Саудитска Арабия

² Департамент по химия на пептидите, Отдел по изследване на химическата индустрия, Национален изследователски център, 12622 Доки, Кайро, Египет

³ Департамент по химия, Научен колеж, Университет „Принцеса Нура Бинт Абдулрахман“, Рияд 11671, Саудитска Арабия

⁴ Департамент по химия, Научен факултет, Тауфски университет, п.к. 888, Ал-Хауа, Тауф 21974, Саудитска Арабия

⁵ Департамент по химия, Научен факултет, Университет на Порт Сауд, Порт Сауд, Египет

⁶ Катедра по изследване на биопродукти, Департамент по зоология, Научен колеж, Университет „Крал Сауд“, Рияд 11451, Саудитска Арабия

⁷ Департамент по ботаника и микробиология, Научен факултет, Университет на Бени-Суеф, Бени Суеф 62111, Египет

Постъпила на 9 януари, 2018 г.; приета на 17 май, 2018 г.

(Резюме)

Получени са комплексите на селен (IV) с аминокиселините аспарагин (*Asn*), пролин (*Pro*), глутамин (*Gln*), метионин (*Met*) и цистеин (*Cys*) и са охарактеризирани чрез елементарен анализ, измерване на молната проводимост, спектрални изследвания (IR, Раман, UV-Vis, ¹H-NMR и мас-) и термогравиметричен анализ (TG/DTG). Изследванията на рентгеновата дифракция са проведени на дифрактометър PANalytical, повърхностната хомогенност на пробите е изследвана със сканиращ електронен микроскоп Quanta FEG 250 (SEM), а химичният състав на пробите е определен чрез енергийно-дисперсивен рентгенов анализ. Всички комплекси на селен (IV) (**I-V**) са от вида $[Se^{+4}(AA^{-1})_2Cl_2]$, където AA = (*Asn*, *Pro*, *Gln*, *Met* и *Cys*) се отнасят като монобазични лиганди. Масовите фрагменти на комплекса $[Se(Cys)_2(Cl)_2]$ (**V**) подкрепят твърдението за монобазичност. Предполагаемата геометрия на 1:2 комплексите е октаедрична конфигурация с два хлорни атома и два бидентатни лиганда, заемащи ъгловите места в октаедричните комплекси. В комплексите на селен с *Asn*, *Pro*, *Gln* и *Met*, amino и карбоксилните групи участват в координирането с метала, докато *Cys* се координира посредством сулфхидрилната и карбоксилната група. Активността на новосинтезираните комплекси на селен (IV) за отстраняване на свободни радикали е определена при концентрация от 10, 20 и 30 ppm въз основа на взаимодействието със стабилния свободен радикал 1,1-дифенил-2-пикрилхидразил (DPPH). Всички комплекси проявяват добра антиоксидантна активност.

Identification of volatile compounds from maize aerial parts infested by *Chilo partellus* (swine hoe) using GC-MS analysis

D. Pedda Kasim¹, P. Suneetha², M. S. R. Krishna^{1*}, B. Dinesh¹, R. Sri Deepthi¹, U. Lakshmi Sahitya¹

¹Department of Biotechnology, KL University, Green Fields, Vaddeswaram, Guntur- 522502, AP, India.

²Institute of Biotechnology, Prof. Jaya Shankar Telangana State Agricultural University, Hyderabad, India

Received May 25, 2017; Revised May 18, 2018

Zea mays is one of the most important staple foods in Asian and African countries and is the second-largest cultivated and highest-yielding crop in India. Lepidopteron stem borer *Chilo partellus* is a dangerous insect pest in maize. The stem borer makes holes on the stem and leaves and enters inside the stem for feeding. The plant was therefore investigated for its bioactive components. The present study was carried out to identify the volatile compounds present in the n-hexane extract of *Zea mays* by GC-MS analysis. Total 30 compounds were identified in both infected and uninfected samples. Among the 30 compounds butylated hydroxytoluene, n-hexadecanoic acid and 9,12,15-octadecatrienoic acid, (Z,Z,Z)- were identified as three common major components. Differences in their concentrations reveal their role in plant-insect interactions.

Keywords: *Zea mays*, GC-MS, n-Hexadecanoic acid and volatile compounds.

INTRODUCTION

Maize (*Zea mays* L.) is the third major cereal crop grown worldwide. It is extensively grown in temperate, subtropical and tropical regions of the world. Among several limiting factors, stem borer *Chilo partellus* is a serious insect pest affecting maize yield. For nutrition, the stem borer enters the host plant by forming holes on the stem and leaves. Attack of pest begins with laying eggs on leaves. Larvae then feed on leaves causing lesions. Further they bore into the stem feeding on tissues. This results in reduction in the surface area of photosynthesis in leaves. On the other side, plants possess several dynamic defense mechanisms against insect herbivores which include morphological, biochemical and molecular alterations [1]. The defense strategies against herbivores could be attained by physical barriers like trichomes, silica deposition and cell wall lignifications. Chemically, some toxic chemicals (alkaloids, terpenoids and phenolics) are synthesized by plants, which act as repellents, deterrents, antinutrients and significant part in pest control by the attracting carnivores [2, 3]. Herbivore-induced plant volatiles (HIPVs) are helpful to communicate between infected plants and natural enemies by attacking the insects, as well as they warn neighboring undamaged plants of the forthcoming danger [4]. These HIPVs help in feeding or oviposition or both of insects [5,6]. Generally HIPVs are released from the plant leaves, flowers and fruits into the atmosphere, or into the soil from the roots in response to herbivore attack

[7-9]. The HIPVs are emitted by both infected and uninfected plant parts, which increases the signal detection [10].

Around 2,000 volatile compounds were reported to be released from 900 plant families, in response to herbivore attack [5]. The nature of volatile compounds produced is highly specific to the insect-plant system [11-13]. The plants exposed to HIPVs have modified levels of defense-related metabolites, for example terpenoids [14], proteinase inhibitors and phenolic compounds [15]. The main objective of the present study is to analyze the various phytochemical constituents found in the aerial parts of *Zea mays* infected and uninfected by *Chilo partellus*.

MATERIALS AND METHODS

Plants

The maize seeds were collected from the farmers' fields; the seeds were sterilized with fungicides and planted in individual pots filled with fertilized soil in an insect-proof screen house in the KL University Guntur, Andhra Pradesh. All seedlings were grown at natural conditions; when they were 4-5 weeks old, the leaves and stem were collected for GC-MS analysis.

Insects

The *Chilo partellus* moths were obtained from a mass rearing unit at the Department of biotechnology, KL University. The stem borer larvae were collected and infected to the plants under closed conditions for trapping of volatile compounds.

* To whom all correspondence should be sent:

E-mail: msrkrishna81@gmail.com

Extraction of plant samples

The *Chilo partellus* infected and uninfected maize aerial parts (stem and leaves) were cleaned with tap water followed by Tween-20 and finally cleaned with distilled water; shade dried and cut in small pieces. The required quantity of these small pieces was weighed and transferred to soxhlet bags and soxhleted with n-hexane solvent until the pieces were fully immersed. Further, to remove high molecular weight compounds, waxes and heavy fractions, extracts were purified by following the method described by Rodríguez-Solana *et al.*, (2014) [16]. Treated extract was collected and evaporated to dryness by using a vacuum distillation unit. The final residue thus obtained was then subjected to GC-MS analysis.

GC-MS Analysis

GC-MS analysis of these extracts was performed using a Thermo Fisher scientific system and a gas chromatograph interfaced to a mass spectrometer (GC-MS) equipped with a Xcaliber software. For GC-MS detection, an electron ionization system with ionizing energy of 70 eV was used. Helium gas (99.999%) was used as the carrier gas at constant flow rate of 1 ml/min and an injection volume of 2µl was employed (split ratio of 10:1); Injector temperature 250°C; ion-source temperature 280°C. The oven temperature was programmed from 110°C (isothermal for 2 min), with an increase of 10°C/min, to 200°C, then at

5°C/min to 280°C, ending with a 9 min isothermal stay at 280°C. Mass spectra were taken at 70 eV; a scan interval of 0.5 sec and fragments from 45 to 450 Da. Total GC running time was 36 min. The relative % amount of each component was calculated by comparing its average peak area to the total areas, software adopted to handle mass spectra and chromatograms was Xcaliber. Data handling was done by using GCMS solution software. The identification of compounds was based on the comparison of their mass spectra with those of WILEY and NIST Libraries. The name, structure and molecular weight of the components of the test materials were determined.

RESULTS AND DISCUSSION

GC MS Analysis

The n-hexane extracts of uninfected and infected maize plant volatiles were identified by GC-MS. The chromatograms of both treated and control samples are depicted in Figures 1 and 2, respectively.

From the GC-MS analysis a total of 30 compounds (Table 1) were identified in both infected and uninfected samples. Analysis revealed that in both control and treated samples, three compounds, namely butylated hydroxytoluene, n-hexadecanoic acid and 9,12,15-octadecatrienoic acid, (Z,Z,Z)- (Table 2), displaying high peak areas, form the major components.

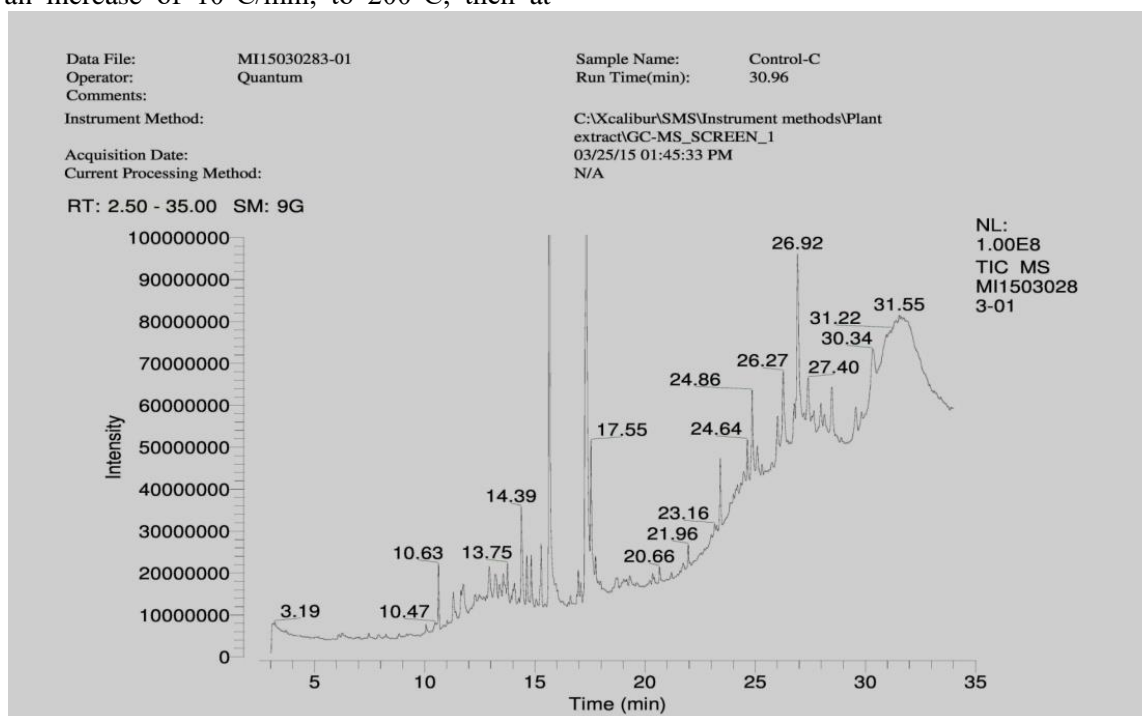


Fig. 1. GC – MS chromatogram of n-hexane extract from uninfected maize aerial parts.

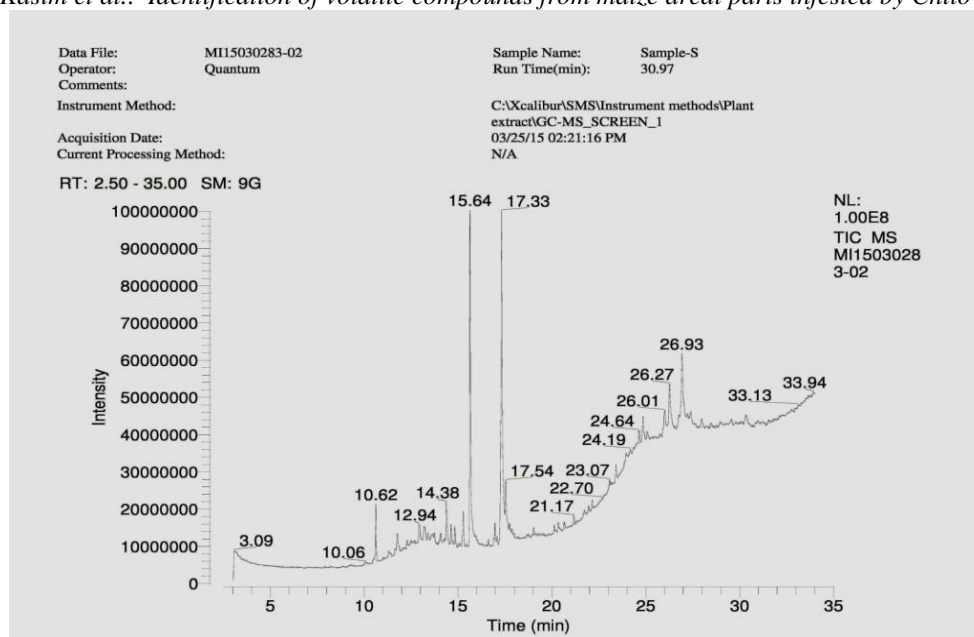


Fig. 2. GC – MS chromatogram of n-hexane extract from infected maize aerial parts

Table 1. List of volatile compounds identified in infected and uninfected maize aerial parts.

S. No	Compounds from larvae uninfected sample	Compounds from larvae infected sample
1	Tramadolo	6-Octadecenoic acid, methyl ester, (Z)-
2	Dodecane, 2,6,10-trimethyl	Hexacosane, 9-octyl-
3	Butylated hydroxytoluene	Butylated hydroxytoluene
4	Dodecanoic acid	Diethyl phthalate
5	Diethyl phthalate	Tridecane, 2-methyl-
6	Dodecane, 5,8-diethyl-	Heneicosane, 11-(1-ethylpropyl)-
7	Clocortolone pivalate	Benzene, (1-butyloctyl)-
8	Dodecane, 2,6,11-trimethyl-	Benzene, (1-propylnonyl)-
9	Selenium(IV) oxide	Octadecane, 3-ethyl-5-(2-ethylbutyl)-
10	Benzene, (1-propylnonyl)-	Benzene, (1-methylundecyl)-
11	Tetradecanoic acid	3,7,11,15-Tetramethyl-2-hexadecen-1-ol
12	2-Propenal, 3-(2,6,6-trimethyl-1-cyclohexen-1-yl)-	1,2-Benzenedicarboxylic acid, butyl 8-methylnonyl ester
13	Dodecane, 5,8-diethyl-	3,7,11,15-Tetramethyl-2-hexadecen-1-ol
14	Benzene, (1-methylundecyl)-	Hexadecanoic acid, methyl ester
15	3,7,11,15-Tetramethyl-2-hexadecen-1-ol	n-Hexadecanoic acid
16	9-Octadecen-1-ol, (Z)-	9,12-Octadecadienoic acid (Z,Z)-, methyl ester
17	1,2-Benzenedicarboxylic acid, butyl 8-methylnonyl ester	9,12,15-Octadecatrienoic acid, ethyl ester, (Z,Z,Z)-
18	3,7,11,15-Tetramethyl-2-hexadecen-1-ol	Phytol
19	Hexadecanoic acid, methyl ester	9,12-Octadecadienoic acid (Z,Z)-
20	1,2-Benzenedicarboxylic acid, butyl cyclohexyl ester	9,12,15-Octadecatrienoic acid, (Z,Z,Z)-
21	n-Hexadecanoic acid	Octadecanoic acid
22	9,12,15-Octadecatrienoic acid, methyl ester, (Z,Z,Z)-	Cyclononasiloxane, octadecamethyl-
23	Phytol	1H-Indene, 1-hexadecyl-2,3-dihydro-
24	9,12-Octadecadienoic acid (Z,Z)-	Bufo-20,22-dienolide, 3,14-dihydroxy-, (3á,5á)-
25	9,12,15-Octadecatrienoic acid, (Z,Z,Z)-	Phenanthrene, 9-dodecyltetradecahydro-
26	Octadecanoic acid	Spirolactone
27	1H-Indene, 1-hexadecyl-2,3-dihydro-	Lumicolchicine
28	Bis(2-ethylhexyl) phthalate	Xanthylum, 9-[2-(ethoxycarbonyl)phenyl]-3,6-bis(ethylamino)-2,7-dimethyl-, chloride
29	Triacotane	Heptadecane, 9-hexyl-
30	Tetratetracontane	Benzene, (1-ethyldecyl)

Table 2. Major volatile compounds identified in both uninfected and infected samples

Sample	RT	Compound name	Area percentage	Formula	Molecular weight
Uninfected sample	10.63	Butylated hydroxytoluene	4.42	C ₁₅ H ₂₄ O	220
	15.66	n-Hexadecanoic acid	28.45	C ₁₆ H ₃₂ O ₂	256
	17.34	9,12,15-Octadecatrienoic acid, (Z,Z,Z)-	24.23	C ₁₈ H ₃₀ O ₂	278
Infected sample	10.62	Butylated hydroxytoluene	10.42	C ₁₅ H ₂₄ O	220
	15.64	n-Hexadecanoic acid	21.62	C ₁₆ H ₃₂ O ₂	256
	17.32	9,12,15-Octadecatrienoic acid, (Z,Z,Z)-	26.84	C ₁₈ H ₃₀ O ₂	278

Out of the three compounds, two compounds, viz., n-hexadecanoic acid (palmitic acid) and 9,12,15-octadecatrienoic acid, (Z,Z,Z)- (linolenic acid) belong to the group of fatty acids, the other (butylated hydroxytoluene) being a phenol derivative. These three compounds are biologically active molecules as they play a major role in plants defense system and thence are included in the large group of protective molecules found in plants, called phytoprotectants [17].

Though the major components are the same in both samples, the concentrations of each compound varied between larvae infested and larvae uninfected samples. This shows that under the influence of herbivores, plants secrete different components with different concentrations. A higher concentration of n-hexadecanoic acid was found in larvae uninfected sample (28.55%), compared with infected sample (21.62%). The concentrations of butylated hydroxytoluene (4.42%) and 9,12,15-octadecatrienoic acid, (Z,Z,Z)- (24.23) were identified to be low in the uninfected sample while the same compounds showed high concentrations in infected samples. Increased concentration of butylated hydroxytoluene would play a protective role in the infected sample against oxidative stress. Butylated hydroxytoluene is a phenol compound which is known to have antioxidant activity which effectively prevents oxidation [18]. Increased linolenic acid would further increase the production of pheromones by insects as insects utilize compounds released by the host plant as pheromone precursors [19]. Also, the identified compounds may act as synomones which would attract parasitoids. Hilker *et al.*, 2001 [20] reported the ability of plants to produce synomones that would defend plants against the damage caused by feeding larvae.

GC-MS analysis is the initial step towards understanding the nature of plant volatile compounds. However, isolation of individual phytochemical constituents and subjecting them to biological activity analysis will definitely give fruitful results. It could be concluded that, *Zea mays* contains various bioactive compounds which are of importance in plant-insect interactions. However, further studies are needed to study its bioactivity, toxicity profile and IPM values.

CONCLUSION

In the present study total 30 compounds from the n-hexane aerial parts extracts of *Zea mays* were identified by gas chromatography–mass spectrometry (GC-MS) analysis. The nature of the identified volatile compounds is mostly fatty acids. The research findings have shown that the aerial part of *Zea mays* is extensively rich in secondary metabolites and the identified compounds can be used as synomones for controlling the maize stem borer.

Acknowledgement: Authors are thankful to K L University for providing the lab facilities and to Dr. K. Srinivasulu, Department of Biotechnology, for the constant support to carrying out this work.

REFERENCES

1. H. C. Sharma, G. Sujana, D. M. Rao, *Arthropod-Plant Interact.*, **3**, 151 (2009).
2. A. R. War, M. G. Paulraj, M. Y. War, S. Ignacimuthu, *J. Plant Growth Regul.*, **30**, 512 (2011).
3. R. Karban, I. T. Baldwin, K. J. Baxter, G. Laue, G. W. Felton, *Oecologia*, **125**, 66 (2000).
4. A. Kessler, I. T. Baldwin, *Science*, **291**, 2141 (2001).

D. Pedda Kasim et al.: Identification of volatile compounds from maize areal parts infested by *Chilo partellus* ...

5. A. A. Agrawal, Current trends in the evolutionary ecology of plant defense, *Funct. Ecol.*, **25**, 420 (2011).
6. S. Rasmann, A. A. Agrawal, *Curr. Opin. Plant Biol.*, **12**, 473 (2009).
7. G. Arimura, K. Matsui, Takabayashi, *J. Plant Cell Physiol.*, **50**, 911 (2009).
8. N. Dudareva, F. Negre, D. A. Nagegowda, I. Orlova, *Crit. Rev. Plant Sci.*, **25**, 417 (2006).
9. G. von Mérey, N. Veyrat, G. Mahuku, R. L. Valdez, T. C. J. D. Turlings, M. Alessandro, *Phytochem.*, **72**, 1838 (2011).
10. C.J. Frost, M.C. Mescher, J.E. Carlson, C.M. De Moraes, *Plant Physiol.*, **146**, 818 (2008).
11. C.R. Rodriguez-Saona, C.J. Rodriguez-Saona, L.E. Frost, *J. Chem. Ecol.*, **35**, 163 (2009).
12. M. Dicke, J. J. A. van Loon, R. Soler, *Nat. Chem. Biol.*, **5**, 317(2009).
13. C. Kost, M. Heil, *J Ecol.* **94**, 619 (2006).
14. J. Engelberth, H. T. Alborn, E. A. Schmelz, J. H. Tumlinson, *Proc. Natl. Acad. Sci. USA*, **101**, 1781 (2004).
15. J. Ruther, S. Kleier, *J. Chem. Ecol.*, **31**, 2217 (2005).
16. R. Rodríguez-Solana, J. M. Salgado, J. M. Domínguez, S. Cortés-Diéguez, *Phytochem. Anal.*, **26**(1), 61(2015).
17. T. Tschardtke, S. Thiessen, R. Dolch, W. Boland, *Biochem. Syst. Ecol.*, **29**, 1025 (2001).
18. M. S Brewer, *Compr. Rev. Food Sci. Food Saf.*, **10**, 221 (2011).
19. P. Zito, M. Sajeva, M. Bruno, A. Maggio, S. Rosselli, C. Formisano, F. Senatore, *Molecules*, **15**(2), 627 (2010).
20. M. Hilker, C. Kobs, M. Varama, K. Schrank, *J. Exp. Biol.*, **205**(4), 455(2002).

ИДЕНТИФИЦИРАНЕ НА ЛЕТЛИВИТЕ СЪЕДИНЕНИЯ ОТ НАДЗЕМНИТЕ ЧАСТИ НА ЦАРЕВИЦА, ИНФЕКТИРАНИ С *Chilo partellus*, С ПОМОЩТА НА GC-MS АНАЛИЗ

Д. Педа Касим¹, П. Сунета², М. С. Р. Кришна^{1*}, Б. Динеш¹, Р. Шри Дефти¹, У. Лакшми Сахити¹

¹ Департамент по биотехнология, КЛ университет, ГрийнФийлдс, Вадесварам, Гунтур - 522502, АП, Индия

² Институт по биотехнология, Държавен селскостопански университет "Проф. Джая Шанкар Телангана", Хайдерабад, Индия

Постъпила на 25 май, 2017 г.; коригирана на 18 май, 2018 г.

(Резюме)

Царевицата (*Zea mays*) е една от най-важните храни в страните от Азия и Африка и е на второ място по култивиране и с най-голям добив в Индия. Представителите на *Chilo partellus* са едни от най-вредните насекоми за царевицата. Те пробиват дупки в ствола и листата и влизат в тях, за да се хранят. По тази причина са изследвани биоактивните компоненти в растението. В настоящото изследване са идентифицирани летливите съединения, намиращи се в н-хексанов екстракт от *Zea mays* чрез GC-MS анализ. Общо 30 съединения са идентифицирани както в инфектираните, така и в неинфектираните растения, като основните компоненти са бутилиран хидрокситолуен, н-хексадеканова киселина и (Z,Z,Z)-9,12,15-октадекатриенова киселина. Разликите в концентрациите им разкриват ролята им във взаимодействията растение-насекомо.

Antioxidant potential, total phenolic and flavonoid contents of three culinary medicinal plant species of Lesser Hamalya, Pakistan

M. Ishaque¹, Y. Bibi¹, A. Qayyum^{2*}, M. Khalid Rafiq³, M. Arshad¹, S. M. Saqlan Naqvi⁴, S. Nisa⁵, M. A. Jenks⁶

¹Department of Botany, Pir Mehr Ali Shah, Arid Agriculture University Rawalpindi, 46000 Pakistan

²Department of Agronomy, The University of Haripur, 22620 Pakistan

³School of Geosciences, The University of Edinburgh, EH3 9FF, United Kingdom

⁴Department of Biochemistry, Pir Mehr Ali Shah, Arid Agriculture University Rawalpindi, 46000 Pakistan

⁵Department of Microbiology, The University of Haripur, 22620 Pakistan

⁶School of Plant Sciences, University of Arizona, Tucson, Arizona, 85721 USA

Received November 30, 2017; Revised February 15, 2018

It is well known that oxidative stress due to free radicals can lead to many human illnesses, like cancer. Antioxidants are the agents which scavenge these free radicals and protect the biological system. Food of plant origin is an essential source of reliable antioxidants. These plant-derived antioxidants belong to many biochemical categories but most are phenolics or flavonoids. The Galyat region of Pakistan is rich in plant biodiversity, and local inhabitants frequently use medicinal plants to treat common ailments. Three of these common regional medicinal plants (*Dryopteris ramosa*, *Quercus leucotricophora* and *Arisaema flavum*) were selected and their free radical scavenging potential was investigated using DPPH assay. The crude extract of *D. ramosa* exhibited the maximum free radical scavenging potential ($93.8 \pm 0.2\%$) while *A. flavum* ($56.4 \pm 0.4\%$) showed the lowest radical scavenging potential at 250 $\mu\text{g/ml}$. A low SC_{50} value of the crude extract of *D. ramosa* ($88.9 \pm 0.4 \mu\text{g/ml}$) confirmed the relatively high antioxidant potential of this plant species. Among the polarity-based fractions obtained from crude extract of *D. ramosa*, the ethyl acetate soluble fraction showed maximum free radical scavenging potential. The *D. ramosa* contained higher amounts of total phenolic and flavonoid compounds than *Quercus* and *Arisaema* species. A significant Pearson correlation at the 0.01 level (2 tailed) was also noticed between SC_{50} and total phenolic contents of all extracts. A significant difference in percentage scavenging activities of the various extracts was observed. The ethyl acetate soluble phase of *D. ramosa* may prove to be an especially useful source of natural antioxidants for a variety of medicinal uses. Further studies are in progress.

Keywords: Antioxidant, Total phenolics, Total flavonoids, *Dryopteris ramosa*, *Quercus leucotricophora*, *Arisaema flavum*

INTRODUCTION

Recent studies have confirmed the detrimental role of free radicals (reactive oxygen species ROS) and their direct role in causing oxidative stress leading to many human disorders. These free radicals are produced in the biological system by a variety of environmental factors, such as a poor diet, exposure to toxins, and emotional stress. Antioxidants are compounds that scavenge ROS and other free radicals and protect living cells. Antioxidants are not only prescribed as preventive measures against ROS to protect human health, but are also used for the treatment of various human diseases [1,2]. Plant-derived antioxidants belong to different biochemical categories, but are typical secondary metabolites concentrated in various plant organs specific to the different species [3-5]. Recently, plant antioxidants belonging to the phenolic and flavonoid classes, including ascorbic acid, tocopherol, various tocotrienols and carotenoids [6] have gained much importance. The

Galyat area ~ 50 km North East of Islamabad, Pakistan, is a moist temperate forest with an area of 1011.714 km² [7], lacking modern facilities, especially for health care, and as such the inhabitants are much dependent on indigenous medicinal plant species [8]. The area is rich in medicinal plants [9], and the local people use many plant species to cure various ailments including gastric ulcers, digestive problems [10], fever, as astringents, back ache [11], antidote against snake bite, cattle's mouth and foot diseases, skin diseases [12].

The research presented in this paper evaluates the antioxidant properties of three common and extensively used medicinal plants in the Galyat region, and sheds light on the relationship between the antioxidant potential of these species and their total phenolic and flavonoid contents. The selected plant species include *Dryopteris ramosa* (Hope) C. Chr, *Quercus leucotricophora* A. Camus and *Arisaema flavum* (Forssk.) Schott. The ethnomedicinal uses of these plants are given in Table 1.

* To whom all correspondence should be sent:

E-mail: aqayyum@uoh.edu.pk

Table 1. Selected plant species and their ethnomedicinal uses.

Botanical name	Local name	Plant's family	Part used	Ethnomedicinal uses
<i>Dryopteris ramosa</i> (Hope) C. Chr.	Pakha	Dryopteridaceae	Fronde	Tonic, gastro-intestinal, antimicrobial and anti-cancer (13) gastric ulcer, constipation and aphrodisiac (10)
<i>Quercus leucotricophora</i> A. Camus	Rein	Fagaceae	Leaves, bark	Antitumor (14) diarrhea, indigestion, asthma and gonorrhoea (10)
<i>Arisaema flavum</i> (Forssk.) Schott.	Saap Booti	Aeraceae	Rhizome	Antidote (Snake bite) (15) Rhizome juice is applied on earache and skin diseases (16)

EXPERIMENTAL

Plant species

Leaves of the Pakistan wood fern *Dryopteris ramosa* (Hope) C. Chr., the Banj oak *Quercus leucotricophora* A. Camus, and rhizomes of yellow cobra lily *Arisaema flavum* (Forssk.) Schott were collected from the Galyat area, Pakistan. The plants were identified by Dr. Rehmatullah Qureshi at the Department of Botany, PMAS-Arid Agriculture University Rawalpindi, Pakistan. Herbarium specimens were deposited in the Herbarium of Quaid-i-Azam University, Islamabad, Pakistan.

Preparation of crude methanolic extract

The crude methanolic extracts were prepared by maceration technique as described in [17] with some modifications and the dried crude methanolic extracts were stored in air-tight containers at 4 °C.

Evaluation of free radical scavenging (antioxidant) activity

Each extract was evaluated for its antioxidant potential using a free radical scavenging assay as described in [18, 19] with some modifications. The extract solution was prepared in methanol at a 1:40 ratio (mg/ml) w/v. Ascorbic acid was used as a standard, while methanol was used as a blank. A stock solution (5 mg/ml) of each extract was made in methanol and subsequent dilutions of 25, 50, 100, 150, 200 and 250 µg/ml were prepared. Then, 200 µl from each dilution was mixed with 200 µl of DPPH (di(phenyl)-(2,4,6-trinitrophenyl)iminoazanium) solution and placed in dark at 25-30 °C for 30 min. Next, the contents of each reaction tube were subjected for spectrophotometric analysis at 517 nm, and free radical quenching potential was determined using the following equation:

$$\text{Scavenging (\%)} = \left[\frac{\text{Absorbance}_{(\text{control})} - \text{Absorbance}_{(\text{sample})}}{\text{Absorbance}_{(\text{control})}} \right] \times 100$$

The scavenging concentration 50 % (SC₅₀) was calculated by regression equation. SC₅₀ is the half maximal scavenging concentration. (SC₅₀) is a measure of the effectiveness of a substance in

scavenging the free radicals in specific biological or biochemical function. The terms IC₅₀ and SC₅₀ may be used as synonym by the fact that both have been used to demonstrate 50 % potential concentration. According to the FDA, IC₅₀ represents the concentration of a drug that is required for 50 % inhibition *in vitro*. For competitive binding assays and functional antagonist assays the most common summary measure of the dose-response curve is the IC₅₀, the concentration of substance that provides 50 % inhibition [20]. *In vitro* IC₅₀ is a very basic starting point in determining the potential efficacy of a developmental drug.

Estimation of total phenolic contents

For the purpose of estimation of total phenolic contents of the extracts, a standard method was used as described in [21]. For plotting a reference standard calibration curve, different dilutions (25, 50, 100, 150, 200 and 250 µg/ml) of gallic acid were used. The reaction mixture contained 500 µl from each dilution of gallic acid, 10 × diluted 2.5 ml of Follin-Ciocalteu reagent and 2.5 ml of 7 % (w/v) Na₂CO₃. Gallic acid was replaced with 500 µl of plant extract (1 mg/ml) to the obtained reaction mixture for the test sample. Each reaction tube was vortexed and incubated at 25-30 °C for half an hour and then spectrophotometric analysis was carried out at 760 nm.

Estimation of total flavonoid contents

For the determination of total flavonoid contents of each extract, a standard AlCl₃ method was used as suggested in [22], with slight modifications. For plotting a reference standard calibration curve, different dilutions (25, 50, 100, 150, 200 and 250 µg/ml) of quercetin were used. The reaction mixture contained 500 µl from each dilution of quercetin, vortexed with 10 % AlCl₃ (100 µl), and after one min 100 µl of CH₃COOK (1 M) was added and vortexed again, followed by addition of distilled water (2.8 ml) after one min and once again vortexed. Quercetin was replaced with 500 µl of plant extract (1 mg/ml) to the obtained reaction mixture for the test sample. Each of these reaction

M. Ishaque et al.: Antioxidant potential, total phenolic and flavonoid contents of three culinary medicinal plant species
 tubes was incubated at room temperature for 30 min and spectrophotometric analysis was carried out at 415 nm.

Polarity based fractions of D. ramosa

The crude methanolic extracts of *D. ramosa* were fractionated into n-hexane, chloroform, ethyl acetate, and the aqueous phase was treated as suggested in [23]. All fractions thus obtained were evaluated for their free radical scavenging potential, total phenolic content and total flavonoid content as described earlier.

Statistical analysis

All values are mean of triplicates \pm standard deviation (SD). Using Statistical Package for Social Science (SPSS) Programme 16.0, univariate analyses of all extracts were performed at $p \leq 0.05$. Pearson correlation at the 0.01 level (2 tailed) was also determined between SC_{50} and total phenolic contents of plant extracts.

RESULTS

Antioxidant potential

The free radical scavenging potential (% scavenging) of crude extracts of *D. ramosa*, *Q. leucotricophora* and *A. flavum* and various fractions of *D. ramosa* at different concentrations are shown in Table 2. Among the crude extracts, those of *D. ramosa* exhibited a higher scavenging potential than the other species. For instance, at a concentration of 250 $\mu\text{g/ml}$, the percent free radical scavenging was 93.8 ± 0.2 , 86.0 ± 0.2 and 56.4 ± 0.4 for *D. ramosa*, *Q. leucotricophora* and *A. flavum* species, respectively. Similarly, among the various solvent polarity-based fractions of *D. ramosa*, the ethyl acetate fractions showed the highest free radical percentage scavenging potential, while the least antioxidant potential was exhibited by the chloroform soluble fraction of *D.*

ramosa (Table 2). Regression line equations were used to determine the SC_{50} of each crude extract and the various fractions obtained from *D. ramosa*. Ascorbic acid was used as a standard and its SC_{50} was $44.5 \pm 0.2 \mu\text{g/ml}$. The crude methanolic extract of *D. ramosa* showed the lowest SC_{50} while *A. flavum* had the highest SC_{50} . Among the fractions of *D. ramosa*, the ethyl acetate fraction had the lowest SC_{50} value (Table 3). The low SC_{50} value indicates a higher antioxidant potential and so the ethyl acetate fraction of *D. ramosa* was revealed to have the best antioxidant potential.

Total phenolic contents

The total phenolic contents of crude extracts and fractions were calculated by a linear regression equation ($y = 0.0071x + 0.4332$, $R^2 = 0.9606$) primed with a gallic acid standard calibration curve, and expressed in terms of gallic acid equivalent. Crude methanolic extract of *D. ramosa* had the highest amount of phenolic constituents, followed by *Q. leucotricophora* and *A. flavum* (Table 3). Among the polarity-based solvent soluble fractions of *D. ramosa*, higher phenolic contents were shown by ethyl acetate soluble fractions ($55.7 \pm 0.5 \mu\text{g/mg GAE}$), while the least ones ($13.8 \pm 0.6 \mu\text{g/mg GAE}$) were present in the chloroform fractions of *D. ramosa*.

Total flavonoid contents

The total flavonoid contents of crude extracts and fractions were calculated from a linear regression equation ($y = 0.0063x + 0.395$, $R^2 = 0.9697$) primed from a quercetin standard calibration curve. Crude methanolic extract of *D. ramosa* has higher total flavonoids than all other crude extracts in the present study, while the ethyl acetate soluble fraction showed higher total flavonoids than all other fractions obtained from *D. ramosa* (Table 3).

Table 2. DPPH free radical scavenging potential of selected plant species.

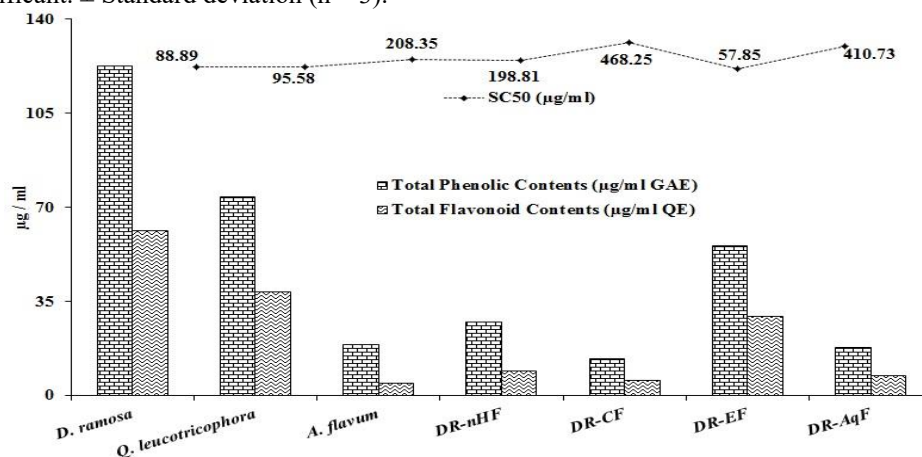
Concentrations		25 $\mu\text{g/ml}$	50 $\mu\text{g/ml}$	100 $\mu\text{g/ml}$	150 $\mu\text{g/ml}$
Crude extracts (% scavenging)*	<i>D. ramosa</i>	23.7 ± 0.8	30.8 ± 1.6	68.8 ± 1.8	73.7 ± 1.6
	<i>Q. leucotricophora</i>	21.5 ± 0.6	38.1 ± 0.1	53.3 ± 0.2	76.3 ± 0.4
	<i>A. flavum</i>	05.9 ± 0.2	24.7 ± 0.3	32.8 ± 0.1	38.5 ± 0.4
Fractions of <i>D. ramosa</i> (% scavenging)*	n-Hexane fraction	26.6 ± 0.5	33.3 ± 0.4	33.2 ± 0.2	44.7 ± 0.9
	Chloroform fraction	17.3 ± 0.2	19.9 ± 0.2	21.6 ± 0.3	26.0 ± 0.7
	Ethyl acetate fraction	36.7 ± 0.3	44.1 ± 0.4	69.9 ± 0.6	76.7 ± 0.7
	Aqueous fraction	18.3 ± 0.2	19.1 ± 0.1	26.9 ± 0.5	27.7 ± 0.5
Standard (% scavenging)*	Ascorbic acid	37.1 ± 1.6	54.3 ± 0.5	77.8 ± 2.9	92.0 ± 1.4

*All values are mean of triplicate ($n = 3$) \pm standard deviation.

Table 3. Total phenolics, total flavonoid contents and antioxidant potential of selected plant species.

Extracts (Samples)	Total phenolic contents ($\mu\text{g}/\text{mg}$ GAE)	Total flavonoid contents ($\mu\text{g}/\text{mg}$ QE)	Antioxidant potential [SC_{50} ($\mu\text{g}/\text{ml}$)]		
			Samples (Extracts)	Standard (Ascorbic acid)	
Crude extracts	<i>D. ramosa</i>	122.6 ± 4.4	61.4 ± 17.9	88.9 ± 0.4	
	<i>Q. leucotricophora</i>	74.1 ± 7.7	38.7 ± 11.0	95.6 ± 0.4	
	<i>A. flavum</i>	19.0 ± 6.3	4.6 ± 1.2	208.4 ± 0.1	
<i>D. ramosa</i> fractions	n-Hexan fraction	27.3 ± 0.4	9.4 ± 0.3	198.8 ± 0.0	44.5 ± 0.2
	Chloroform fraction	13.8 ± 0.6	5.8 ± 0.1	468.2 ± 0.0	
	Ethyl acetate fraction	55.7 ± 0.5	29.7 ± 0.4	57.8 ± 0.1	
	Aqueous fraction	18.0 ± 0.4	7.3 ± 0.1	410.7 ± 0.1	

Legend: GAE = Gallic acid equivalent, QE= Quercetin equivalent, Results are mean of three parallel measurements. $P \leq 0.05$ as significant. \pm Standard deviation (n = 3).

**Fig. 1.** Relationship between SC_{50} , total phenolic content and total flavonoid content of the plant extracts.

DISCUSSION

It is noteworthy that various chronic health disorders are due to the stress caused by free radicals in the bodies of living organisms [24]. These free radicals can accumulate in the human body, because of various factors including poor diet, environmental factors, and emotional stress. Within living systems therefore, the necessity of antioxidative systems is essential. It is also important to note that substances exhibiting low antioxidant potential *in vitro* show similar low free radical scavenging abilities *in vivo* [25]. Human health specialists worldwide are interested in antioxidant substances, especially for their potential use in the treatment of various human diseases. Most of these antioxidants have been identified and isolated from plants, although a few have synthetic origins [26]. It is generally considered that natural antioxidants from plants are much safer than synthetic forms [27].

The Galyat region of Pakistan is mountainous, and distant from modern health facilities. For that reason, local inhabitants rely heavily on medicinal plants species of the area to treat many health problems. The ethnomedicinal knowledge of indigenous people is based on experience and traditions that have been transmitted from generation to generation. This cultural knowledge

might provide clues in identifying new therapeutic substances. The findings of this report confirm the medicinal status of three plant species (*D. ramosa*, *Q. leucotricophora* and *A. flavum*) commonly used as medicinal plants in this region (Table 1, Table 2), and is consistent with the findings of previous studies of these species [28-30].

In the DPPH antioxidant assay, the IC_{50} , and the antioxidant potential exhibited an inverse relationship. The order of SC_{50} among the selected crude extract was *D. ramosa* < *Q. leucotricophora* < *A. flavum*, findings that indicate that *A. flavum* has the least ability to scavenge free radicals. Ethyl acetate soluble fraction of *D. ramosa* showed better antioxidant potential (SC_{50} 57.8 ± 0.1 $\mu\text{g}/\text{ml}$) than crude methanol extracts of the same plant. The reason might be that antioxidant components have polar nature. In a similar study, Lee *et al.*, 2003, isolated two antioxidant compounds from the ethyl acetate soluble fraction of a fern that is closely related to *D. ramosa*, called thick-stemmed wood fern, *Dryopteris crassirhizoma* Nakai [30].

Phenolic constituents have recently shown their worth in the food industry through their ability not only to protect lipids from oxidative degradation, but also in their ability to improve the nutritional value and quality of food [31]. The phenolics examined in these studies were primarily derived

M. Ishaque et al.: Antioxidant potential, total phenolic and flavonoid contents of three culinary medicinal plant species from plants, and belonged to several biochemical categories, mainly flavonoids, flavones, and flavonols that exhibited excellent antioxidant properties [2]. It is also important to note that the plant extracts examined in that study had higher total phenolic and flavonoid contents, showed lower IC₅₀ values, and hence a higher free radical scavenging potential (Fig. 1), consistent with the results of the present study. For instance, the total phenolic contents of the methanolic extracts of *D. ramosa* were higher compared to the extracts of other species, and similarly, the total phenolic contents of *D. ramosa* ethyl acetate fractions were higher compared to all other fractions obtained from *D. ramosa*. Significant Pearson correlation at the 0.01 level (2-tailed) was also noticed between IC₅₀ and total phenolics contents of all crude extracts and fractions, as reported by others [32-34]. Our results are in accordance with previous reports suggesting that the high antioxidant potential of the ethyl acetate phase of *D. ramosa* is due to higher contents of phenolics and flavonoids.

CONCLUSION

Our results show that the antioxidant potential is related to the total phenolics contents of the plants, and also that plant phenolics contents are more concentrated in medium-polarity solvent-soluble fractions, like the ethyl acetate fraction. These findings reveal a significant and potentially useful variation in antioxidant potential for important medicinal plants in the Galyat region of Pakistan, as well as a potential for future research seeking to isolate and identify novel antioxidants from ethnobotanically-associated medicals.

Acknowledgement: The authors express their gratitude to the Department of Biochemistry, PMAS- Arid Agriculture University Rawalpindi, Pakistan for providing spectroscopic facility.

REFERENCES

1. B. Halliwell, J. M. C. Gutteridge, *FEBS Lett.*, **128**, 347 (1981).
2. P. Nunes, S. Silva, R. Guedes, S. Almeida, *J. Phytochem.*, **2**(4), 344 (2012).
3. R. Apak, K. Guclu, B. Demirata, M. Ozyurek, C. S. Esin, B. Bektasoglu, K. Berker, D. Ozyur, *Molecules*, **12**, 1496 (2007).
4. A. Sharma, C. Shankar, L. Tyagi, M. Singh, C. Rao, *Academic J Plant Sci.*, **2**, 26 (2008).
5. L. Samuel, R. Muthukumaran, R. Vanlalhraaii, G. Gurusubramanian, N. K. Senthil, *SciVision*, **13**(4), 149 (2013).
6. J. Dai, R. Mumper, *Molecules*, **15**, 7313 (2010).
7. S. Jamal, M.Sc. Thesis, Hazara University, Pakistan, 2009

8. S. Khan, M.Sc. Thesis, University of Peshawar, Pakistan, 2003.
9. S. Irshad, S. Khan, *J. Env.*, **1**(4), 119 (2012).
10. A. M. Abbasi, M. A. Khan, M. H. Shah, M. M. Shah, A. Pervez, M. Ahmad, *J. Ethnobiol. Ethnomed.*, **9**, 66, (2013).
11. M. Kumar, M. A. Sheikh, R. W. Bussmann, *J. Ethnobiol. Ethnomed.*, **7**, 32 (2011).
12. M. Kumar, Y. Paul, V. K. Anand, *J. Ethnobotanical Leaflets*, **13**, 1240 (2009).
13. A. Tariq, M. Adnani, S. Begum, *Pak. J. Bot.*, **48**(4), 1537 (2016).
14. V. Patni, N. Sharma, P. Mishra, *Int. J. Life Sci.*, **1**(3), 186 (2012).
15. Q. Zabihullah, A. Rashid, N. Akhtar, *Pak. J. Plant Sci.*, **12**(2), 115 (2006).
16. R. M. Kunwar, K. P. Shrestha, R. W. Bussmann, *J. Ethnobiol. & Ethnomed.*, **6**, 35 (2010).
17. S. S. Handa, S. S. Khanuja, G. Longo, D. D. Rakesh, *Extraction Technologies for Medicinal and Aromatic Plants*, (1st ed.), 2008.
18. T. Kulisic, A. Radonic, V. Katalinic, M. Milos, *J. Food Chem.*, **85**, 633 (2004).
19. H. K. Obeid, M. S. Allen, D. R. Bedgood, P. D. Prenzler, K. Robards. *J. Agric. Food Chem.*, **53**, 9911 (2005).
20. J. L. Sebaugh, *Pharm. Stat.*, **10**(2), 1539 (2011).
21. V. L. Singleton, J. J. A. Rossi, *Am. J. Enol. Viticult.*, **16**, 144 (1965).
22. J. Zhishen, T. Mengcheng, W. Jianming, *J. Food Chem.*, **64**, 555 (1999).
23. Y. Bibi, S. Nisa, F. M. Chaudhary, M. Zia, *J. Complement. Alt. Med.*, **11**, 52 (2011).
24. L. A. Pham-Huy, H. He, C. Pham-Huy, *Int. J. Biomed. Sci.*, **4**, 89 (2008).
25. P. Kalita, T. K. Barman, T.K. Pal, R. Kalita, *J. Drug Dev. Therap.*, **3**(4), 33 (2013).
26. S. Sannigrahi, U. K. Mazumder, D. Pal, S. L. Mishra, *Indian J. Exp. Biol.*, **5**(20), 394 (2009).
27. W. Zheng, S. Y. Wang, *J. Agric. Food Chem.*, **49**, 5165 (2001).
28. A. Sekendar, M. Kawsarul, R. Obayed, R. Khalilur, H. Aslam, A. Shah, *Int. J. Drug Dev. Res.*, **4**(2), 223 (2012).
29. K. Kriechbaum, *Tibetan Medicinal Plants, Arisaema* (Araceae) (Chap.12), 2001, p. 77.
30. S. M. Lee, M. K. Na, R. B. An, B. S. Min, H. K. Lee, *J. Biol. Pharm. Bull.*, **26**(9), 1354 (2003).
31. M. Kähkönen, A. Hopia, H. Vuorela, J. Rauha, K. Pihlaja, T. Kujala, M. Heinonen, *J. Agric. Food Chem.*, **47**, 3954 (1999).
32. G. Yasin, Y. Merve, H. Şebnem, K. Ayşe, *J. Pharm. Sci.*, **37**, 17 (2012).
33. D. Krishnaiah, R. Sarbatly, R. Nithyanandam, *J. Food Bioprod.*, **89**, 217 (2011).
34. X. J. Duan, W. W. Zhang, X. M. Li, B. G. Wang, *J. Food Chem.*, **95**(1), 37 (2006).

АНТИОКСИДАНТЕН ПОТЕНЦИАЛ, ОБЩО СЪДЪРЖАНИЕ НА ФЕНОЛИ И ФЛАВОНОИДИ В ТРИ ВИДА КУЛИНАРНИ РАСТЕНИЯ В ЛЕСЕР ХАМАЛИЯ, ПАКИСТАН

М. Ишак¹, Я. Биби¹, А. Кайум^{2*}, М. Халид-Рафик³, М. Аршад¹, С. М. Саклан Накви⁴, С. Низа⁵, М. А. Дженк⁶

¹ Департамент по ботаника „Пир Мер Али Шах“, Селскостопански университет „Арид“, Равалпинди, 46000 Пакистан

² Департамент по селскостопански науки, Харипурски университет, 22620 Пакистан

³ Рейнджланд Изследователски институт, Национален селскостопански изследователски център, Исламабад, 44000 Пакистан

⁴ Департамент по биохимия, „Пир Мер Али Шах“, Селскостопански университет „Арид“, Равалпинди, 46000 Пакистан

⁵ Департамент по микробиология, Харипурски университет, 22620 Пакистан

⁶ Отдел по науки за растенията и почвите, Университет на Западна Вирджиния, Моргантаун, WV 26506-6108, САЩ

Постъпила на 30 ноември, 2017 г.; коригирана на 15 февруари, 2018 г.

(Резюме)

Добре е известно, че оксидативният стрес, дължащ се на свободни радикали, може да доведе до много болести при човека, например, рак. Антиоксиданти са агентите, които отстраняват свободните радикали и предпазват биологичната система. Храните от растителен произход са съществен източник на антиоксиданти. Антиоксидантите, извлечени от растенията принадлежат на различни биохимични категории, но повечето са феноли или флавоноиди. Районът „Галят“ в Пакистан е богат на различни растения и местните жители често използват медицински растения за лечение на различни болести. Избрани са три от тези разпространени в района медицински растения (*Dryopteris ramosa*, *Quercus leucotricophora* и *Arisaema flavum*) и е изучен потенциалът им за отстраняване на свободни радикали с помощта на DPPH анализ. При концентрация 250 µg/ml суровият екстракт на *D. ramosa* проявява максимален радикал-отстраняващ потенциал (93.8 ± 0.2 %), а *A. Flavum* – минимален потенциал (56.4 ± 0.4 %). Ниската стойност на SC_{50} на суровия екстракт на *D. ramosa* (88.9 ± 0.4 µg/ml) повърди сравнително високия антиоксидантен потенциал на този растителен вид. Между полярните фракции, получени от суровия екстракт на *D. ramosa*, фракцията, разтворима в етилацетат показва най-висок потенциал за отстраняване на свободни радикали. Видът *D. ramosa* съдържа по-големи количества общи фенолни и флавоноидни съединения в сравнение с видовете *Quercus* и *Arisaema*. Установена е значима корелация на Pearson на ниво 0.01 (двустранна) между SC_{50} и общото фенолно съдържание на всички екстракти. Има съществена разлика в процентната отстраняваща активност на различните екстракти. Фазата от *D. ramosa*, разтворима в етилацетат може да се окаже полезен източник на природни антиоксиданти с различни медицински приложения. По-нататъшни изследвания са в ход.

Study of phytochemical changes, enzymatic and antioxidant activity of two halophyte plants: *Salsola dendroides* Pall and *Limonium reniforme* (Girard) Lincz in different seasons

S. Bakhshi¹, H. Abbaspour*¹, S. Saeidisar²

¹ Department of Biology, Damghan Branch, Islamic Azad University, Damghan, Iran.

² Dr.Shariaty Technical College, Technical and Vocational University, Tehran, Iran.

Received December 8, 2017; Revised December 16, 2017

In order to study phytochemical changes, enzymatic and antioxidant activity of *Salsola dendroides* Pall. and *Limonium reniforme* (Girard) Lincz halophytes, leaf and root samples of these plants were collected from Incheh Borun region in northern Gorgan, Iran, in three seasons (spring in May, summer in August, and autumn in November) in four iterations. The results showed that soil salinity level increased in autumn and significantly increased enzyme activities and antioxidant activities in shoots and roots of both species in most cases. Phytochemical studies showed that phenol content significantly increased in shoot and root of *Salsola dendroides* in summer and autumn and in *Limonium reniforme* in summer, compared to the other two seasons. Flavonoid content also significantly changed with seasonal variation. The highest flavonoid accumulation was observed in shoots and roots of the plants in summer; most of these changes were related to activation of physiological and biochemical processes which allow the plants to adapt to salinity conditions.

Keywords: Phenol, Flavonoid, Antioxidant enzymes, Salinity

INTRODUCTION

Variability of environmental conditions, such as fluctuations in temperature, humidity, salinity, and UV radiation, results in increased production of reactive oxygen species (ROS) inducing oxidative stress in plant cells [1,2]. Antioxidants are compounds which inhibit oxidative reactions of plants by free radicals. Also called reactive oxygen species (ROS), free radicals are frequently produced as by-products of various metabolic mechanisms in plants and are accumulated in different cellular compartments such as chloroplasts, mitochondria, and peroxisomes [3,4]. Accumulation of free radicals such as hydrogen peroxide (H₂O₂), superoxide (O₂⁻), hydroxyl radical (HO[•]), and singlet oxygen causes oxidative damage to proteins, lipids, nucleic acid, and photosynthetic enzymes; therefore, it disrupts normal plant metabolism [5].

Halophytes are natural herbs in saline habitats and can be a good candidate for having unsaturated fatty acids, beta-carotene, sterols, as well as active enzymatic and phytochemical compounds, for example, phenolic compounds, and more specifically fluorutanins, terpenes and alkaloids that have antioxidant and anti-microbial properties [6].

In the past decade, there has been a new interest in the search for phytochemical compounds from natural native plants to provide pharmaceutical and nutritional materials [7] recognizing that the products derived from them can be useful for

pharmaceutical purposes [8]. This is mainly due to their high biological activity and antioxidant compounds [9]. Among herbal antioxidant compounds, phenolic compounds such as phenol and flavonoids are widely distributed in many plants which synthesize and accumulate them in response to biological and non-biological stresses such as salinity [10].

Antioxidant properties of phenolic compounds are deliberately due to regenerative capacity of their chemical structure, which enables them to neutralize free radicals, form complexes with metal ions, silence single and triple oxygen molecules and reduce oxidative damages caused by ions. By inhibiting lipoxygenase, they inhibit peroxidation of lipids [11]. Since there is a significant interest in natural antioxidants, efforts have been made to find alternative sources of these antioxidants. Therefore, it is logical that plants such as halophytes are identified due to their high antioxidant properties. Thus, this study tends to investigate phytochemical changes and enzymatic and antioxidant activity in *Salsola dendroides* from the *Chenopodiaceae* family and *Limonium reniforme* from the *Pallumbazinasea* family under naturally applied stress in different seasons.

MATERIALS AND METHODS

Samples of two species, *Salsola dendroides* Pall. (chenopodiaceae family) and *Limonium reniforme* (Girard) Lincz (plumbaginaceae family) were

* To whom all correspondence should be sent:

E-mail: h.abbaspour75@hotmail.com

randomly obtained from their natural habitats in Inchehboron region, Gorgan, North Eastern Iran (37° 27' N, 54° 43' E) in 4 iterations during spring (May), summer (August), and autumn (November), 2015. The samples were then transferred to a laboratory for testing peroxidase, ascorbate peroxidase, polyphenol oxidase, and catalase enzyme activities, antioxidant activity (DPPH test) as well as content of phytochemical compounds. Samples were rinsed by distilled water before the tests.

Enzyme extraction

Proteins were extracted as suggested in [12]. For this purpose, 5 ml 0.05 M Tris buffer-HCl, pH 5.7, was added to fresh leaf tissues in a mortar and kept for 30 min. Then, the tissues were ground by pestle in an ice bath. The solution was centrifuged at 13000 rpm and 4°C. Protein extraction was used for testing peroxidase, catalase, and polyphenol oxidase activities. Ascorbate peroxidase is vulnerable in the absence of ascorbate. Therefore, 0.2 ml 0.5 µM ascorbate was added to test ascorbate peroxidase activity.

Peroxidase measurements

Peroxidase activity was determined as suggested in [13]. For this purpose, 0.1 ml of enzyme extract was added to a mixture containing 2 ml of 0.2 M acetate buffer (pH 5.0), 0.4 ml of 3% H₂O₂ and 0.2 ml of 0.01 M benzidine solution in 50% alcohol. Enzyme activity was determined spectrophotometrically (2800, UV/VIS, UNICO, USA) by recording the absorbance at 530 nm. In order to protect enzyme activity, the procedure was carried out in an ice bath. Enzyme activity was calculated in terms of changes in absorption per min for 1 g fresh weight of the plant tissue.

Ascorbate Peroxidase Measurements

The method reported in [13] was used to test ascorbate peroxidase activity. For this purpose, 2 ml of 0.05 M phosphate buffer (pH 7), 0.2 ml of 3% (v/v) H₂O₂ and 0.2 ml of 50 mM ascorbate were mixed in an ice bath. Then, 0.1 ml of enzyme extract was immediately added to the indicator and the absorbance changes were recorded at 290 nm (2800UV/VIS, UNICO, USA). Ascorbate peroxidase activity was calculated in terms of changes in absorption per min for 1 g fresh weight of the plant tissue.

Polyphenol oxidase measurements

Polyphenol oxidase was determined as reported in [15]. Reaction solution contained 1.5 ml of Tris buffer (pH 7.6), 0.4 ml of 0.02 mM pyrogallol, and 0.1 ml of enzyme extract.

Incubating at 25°C for 5 min, the reaction was stopped by adding 1 ml of 10% H₂SO₄. The absorbance was then measured at 420 nm using a spectrophotometer (2800 UV/VIS, UNICO, USA). Polyphenol oxidase activity was calculated in terms of changes in absorption per min for 1 g fresh weight of the plant tissue.

Catalase measurements

Catalase activity was measured as suggested in [16]. Reaction mixture containing 2.5 ml of phosphate buffer (50 mM, pH 7.0) and 0.3 ml of 3% (v/v) H₂O₂ was mixed in an ice bath. Then, 0.2 ml of enzyme extract was added to the mixture. Absorbance changes were read at 240 nm (2800UV/VIS, UNICO, USA). Catalase enzyme activity was calculated in terms of changes in absorption per min for 1 g fresh weight of the plant tissue.

Extract preparation

Fresh roots and shoots of the plants were rinsed by distilled water and dried in an oven at 40°C. One gram of the dried plant material was soaked in 10 ml of methanol at room temperature for 24 h and filtered through a Whatman filter paper. The extract was then stored in dark at 4°C for analysis.

Antioxidant activity by DPPH measurements

The reagent 1,1-diphenyl-2-picryl hydrazyl (DPPH) radical was used for measuring free radical scavenging activity of the extracts as described in [17]. Different concentrations of methanol extract were first prepared and then 1 ml of various concentrations of the solvent extracts was added to 0.5 ml of a 0.2 mM methanol solution of DPPH. The reaction mixture was then vigorously shaken and kept at room temperature in dark for 30 min. Absorbance of the resulting solution was then measured using a spectrophotometer at 517 nm after 30 min. The ability to scavenge DPPH radical was calculated using the following equation:

$$\text{DPPH radical scavenging activity (\%)} = \frac{[(\text{Abs control} - \text{Abs sample}) / (\text{Abs control})] \times 100}{}$$

Phenolic compounds measurements

For extraction of phenolic compounds, the procedure was: (i) the samples were dried at a temperature of 40-45°C; (ii) 10 ml of 80% methanol was added per one gram of sample; it was placed on a shaker for 24 h, after which it was laid on a filter paper; (iii) total phenolic compounds were measured as follows: 20 µl of the extract was mixed with 1.16 ml of distilled water and 100 µl of folicin reagent was added to the solution. After 5 min, 300

µl of 20% sodium carbonate solution was added to the solution and the samples were kept at 40°C in a water bath for 30 min. Then, the absorbance of the samples was read on a spectrophotometer at a wavelength of 760 nm and the phenol content was calculated in mg of gallic acid per gram of dry weight of the sample [18].

Flavonoid content measurement

For extraction, 10 ml of 80% methanol was added to 1 g of the dried plant powder sample, and the mixture was placed on a shaker for 24 h and filtered with a filter paper. The extract was then used to measure the flavonoid content. Flavonoid measurement was based on the aluminum chloride colorimetric method. According to this method, 0.5 ml of methanolic extract was mixed with 1.5 ml of methanol, 0.1 ml of 10% aluminum chloride, 0.1 ml of 1M potassium acetate and 2.8 ml of distilled water, and was placed in darkness for half an hour. Then, the absorption was read on a spectrophotometer at 415 nm. Flavonoid content was calculated and set at 1 mg quercetin per gram of dried powder [19].

Statistical analysis

The obtained data were analysed by SPSS Ver. 21 by comparing the means by Duncan's multiple-range test ($P \leq 0.05$) in 4 replications for each study.

RESULTS

The highest peroxidase activities were recorded in shoots of *Salsola dendroides* and *Limonium reniforme* in summer and spring, respectively, while the lowest peroxidase activities were observed in shoots of both species in spring and autumn, respectively. Peroxidase activity increased in roots of both species in summer, while it decreased in spring (Table 1). There is a significant relationship between different seasons and enzyme activities in both species ($P \leq 0.05$).

The highest and lowest ascorbate peroxidase activities were observed in shoots of *S. Dendroides* and *L. reniforme* in summer and autumn, respectively. There are significant differences in enzyme activities in the three seasons ($P \leq 0.05$). Ascorbate peroxidase activity significantly

increased and decreased in roots of both plants in summer and autumn, respectively (Table 2).

Polyphenol oxidase activities significantly increased in summer in shoots of *S. dendroides* and *L. reniforme*. On the other hand, enzyme activities significantly decreased in spring and autumn, respectively ($P \leq 0.05$). Polyphenol oxidase activities significantly increased in roots of *S.dendroides* and *L. reniforme* in summer and autumn, while they decreased in autumn and summer (Table 3).

The highest and lowest catalase activities of shoots of *S .dendroides* were recorded in autumn and spring, respectively, while maximum and minimum catalase activities of shoots of *L. reniforme* were recorded in spring and autumn, respectively. There are significant differences between enzyme activities of the plants in different seasons. Catalyse activities increased in the roots of both species in summer, while it decreased in spring; these differences are significant, as shown in Table 4 ($P \leq 0.05$).

Methanol extracts of shoots showed the highest level of antioxidant activities in both plants in summer, whereas the lowest antioxidant activities were observed in the methanol extracts of shoots of *S. dendroides* and *L. reniforme* in spring and autumn, respectively, suggesting a significant difference ($P \leq 0.05$). Antioxidant activities (DPPH) significantly increased in root extracts of *S. dendroides* in autumn and decreased in summer; in root extracts of *L. reniforme*, these activities significantly increased in summer, while they decreased in autumn; these differences are significant, as shown in Table 5 ($P \leq 0.05$).

Phenol content of shoots significantly increased in both *S. dendroides* and *L. reniforme* plants in summer and decreased in *S. dendroides* in spring and in *L. reniforme* in autumn. In *S. dendroides*, the highest phenol content of roots was observed in autumn and the lowest phenol content was observed in summer. In *L. reniforme*, the highest phenol content of roots was observed in summer and the lowest content was observed in spring; a significant difference was found between different seasons in the phenol content of roots (Table 6).

Table 1. Effect of seasonal variation in peroxidase activity in shoots and roots of *Salsola dendroides* and *Limonium reniforme* (min g⁻¹FW)

	Shoots			Roots		
	Spring	Summer	Autumn	Spring	Summer	Autumn
<i>Salsola dendroides</i>	0.246 ± 0.005c	0.491 ± 0.028a	0.403 ± 0.012b	0.129 ± 0.004c	0.203 ± 0.012a	0.153 ± 0.003b
<i>Limonium reniforme</i>	0.202 ± 0.006a	0.172 ± 0.002b	0.141 ± 0.004c	0.116 ± 0.005c	0.158 ± 0.005a	0.124 ± 0.003b

Different letters in each row indicate significant difference at $P \leq 0.05$ by Duncan test; FW: fresh weight

Table 2. Effect of seasonal variation in ascorbate peroxidase activity in shoots and roots of *Salsola dendroides* and *Limonium reniforme* (min g⁻¹FW)

	Shoots			Roots		
	Spring	Summer	Autumn	Spring	Summer	Autumn
<i>Salsola dendroides</i>	0.063 ± 0.004b	0.092 ± 0.004a	0.045 ± 0.003c	0.036 ± 0.001b	0.057 ± 0.003a	0.028 ± 0.001c
<i>Limonium reniforme</i>	0.049 ± 0.002b	0.071 ± 0.004a	0.036 ± 0.002c	0.035 ± 0.002b	0.047 ± 0.004a	0.026 ± 0.003c

Different letters in each row indicate significant difference at P≤0.05 by Duncan test; FW: fresh weight

Table 3. Effect of seasonal variations in polyphenol oxidase activities in shoots and roots of *Salsola dendroides* and *Limonium reniforme* (min g⁻¹FW)

	Shoots			Roots		
	Spring	Summer	Autumn	Spring	Summer	Autumn
<i>Salsola dendroides</i>	0.181 ± 0.009c	0.511 ± 0.023a	0.249 ± 0.013b	0.431 ± 0.041b	0.631 ± 0.033a	0.325 ± 0.031c
<i>Limonium reniforme</i>	0.271 ± 0.007b	0.349 ± 0.018a	0.236 ± 0.004c	0.117 ± 0.003b	0.091 ± 0.005c	0.152 ± 0.005a

Different letters in each row indicate significant difference at P≤0.05 by Duncan test; FW: fresh weight

Table 4. Effect of seasonal variations in catalase activities in shoots and roots of *Salsola dendroides* and *Limonium reniforme* (min g⁻¹FW)

	Shoots			Roots		
	Spring	Summer	Autumn	Spring	Summer	Autumn
<i>Salsola dendroides</i>	0.045 ± 0.003c	0.058 ± 0.005b	0.105 ± 0.005a	0.041 ± 0.004c	0.073 ± 0.004a	0.054 ± 0.005b
<i>Limonium reniforme</i>	0.151 ± 0.005a	0.126 ± 0.002b	0.118 ± 0.006c	0.043 ± 0.004c	0.086 ± 0.004a	0.052 ± 0.004b

Different letters in each row indicate significant difference at P<0.05 levels by Duncan test; FW: fresh weight

Table 5. Effect of seasonal variations in activities of antioxidant (DPPH) in shoots and roots of *Salsola dendroides* and *Limonium reniforme*

	Shoots			Roots		
	Spring	Summer	Autumn	Spring	Summer	Autumn
<i>Salsola dendroides</i>	60.32 ± 0.8c	83.08 ± 3.7 a	65.58 ± 0.9b	84.35 ± 1.2b	66.08 ± 1.3c	91.23 ± 2.1a
<i>Limonium reniforme</i>	59.07 ± 0.3b	69.91 ± 0.6a	57.06 ± 0.8c	64.62 ± 0.4b	70.04 ± 1.4a	59.98 ± 0.4c

Different letters in each row indicate significant difference at P≤0.05 levels by Duncan test.

Table 6. Effect of seasonal variations in activities of phenol shoots and roots of *Salsola dendroides* and *Limonium reniforme* (mg GAEg⁻¹DW)

	Shoots			Roots		
	Spring	Summer	Autumn	Spring	Summer	Autumn
<i>Salsola dendroides</i>	0.896 ± 0.048 a	1.398 ± 0.066 b	1.184 ± 0.066 c	0.455 ± 0.044b	0.223 ± 0.008 c	0.837 ± 0.066a
<i>Limonium reniforme</i>	1.626 ± 0.068b	1.887 ± 0.110 a	1.144 ± 0.060 c	0.265 ± 0.010a	0.695 ± 0.017 b	0.476 ± 0.027 c

Different letters in each row indicate significant difference at P≤0.05 levels by Duncan test. GAE: Gallic acid equivalent; DW: dry weight

Table 7. Effect of seasonal variations in activities of flavonoid shoots and roots of *Salsola dendroides* and *Limonium reniforme* (mg QUEg⁻¹DW)

	Shoots			Roots		
	Spring	Summer	Autumn	Spring	Summer	Autumn
<i>Salsola dendroides</i>	5.47 ± 0.450 c	9 ± 0.309 a	6.46 ± 0.467 b	5.02 ± 0.46 b	6.01 ± 0.73a	3.91 ± 0.31 c
<i>Limonium reniforme</i>	2.97 ± 0.409 c	7.44 ± 0.384 a	5.40 ± 0.616 b	2.75 ± 0.31 c	5.61 ± 0.33 a	3.82 ± 0.37 b

Different letters in each row indicate significant difference at P≤0.05 levels by Duncan test. QUE: Quercetin equivalent; DW: dry weight

The highest flavonoid content was observed in shoots of *S. dendroides* and *L. reniforme* in summer and the lowest content was observed in spring. This difference was statistically significant between seasons. In roots of both *S. dendroides* and *L. reniforme*, the highest flavonoid content was observed in summer; the lowest root flavonoid content was observed in *S. dendroides* in autumn and in *L. reniforme* in spring. The results showed statistically significant difference between seasons (Table 7).

DISCUSSION

Halophytes are a group of plants with strong antioxidant systems including enzymatic and non-enzymatic components. Non-enzymatic components include antioxidants such as tocopherol, carotenoids, ascorbate and glutathione; enzymatic components include enzymes such as superoxide dismutase, catalase, peroxidase, ascorbate peroxidase, monodehydroascorbate reductase, dehydroascorbate reductase and glutathione reductase, which protect their important biomolecules including lipoproteins and DNA from destruction by ROS [20,21]. It has been suggested that high antioxidant capacity of halophytes compared with glycophytes is one of the important reasons for increasing tolerance and adaptation of these plants to salinity stress [22,23]. Since the severity of damages caused by salinity varies in different plant species, plant organs, or at different stages of growth, the performance of various plant species can be different in synthesis and accumulation of organic compounds, change in capacity and activity of antioxidant enzymes in response to salinity [24].

Studies have shown that enzyme activities increased in plants as an antioxidant defense mechanism against oxidative stress induced by various abiotic stresses [25].

Peroxidases (POXs) are a family of isoenzymes primarily found in apoplastic species of plants which can scavenge H_2O_2 [26]. Peroxidase is considered as the first line of plant defense against abiotic stresses such as salinity; increased activity is reported in plants exposed to salt stress [27].

In organic plants, it has been shown that peroxidase enzyme participates in a number of cellular processes such as host defense mechanism, lignin and suberin wall, resistance to pathogens, tolerance to salinity and aging [28].

In the present study, peroxidase activity significantly increased in shoots of *S. dendroides* and *L. reniforme* in summer compared to autumn. In fact, the highest and lowest levels of peroxidase were recorded in roots of both species in summer

and spring, respectively. Significant increase was also observed in peroxidase activities of species such as *Suaeda arcuata*, *Cressacretica* and *Salsola turcomanic* as abiotic stresses, particularly salinity stress, increased in spring to summer [29]. These results support the findings of the present study. Increased peroxidase activity under salinity stress has been reported in many plants, e.g. genotypes of wheat [30], *Suaeda salsa*[31], *Cakile maritime* [32], *Atriplex halimus*[33], and *Hordeum marinum*[34]. Increased peroxidase activity was also reported in callus cultures of *Suaeda nudiflora* where higher concentrations of NaCl increased peroxidase activity in salinized cells of *S. nudiflora* improving their capacity for decomposing H_2O_2 [35]. These findings are consistent with the present study, where salinity significantly increased peroxidase activity of both species in dry seasons.

Ascorbate peroxidase is an antioxidant with generally the same function as peroxidase and catalase. However, this antioxidant enzyme catalyzes scavenging H_2O_2 by using ascorbate as a reductant [36,37]. In this study, ascorbate peroxidase activities increased in shoots and roots of both species in summer compared with spring. This is consistent with the study of Ghorbanliet al.[38] who studied *Flavoparmelia caperata* and *Physcia dubia* and reported higher activity of ascorbate peroxidase in both species during summer compared to spring for protection of plants. Moreover, some scientists have reported increased ascorbate peroxidase activity under saline conditions in halophyte plants, e.g. *Atriplex portulacoides*[39], and *Bruguiera parviflora*[36]. Ascorbate peroxidase induction clearly shows that this enzyme plays a critical role in controlling H_2O_2 level in plant cells under initial salt-induced oxidative stress [40].

Polyphenol oxidase is part of an enzymatic mechanism for eliminating reactive oxygen species (ROS) under UV radiation, heat, and stress conditions [41]. This study showed that polyphenol oxidase activity significantly increased in shoots and roots of both species in summer and autumn, respectively. This is consistent with the study of Szecskoet al.[42] who found maximum level of polyphenol oxidase activities in rootstocks of plum cultivars during autumn (November) and Sen and Mukherji [43] who studied *Lycopersicon esculentum* and reported an increase in polyphenol oxidase activities during summer. Increased activity of polyphenol oxidase in summer and rainy seasons could be attributed to protective function of plants in response to abiotic stress.

Increased polyphenol oxidase activity under salt stress was already reported in halophytes such as

Sesuvium portulacastrum [44] and *Excoecaria agallocha* [45]. Subhashini and Reddy [46] argued that increased polyphenol oxidase activity under salinity stress implies that this enzyme is able to oxidize and degrade the toxic compounds which are generally accumulated under saline conditions.

Catalases are tetramer enzymes with four heme groups per tetramer, capable of direct dismutation of H₂O₂ into H₂O and O₂ which are indispensable for ROS detoxification under stress conditions [47]. Findings of this study revealed a significant increase in catalase activity in shoots of *S. dendroides* in summer compared with spring, while the enzyme activity was higher in *L. reniforme* in summer compared with autumn. The highest catalase activity was recorded in roots in summer, while the enzyme activity was at its lowest in spring. This is consistent with Farzamisepehr et al. [48] who studied *Populus deltoids* and showed that increase in temperature and drought during summer increases catalase activities in comparison with spring and autumn.

Effects of salt stress on catalase activity were evaluated in different groups of halophytes such as *Hordeum marinum* [34], *Suaeda maritima* [49], and *Limonium bicolor* [50]. All these studies reported a significant increase in catalase activity under salt stress conditions, which is consistent with the present study. Increased catalase activity seems to be linked to gene expression regulation. Lower oxidative damage has generally been reported in plants with higher catalase activity, suggesting the protective function of this enzyme [51].

Many plant extracts have potential chemopreventive properties against cancer through antioxidant mechanism and scavenging reactive oxygen species (ROS), inhibiting lipid peroxidation or stimulating cellular antioxidant defense [52]. There are many reports on polyphenol accumulation and enhanced antioxidant ability in halophytes [53,22]. Superior Fe²⁺ reduction power and DPPH radical scavenging ability were reported in shoot extracts of halophytes compared with glycophytes [53]. In this study, methanol extracts of shoots and roots of both species had the highest antioxidant activities in summer and autumn, respectively. This variability could be due to meteorological factors such as solar irradiation, photoperiod, temperature, and relative humidity [54] or edaphic effects such as salinity.

Findings of the present study are consistent with those of Zhanget al. [55] who studied antioxidant activity of *Suaeda salsa* *in vitro* and reported that extracts had the highest antioxidant activity in summer, as well as of Jallali et al. [56] who studied

Crithmum maritimum and found that the plant extracts had richer phenolic compounds at reproductive stage (summer), suggesting higher antioxidant activities in comparison with extracts at vegetative stage in spring.

Phytochemical studies showed that phenolic compounds significantly increased in shoots of the species in summer and significantly decreased in *S. dendroides* in spring and in *L. reniforme* in autumn. In roots of the studied plants, the highest phenolic compounds were observed in *S. dendroides* in autumn and in *L. reniforme* in summer. The results of this study were consistent with those of Jallali et al. [56] who showed that phenolic compounds significantly increased in *Crithmum maritimum* species in summer compared with spring. Medini et al. [57] studied the halophytic species *Limonium densiflorum* and found that phenolic compounds increased in summer and decreased in autumn. Variation in production of phenolic compounds in different seasons may be due to various environmental factors such as weather, precipitation, salt increase in soil and sunlight, which may affect biosynthesis and accumulation of phenolic compounds in stressed plants. Many reports confirm the role of phenolic compounds as an important antioxidant in many plants, particularly halophyte plants [20]. Bagal et al. [58] claimed that the reason for increase in phenolic compounds in plants exposed to biological and non-biological stresses is rapid induction of expression of phenylalanine ammonia-lyase gene. Phenylalanine ammonia-lyase enzyme plays a key role in biosynthesis of phenolic compounds and regulation of products derived from phenylpropanoid pathway. These compounds play important roles in plants such as protection against alive and non-alive stresses, UV protection, and intercellular signals. Studies show that high levels of phenolic compounds are the main reason for high antioxidant activity of some plant extracts, because evidence suggests a positive relationship between phenolic compounds and antioxidant strength of plants which can be extracted through plant extracts [59,60]. This is consistent with our results that antioxidant activity of the samples is directly related to phenolic and flavonoid compounds, so that methanolic extract of the studied plants with the highest levels of phenolic and flavonoid compounds has the highest antioxidant activity. For example, *Hyoscyamus aureus* [61] and *Solanum guaraniticum* [62] exhibited high antioxidant activity in DPPH-free radical inhibitors due to high polyphenolic compounds. Moreover, studies on *Hypericum brasiliense* showed a positive relationship between

phenolic compounds and their antioxidant function; in dry and saline environments, increase in total phenol content added to antioxidant function of plants, that is, chemical and active compounds of the plant, and most importantly, their antioxidant properties vary by various environmental factors [63].

According to the results, flavonoid content was significantly higher in shoots and roots of the studied species in summer than in other seasons. Studying seasonal variations, Fardus *et al.* [64] measured phenolic compounds such as flavonoids in *Oenothera biensis* and showed that flavonoid content varied as seasons changed; the highest level was observed in summer. Kheira *et al.* [65] observed the highest flavonoid content in the *Ballota hirsuta* Benth plant in summer, which is consistent with the findings of this study. Flavonoids are a group of secondary polyphenolic metabolites of the plant derived from phenylpropanoid pathway, which plays a major role in plant responses to environmental conditions, particularly under biological and non-biological stresses. Flavonoids have been reported to have an antioxidant effect and, by eliminating free radicals, can protect cells [66]. Accumulation of secondary metabolites is known as a defense mechanism in plants, and plants can respond and adapt to stress by altering their cellular metabolism by various defense mechanisms [67].

CONCLUSION

Generally, the findings of this study suggest that accumulation of antioxidant compounds and their activities in the studied plants change as the seasons change; in most cases, the highest antioxidant contents and activities were observed in roots and shoots of the studied plants during summer (along with an increase in draught and salinity levels). Therefore, it seems that there is a strong relationship between tolerance against oxidative stresses due to abiotic conditions and increase in antioxidant activities and phytochemical compounds in the studied plants. In their attempt to reduce oxidative damages due to salinity stress, these plants increase activities of their enzymes such as catalase, peroxidase, ascorbate peroxidase, and polyphenol oxidase and phytochemical compounds, responding to various salinity levels in different seasons and adapting to conditions. Further studies are required to understand the nature of adaptation and the defense mechanisms of halophytes and their tolerance, which in turn may result in identification of the genes which play a role in adaptability of these plants to abiotic stresses.

REFERENCES

1. S.Bhattacharjee, *Biologia Plantarum*, **52**, 137 (2008).
2. J.A.Imlay, *Ann. Rev. Biochem.*, **77**, 755 (2008).
3. L. A.del Rio, L. M.Sandalio, F. J.Corpas, J. M.Palma, J. B. Barroso, *Plant Physiology*, **141**, 330(2006).
4. N.Navrot, N.Rouhier, E.Gelhaye, J.P.Jacquot, *Physiologia Plantarum*, **129**, 185(2007).
5. O. Ozkur, F.Ozdemir, M.Bor, I.Turkan, *Environmental and Experimental Botany*, **66**, 487 (2009).
6. R. Ksouri, H. Falleh, W. Megdiche, N. Trabelsi, B. Mhamdi, K. Chaieb, A. Bakrouf, C. Magné, C. Abdelly, *Food and Chemical Toxicology*, **47**, 2083(2009).
7. H.Wangensteen, A.B. Samuelson, K.E.Malterud, *Food Chemistry*, **88**, 293 (2004).
8. J. R. Borchardt, D. L.Wyse, C. C. Sheaffer, K. L. Kauppi, R. G. Fulcher, N. J. Ehlke, D. D. Biesboer, R. F. Bey, *Journal of Medicinal Plants Research*, **2**, 081 (2008).
9. M. Suhaj, *Journal of Food Composition and Analysis*, **19**, 531 (2006).
10. J. M. Navarro, P. Flores, C. Garrido, V. Martinez, *Food Chemistry*, **96**, 66 (2006).
11. J. Pokorný, *European Journal of Lipid Science and Technology*, **109**, 629 (2007).
12. M. P. Benavides, P. L. Marconi, S. M. Gallego, M. E. Comba, M. L. Tomaro, *Functional Plant Biology*, **27**, 273 (2000).
13. S. A. A. Koroi, *Physiological Reviews*, **20**,15(1989).
14. Y. Nakano, K. Asada, *Plant Cell Physiology*, **22**,867 (1981)
15. M. Kar, D. Mishra, *Plant Physiology*, **57**, 315 (1976).
16. H. Aebi, *Methods in Enzymology*, **105**, 121 (1984).
17. T. Hatano, H. Kagawa, T. Yasuhara, T. Okuda, *Chemical and Pharmaceutical Bulletin*, **36**, 2090 (1988).
18. S. McDonald, P. D. Prenzler, M. Autolovich, K. Robards, *Food Chemistry*, **73**,73 (2001).
19. C. C. Chang, M. H. Yang, H. M. Wen, J. Ch. Chern, *Journal of Food and Drug Analysis*, **10**, 178 (2002).
20. R. Ksouri, W. Megdiche, H. Falleh, N. Trabelsi, M. Boulaba, A. Smaoui, *Comptes Rendus Biologies*, **331**,865 (2008).
21. S. Oueslatia, R. Ksouri, H. Falleh, A. Pichette, C. Abdelly, J. Legault, *Food Chemistry*, **132**, 943 (2012).
22. R. Ozgur, B. Uzilday, A. H.Sekmen, I. Turkan, *Functional Plant Biology*, **40**, 832 (2013).
23. T. J. Flowers, T. D. Colmer, *New Phytologist*, **179**, 945 (2008).
24. A. Abraham, P. Salamo, C. Koncz, L. Szabados, *Acta Biologica Szegediensis*, **55**, 53 (2011).
25. P., Sharma, A. B. Jha, R. Sh. Dubey, M. Pessarakli, *Journal of Botany*, **1** (2012).
26. K. V. Fagerstedt, E. M.Kukkola, V. V. Koistinen, J. Takahashi, K. Marjamaa, *Journal of Integrative Plant Biology*,**52**,186 (2010).
27. H. Chang, B. Z. Siegel, S. M. Siegel, *Phytochemistry*, **23**, 233 (1981).

28. C. Atak, O. Celik, A. Olgun, S. Alikamanoglu, A. Rzakoulieva, *Biotechnology*, **2**, 21 (2007).
29. M. Ghorbanli, M. Dasturani, R. Bonyadi, B. A. Mamaghani, *Iranian Journal of Plant Physiology*, **5**, 1297 (2015).
30. M. A.Rahman, M. Saqib, J. Akhtar, R. Ahmad, *Scholarly Journal of Agricultural Science*, **4**, 386 (2014).
31. H. Wu, X. Liu, L. You, L. Zhang, D. Zhou, J. Feng, J. Zhao, J. Yu, *Journal of Plant Growth Regulation*, **31**, 332 (2012).
32. H. Ellouzi, K. Ben Hamed, J. Cela, S. Munne-Bosch, C. Abdelly, *Physiologia Plantarum*, **142**, 128 (2011).
33. F. Boughalleb, M. Mhamdi, H. Hajlaoui, M. Denden, *Research Journal of Biological Science*, **5**, 773 (2010).
34. B. Seckin, I. Turkan, A. H. Sekmen, C. Ozfidan, *Environmental and Experimental Botany*, **69**, 76 (2010).
35. S. Cherian, M. P. Reddy, *Biologia Plantarum*, **46**, 193 (2003).
36. A. K. Parida, A. B. Das, P. Mohanty, *Journal of Plant Physiology*, **161**, 531 (2004).
37. S. Shigeoka, T. Ishikawa, M. Tamoi, Y. Miyagawa, T. Takeda, Y. Yabuta, K. Yoshimura, *Journal of Experimental Botany*, **53**, 1305 (2002).
38. M. Ghorbanli, T. Amirkian Tehran, M. Niyakan, *Iranian Journal of Plant Physiology*, **2**, 461 (2012).
39. M. Benzarti, K. B.Rejeb, A. Debez, D. Messedi, C. Abdelly, *Acta Physiologiae Plantarum*, **34**, 1679 (2012).
40. I. Slesak, Z. Miszalski, B. Karpinska, E. Niewiadomska, R. Ratajczak, S. Karpinski, *Plant Physiology Biochemistry*, **40**, 669 (2002).
41. V. Balakrishman, K. Venkatesan, K. C. Ravindran G. Kulandaivelu, *Plant Protection Science*, **41**, 115 (2005).
42. V. Szecsko, K. Hrotko, E. S. Banyai, *Acta Biologica Szegediensis*, **46**, 211 (2002).
43. S. Sen, S. Mukherji, *Journal of Environmental Biology*, **30**, 479 (2009).
44. M. Rajaravindran, S. Natarajan, *International Journal of Research in. Biological Sciences*, **2**, 18 (2012).
45. R. Sozharajan, S. Natarajan, *Asian Pacific Journal of Reproduction*, **2**, 304 (2013).
46. K. Subhashini, G. M. Reddy, *Indian Journal of Experimental Biology*, **28**, 277 (1990).
47. N. Garg, G. Manchanda, *Plant Biosystem*, **143**, 81 (2009).
48. M.Farzamisepehr, M.Ghorbanli, M. Mohammadi, *World Applied. Science Journal*, **17**, 557 (2012).
49. S.Mallik, M.Nayak, B. B.Sahu, A. K. Panigrahi, B. P. Shaw, *Biologia Plantarum*, **55**, 191 (2011).
50. Y. Li, *Plant, Soil and Environment*, **54**, 493 (2008).
51. A. Sofo, A. Scopa, M. Nuzzaci, A. Vitti, *International Journal of Molecular Sciences*, **16**, 13561 (2015).
52. H. Keles, F. Fidan, H. Cigerci, I. Kucukkurt, E. Karadas, Y. Dundas. *Veterinary Immunology and Immuno Pathology*, **133**, 51 (2010).
53. R. Ksouri, A. Smaoui, H. Isoda, C. Abdelly, *Journal of Arid Land Studies*, **22**, 41 (2012).
54. M. L. Ferreira, M. B. Domingos, *Brazilian Journal of Biology*, **72**, 831 (2012).
55. Z. S. Zhang, H. Mu, L. Zhao, J. Qian, *Food Research and Development*, **31**, 4 (2010).
56. I. Jallali, W. Megdich, B. M. Hamdi, S. Oueslati, A. Smaoui, C. Abdelly, R. Ksouri, *Acta Physiologiae Plantarum*, **34**, 1451 (2012).
57. F. Medini, R. Ksouri, H. Falleh, W. Megdiche, N. Trabelsi, C. Abdelly, *Journal of Medicinal Plants Research*, **5**, 6719 (2011).
58. U. R. Bagal, J. H. Leebensmack, W.W. Lorenz, J. F. D. Dean, *BMC Genomics*, **13**, 1471 (2012).
59. F. Candan, M. Unlu, B. Tepe, D. Daferera, M. Polissiou, A. H. Sokmen, A. Akpulat, *Journal of Ethnopharmacology*, **87**, 215 (2003).
60. K. Muret, K. Sevgi, K. Sengul, U. Esra, B. Cemalettin, V. Fedra, *Food Chemistry*, **100**, 526 (2007).
61. F. Q. Alali, K. Tawaha, T. El-Elimat, M. Syouf, M. El-Fayad, K. Abulaila, S. J. Nielsen, W. D. Wheaton, J. O. Falkinham, N. H. Oberlies, *Natural Product Research*, **21**, 1121 (2007).
62. M. Zadra, M. Piana, T. F. de Brum, A. A. Boligon, R. B. de Freitas, M. M. Machado, S. T. Stefanello, F. A. Antunes Soares, M. L. Athayde, *Molecules*, **17**, 12560 (2012).
63. N. de Abreu, P. Mazzafera, *Plant Physiology and Biochemistry*, **43**, 241 (2005).
64. S. Fardus, A. Wahid, F. Javed, B. Sadia, *International Journal of Agriculture & Biology*, **16**, 819 (2014).
65. K. Kheira, H. Benchaben, B. D. Adiba, A. Nadira, A. Abbassia, *Biochemistry & Molecular Biology Letters*, **1**, 001 (2015).
66. C. Rice-Evans, N. Miller, G. Paganga, *Trends in Plant Science*, **2**, 152 (1997).
67. M. A. El-Tayeb, *Plant Growth Regulation*, **42**, 215 (2005).

ИЗСЛЕДВАНЕ НА ФИТОХИМИЧНИТЕ ПРОМЕНИ, ЕНЗИМНАТА И АНТИОКСИДАНТНАТА АКТИВНОСТ НА ДВЕ ХАЛОФИТНИ РАСТЕНИЯ - *Salsola dendroides* PALL. И *Limonium reniforme* (GIRARD) LINCZ ПРЕЗ РАЗЛИЧНИТЕ СЕЗОНИ

С. Бакши¹, Х. Абаспур^{1*}, С. Саедисар²

¹ Департамент по биология, клон Дамган на Ислямски Азад университет, Дамган, Иран

² Технически колеж „Д-р Шариати“, Технически и специализиран университет, Техеран, Иран

Постъпила на 8 декември, 2017 г.; коригирана на 16 декември, 2017 г.

(Резюме)

С цел да се изследват фитохимичните промени, ензимната и антиоксидантната активност на халофитните растения *Salsola dendroides* Pall. и *Limonium reniforme* (Girard) Lincz, проби от листа и корени на тези растения са събрани от района Инчех Борун в Северен Горган, Иран през три сезона (пролет – май, лято – август и есен - ноември). Установено е, че засолеността на почвата се увеличава през есента и в повечето случаи значително повишава ензимната и антиоксидантната активност в стъблата и корените на двете растения. Фитохимичните изследвания показват, че съдържанието на феноли в стъблата и корените на *Salsola dendroides* значително нараства през лятото и есента, а на *Limonium reniforme* – през лятото. Съдържанието на флавоноиди също се променя значително през сезоните. Най-високо натрупване на флавоноиди в стъблата и корените на растенията се наблюдава през лятото. Повечето от тези промени са свързани с активиране на физиологичните и биохимичните процеси, позволяващи на растението да се адаптира към условията на засоляване.

Evaluation of the plasma jet effects on the Citrinin and Ochratoxin A producing species of the genus *Penicillium*

N. Vaseghi¹, M. Bayat^{1*}, A. Ch. Nosrati², M. Ghorannevis³, S. Hashemi⁴

¹Department of Microbiology, Science and Research Branch, Islamic Azad University, Tehran, Iran

²Department of Molecular & Cell Biology, Lahijan Branch, Islamic Azad University, Lahijan, Gilan, Iran

³Plasma Physics Research Center, Science and Research Branch, Islamic Azad University, Tehran, Iran

⁴Department of Medical Parasitology and Mycology, School of Public Health, Tehran University of Medical Science, Tehran, Iran

Received November 23, 2017; Revised February 15, 2018

Mycotoxins are small toxic molecules produced by a variety of microorganisms. They are often made of several secondary metabolites and often have a variety of chemical functions and structures. Citrinin and Ochratoxin A produced by different species of *Penicillium* contaminate various types of foods. Today, the cold atmospheric pressure plasma method has potential for mycotoxin detoxification. In this study, cold atmospheric pressure plasma (CAPP) operating parameters were investigated and optimized to increase the effect on Citrinin and Ochratoxin A in wheat, oat, corn and rice. In this study, the output of power supply first was set to 50 kV, 100 watts and the electron frequency of 30 kHz (optimum conditions for stable and effective plasma) to perform the tests. Then, the effect of cold atmospheric plasma jet (argon) on the gas flow establishment (gas rate 6.6 l/min) for 30, 60 and 360 sec was investigated. The results showed that CAPP method effectively reduces the pure mycotoxins. Overall, there are more than 40% and 50% reduction in the mean initial concentrations of Ochratoxin A and Citrinin, when plasma-treated at 100 W powers. The degree of destruction of various mycotoxins varies according to their structure. It was also shown that the presence of a combination of mycotoxins in foods reduces the plasma's effect but does not prevent their destruction. Finally, in this study, Citrinin and Ochratoxin A were successfully detoxified on all specimens. In addition to mycotoxin detoxification, the CAPP method is neutral in terms of biologic effects and has least negative effects on the nutrients compared to the conventional methods of disinfection of food products.

Keywords: Mycotoxin, Citrinin, Ochratoxin A, *Penicillium*, Cold atmospheric pressure plasma, Detoxification

INTRODUCTION

Penicillium is one of the most commonly found fungi in nature. They belong to the class of *Ascomycota* and subdivide into subgenera such as *Furcatum*, *Aspergilloides*, *Brevitium* and *Penicillium*. *Penicillium* is present in nature (water, air, soil and plants). They have many benefits, including the ability to produce various enzymes, antibiotics, antitumor and antifungal drugs, as well as effective compounds against insects. The study aimed to investigate the effect of atmospheric cold plasma on the reduction of mycotoxins produced by *Penicillium* isolated from 5 different food sources (wheat, oat, corn, rice and flour).

Today, plasma science is a new way of overcoming the problems faced by food biotechnology researchers. The unique properties of plasma make it widely available in industry and medicine. Classification from a point of view of pressure, divides the plasma into two general classes: low pressure plasma and atmospheric pressure plasma (APP). Currently, more attention is paid to APP due to its simplicity and low cost compared to low pressure plasma. Atmospheric electrical discharge has been extensively

investigated in recent years due to advantages such as cost-effectiveness of the test, performance without vacuum, accessibility and sample processing without limitations in size and high reactivity. The use of APP is a new technology that has been considered as a non-thermal method in recent years due to its high potential for the destruction of microorganisms and its low cost.

For the first time, Kung *et al.* [1] stated that cold plasma is a very effective bacteria killer. Cold atmospheric plasmas have the ability to generally disable microorganisms under controlled laboratory conditions [1]. Mortazavi *et al.* [2] announced that plasma would degrade proteins and cause lipid peroxidation of *E. coli* gram-negative bacteria, thereby destroying the bacterial membrane of the microorganisms [2].

Mortazavi *et al.* [2] also reported that one of the most important mechanisms for killing bacteria, in addition to destruction of DNA, proteins, etc. by cold plasma, is the destruction of bacterial membrane through membrane lipid oxidation. Since plasma can produce reactive oxygen species, therefore, by increasing treatment time, the level of membrane lipids oxidation should increase, as a result more bacteria in different times will be

* To whom all correspondence should be sent:

E-mail: Dr_mansour_bayat@yahoo.com

eliminated [2]. Fernandes and Thomson [3] reported that the need to meet the consumer demand for fresh products without challenging the microbial safety of food and its quality, has attracted the interest of the food industry to new low-temperature products. Compared to the thermal processes, these technologies depend on physical processes, such as high hydrostatics, ionizing radiation, ultrasonic, ultraviolet light and cold plasma, which are capable of destroying microorganisms at limited temperatures. This latter treatment (plasma jet) is one of the promising technologies for food maintenance [3].

In this study, 5 *Penicillium* samples from flour, wheat, corn, oat and rice (their storage sites) were isolated and then cultured for observing their important features in oatmeal agar. After the preparation of the culture slide, the morphological features such as colony surface and back color, colony texture and pigmentation production were determined. To increase the mycotoxin production, their fungal isolates were cultured in two broth types (malt extract + sabouraud dextrose broth) and (yeast extract + sabouraud dextrose broth) and after an incubation period, the toxins produced by superior strains were isolated by solvent extraction and their initial concentrations before the treatment were examined by ELISA test, finally the effect of mycotoxin detoxification of APP was studied at 3 different times - 60, 120 and 360 sec.

MATERIALS AND METHODS

In this study, a non-thermal atmospheric plasma (99% argon and 1% air with a gas flow rate of 6 l/min for a single jet with high sinus voltage at a frequency of 30 KHz for treatment of samples was used). The general stages are:

- Sampling
- Initial tests (identification)
- Culture tests and detoxification testing
- Culturing and determining the amount of toxic production by ELISA method
- Execution of plasma radiation and measurement of mycotoxin detoxification
- Review of raw data and statistical data analysis

Materials and culture media

In this study, an oatmeal agar medium was used, and sabouraud dextrose broth 250 ml + malt extract 7.5 ml and sabouraud dextrose broth 250 ml + yeast extract 7.5 ml were used (to enrich and increase mycotoxin production by collected samples). All culture media and chemical materials used to isolate and produce mycotoxins were from the German Merck Co. (According to the instruction on

the cans of culture media) [4-6].

Sampling

In this research, samples were from the northern regions of Iran including wheat, corn, oats, flour and rice. These samples were collected by Dr. Arash Chaichi Nosrati and were available for the study. Samples were transferred to the laboratory immediately after collection, and were kept in the refrigerator at 4 °C to determine the amount of Citrinin, Ochratoxin A, as well as mycotoxin detoxification by plasma.

Needle culture of samples in oatmeal agar media (culture in a solid medium)

To isolate the Citrinin and Ochratoxin A generic fungi, the collected samples were cultured in an oatmeal agar medium (specific culture medium) as needle culture (in 3 points at a distance of 2 cm from the edge of the plate). Each plate was transferred to the incubator for 7 days at 25 °C. Plates were examined during the incubation (every 3 days from the 7 days incubation period). Identification of isolated fungi was done according to the morphological and macroscopic characteristics of fungal colonies such as colony surface and back color, smooth or rough colony surface, powder, cotton or more, with the help of Klich, Barnett and Hunter's identification keys [7, 8].

Culture in a liquid medium (transfer of samples from solid to liquid medium)

In this step, two broths, sabouraud dextrose broth + malt extract (SB + ME) and sabouraud dextrose broth + yeast extract (SB + YE) in 10 ml falcon tubes containing 5 ml of liquid medium with sterile glass (in this study, it was used to accelerate the cell breakdown process, to extract mycotoxins from beads glass). To inoculate the samples from solid to liquid medium, the pure and isolated samples were picked by sterile loops, transferred to the liquid medium and were kept in an incubator shaker at 25 °C, 200 rpm for 7 days. To prevent drying of liquid medium during incubation (on day 3 of the 7-day incubation period) 0.5 cc of phosphate buffered saline solution (PBS) was added to each of the falcon tube by a sampler [5, 6].

Preparing culture slides from selected samples

In the preparation of culture slide in this study, the oatmeal agar medium was used. Using sterilized scalpel, parts of the medium as 1 × 1 cm² were cut and placed on the slide by observing the sterilization rules (Fig. 1). After placing the agar completely in the center of the slide, it was

horizontally placed on a "U-shaped" tube in a large glass plate (containing 10 ml of sterile distilled water). Then using a sterile anse, the pure isolation samples were inoculated on 4 points on the slide (Fig. 2). Subsequently, the sterilized slide was placed on an inoculated agar portion and stored in an incubator at 25 °C for 7 days [9]. During incubation (each 3 days from the 7-day incubation period), the plates were examined and distilled water was used to prevent the plates from drying. After the 7-day incubation period, the microscope slide was separated and two drops of lactophenol were poured on another clean slide and placed the microscope slide with a mold (purified sample) attached to it on the slide and then examined and photographed them with a (10×), (40×) and (100×) lens with an optical microscope on the next day [9].

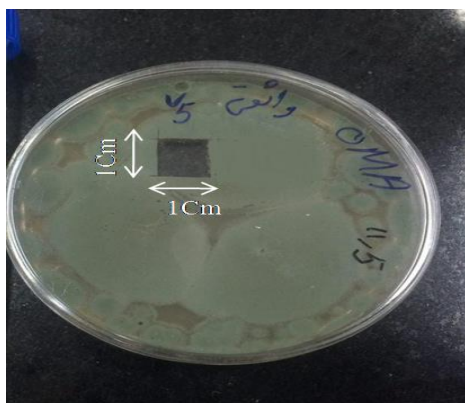


Fig.1. Slide culture from selected strains



Fig.2. Preparation of culture slide on U-shaped loop

Extraction of mycotoxins from liquid

Extraction of mycotoxins from liquid media (sabouraud dextrose broth with malt and yeast extract) after incubation (seventh day) to extract and purify mycotoxins produced by pure strains requires cell-free media. For this purpose, the falcon tubes containing the liquid medium were placed in a freezer for 15 min with a 35 degree angle vortex at -70 °C. In the next step, the falcon

tubes were removed from the freezer and de-frozen at the laboratory temperature. Then, 2.5 ml of extraction solvent was added to the falcon tubes and vortexed three times in three 15-minute periods at 30 to 35 degrees angle (this step was repeated to increase the extraction). A total of 5 ml of extraction solvent was used for each falcon. At the final stage of mycotoxin extraction (after two times during the vortex process and adding extraction solvent) the obtained liquid was separated by sterile Whatman filter paper (0.5 micron) and transferred to sterile microtubes (2 ml) for ELISA test and kept at a temperature of -4 °C. (Each of them was transferred to a bain-marie for 5-15 min at a temperature of 95-100 °C before the ELISA test for evaporation of the remaining alcohol from the microtubes) [10].

Extraction of mycotoxins from the solid medium (oatmeal agar)

After incubation (seventh day), cell-free media were required for extraction and purification of mycotoxins produced by the pure strains. For this purpose, using a sterile scalpel, the oatmeal agar was cut in 1×3 cm and inoculated to the sterile falcon tubes (10 cc) containing sterile beads glass and 5 cc of phosphate buffered saline (PBS) and was vortexed at 35 °C for 15 min and placed in a freezer at 70 °C.

Cold atmospheric pressure plasma (CAPP)

In this research, Citrinin and Ochratoxin A detoxification of APP of argon gas (output of the device's power supply at 50 kV, 100 watts, electron frequency 30 kHz, and gas flow rate 6 l/min) was investigated. To do the tests, first the output of the power supply was set to 50 kV, 100 watts, and the electron frequency of 30 kHz (optimal conditions for stable and effective plasma) and their exact values were measured with high-voltage probes and oscilloscopes. Then, with the gas flow (gas rate 6 l/min) and the high potential difference between the two connected electrodes, the effect of APP (argon-air) was investigated for 30, 60 and 360 sec. For treatments and mycotoxins (supernants), it was done in three replicates (Fig. 3).

RESULTS

Results of preliminary tests for the selection of mycotoxin producing microorganisms

In this research, samples were collected from northern regions of Iran including wheat, corn, oat, flour and rice. These samples were collected by Dr. Arash Chaichi Nosrati and put into the study.

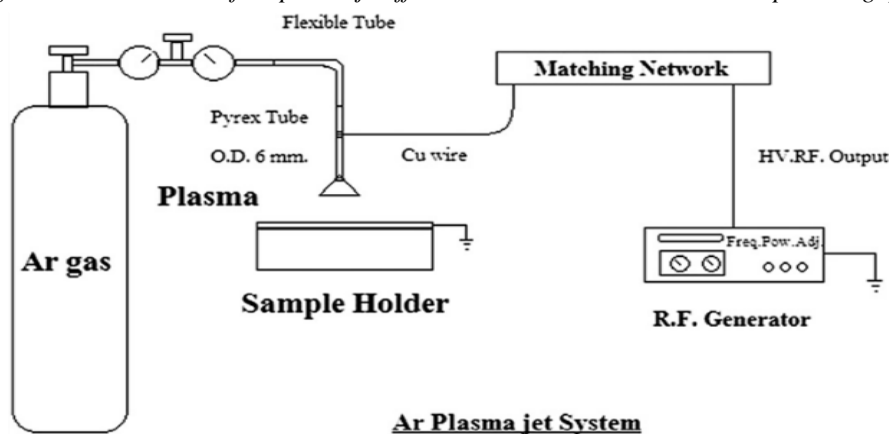


Fig.3. APPJ arrangement: Schematic image of the arrangement of plasma and plate containing the sample, as well as a view of the single-flame plasma jet produced, h of the produced plasma is 27 mm and the effective distance between the samples and the nozzle is 21 mm

In this research, 5 species of *Penicillium* genus were isolated and identified from different sources (wheat, corn, oats, flour and rice) (fungi coding as V1, V2, V3, V4 and V5).

Macroscopically, fungal colonies such as colony surface and back color, smooth or rough colony, powdery, cotton, etc., were examined (Table 1). In this study, the standard strains of *Penicillium digitatum* and *Penicillium italicum* of the microbial bank of the Iranian Institute of Plant Protection were used to compare the results and produce mycotoxins with collected samples. The mean initial concentration of Citrinin reached from 47.203 ppb at 60, 120, and 360 sec to 16.38, 16.23, and 29.27 ppb, respectively (Fig. 5).

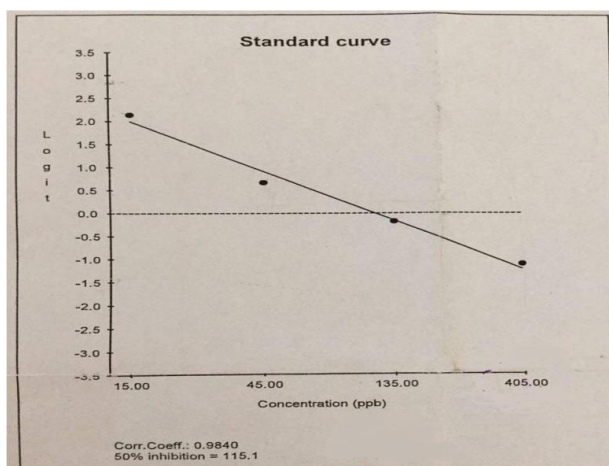


Fig.4. Standard curve of Citrinin

Results of examining the concentration of Citrinin obtained from the analysis of Lin/Log charts in sabouraud dextrose broth + yeast extract (Citrinin / YE + SB)

The mean initial concentration of Citrinin reached from 57.14 ppb at 60, 120, and 360 sec to 24.75, 30.04 and 34.78 ppb, respectively (Fig. 5).

Results of evaluation of Ochratoxin A A concentration obtained from Log/Lin tables analysis in sabouraud dextrose broth + malt extract (Ochratoxin A / ME + SB)

The mean initial concentration of Ochratoxin A in the medium reached from 25.9 ppb at 60, 120, and 360 sec to 13.66, 16.15, and 8.93 ppb, respectively (Table 4).

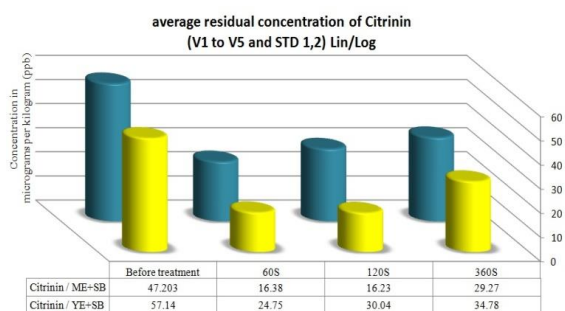


Fig.5. The average concentration of Citrinin before and after plasma radiation

Results of examining the concentration of Citrinin, obtained from the analysis of Log/Lin tables in the sabouraud dextrose broth + malt extract (Citrinin / ME + SB)

The average initial concentration of Citrinin in the medium reached from 36.05 ppb at 60, 120, and 360 sec to 41.66, 11.22 and 20.24 ppb, respectively (Table 2).

Results of examining the concentration of Citrinin obtained from the analysis of Log/Lin tables in sabouraud dextrose broth + yeast extract (Citrinin / YE + SB)

The mean initial concentration of Citrinin in the medium reached from 63.01 ppb at 60, 120, and 360 sec to 29.88, 13.49 and 31.61 ppb, respectively (Table 3).

Table 1. Macroscopic and microscopic characteristics of the isolated samples

Sample	Number/separated sources	Gender/species	Macroscopic characteristics (colony)	Microscopic characteristics
V1, V2	2 samples / rice	<i>Penicillium variable</i>	<ul style="list-style-type: none"> Limited growth Colonial diameter 10-15 mm per 7 days Fluffy and woolly colonies Yellow colonies 	<ul style="list-style-type: none"> Conidiospores are often concentrated in the center Containing spindle-shaped soft conidia Conidiospores with a smooth wall Containing 5-7 units in conidiospore Natural size of conidia is $(2.5 - 2.5) \times (12.5-7.0 \mu\text{m})$
V3	1 sample / corn	<i>Penicillium digitatum</i>	<ul style="list-style-type: none"> Fast growth Colony diameter 40-60 mm in 7 days Low sporulation Powder colony Colony color (first yellow to green-brown) Smooth colony level 	<ul style="list-style-type: none"> Branched and irregular conidiospores with short base and at the end 3-6 phialides Two-row phialides around Round conidia color (green olives) Conidia size is $(3.5 - 8) \times (3 - 4) \mu\text{m}$
V4	1 sample / from the source of wheat	<i>Penicillium nalgiovense</i>	<ul style="list-style-type: none"> The colony diameter is 25-30 mm in 7 days Colony color green to yellow Woolly and fluffy colony Colony back color yellow 	<p>Conidiospores are single but less than <i>P. Italicum</i></p> <ul style="list-style-type: none"> Containing 6-2 units in Conidiospore Conidiospores have a smooth wall Coinidia with a diameter of 3-4 μm Transparent Conidiospores 2-6 high phialides at the end
V5	1 sample / cereal (storage area of wheat and oat)	<i>Penicillium italicum</i>	<ul style="list-style-type: none"> Slow growth Colony diameter 50-60 mm in 14 days Having a fragrant smell Colony back color is colorless or yellow-brown Colony color (green-gray) Smooth colony level 	<ul style="list-style-type: none"> Single conidiospores Conidiospores have a smooth wall having stipe with a size of $(5-5.5) \times (250-100) \mu\text{m}$ Transparent conidiospores 3-6 high phialides Conidia color (green) Coinidia size $(5 - 4) \times (2.5 - 3.5) \mu\text{m}$
STD (1)	Bacterial Bank of Plant Protection Research Institute	<i>Penicillium digitatum</i>	<ul style="list-style-type: none"> Fast growth Colony diameter 40-60 mm in 7 days Low sporulation Powder colony Colonial color (first yellow to green-brown) Smooth colony level 	<ul style="list-style-type: none"> Branched and irregular conidiospores with short base and at the end of 3-6 phialides Two-row phialides around Round conidial color (olive green) Coinidia size $(3.5 - 8) \times (3 - 4) \mu\text{m}$
STD (2)	Bacterial Bank of Plant Protection Research Institute	<i>Penicillium italicum</i>	<ul style="list-style-type: none"> Slow growth Colony diameter 50-60 mm in 14 days Having a fragrant smell Colony back behind is colorless or yellow brown color Colony color (green-gray) Smooth colony level 	<ul style="list-style-type: none"> Single Conidiospores Conidiospores have a smooth wall Having a stipe with a size of $(5-5.5) \times (250-100) \mu\text{m}$ Transparent conidiospores 3-6 long phialides Conidia color (green) Conidia size $(5 - 4) \times (2.5 - 3.5) \mu\text{m}$

Analysis of the concentration of Ochratoxin A in isolated samples in sabouraud dextrose broth + malt extract (SB + ME) and sabouraud dextrose broth + yeast extract (SB + YE) before and after plasma radiation

The output of the power supply was set at 50 kV, 100 watts, 30 kHz electron frequency, and the inlet gas flow rate at 6 l/min. As in the previous method, first the turbidity of Ochratoxin A of the produced samples was measured and in the next step, according to the standard curve of Ochratoxin A (Fig. 6) and standard *Penicillium* samples (STD1/STD2), the concentration of Ochratoxin A was determined before and after treatment with plasma jet as Lin/Log charts and Log/Lin tables.

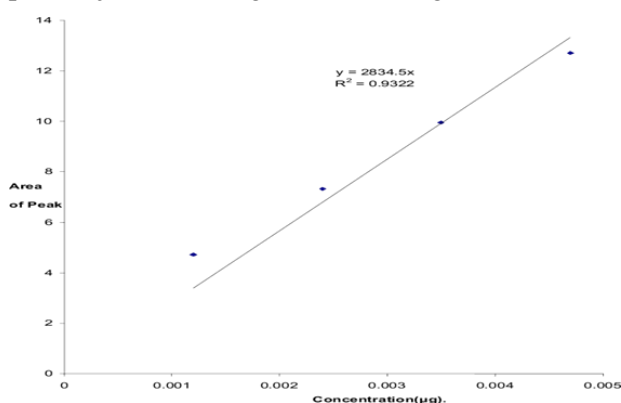


Fig.6. Standard curve of ochratoxin A

Results of examining the Ochratoxin A concentration obtained from analysis of Lin/Log charts in sabouraud dextrose broth + malt extract (Ochratoxin A / ME + SB)

The mean initial concentration of Ochratoxin A reached from 35.264 ppb at 60 and 360 sec to 18.34 and 12.008 ppb, respectively (Fig. 7).

Results of evaluation of Ochratoxin A concentration obtained from analysis of Lin/Log charts in sabouraud dextrose broth + yeast extract (Ochratoxin A / YE + SB)

The mean initial concentration of Ochratoxin A in the media reached from 28.625 ppb at 60 and 360 sec to 196.486 and 14.607 ppb, respectively (Fig. 7).

Results of evaluation of Ochratoxin A concentration obtained from Log/Lin tables analysis in sabouraud dextrose broth + malt extract (Ochratoxin A / ME + SB)

The mean initial concentration of Ochratoxin A in the medium reached from 25.9 ppb at 60, 120,

and 360 sec to 13.66, 16.15, and 8.93 ppb, respectively (Table 4).

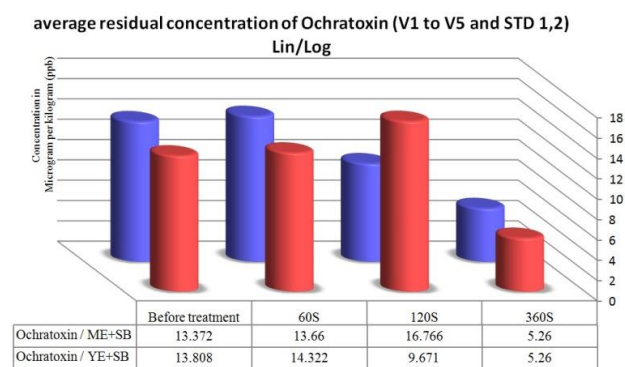


Fig. 7. Mean concentration of Ochratoxin A before and after plasma radiation

Results of evaluation of Ochratoxin A concentration obtained from Log/Lin tables analysis in sabouraud dextrose broth + yeast extract (Ochratoxin A / YE + SB)

The mean initial concentration of Ochratoxin A in the medium reached from 27.51 ppb at 60, 120 and 360 sec to 22.45, 13.83 and 10.63 ppb, respectively (Table 5).

As can be seen from the Log/Lin tables, it can be said that detoxification of Citrinin and Ochratoxin A was investigated by radiating argon gas over 60, 120 and 360 sec, and the mean initial concentrations of samples in sabouraud dextrose broth + malt extract and sabouraud dextrose + yeast extract (before radiation) were compared with the mean residual concentrations after each plasma emission. In these studies, it was found that detoxification of Citrinin and Ochratoxin A was successful in all samples and showed a high efficiency of APP in this field, especially in the food industry.

DISCUSSION

Investigation of Pearson correlation (Lin/Log) on the concentration of pre-irradiation produced mycotoxins (Citrinin and Ochratoxin A) in two media (ME + SB) and (YE + SB)

In this section, statistical correlation between the amount of Citrinin and Ochratoxin A produced by each isolated strain (V1 to V5) was investigated in two media (ME + SB), (YE + SB) and showed that a significant incompatibility is seen between these two toxins. So, the mean concentration of Citrinin was higher than that of Ochratoxin A.

Table 2. Concentration of Citrinin in sabouraud dextrose broth + malt extract

Log/lin	Sample name	Citrinin Malt (ppb)	Citrinin Malt /60s (ppb)	Citrinin Malt /120s (ppb)	Citrinin Malt /360s (ppb)
V1	<i>Penicillium variable</i>	44.99	42.36	9.36	22.39
V2	<i>Penicillium variable</i>	28.68	47.42	8.89	7.52
V3	<i>Penicillium digitatum</i>	40.5	88.28	0.03	0.01
V4	<i>Penicillium nalgiovense</i>	38.1	23.39	0.3	0.01
V5	<i>Penicillium italicum</i>	48.61	64.27	44.61	42.34
V STD(1)	<i>Penicillium digitatum</i>	16.81	10.43	19.82	24.38
V STD(2)	<i>Penicillium italicum</i>	34.66	15.51	5.51	24.54
Mean		36.05	41.66	11.22	20.24

Table 3. Concentration of Citrinin in the sabouraud dextrose broth + yeast extract

Log/lin	Sample name	Citrinin Yeast (ppb)	Citrinin Yeast /60s (ppb)	Citrinin Yeast /120s (ppb)	Citrinin Yeast /360s (ppb)
V1	<i>Penicillium variable</i>	32.43	35.04	13.54	72.2
V2	<i>Penicillium variable</i>	39.53	22.5	7.91	6.72
V3	<i>Penicillium digitatum</i>	226.68	57.8	0.03	0.2
V4	<i>Penicillium nalgiovense</i>	52.36	12.38	0.1	66.01
V5	<i>Penicillium italicum</i>	40.5	55.73	36.3	44.48
V STD(1)	<i>Penicillium digitatum</i>	15.54	12.61	17.08	8.08
V STD(2)	<i>Penicillium italicum</i>	34.04	13.11	19.51	23.58
Mean		63.01	29.88	13.49	31.61

Table 4. Concentration of Ochratoxin A in the sabouraud dextrose broth + malt extract

Log/lin	Sample name	OchraA Malt (ppb)	OchraAMalt /60s (ppb)	OchraA Malt /120s (ppb)	OchraA Malt /360s (ppb)
V1	<i>Penicillium variable</i>	29.95	13.372	20	0.1
V2	<i>Penicillium variable</i>	13.11	13.372	9.03	7.93
V3	<i>Penicillium digitatum</i>	40	13.372	0.03	0.02
V4	<i>Penicillium nalgiovense</i>	11.12	13.372	11.35	5.75
V5	<i>Penicillium italicum</i>	7.13	15.391	45.35	35.71
V STD(1)	<i>Penicillium digitatum</i>	40	13.372	15.57	5.51
V STD(2)	<i>Penicillium italicum</i>	4	13.372	11.23	7.5
Mean		25.9	13.66	16.15	8.93

Table 5. The concentration of ochratoxin A in the sabouraud dextrose broth + yeast extract

Log/lin	Sample name	OchraA Yeast (ppb)	OchraA Yeast /60s (ppb)	OchraA Yeast 120s (ppb)	OchraA Yeast /360s (ppb)
V1	<i>Penicillium variable</i>	23.91	62.7	11.1	0.03
V2	<i>Penicillium variable</i>	13.47	9.03	7.3	9.3
V3	<i>Penicillium digitatum</i>	40	11.6	1.51	0.01
V4	<i>Penicillium nalgiovense</i>	29.47	20.5	8.89	0.02
V5	<i>Penicillium italicum</i>	15.47	15.06	41.66	42.39
V STD(1)	<i>Penicillium digitatum</i>	40	18.8	17.3	13.79
V STD(2)	<i>Penicillium italicum</i>	40	19.5	9.03	8.89
Mean		27.51	22.45	13.83	10.63

Statistical analysis of Pearson correlation (Lin/Log) on the concentration of Ochratoxin A in two media (ME + SB) and (YE + SB)

In the study of Pearson's correlation, the correlation between the amount of Ochratoxin A produced in the two studied media showed that the fungal isolates of the two sabouraud dextrose broth

+ malt extract and sabouraud dextrose broth + yeast extract were able to produce toxin. In the study of the Pearson correlation, according to Table 6, the extent of Ochratoxin A reduction by plasma jet after 60 sec in both studied media showed a statistically significant correlation between them. So in both media, the toxin reduction was on average less than 10% after 60 sec.

Also, there was a significant statistical correlation after 120 sec of plasma jet treatment about comparing the amount of Ochratoxin A in the two media studied. In both media, the amount of toxin reduction after 120 sec was on average less than 5%, which is indicative of the high accuracy of ELISA test in this study.

Statistical analysis of Pearson correlation (Lin/Log) on the concentration of Citrinin in two media (ME + SB) and (YE + SB)

In the study of Pearson's correlation, the reduction of Citrinin in the medium (ME + SB) after 60, 120, and 360 sec of jet plasma treatment was more than its reduction in the medium (YE + SB) and there was a consistent and significant correlation between them.

In the study of Pearson correlation, a significant aligned correlation can be seen between the amounts of Citrinin detoxification produced after 60 sec treatment with plasma jet. The significant correlation shows that with the effect of plasma jet, Citrinin toxin levels were reduced in the ME + SB and YE + SB by 34.7% and 43.31%, respectively (Table 6).

In the study of Pearson's correlation, the statistical correlation between the amount of Citrinin toxin produced in the two studied media showed that the fungal isolates studied in both ME + SB and YE + SB are able to produce toxin. The greatest reduction and effect of plasma jet among treatments was observed for Citrinin toxin after 360 sec of treatment in YE + SB. During this time, the amount of toxin was reduced by 60.86%.

Comparison and statistical analysis of the Pearson correlation (Lin/Log) and concentration and effect of plasma jet on Citrinin and Ochratoxin A

Citrinin is known in the inter-cellular metabolism of producing fungi of the leading toxin of Ochratoxin A. In examining the correlation between Citrinin and Ochratoxin A levels in ME + SB and YE + SB, which are treated for 60 sec with

plasma, there was a significant correlation between them (Table 6).

Wilcoxon test (significant numerical difference) (Lin/Log) on the concentration of pre-irradiation mycotoxins (Citrinin and ochratoxin A) in two media (ME + SB) and (YE + SB)

In evaluating the initial values of Citrinin and Ochratoxin A produced in SB + ME in statistical analysis, the result was acceptable in terms of Wilcoxon test (significant numerical difference). Therefore, the inconsistency in the study of Pearson's correlation indicates that the ratio of Citrinin to Ochratoxin A transform was relatively low. Significant statistical inconsistency between the relative amount of Ochratoxin A as reduced in SB + ME medium after 60, 120, and 360 sec treatment shows that increasing the time of treatment with plasma jet also increases the amount of toxin, although by increasing the time from 120 to 360 sec, the toxin was severely reduced.

Statistical analysis of Pearson correlation (Log/Lin) on the concentration of Ochratoxin A in two media (ME + SB) and (YE + SB)

In the study, the correlation of Ochratoxin A amount in two SB + ME and SB + YE was statistically significant. At the concentration of Ochratoxin A, after 120 and 360 sec of treatment, a correlation was observed between the reduced values. There is a statistically pair significant correlation between the amount of Ochratoxin A in the SB + ME from 120 to 360 sec, and also in the SB + YE from 120 to 360 sec.

For Ochratoxin A, the highest reduction in SB + YE occurs after 120 seconds of treatment, which decreased by about 50.27% after 120 sec. For Ochratoxin A, the highest reduction in SB + ME occurs after 360 sec of treatment, so that after 360 sec, the toxin decreased by 34.47%.

Table 6. Concentration of Citrinin and Ochratoxin A before and after plasma radiation (Lin/Log)

Citrinin and Ochratoxin A	Concentration (Before treatment) (ppb)	Concentration after 60 sec of radiation (ppb)	Concentration after 120 sec of radiation (ppb)	Concentration after 360 sec of radiation (ppb)
Citrinin / ME + SB	47/203	16/38	16/23	29/27
Ochratoxin A / ME + SB	13/372	13/66	16/766	5/26
Citrinin / YE + SB	57/14	24/57	30/04	34/78
Ochratoxin A / YE + SB	13/808	14/322	9/671	5/26

Statistical analysis of Pearson correlation (Log/Lin) with the concentration of Citrinin in two media (ME + SB) and (YE + SB)

However, Pearson's correlation (significant and consistent correlation) between Citrinin and Ochratoxin A can be achieved, but the decreasing amounts of Citrinin and Ochratoxin A do not occur after these treatments, which can be detected by ELISA method and we cannot prove the extent of treatment with plasma jet, so it should be with plasma jet, reached from 25.9 to 8.93, indicating a non-uniform significant correlation between the data. This correlation was statistically significant in comparison with the amount of Ochratoxin A reduction in SB + ME after 120 and 360 sec of plasma jet treatment, and there was a significant inconsistent correlation in increasing the time and the requirement for toxin reduction.

The results of this study are consistent with other studies carried out in recent years, including that of Siciliano *et al.*, on the effect of APP that uses argon gas to produce plasma, to study the effect of plasma on the elimination of mycotoxins produced by *Aspergillus*. In this study, they were able to use a plasma with the characteristics of a power supply output of 50 kV, 400 watts, an electron frequency of 30 kHz, aflatoxin, and ochratoxin A produced by isolates at a concentration of 25 ng/g to remove 95% after one min of radiation [5]. Also, Ouf *et al.* used the effect of APP, which uses argon gas to make plasma, to study the effect of plasma on the elimination of mycotoxins produced by *Aspergillus*. In this study, they were able to remove more than 97% of aflatoxin B1 produced by *Aspergillus parasiticus* with a power of 60 watts over a period of 15 min. In this study, they removed more than 95% of aflatoxins produced by *Aspergillus flavus* by the radiation of plasma of 60 watts in 12 min. [11].

CONCLUSIONS

In this research, detoxification of Citrinin and Ochratoxin A by APP of argon gas (output of the

6. Prella, D. Vallauri, M. C. Cavallero, A. Garibaldi, M. L. Gullino, Use of cold atmospheric plasma to detoxify hazelnuts from aflatoxins, *Toxins*, **8**, 110 (2016).
7. Y. Devi, R. Thirumdas, C. Sarangapani, R. R. Annature, Influence of cold plasma on fungal growth and aflatoxins production on groundnuts, *Food Control*, **77**, 187 (2017).
8. M. A. Klich, Identification of Common *Aspergillus* Species, United States. *Centraal Bureau Voor Schimmel Cultures*, **13**, 959 (2002).

considered in another research.

Examining Wilcoxon test (Log/Lin) on the concentration of mycotoxins produced before radiation (Citrinin and Ochratoxin A) in two media (ME + SB) and (YE + SB)

Considering the significance of the numerical difference (Wilcoxon), the mean Ochratoxin A produced from the fungi studied in SB + ME medium after 360 sec treatment

power supply 50 kV, 100 watts, electron frequency 30 kHz, and gas flow rate 6 l/min) was investigated. In summary, it can be said that many disinfection methods, including chemical, physical, dry or wet heat methods, are used to disinfect solid surfaces or liquids and biological surfaces such as skin with functional limitations. The use of non-thermal plasma technology in cleaning, sterilization and detoxification has advantages over existing ones, including high detoxification properties during short flow, lack of remaining toxicity, and the cost-effectiveness of argon gas. In this study, Lin/Log and Log/Lin charts and tables were statistically evaluated (mean, standard deviation, variance, covariance, correlation coefficient, etc.).

REFERENCES

1. M. G. Kong, G. Kroesen, G. Morfill, T. Nosenko, T. Shimizu, J. Van Dijk, Plasma medicine: an introductory review, *New Journal of Physics*, **29**(11), 115012 (2007).
2. S. M. Mortazavi, A. H. Colagar, F. Sohbatzadeh, The Efficiency of the Cold Argon-oxygen Plasma jet to reduce *Escherichia coli* and *Streptococcus pyogenes* from solid and liquid ambient, *Iran J. Med. Microbiol.*, **10**, 214 (2016).
3. A. Fernández, A. Thompson, The inactivation of *Salmonella* by cold atmospheric plasma treatment, *FRIN*, **45**, 678 (2012).
4. F. J. Cabañes, M. R. Bragulat, G. Castella, Ochratoxin A Producing Species in the Genus *Penicillium*, *Toxins*, **2**, 1111 (2010).
5. I. Siciliano, D. Spadaro, A.
9. H. Barnett, B. Hunter, Illustrated Genera of Imperfect Fungi, 4th ed. Minneapolis, Burgess, **88**, 154 (1998).
10. L. James, Modified Method for Fungal Slide Culture. *Harris Journal of Clinical Microbiology*, **23**, 460 (1986).
11. A. Rahmani, S. Jinap, F. Soleimani, Qualitative and Quantitative Analysis of Mycotoxins, *Comprehensive Review in Food Science and Food Safety*, **8**, 432 (2009).

- N. Vaseghi et al.: Evaluation of the plasma jet effects on the Citrinin and Ochratoxin A producing species ...*
12. S. A. Ouf, A.H. Basher, A. A. Mohamed, Inhibitory effect of double atmospheric pressure argon cold plasma on spores and mycotoxin production of *Aspergillus* contaminating date palm fruits, *J. Sci. Food Agric.*, **15**, 3204 (2015).

ВЛИЯНИЕ НА ПЛАЗМЕНИТЕ РЕАКТИВНИ ЕФЕКТИ ВЪРХУ ЦИТРИНИН- И ОХРАТОКСИН-ПРОИЗВЕЖДАЩИТЕ ФОРМИ НА *PENICILLIUM*

Н. Вазеги¹, М. Баят^{1*}, А. Х. Носрати², М. Гораневис³, С. Хашеми⁴

¹ Департамент по микробиология, Научен и изследователски клон на Ислямски Азад университет, Техеран, Иран

² Департамент по молекулярна и клетъчна биология, Лахиджански клон на Ислямски Азад университет, Лахиджан, Гилан, Иран

³ Изследователски център по плазмена физика, Научен и изследователски клон на Ислямски Азад университет, Техеран, Иран

⁴ Департамент по медицинска паразитология и микология, Училище за обществено здраве, Техерански университет по медицински науки, Техеран, Иран

Постъпила на 23 ноември, 2017 г.; коригирана на 15 февруари, 2018 г.

(Резюме)

Микотоксините са малки токсични молекули, произвеждани от различни микроорганизми. Те често се състоят от вторични метаболити и имат различни функции и структури. Цитринин и охратоксин А, произвеждани от различни форми на *Penicillium*, замърсяват храните. Методът на студената плазма при атмосферно налягане има потенциал за детоксикация на микотоксини. В тази статия са изследвани и оптимизирани работните параметри на студената плазма при атмосферно налягане (САРР) за засилване на ефекта върху цитринин и охратоксин А в пшеница, овес, царевича и ориз. Първоначалните опити са проведени при мощност на захранване 50 kV, 100 вата и електронна честота от 30 kHz (оптимални условия за стабилна и ефективна плазма). След това е изследвано влиянието на студената плазмена струя (аргон) върху създаването на газовия поток (скорост на газа 6 l/min) за 30, 60 и 360 sec. Установено е, че САРР методът ефективно намалява количеството на микотоксини. Намалението с използване на плазма с мощност от 100 W е над 40% и 50% от първоначалната концентрация съответно на цитринин и охратоксин А. Степента на разрушаване на различните микотоксини варира в зависимост от тяхната структура. Показано е, че в присъствие на комбинация от микотоксини разрушаването им от плазмата е по-малко ефективно. В настоящото изследване цитринин и охратоксин А са успешно детоксикирани във всички образци. В допълнение, САРР методът няма биологични ефекти и се отразява минимално на хранителните продукти в сравнение с конвенционалните методи на дезинфекция на хранителни продукти.

Impact of 50 Hz magnetic field on the content of polyphenolic compounds from blackberries

M. Răcuci¹, S. Oancea^{2*}

¹“Lucian Blaga” University of Sibiu, Department of Environmental Sciences and Physics, 5-7 Ion Ratiu Str., 550024 Sibiu, Romania²“Lucian Blaga” University of Sibiu, Department of Agricultural Sciences and Food Engineering, 7-9 Ion Ratiu Str., 550012 Sibiu, Romania

Received February 20, 2018; Accepted April 24, 2018

Blackberries are fruits abundant in bioactive compounds which may be extracted from the matrix by several strategies. Different physical or (bio)chemical pre-treatment of samples might favour the extraction of specific compounds. Little is known about the magnetic field influence on anthocyanins and phenolics extraction, which determined the purpose of this work. Fresh wild and cultivated blackberries were exposed to homogenous 50 Hz frequency magnetic field of 3 mT for up to 12 h. The results showed a significant increase of total anthocyanins and antioxidant activity of all samples exposed up to six hours, compared to control sample. Longer exposure time to magnetic field determined a decrease of total anthocyanins content of wild blackberries. The recovery of high amounts of valuable bioactive compounds using the investigated non-thermal strategy renders the technique useful for applications in food, pharmaceutical or cosmetic industry.

Keywords: Blackberry, Low-frequency magnetic field, Anthocyanins, Phenolics

INTRODUCTION

Apart from their nutritional profile, berry fruits – in particular from *Rubus* species, are abundant in valuable chemical compounds, mainly of polyphenolic structure, such as flavonoids / anthocyanins [1,2]. These compounds are powerful antioxidant biomolecules known for their human health benefits [3].

Considering the bioactive compounds and the health promoting properties of blackberries [4], a lot of research has been conducted toward their valorisation in innovative and value-added products for food or pharmaceutical industry. The main focus for such applications is the recovery of high amounts of biologically active compounds extracted by different, conventional or non-conventional extraction techniques. At the same time, it is known that fresh berries are susceptible to microbial contamination. Several techniques have been proposed for their preservation [5]: (i) chemical (chlorine-based surface disinfectants, ozone, edible coatings); (ii) physical (temperature, ionizing radiation, UV), or (iii) biological (non-pathogenic microorganisms, essential oils, plant extracts). Thermal treatments (heat) are very popular for food preservation, but may lead to degradation of various thermolabile compounds, in particular anthocyanins. Based on the great demand for healthy foods with required quality characteristics, new mild preservation techniques have emerged as useful tools for enzyme and

microbial inactivation, such as pulse electric field, high pressure, microwave, ultrasound, X-ray, or magnetic field [6].

Application of magnetic field (static or oscillating) has been taken into consideration as non-thermal new technology of foods preservation, showing the advantage of maintaining the sensory and nutritional quality of the product, because of the small temperature increase (below 5°C), and of no adverse effects compared to other types of irradiation. Both inhibitory and stimulatory effects were observed on microorganisms exposed to magnetic field [7]. The effect depends on the magnetic field strength and frequency, or time of pulse duration. Low-frequency oscillation magnetic field (10 mT) was successfully applied for inactivation of *Escherichia coli* [8], while low-frequency static magnetic field (40 mT) was found useful to inhibit wine yeast [9]. The mechanism of microbial inactivation by exposure to magnetic fields has not been completely elucidated, but it is considered that membrane integrity and DNA is affected [6]. Little is known about the impact of magnetic field on the extraction and recovery of bioactive compounds from plant foods. It is known that physical processes such as ultrasound or high-voltage pulsed electric fields may significantly increase the extraction of phenolics and anthocyanins [10,11]. The literature is scarce in studies regarding the evaluation of the nutritional composition and/or content of phytochemicals in plant foods which have been exposed to magnetic field. Several studies reported higher enzymatic

* To whom all correspondence should be sent:
E-mail: simona.oancea@ulbsibiu.ro

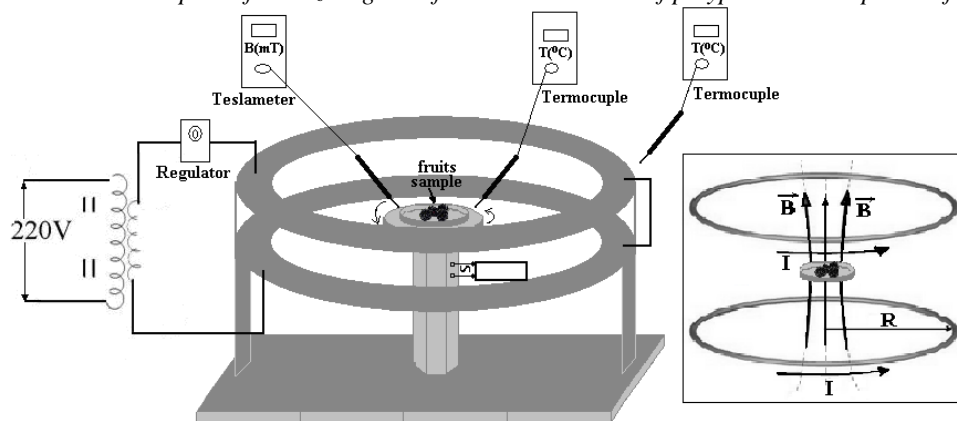


Fig. 1. Magnetic field exposure design setup used for blackberry samples irradiation.

activity in seedlings originating from wheat seeds exposed to low- frequency alternating magnetic field [12] or improved respiration in sugar beet seeds treated with magnetic field [13].

The aim of the present paper was to investigate the changes induced in total anthocyanins content and total antioxidant activity in blackberry fruits (wild and cultivated) exposed to low-frequency magnetic field (50 Hz sinusoidal magnetic field, 3 mT).

EXPERIMENTAL

Plant material and reagents

The experimental study was carried out using two types of blackberry samples grown in Romania: *Rubus sulcatus* Vest, harvested from spontaneous flora of Șanta area, Săliște (Sibiu County) and *Rubus fruticosus* L., Thornfree variety harvested from Târgoviște (Dâmbovița County) cultivated area. The moisture content of the samples was determined at 105°C using the moisture analyser (MAC 210 - RADWAG, Poland). Chemical reagents of analytical grade without further purification were used.

Magnetic field treatment

Samples were exposed to magnetic field using a laboratory Helmholtz coil system formed of two coils (each 1000 turns of 1 mm copper wire) with 260 mm diameter each, mounted coaxially and placed at a mean distance of 130 mm from each other (Fig. 1). The coil system was powered through a power terminal of 50 Hz sinusoidal voltage (220V) equipped with variable transformer, for generation of a vertical homogenous magnetic field with 3mT of magnetic flux density in the centre of the coil system. A low-frequency field analyser (NARDA EFA-300) was used as no significant variations of the magnetic field value were detected within the central zone (10 cm diameter) of the Helmholtz coil system. During the

exposure, no temperature variation was registered. The vertical magnetic field background was measured ($0.13 \pm 0.01 \mu\text{T}$) using the C.A.40 Gaussmeter. The magnetic field treatment of samples was performed by placing a 9 cm diameter Petri dish containing the same number of fruit samples of similar weight in the centre of the Helmholtz coil system. Blackberry samples were exposed to a homogenous 50 Hz magnetic field with 3 mT magnetic flux density, at room temperature ($22.0 \pm 0.5^\circ\text{C}$) at different exposure times (between 1 and 12 h).

The magnetic field dose was expressed using the following formula:

$$D = \frac{B^2}{2\mu_0} \cdot t \quad (1)$$

where $B[\text{T}]$ is the magnetic flux density, $t[\text{s}]$ is the exposure time under magnetic field and μ_0 is the magnetic permeability of free space ($4\pi \cdot 10^{-7} \text{ H/m}$).

The applied magnetic doses ranged between $12.89 \text{ kJ}\cdot\text{s}/\text{m}^3$ and $154.69 \text{ kJ}\cdot\text{s}/\text{m}^3$.

Extraction and assay of total anthocyanins

Extraction of anthocyanins was performed immediately after the magnetic treatment, in 70 % (V/V) ethanol solution. Untreated samples were used for comparison studies. The total anthocyanins content in the extracts was determined spectrophotometrically by the pH differential method [14]. The Specord 200Plus UV-Vis spectrophotometer (Analytik Jena, Germany) was used. The results were expressed as mg Cyn-3-O-G equivalents $100 \text{ g}^{-1} \text{ DM}$.

Total antioxidant activity

The total antioxidant activity in the blackberry extracts was measured by determination of total phenolics according to the Folin-Ciocalteu method [15] and was expressed as mg gallic acid equivalents GAE $100 \text{ g}^{-1} \text{ DM}$.

All experiments were done in duplicate. The results were presented as mean values \pm standard error. The statistical analysis of the experimental data was carried out using the Systat v.10 software. The statistical model for several regression curves was done using the Statistics v.7.0 software.

RESULTS AND DISCUSSION

By exposure of fresh wild and cultivated blackberries to 50 Hz magnetic field (MF) at 3 mT of magnetic flux density for relatively short periods – 1, 2, 4 and 6 h – there was an increase of total anthocyanins content (TAC) compared to control (untreated sample), as shown in Fig. 2.

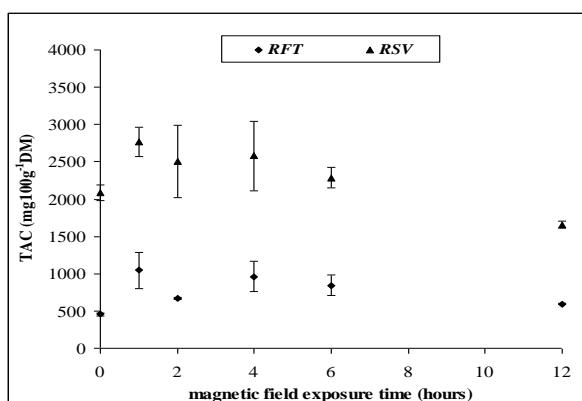


Fig. 2. Comparative total anthocyanins content (TAC) (mg 100 g⁻¹DM) changes in wild blackberries *Rubus sulcatus* Vest (RSV) and cultivated blackberries *Rubus fruticosus* Thornfree variety (RFT), exposed to magnetic field of 3 mT. Values are expressed on dry mass (DM) basis, as mean \pm standard error of two replicates.

The MF pre-treatment caused an increase in the level of anthocyanins by 9 – 33% in wild blackberries (*Rubus sulcatus* Vest) and by 30 – 129% in cultivated ones (*Rubus fruticosus* Thornfree variety) depending of irradiation time. The highest level was recorded at 1 h, both in wild and cultivated blackberries. Long MF exposure (12 h) caused a decrease of TAC in wild blackberries by 20% compared to control.

As previously reported [16], wild berries contain much higher amounts of anthocyanins compared to cultivated ones. The present investigation showed that wild blackberries (*Rubus sulcatus* Vest) contained a 4.5 times higher concentration of anthocyanins (2085.64 mg 100 g⁻¹ DM) than cultivated ones (*Rubus fruticosus* Thornfree variety) (454.96 mg 100 g⁻¹ DM). TAC was expressed on dry mass basis, in order to have homogenous results to be compared. These values are within the range of TAC of blackberries

measured with the same method reported by other authors [17].

The regression analysis revealed a third order polynomial dependence between the TAC and the MF energy dose (D). The regression model ($R^2=0.93$) for wild blackberry is presented in Fig. 3. The total antioxidant activity as measured by total phenolics content (TPC) of fresh wild and cultivated blackberries exposed to 50 Hz MF of 3 mT of magnetic flux density, increased up to 63% compared to control.

The TPC changes with exposure time (1 - 12 h) are comparatively presented in Fig. 4. The MF pre-treatment generated an increase in the level of TPC of wild blackberries by 5 - 27% and of cultivated blackberries by 6.5 - 63% in relation to the exposure time. The highest TPC of both wild and cultivated blackberry samples was recorded after 1 h.

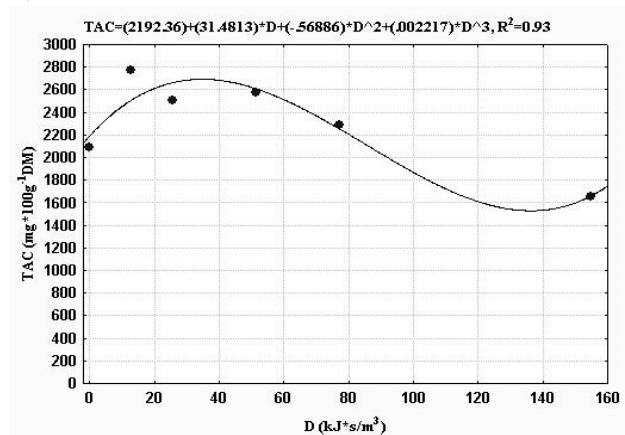


Fig. 3. Dependence between the total anthocyanins content (TAC) (mg 100 g⁻¹DM) of wild blackberries *Rubus sulcatus* Vest (RSV) and the magnetic field energy dose (D) (kJ s/m³). Values are expressed on dry mass (DM) basis, as mean of two replicates.

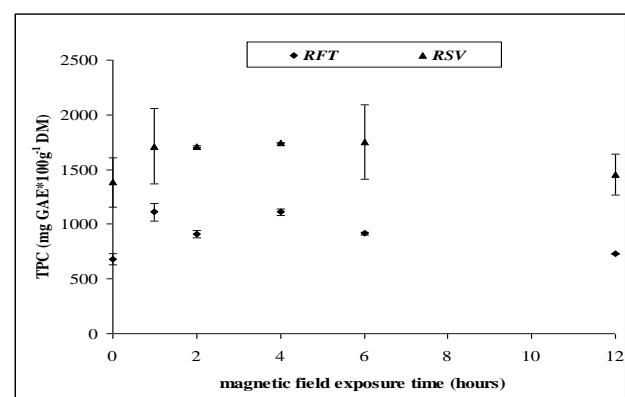


Fig. 4. Comparative total phenolics content (TPC) (mg GAE 100 g⁻¹ DM) changes in wild blackberries *Rubus sulcatus* Vest (RSV) and cultivated blackberries *Rubus fruticosus* Thornfree variety (RFT), exposed to magnetic field of 3 mT. Values are expressed on dry mass (DM) basis, as mean \pm standard error of two replicates.

The TPC of wild blackberries (*Rubus sulcatus Vest*) was 2 times higher than that of cultivated ones (*Rubus fruticosus* Thornfree variety), which indicates the higher total antioxidant activity of wild blackberries. TPC was expressed on dry mass basis, in order to have homogenous results to be compared. TPC of blackberries was reported to vary from 114 to 1056 mg 100 g⁻¹ FW [4] depending on variety, environmental factors and methods of analysis.

Fig. 5 indicates the polynomial dependence between the TPC of the wild blackberries and the MF energy dose (D), resulted from the regression analysis (the coefficient of determination R²=0.93). By calculation of the correlation coefficients, a positive linear correlation between TPC and TAC levels was found for cultivated blackberries (R=0.9572; p=0.002) (Fig. 6).

Enhanced levels of TAC and TPC of blackberries were obtained for samples exposed to homogeneous magnetic field (50 Hz, 3 mT) for relatively short times (1-6 h) compared to control. A tendency of TAC decrease was registered in samples exposed to magnetic field for longer periods (12 h).

To our knowledge, there is a scarcity of such studies regarding the influence of magnetic fields on total phenolics and anthocyanins level in fruits. Lipiec *et al.* [18] reported a 1.5-fold increase of TPC in sprouts of naked oat (cv. Akt) under the treatment with oscillating magnetic field pulses of 10 × 3 T. Most of the previous studies reported the effects of magnetic field on the growth of various plants. Esitken [19] studied the influence of 50 Hz magnetic field with magnetic induction of 96, 192 and 384 mT, respectively, on raspberry (*Camarosa* variety) during its growth in a greenhouse. Their results showed a positive influence on plant growth and fruit production. In another study, the pre-treatment of seeds of *Artemisia sieberi* with MF of 200 mT for 20 min before germination, led to a considerable increase in the concentration of polyphenols and antioxidant activity of plant shoots, compared to control [20].

The mechanism by which magnetic fields impact living cells is still unclear, but most hypotheses refer to the change in the Ca²⁺ balance, antioxidant enzymes and different metabolic processes [21,22].

Another hypothesis regarding the mechanism of interaction of low-frequency magnetic fields with the absorbing material is based on the induction of electric fields, their distribution being related to the electrical conductivity of tissues [23].

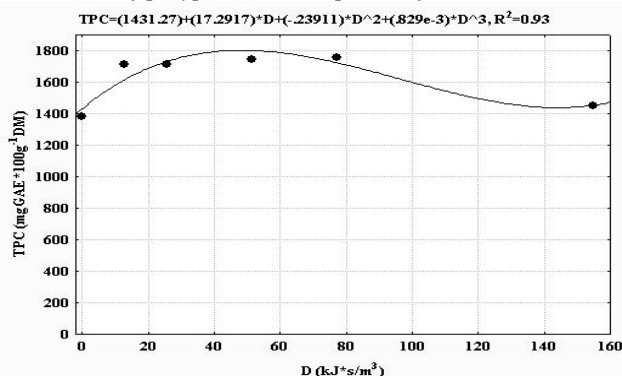


Fig. 5. Dependence between the total phenolics content (TPC) (mg GAE 100 g⁻¹ DM) of wild blackberries *Rubus sulcatus Vest* (RSV) and the magnetic field energy dose (D) (kJ s/m³). Values are expressed on dry mass (DM) basis, as mean of two replicates.

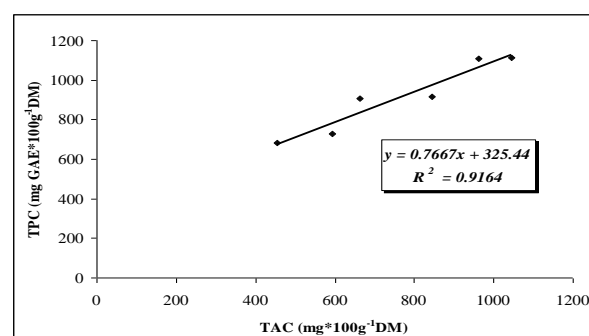


Fig. 6. Linear correlation between TPC (mg GAE 100 g⁻¹ DM) and TAC (mg 100 g⁻¹ DM) of cultivated blackberries *Rubus fruticosus* Thornfree variety (RFT).

As water is dominant in all living cells, unusual impact of the magnetic field on the water could explain some of the reported effects since the energy of the extremely low MF (50 Hz) is much lower than the energy required for breaking the bonds of water molecules. Nevertheless, at present, there is no clear mechanism of influence of low MF on water. Some researchers have noticed changes in the electrical conductivity of water due to the action of 50 Hz MF [24]. An increase of water evaporation due to exposure to weak static MF (15 mT) was also reported [25]. However, there are quite a lot of controversial results in the literature on this subject.

Regarding the possible mechanism by which the MF increased the levels of anthocyanins and the antioxidant activity in the hereby investigated fresh blackberries, probably membrane permeability processes are involved favouring the release of intracellular biologically active compounds (enhancement of extraction).

CONCLUSIONS

The results of our study showed that magnetic field exposure produced changes in the content of

M. Răcuciu and S. Oancea: Impact of 50 Hz magnetic field on the content of polyphenolic compounds from blackberries
 main antioxidant compounds of polyphenolic structure in fresh blackberries, either wild or cultivated. The treatment of blackberry fruits with low magnetic field (50 Hz, 3 mT) for up to six hours resulted in the increase of total anthocyanins and phenolics content, which was more pronounced in cultivated species. Long exposure time (12 h) determined a decrease of total anthocyanins content of wild blackberries. In all experiments, wild blackberries showed higher concentrations of the investigated phytochemical compounds compared to cultivated ones, for both MF irradiated and non-irradiated samples.

Our findings may be used for the improvement of extraction of polyphenolic compounds from berry fruits using pre-treatment with MF.

REFERENCES

1. N. Deighton, R. Brennan, C. Finn, H. V. Davies, *J. Sci. Food Agr.*, **80**(9), 1307 (2000).
2. A. Z. Mercadante, F. O. Bobbio, in: *Food Colorants: Chemical and Functional Properties*, Socaciu C (ed.), Taylor & Francis Group, CRC Press, NY, USA, 2008, p.241.
3. J. M. Kong, L. S. Chia, N. K. Goh, T. F. Chia, R. Brouillard, *Phytochemistry*, **64**, 923 (2003).
4. L. Kaume, L. R. Howard, L. Devareddy, *J. Agr. Food Chem.*, **60**, 5716 (2012).
5. M. A. Daeschel, P. Udampijitkul, in: *Berry fruit: value-added products for health promotion*, Y. Zhao (ed.), Taylor & Francis Group, CRC Press, NY, USA, 2007, p. 229.
6. J. Ahmed, H. S. Ramaswamy, in: *Handbook of food preservation*, M.S. Rahman (ed.), Taylor & Francis Group, CRC Press, NY, USA, 2007, p. 855.
7. N. Yoshimura, *Shokuhin Kaihatsu*, **24**(3), 46 (1989).
8. L. Fojt, L. Strasak, V. Vetterla, J. Smarda, *Bioelectrochemistry*, **63**, 337 (2004).
9. G.C. Kimball, *J. Bacteriol.*, **35**(2), 109 (1938).
10. V. Kannan, Master degree thesis in Food Science and Technology, University of Nebraska – Lincoln, USA, 2011.
11. S. Oancea, C. Grosu, O. Ketney, M. Stoia, *Acta Chim. Slov.*, **60**(2), 383 (2013).
12. M. Rochalska, K. Grabowska, *Int. Agrophys.*, **21**, 185 (2007).
13. M. Rochalska, A. Orzeszko-Rywka, *Int. Agrophys.*, **22**, 255 (2008).
14. S. J. Schwartz, in: *Current protocols in food analytical chemistry*, John Wiley & Sons Inc., NY, USA, 2001.
15. V. L. Singleton, J. A. Rossi, *Am. J. Enol. Viticult.*, **16**, 144 (1965).
16. S. Oancea, F. Moiseenco, P. Traldi, *Rom. Biotech. Lett.*, **18**(3), 8350 (2013).
17. G. Mazza, E. Miniati, in: *Anthocyanins in Fruits, Vegetables, and Grains*, Boca Raton: CRC Press, Florida, 1993.
18. J. Lipiec, P. Janas, W. Barabasz, M. Pysz, P. Pisulewski, *Acta Agroph.*, **5**(2), 357 (2005).
19. A. Esitken, *J. Hortic. Sci. Biotech.*, **78**, 145 (2003).
20. F. Azimian, P. Roshandel, *Indian J. Plant Physiol.*, **20**, 264 (2015).
21. Ö. Çelik, N. Büyüksulu, Ç. Atak, A. Rzakoulieva, *Pol. J. Environ. Stud.*, **18**(2), 175 (2009).
22. A. R. Liboff, *J. Biol. Phys.*, **9**, 99 (1985).
23. International Commission on Non-Ionizing Radiation Protection (ICNIRP) Guidelines for limiting exposure to time-varying electric and magnetic fields (1 Hz To 100 kHz), *Health Phys.*, **99**(6), 818 (2010). www.icnirp.de/PubMost.htm
24. S. N. Akopian, S. N. Aïrapetian, *Biofizika*, **50**(2), 265 (2005).
25. L. Holysz, A. Szczes, E. Chibowski, *J. Colloid Interf. Sci.*, **316**, 996 (2007).

ВЛИЯНИЕ НА 50 Hz МАГНИТНО ПОЛЕ ВЪРХУ СЪДЪРЖАНИЕТО НА ПОЛИФЕНОЛНИ СЪБЕДИНЕНИЯ В КЪПИНИ

М. Ракучу¹, С. Оанча^{2*}

¹ Университет на Сибиу “Луциан Блага”, Департамент по науки за околната среда и физика, 550024 Сибиу, Румъния

² Университет на Сибиу “Луциан Блага”, Департамент по селскостопански науки и хранително инженерство, 550012 Сибиу, Румъния

Постъпила на 24 февруари, 2018 г.; приета на 24 април, 2018 г.

(Резюме)

Къпините са плодове, богати на биоактивни вещества, които могат да се екстрахират от матрицата по различни методи. Различната физична или (био)химична обработка на пробите може да благоприятства екстракцията на специфични вещества. Влиянието на магнитно поле върху екстракцията на антоцианини и феноли е малко известно, което определи целта на настоящата работа. Пресни диви и култивирани къпини са изложени на хомогенно магнитно поле от 3 mT и честота 50 Hz за срок до 12 часа. Установено е значително нарастване на общите антоцианини и на антиоксидантната активност на всички проби, изложени за срок до 6 ч в сравнение с контролната проба. По-дълга експозиция на магнитно поле води до понижаване на общото съдържание на антоцианини в дивите къпини. Добиването на големи количества ценни биоактивни вещества с изолзване на изследвания нетермичен подход прави тази техника подходяща за прилагане в хранителната, фармацевтичната и козметичната индустрия.

Voltammetric and theoretical study of the interaction of ceftriaxone with phenylalanine

H. S. Sayiner¹, T. Bakir^{2*}, F. Kandemirli³

¹Infectious Diseases, Medicine Department, Adiyaman University, Adiyaman, Turkey

²Chemistry Department, Faculty of Science, Art and Architecture, Kastamonu University, Kastamonu, Turkey

³Biomedical Engineering Department, Faculty of Engineering and Architecture, Kastamonu University, Kastamonu, Turkey

Received August 13, 2017; Accepted April 13, 2018

The interaction between ceftriaxone and phenylalanine (PA) was investigated by cyclic voltammetry and quantum chemical study using DFT (density functional theory) method. The study was carried out in phosphate buffer solution (PBS) at pH 7.0 (which was also used as the supporting electrolyte) by directly dissolving it in twice distilled water. The voltammetric study of ceftriaxone showed well expressed redox peaks at 0.090 V on a GCE in phosphate buffer of pH 7.0 at 50 mVs⁻¹. The cathodic peak currents were linear with different scan rates from 25 to 275 mVs⁻¹ and the correlation coefficient was found to be 0.971 9 and 0.9592 for ceftriaxone and ceftriaxone-PA systems, respectively in the potential range of 0.8(-0.2) V. The electron transfer rate constant (k_s) was calculated for the reduction of ceftriaxone and ceftriaxone-PA interactions as 2.031 and 4.831 s⁻¹, respectively. After the addition of PA to the ceftriaxone solution, the redox binding constant was obtained as $K = 1.32 \times 10^3 \text{ M}^{-1}$ for ceftriaxone-PA interaction, and quantum chemical calculations were performed for ceftriaxone and ceftriaxone-PA complex by the B3LYP method.

Keywords: Ceftriaxone, Phenylalanine, DFT (density functional theory) method, Cyclic Voltammetry (CV)

INTRODUCTION

The bactericidal activity of ceftriaxone antibiotic belonging to the third generation of cephalosporin is due to its inhibition of the synthesis of the bacterial cell wall [1]. Ceftriaxone shows a broad spectrum of activity against Gram-negative and Gram-positive pathogens; it is effective against a wide range of infections such as skin and skin structure infections, pelvic inflammatory disease, meningitis, uncomplicated gonorrhoea, intra-abdominal infections [2].

Reynold suggested that ceftriaxone, when dissolved in balanced salt solutions, enters normal rat brain with a PS product similar to that of mannitol and that the penetration of ¹⁴C-labeled ceftriaxone from the perfusate into the substance of the brain can be inhibited by the weak acid transport-system blocker probe [3].

Abu Teir *et al.* [4] studied the interaction between human serum albumin and ceftriaxone under physiological conditions by UV absorption and fluorescence spectroscopy and reported that ceftriaxone showed a strong ability to quench the intrinsic fluorescence of human serum albumin and estimated the binding constant (k) as $K = 1.02 \times 10^3 \text{ M}^{-1}$ at 298 K.

Song *et al.* [5] performed electrochemical synthesis of gold nanoparticles on the surface of glassy carbon electrode and prepared GNPs in

aqueous solution with ceftriaxone as an innocuous stabilizing agent and reported that the modified electrode has excellent repeatability. Sayiner *et al.* [6] studied the concerted and stepwise mechanisms for the peptide bond formation of the carboxyl group of ceftriaxone with the amino group of phenylalanine and the carboxyl group of phenylalanine with the amino group of ceftriaxone with the semi-empirical PM6 method. Jabbar *et al.* [7] studied the interaction of riboflavin with cadmium (Cd) in aqueous media by cyclic voltammetry, differential pulse anodic stripping voltammetry and chronocoulometry.

Due to their high sensitivity and selectivity, voltammetric methods have been successfully used to investigation of the redox behavior of various biological compounds. Electrochemical techniques are excellent diagnostic techniques that have been used for the determination of biological properties of electroactive species and organic molecules, including amino acids. Amino acids and proteins are important electroactive species in all basic biological processes in the cell [8].

Phenylalanine (2-amino-3-phenylpropanoic acid), a component of many central nervous system neuropeptides, is an essential amino acid for humans. It is widely used as a food or feed additive in infusion fluids or for chemical synthesis of pharmaceutically active compounds [9].

The binding ability of drug with protein is an important subject in life process that helps us to understand the absorption, transport, metabolism

* To whom all correspondence should be sent:
E-mail: temelkan@kastamonu.edu.tr

and the target molecules of the drugs at the cellular level. Therefore, this interaction will significantly affect the apparent distribution volume of the drugs and also affect the elimination rate of drugs in most cases. On the other hand, clarification of the nature of the interaction between the drug molecule and the target protein is a key process in the development of new drugs, which can contribute to the elucidation of the interaction of drug with biomolecules [10-11].

There are a variety of techniques currently available for the measurement of binding constants for redox active species. Compared with these methods, cyclic voltammetry which is a frequently used electrochemical assay, is simple, low-cost, easily implemented, and has fast response [12-16].

To our knowledge, there is no scientific report on the study of ceftriaxone interaction with phenylalanine, the electrochemical behavior, or their quantum chemical study. In this paper, quantum chemical studies were performed for the cationic form of ceftriaxone, the protonated form of ceftriaxone, the complex form of ceftriaxone with phenylalanine using the density functional theory (DFT), within a standard Gaussian 09 (Revision B.05) [17]. The lowest unoccupied molecular orbital energy (E_{LUMO}), the highest occupied molecular orbital energy (E_{HOMO}), the energy gap between the energy of HOMO and LUMO, hardness, softness, polarizabilities and hyper polarizabilities were calculated.

EXPERIMENTAL

Reagents and apparatus

All chemical substances of analytical reagent grade were supplied by E. Merck AG (Darmstadt, Germany) and accepted for use without further purification. Stock solutions were prepared by dissolving the appropriate amount of ceftriaxone in 200 mM phosphate buffer solution (PBS) at pH 7.0 (which was also used as the supporting electrolyte) by directly dissolving it in twice distilled water. The working solutions of phenylalanine and ceftriaxone were obtained by diluting their stock solutions with PBS. All reagents used freshly prepared. The pH measurements were made using a Metrohm 632 Digital pH-meter (Metrohm AG, CH-9100 Herisau, Switzerland) with a combined glass electrode. Electrochemical measurements were carried out with PC-controlled BASi potentiostat C3 stand connected with a N₂ gas cylinder, produced by Bioanalytical System Inc., (BASi) USA. The working electrode was a glassy carbon electrode (GCE) (2 mm diameter). Before use the working electrode was sequentially polished with graded 10 μ M alumina powder, and rinsed

with doubly distilled water. A saturated Ag/AgCl and a platinum wire were used as the reference and the auxiliary electrode, respectively. This three-electrode micro-cell was completely shielded from any perturbing noises by a Faraday Cage. A continuous flow of nitrogen was ensured before start of any electrochemical experiment. All solutions were purged with pure nitrogen for 10 min before the voltammetric runs. Cyclic voltammetry (CV) measurements were made at a 50 mV s⁻¹ scan rate.

Calculation methods

All calculations were performed with complete geometry optimization by using the standard Gaussian 09 software package with DFT and B3LYP hybrid method with 6-311G(d) basis sets [17]. Fukui function indicating the change in electron density of a molecule at a given position, when the number of electrons has changed, were calculated by using AOMix program from singlepoint calculations with B3LYP/6-311G(d,p) [18-19].

RESULTS AND DISCUSSION

Influence of scan rate

Cyclic voltammetry (CV) of ceftriaxone and ceftriaxone phenylalanine (PA) systems were carried out separately. We examined the influence of the scan rate on the electrochemical behavior of ceftriaxone, to understand the nature of the electrode process. For this, we recorded the cyclic voltammogram of the 5×10^{-4} M ceftriaxone on GCE in 0.2 M phosphate buffer solution at pH 7.0. The cathodic peak currents increased linearly when the scan rate varied from 25 to 275 mVs⁻¹ and the correlation coefficient was found to be 0.9719 and 0.9592 for ceftriaxone and ceftriaxone-PA systems, respectively, in the potential range of 0.8-(-0.2) V. The reduction peak current of ceftriaxone was noted to increase with increasing scan rate.

On addition of PA, a decrease in the cathodic peak current was observed. The competitive adsorption between ceftriaxone and PA on the GCE for the formation of electroinactive complex without the changes of electrochemical parameters may be effective for decreasing of the reductive peak current. The peak current of ceftriaxone did not disappear completely with the increase in the concentration of PA, which was not typical for competitive adsorption. The competitive adsorption factor can be excluded by recording a cyclic voltammogram of ceftriaxone in the excess of PA.

Consequently, the decrease in the peak current without any changes in electrochemical parameters is an evidence of [ceftriaxone-PA] electroinactive

H. S. Sayiner et al.: Voltammetric and theoretical study of the interaction of ceftriaxone with phenylalanine complex formation, which results in the decrease of equilibrium concentration of ceftriaxone in solution.

The effect of scan rate on peak current showed that the plot of current *vs.* ν is linear for a limited scan rate, indicating that the electrochemical process is virtually an adsorption-controlled process. However, the process is also diffusion-controlled, as shown by the *I* peak *versus* $\nu^{1/2}$ plot in Fig. 1. It can be concluded that the electrochemical process of the ceftriaxone-PA system actually includes both diffusion and adsorption-controlled processes, depending on the scan rate.

Voltammetric study of ceftriaxone, ceftriaxone and phenylalanine systems

The probable interaction of ceftriaxone and phenylalanine was studied by comparing the voltammetric data between ceftriaxone and ceftriaxone – phenylalanine systems in aqueous PBS solution.

The voltammetric behavior of 5×10^{-4} M ceftriaxone in the absence and presence of PA at bare GCE is shown in Figs. 2 and 3, respectively. The

voltammogram without PA featured a cathodic peak in the potential range of (-0.2) – 0.8 V. As it is shown, by increasing the scan rate, the peak potential is shifted to lower positive potentials.

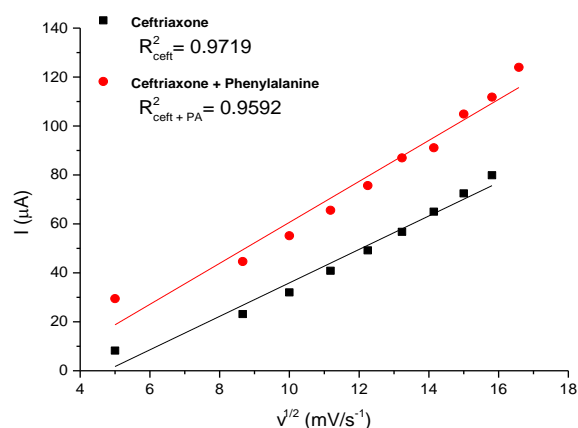


Figure 1. Plot of *I* peak *vs.* $\nu^{1/2}$ for 5×10^{-4} M ceftriaxone in absence and presence of PA (5×10^{-4} M) at various scan rates: 25,50,75,100,125,150,175,200,225,250 and 275 mV s^{-1}

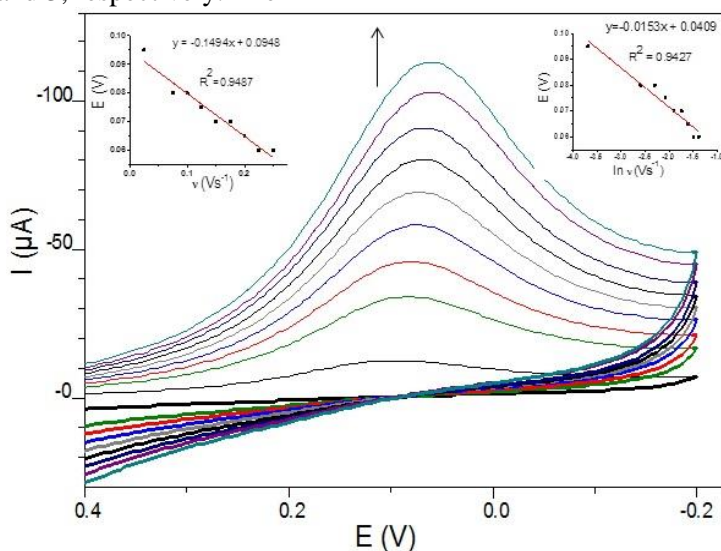


Figure 2. Cyclic voltammograms of 0.5 mM ceftriaxone at various scan rates. Inset left: linear plot of E_p *vs.* ν ($y = -0.1494x + 0.0948$, $R^2 = 0.9487$). Inset right: linear plot of E_p *vs.* $\ln(\nu/\text{V s}^{-1})$ ($y = -0.0153x + 0.0409$, $R^2 = 0.9427$). pH 7.0 PBF solution at glassy carbon electrode. Scan rates: 25,75,100,125,150,175,200,225 and 250 mV s^{-1} .

The electron transfer rate constant (k_s) and αn were calculated using Laviron's equations for the irreversible surface electrode process of the reduction of ceftriaxone [20-21]:

$$E = E^0 + \left(\frac{RT}{\alpha F}\right) \ln \left[\frac{RTk_s}{\alpha F}\right] - \left[\frac{RT}{\alpha F}\right] \ln[\nu] \quad (1)$$

where R is the universal gas constant $R = 8.314 \text{ J mol}^{-1} \text{ K}^{-1}$, T is Kelvin temperature $T = 298 \text{ K}$, F is the Faraday constant $F = 96487 \text{ C mol}^{-1}$, α is the electron transfer coefficient, k_s is the standard rate

constant of the surface reaction. The results are shown in Table 1. ν is the scan rate (Vs^{-1}) and E^0 is the formal potential. If the E^0 is known, k_s and α values can be calculated according to the linear plot of E *versus* $\ln \nu$ (insets right, (Figs. 2 and 3)). The E^0 value can be obtained from the intercept of E *vs.* ν plot (insets left, (Figs. 2 and 3)).

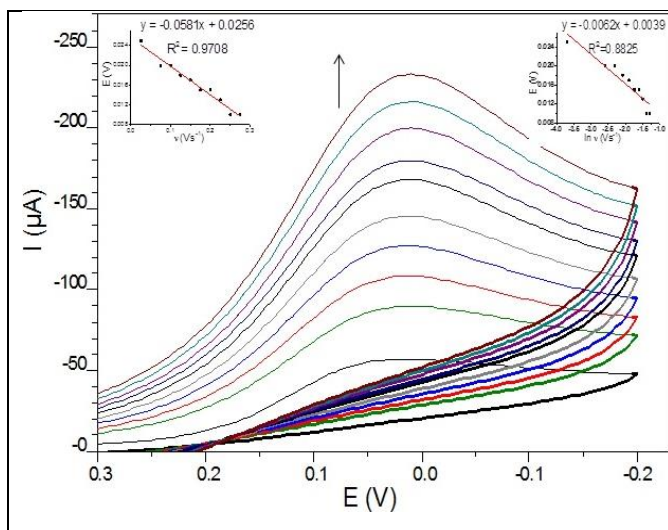


Figure 3. Cyclic voltammograms of 0.5 mM ceftriaxone + 0.5 mM PA at various scan rates. Inset left: linear plot of E_p vs. v ($y = -0.0581x + 0.0256$, $R^2 = 0.971$). Inset right: linear plot of E_p vs. $\ln(v/V s^{-1})$ ($y = -0.0062x + 0.0039$, $R^2 = 0.883$). pH 7.0 PBF solution at glassy carbon electrode. Scan rates: 25, 75, 100, 125, 150, 175, 200, 225, 250 and 275 $mV s^{-1}$

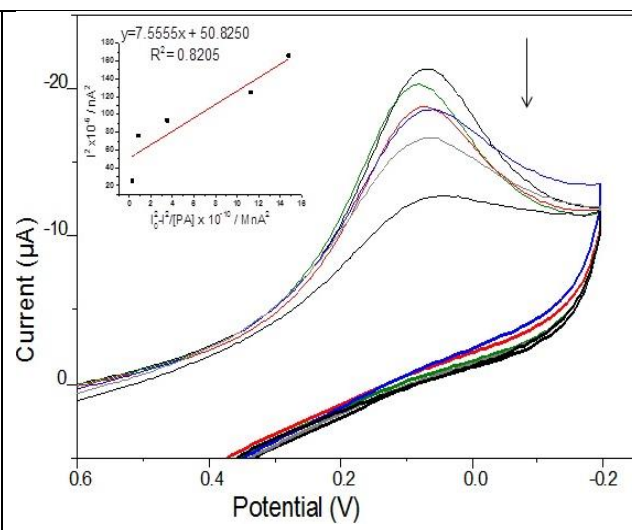


Figure 4. Cyclic voltammograms of 0.5 mM ceftriaxone in 0.2 M phosphate buffer of pH 7.0 without PA and in the presence of $C_{PA} = 0.1, 0.5, 2.5, 12.5, 62.5$ mM PA at 50 $mV s^{-1}$. Inset left: plot of I^2 vs. $(I_0^2 - I^2)/[PA]$ used to calculate the binding constant

Table 1. E^0 , k_s and α values of ceftriaxone in the absence and presence of PA.

	Ceftriaxone	Ceftriaxone + PA
E^0 (V)	0.094	0.026
α	1.678	4.142
k_s (s^{-1})	2.031	4.831

Cyclic voltammetric measurements of PA with ceftriaxone were carried out to determine the binding constant using the following equation:

$$I^2 = \frac{1}{K[PA]} (I_0^2 - I^2) + I_0^2 - [PA] \quad (2)$$

where I_0 and I are the peak currents of [ceftriaxone] in the absence and presence of PA, respectively [22]. A plot of I^2 vs. $(I_0^2 - I^2)/[PA]$ was described with a straight line to give a binding constant of $K = 1.32 \times 10^3 M^{-1}$ (Fig. 4).

Theoretical aspects

The reaction between ceftriaxone and phenyl alanine was thought as two forms. One of the reactions was performed between the carboxyl group of ceftriaxone and the amino group of phenylalanine (compound A) the other one was considered between the carboxyl group of phenylalanine and the amino group of ceftriaxone (compound B).

Optimized form, the highest occupied molecular orbital - HOMO, and the lowest molecular orbital - LUMO, and electron density of ceftriaxone, molecule A, molecule B, calculated with B3LYP/

6-311++g(2d,2p) are given in Fig. 5. There are three rings in ceftriaxone. These are triazine (ring 1), azobicyclo (ring 2) and thiazole (ring 3). The calculation of ceftriaxone molecule was performed in cationic form. HOMO of the cationic form of ceftriaxone mainly consists of ring 1, ring 3, carbonyl and amino groups. LUMO of the cationic form of ceftriaxone mainly consists of ring 1, ring 2, and ring 3. HOMO of the complex A is mainly concentrated on ring 3 and the imino group attached to ring 3. LUMO of the complex A mainly consists of ring 3. HOMO of the complex B is mainly concentrated on ring 1 and LUMO of the complex A mainly consists of ring 3. The common descriptors of site reactivity are related with Fukui functions which can be enunciated in a finite-difference approximation by the following equations:

$$f_k^+ = \rho_k(N+1) - \rho_k(N) \quad (3)$$

$$f_k^- = \rho_k(N) - \rho_k(N-1) \quad (4)$$

The first equation (3) expresses a condensed Fukui function for a nucleophilic attack; the second equation (4) means a condensed Fukui function for an electrophilic attack. Table 2 shows the compositions of the HOMO and the LUMO of the molecule calculated at B3LYP/6-311G(d,p) level.

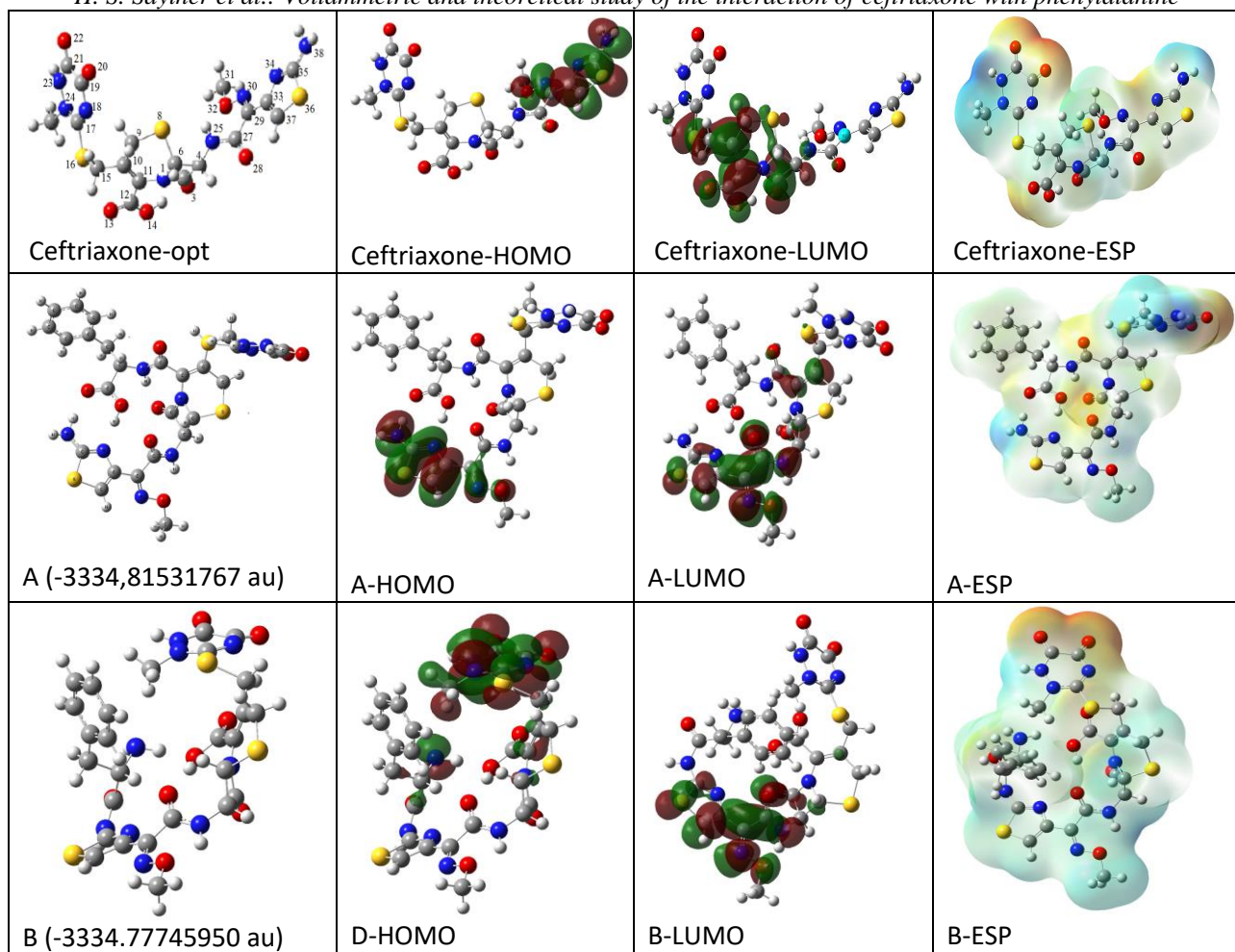


Figure 5. Optimized form, HOMO, LUMO, and electron density of ceftriaxone, molecule A, molecule B

Table 2. Compositions of the HOMO and the LUMO of the ceftriaxone, A and B molecule at the B3LYP/6-311G(d,p) level

Ceftriaxone			A			B		
Atom No	HOMO	LUMO	Atom No	HOMO	LUMO	Atom No	HOMO	LUMO
C2		9.89	C10		2.55	S16	3.86	
O3		5.33	N25		3.62	N18	12.29	
C10		29.61	C26		11.36	O20	7.66	
C11		17.27	O27		8.67	O22	12.95	
C12		8.66	O28		21.29	N23	20.97	
O13		2.64	C29	4.89	26.69	N24	25.08	
O14		6.82	O30	3.05	3.54	N26		4.30
C15		3.07	C32	13.61	2.15	C27		11.76
S16		5.97	C33	9.00		O28		7.76
N30	7.76		N34	7.32		29C		20.05
O31	4.97		C35	11.87	2.83	N30		27.33
C33	14.76		S36	24.66	7.59	31O		3.96
N34	5.66		C37	23.24		33C		2.62
C35	9.28					S36		4.74
S36	11.43					C37		11.35
C 37	25.27					N53	4.32	
38N	17.76							

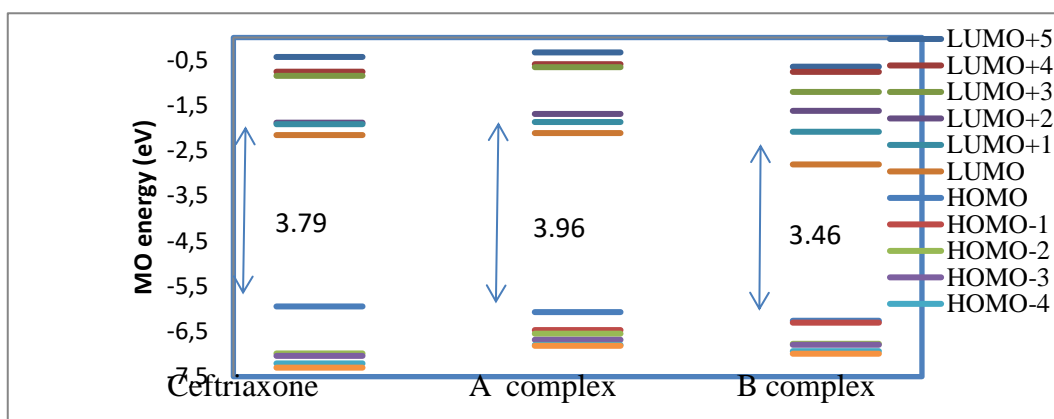


Figure 6. E_{HOMO} , E_{LUMO} , and the energy of 5 molecular orbitals close to these orbitals ceftriaxone, A and B molecules

The HOMO composition represents the condensed Fukui function for an electrophilic attack. For the HOMO, the contributions of the C33, N34, C35, S36, C37 for thiazole group of ceftriaxone are 14.76 %, 5.66 %, 9.28 %, 11.43 %, 25.27 %, respectively. For the HOMO, the contributions of C33, C34, C35, S36, C37 belonging to the thiazole group of complex A are 13.61 %, 9.00 %, 7.32 %, 11.87 %, 24.66 %, 23.24 %, respectively. The contributions of N18, O22, N23, N24 of the triazine group of complex B are 12.29 %, 12.95 %, 20.97 %, 25.08 %, respectively.

The LUMO composition represents the condensed Fukui function for a nucleophilic attack. The LUMO contributions mainly belong to azobicyclo group and thiazole group of ceftriaxone.

CONCLUSION

The electrochemical investigation of the redox behavior of ceftriaxone and the interaction of ceftriaxone with phenyl alanine was performed. From our findings we conclude that ceftriaxone reacts with phenylalanine following an irreversible charge transfer reaction at a glassy carbon electrode. Cathodic currents of ceftriaxone-phenyl alanine were reduced. This is the evidence of [ceftriaxone-PA] electroinactive complex formation. According to the theoretical calculation form A is preferred to form B.

REFERENCES

1. J.F. Fisher, S.O. Meroueh, S. Mobashery, *Chem. Rev.*, **105**, 395 (2005).
2. M.G. Quaglia, E. Bossu, C. Dell'Aquila, M. Guidotti, *J.Pharm. Biomed. Analysis*, **15**, 1033 (1997).
3. R. Spector, *J. Infect. Dis.*, **156**, 209 (1987).
4. M.M. Abu Teir, J. Ghithan, M.I. Abu-Taha, S.M. Darwish, M.M. Abu-hadid, *J. Biophy. Struct. Biol.*, **6**, 1 (2014).
5. Y. Song, A. Zhu, Y. Song, Z. Cheng, J. Xu, J. Zhou, *Gold. Bull.*, **45**, 153 (2012).

For complex A the compositions belong to S35, C36 on the thiazole group and the groups attached to thiazole group (for N25, C26, O27, C28, C29, O30 are 3.62 %, 11.36 %, 8.67 %, 21.29 %, 26.69%, 3.54%, respectively). For complex B the compositions belong to C33, S36, C37 (2.62 %, 4.74 %, 11.35 %) on the thiazole group and the groups attached to the thiazole group (for N26, C27, O28, C29, N30, O31 are 4.30 %, 11.76 %, 7.76 %, 20.05 %, 27.33%, 3.96%, respectively).

The highest occupied molecular orbital energy (E_{HOMO}), the lowest unoccupied molecular orbital energy (E_{LUMO}), and the energy of 5 molecular orbitals close to these orbitals energetically are given in Fig. 6. Energy gaps for ceftriaxone, A and B molecules are 3.79, 3.96, 3.46 eV, respectively.

6. H.S. Sayiner, F. Kandemirli, *J. Int. Res. Med. Phar. Sci.*, **9**, 83 (2016)
7. M.A. Jabbar, S. Salahuddin, A.J. Mahmood, R.J. Mannan, *J. Saudi. Chem. Soc.*, **20**, 158, (2016).
8. A. Masek, E. Chrzescijanska, M. Zaborski, *Int. J. Electrochem. Sci.*, **9**, 7904 (2014).
9. Y. Hua, Z. Zhanga, H. Zhanga, L. Luo, S. Yaob, *Talanta.*, **84**, 305 (2011).
10. M. Mahanthappa, B.G. Gowda, J.I. Gowda, R. Rengaswamy, *J. Electrochem. Sci. Eng.*, **6**, 155 (2016).
11. L. Fotouhi, S. Banafsheh, M.M. Heravi, *Bioelectrochem.*, **77**, 26 (2009).
12. M. Aslanoglu, *Anal. Sci.*, **22**, 439 (2006).
13. B. Gowda, M. Mallappa, J.I. Gowda, R. Rengasamy, *Pharm. Sci.*, **5**, 37 (2015).
14. B. Cheng, X. Cai, Q. Miao, Z. Wang, M. Hu, *Int. J. Electrochem. Sci.*, **9**, 1597 (2014).
15. J. Lohrman, C. Zhang, W. Zhang, S. Ren, Semiconducting Single-Wall Carbon Nanotube and Covalent Organic Polyhedron-C60 Nanohybrids for Light Harvesting, *Electronic Supplementary Material (ESI) for Chemical Communications*, (2012).
16. C.L. Brosseau, S.G. Roscoe, *Electrochim. Acta.*, **51**, 2145 (2006).

- H. S. Sayiner et al.: Voltammetric and theoretical study of the interaction of ceftriaxone with phenylalanine*
17. Gaussian 09, Revision E.01: M. J. Frisch, G. W. Trucks, H. B. Schlegel, G. E. Scuseria, M. A. Robb, J. R. Cheeseman, G. Scalmani, V. Barone, B. Mennucci, G. A. Petersson, H. Nakatsuji, M. Caricato, X. Li, H. P. Hratchian, A. F. Izmaylov, J. Bloino, G. Zheng, J. L. Sonnenberg, M. Hada, M. Ehara, K. Toyota, R. Fukuda, J. Hasegawa, M. Ishida, T. Nakajima, Y. Honda, O. Kitao, H. Nakai, T. Vreven, J. A. Montgomery, Jr., J. E. Peralta, F. Ogliaro, M. Bearpark, J. J. Heyd, E. Brothers, K. N. Kudin, V. N. Staroverov, R. Kobayashi, J. Normand, K. Raghavachari, A. Rendell, J. C. Burant, S. S. Iyengar, J. Tomasi, M. Cossi, N. Rega, J. M. Millam, M. Klene, J. E. Knox, J. B. Cross, V. Bakken, C. Adamo, J. Jaramillo, R. Gomperts, R. E. Stratmann, O. Yazyev, A. J. Austin, R. Cammi, C. Pomelli, J. W. Ochterski, R. L. Martin, K. Morokuma, V. G. Zakrzewski, G. A. Voth, P. Salvador, J. J. Dannenberg, S. Dapprich, A. D. Daniels, Ö. Farkas, J. B. Foresman, J. V. Ortiz, J. Cioslowski, and D. J. Fox, Gaussian, Inc., Wallingford CT, 2010.
 18. S.I. Gorelsky, AOMix Program. <http://www.wsg-chemnet/>.
 19. S.I. Gorelsky, A.B.P. Lever, *J. Org. Chem.*, **635**, 187 (2001).
 20. E. Laviron, *J. Electroanal. Chem.*, **101**, 19 (1979).
 21. G.C. Zhao, J.J. Zhu, J.J. Zhang, H.Y. Chen, *Anal. Chim. Acta*, **394**, 337 (1999).
 22. J. Niu, G. Cheng, S. Dong, *Electrochim. Acta*, **39**, 2455 (1994).

ВОЛТАМПЕРОМЕТРИЧНО И ТЕОРЕТИЧНО ИЗСЛЕДВАНЕ НА ВЗАИМОДЕЙСТВИЕТО МЕЖДУ ЦЕФТРИАКСОН И ФЕНИЛАЛАНИН

Х. С. Сайнер¹, Т. Бакир^{2*}, Ф. Кандемирли³

¹ *Инфекциозни болести, Медицински департамент, Адиямански университет, Адияман, Турция*

² *Химически департамент, Факултет по наука, изкуство и архитектура, Университет на Кастамону, Кастамону, Турция*

³ *Департамент по биомедицинско инженерство, Факултет по инженерство и архитектура, Университет на Кастамону, Кастамону, Турция*

Постъпила на 13 август, 2017 г. ;приета на 13 април, 2018 г.

(Резюме)

Взаимодействието между цефтриаксон и фенилаланин (РА) е изследвано чрез циклична волтамперометрия и квантово-химични изчисления с помощта на DFT метод. Изследването е проведено във фосфатен буфер с рН 7 (използван също като поддържащ електролит чрез директно разтваряне в двойно дестилирана вода). Волтамперометричното изследване на цефтриаксон показва добре изразени редокс пикове при 0.090 V върху електрод от стъкловъглерод във фосфатен буфер с рН 7 при 50 mVs⁻¹. Катодните пикови токове са линейни при скорост на сканиране от 25 до 275 mVs⁻¹ и корелационният коефициент е съответно 0.9719 и 0.9592 за цефтриаксон и цефтриаксон-РА системите в интервала от потенциали 0.8-(-0.2) V. Скоростната константа на електронен пренос (k_s) е изчислена за редукцията на цефтриаксон и взаимодействието между цефтриаксон-РА, съответно 2.031 и 4.831 s⁻¹. След добавяне на РА към разтвора на цефтриаксон е получена константата на редокс свързване $K = 1.32 \times 10^3 \text{ M}^{-1}$ за взаимодействието цефтриаксон-РА. Квантово-химични изчисления за цефтриаксон и цефтриаксон-РА комплекс са проведени с помощта на B3LYP метод.

Characterization and drug release from extended-release matrix pellets with montelukast sodium

T. M. Popova^{1*}, St. A. Ivanova², M. V. Dimitrov¹

¹Medical University of Sofia, Faculty of Pharmacy, Department of Pharmaceutical Technology and Biopharmacy, 2, Dunav Str., Sofia, 1000, Bulgaria

²Medical University of Sofia, Faculty of Pharmacy, Department of Pharmaceutical Chemistry, 2, Dunav Str., Sofia, 1000, Bulgaria

Received, February 20, 2018; Accepted March 20, 2018

The undisputable benefits of pellets, associated with improved bioavailability, make them ideal for presenting in extended-release formulations. Unfortunately, despite the many advantages of wet extrusion and spheronization, extended release is difficult to be achieved, even with commonly used release modifying agents like cellulose derivatives, polyethylene oxides, sodium alginate, etc. In order to sort out this problem, we included ethanol in the kneading liquid and investigated its influence on the properties of ethylcellulose (EC) pellets and the release behaviour of montelukast sodium. Differential scanning calorimetry of EC showed increase in heat capacity, associated with increased amount of ethanol, which proved that ethanol changes the thermo-mechanical properties of EC. Moreover, evaporation of ethanol during spheronization caused partial melting and dissolution of EC provoking agglomeration, rounding and smoothing, which reflected in the formation of a hydrophobic film around the particle. As a result, the increase in ethanol concentration in the kneading liquid led to obtaining pellets with narrower particle size distribution, higher dimensions, improved sphericity, flatter surface, longer mean dissolution time (MDT) and slower release of montelukast sodium.

Keywords: Matrix pellets; Wet extrusion and spheronization; Extended-release; Ethylcellulose

INTRODUCTION

Utilization of pellet systems is gaining much attention due to their potential advantages: increased bioavailability; reduced local stomach irritation; no risk of dose dumping; flexibility to mix pellets with different compositions or release patterns in order to achieve desired release rate, etc. Several technologies for preparation of pellets are available (spray-drying, extrusion/spheronization, solution/suspension layering, etc.), but wet extrusion/spheronization technique has the advantages of obtaining high-density matrix pellets with high drug loading capacity [1]. The desirable properties of the pellets include uniform spherical shape and size, good flow properties, high mechanical strength, low friability, low dust and smooth surface. Most workers usually report the size and size distributions produced as an indication of the quality of the product, because they have significant influence on the release kinetics, as well as for reproducible packing in hard gelatine capsules or sachets [1]. The shape is critical for a number of processing properties of beads, such as flowability, uniformity of coating, etc., and uniform regular spherical shape is highly desirable [2].

Microcrystalline cellulose (MCC) is the golden standard as a diluent for wet extrusion. However, sometimes it is not the first choice due to the lack of disintegration and the inability to extend the

release [3]. Although a number of polymers such as hydroxypropylmethyl cellulose, polyethylene oxide (PEO), sodium alginate, and even ethylcellulose (EC) are successfully used to produce extended-release matrix tablets, their inclusion in matrix pellet formulations (prepared by wet extrusion/spheronization) does not result in significant delay in the release rate. The small diameter and the large free surface area of the pellets lead to rapid penetration of the solvent into the system and reduction of the drug diffusion pathway [4-7]. However, in the study of Hamelelniel *et al.* [8] a delay in the initial release of a drug was achieved from pellets with MCC and EC caused by changing pure water with 16% ethanol as a kneading liquid. EC swells and dissolves in ethanol, which leads to the formation of a hydrophobic film after evaporation of the solvent. This gives us the reason to investigate the influence of the kneading liquid on the properties of ethylcellulose matrix pellets with montelukast sodium, prepared by wet extrusion and spheronization.

Montelukast sodium was chosen as a model drug because it is an appropriate candidate for presenting in an extended-release formulation due to its intensive hepatic first pass metabolism and short biological half-life (2.5-5.5 hours) [9].

* To whom all correspondence should be sent:
E-mail: tedi_popova_@abv.bg

Materials

The active pharmaceutical ingredient (API) Montelukast sodium was obtained from Inchem Laboratories (India). The excipients sodium alginate, general grade and Avicel PH 101 were obtained from Fisher Scientific (UK) and Evonik (Germany), respectively, and ethylcellulose N46 and PEO 6000000 - from Sigma-Aldrich (USA).

Methods

Differential scanning calorimetry (DSC) of ethylcellulose. For thermal characterization of ethylcellulose, as well as for studying the influence of the type of the solvent on its thermo-mechanical properties, a differential scanning calorimeter, Perkin-Elmer DSC 7, USA, was used. Five samples were prepared for this purpose, as follows: A. Pure substance EC; B. EC treated with water; C. EC treated with 40% ethanol; D. EC treated with 60% ethanol; E. EC treated with 95% ethanol. The experiment required measurement of the loss on drying at 105°C of the pure substance EC N46, which served as a standard (sample A). The treatment of the other samples included spraying of 1.5 g of the corresponding liquid (water, 40%, 60% and 95% ethanol - w/w) onto 3 g of pure substance, manual mixing in glass vials with a steel spatula and subsequent drying to a loss on drying equivalent to that of the pure substance. The analysis was performed with heating/cooling run from 25 to 200°C as follows [10]: 3-5 mg of test sample was placed in a sealed aluminum pan at a 5°C/min heating/cooling rate with a 70 ml/min nitrogen flow rate.

Preparation of matrix pellets with montelukast sodium via wet extrusion and spheronization

The extrusion was performed with a radial screw-feed extruder (4M8Trix, Procept, Belgium) equipped with a standard die having 1.2 mm diameter aperture and rollers rotating at 75 rpm. The extrudate fell directly into the spheronizer fitted with a cross-hatch friction plate, 13.5 cm in diameter where it was rounded off at 2100 rpm rotating speed for 10 min. The appropriate use and level of each excipient, as well as processing parameters were determined by conducting preliminary trials. Based on them for the present experiment MCC was used as diluent, EC as release modifying agent, Na-alginate as pore-forming agent and PEO as spheronization aid (Table 1).

Determination of pellet size and pellet size distribution

Pellet size and pellet size distribution were determined by performing a sieve test using a set of

standard test sieves (0.5–2.5 cm with 2^{0.25} progression) and a sieve shaker (VEB MLW Labortechnik Ilmenau, Thvr 2, Germany) operated with 50 g pellet sample for 5 min at a frequency of 50 Hz and an amplitude of 1 mm.

Table 1. Composition of pellet formulations (weight/weight ratio).

Excipients	Formulation №			
	E1	E2	E3	E4
Montelukast sodium	0.5			
Avicel PH 101	4.15			
EC N46	4.15			
Sodium alginate	1			
PEO 6000000	0.2			
Kneading liquid	water	30% ethanol (w/w)	40% ethanol (w/w)	50% ethanol (w/w)

The weight retained in each fraction was determined by an analytical balance (model AG204, Mettler-Toledo, Greifensee, Switzerland) and the percentage of each fraction was calculated. These results were used for building a cumulative particle size distribution curve and calculating the average pellet diameter ($d_{av.}$) and span value following equations 1 and 2, respectively:

$$d_{av.} = \frac{\sum \% \text{ pellet fraction retained} \times \text{average sieve aperture (mm)}}{100} \quad (1)$$

$$\text{span} = \frac{(d_{90} - d_{10})}{d_{50}} \quad (2)$$

Determination of pellet shape

The shape of the model pellet compositions was characterized by the aspect ratio (AR), which represents the ratio of the maximum and minimum values of Feret diameter of each particle. It can be found in the range of 0-1, as higher value indicates that the shape of the pellets is more regular and spherical. The AR value was obtained by making a series of images for each sample with a digital camera (E61MID02 uEye UI-1545LE-C CMOS 1.3 MP) attached to a tripod and pointing to the surface of the particles, which were spread over a flat surface by spatula. Each image was processed with Image J software and measured in millimeters the maximum and minimum values of Feret diameter of 500 particles.

Determination of pellet morphology

Scanning electron microscope (Jeol JSM-5510, Japan) was used to observe the physical properties (shape and texture) and surface modification of the prepared pellets. Samples of pellets from each formulation were mounted on a disk using an adhesive. For better conductivity, the samples were

T. M. Popova et al.: Characterization and drug release from extended-release matrix pellets with montelukast sodium coated with gold using a Jeol JFC-1200 Fine coater and observed at an accelerating voltage of 25 kV.

In vitro release studies

Due to the pH-dependent solubility of montelukast sodium, as well as the inability to achieve sink conditions with commonly used buffers, a 0.5% aqueous solution of sodium lauryl sulfate was used as a medium for the *in vitro* dissolution study. Drug release from 208 mg bead sample with size fraction of 1.25–1.4 mm in 500 ml medium solution at 37°C was studied using an Apparatus 2 – Paddle Apparatus USP 37 (RC-8D, KHP, Germany) with a 100 rpm stirring rate. Samples were collected at specified time intervals (15 min, 30 min, 1, 2, 3, 4, 5, 6, 7, 8 h) and centrifuged at 150000 rpm for 3 min on a micro-centrifuge (D2012, Dragon Lab., China). The assay of API released at each time interval was measured spectrophotometrically at 285 nm (spectrophotometer RAYLEIGH UV-9200, China) and calculated based on a calibration curve equation. Dissolution tests were repeated six times for all formulations. The mean dissolution time (MDT) was used to characterize drug release and to compare the drug release profiles of the prepared formulations, because this parameter indicates the drug release retarding efficiency of polymers. It was calculated from the dissolution data using equation 3:

$$MDT = \frac{n \cdot K' \left(-\frac{1}{n}\right)}{n+1} \quad (3)$$

RESULTS AND DISCUSSION

Thermal characterization of ethylcellulose

Based on the obtained thermograms (Fig. 1), glass transition temperature (Tg) and heat capacity (delta Cp) were determined by the specific software of the apparatus. The results are presented in Table 2. Glass transition temperature (Tg) is one of the most important characteristics of polymers. This temperature is the temperature range in which the polymer passes from a solid, glass-like state to a soft rubbery state. Tg is characteristic of polymers that have an amorphous structure or have an amorphous region in their molecule (such as ethylcellulose).

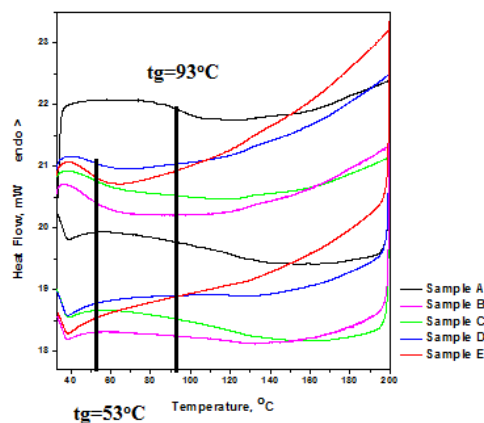


Fig. 1. DSC thermograms of ethylcellulose from samples A-E.

Tg can be lowered by substances called plasticizers, which improve the processability, flexibility and elasticity of the polymers [11]. In this line of thought, it is clear from Table 2 that the contact of ethylcellulose with water (whether pure water or water-ethanol mixtures) had a significant effect on Tg, expressed as a decrease in its value from 93 to 53°C (40°C difference), which confirmed literature data that water had a plasticizing effect on EC [12].

The heat capacity (delta Cp) is a measurable physical quantity equal to the ratio of the heat added to (or removed from) an object to the resulting temperature change or the energy required to raise the sample temperature by 1°C or 1K [11]. A change in the heat capacity means a change in the thermo-mechanical properties of EC. Regardless of the same Tg for samples B-E, a decrease in the water content, respectively an increase in the ethanol content induced an increase in the value of heat capacity: 0.45 J/g*°C - for the sample with pure water and 1.67 J/g*°C - for the sample with 95% ethanol. This gave us a reason to believe that ethanol changes the thermo-mechanical properties of EC, which could affect the release rate of API of systems in which ethanol was included in the kneading liquid.

Table 2. Values of Tg and delta Cp for samples A-E

Sample №	A	B	C	D	E
Composition	Pure EC	EC + water	EC + 40% ethanol	EC + 60% ethanol	EC + 95% ethanol
Tg (°C)	93	53			
delta Cp (J/g*°C)	0.67	0.45	0.78	1.36	1.67

Pellet size and pellet size distribution

The screening experiments indicated unimodal non-monodispersible particle size distribution (Fig. 2) with average pellet diameter varying between 1.029 and 1.901 mm (Table 3), indicating a profound influence of formulation variables. It was demonstrated that with the increase in ethanol concentration in the kneading liquid the average pellet diameter tended to increase significantly, whereas span value decreases. Moreover, except of formulation E1, all the other samples had d_{av} values higher than the extruder's die diameter. This was caused by the agglomeration occurring during spheronization - apart from breaking and smoothing, adhesion of finer to larger particles was observed. Due to the heat generated by the friction of the pellets, the ethanol started to evaporate, which led to the dissolution of EC from the bead surface of formulations E2-E4 and to a partial melting of the polymer, which could explain the occurring agglomeration of formulations E2-E4. Decreasing span value associated with increased amount of ethanol in a kneading liquid was a reflection of the homogeneity and narrower size distribution.

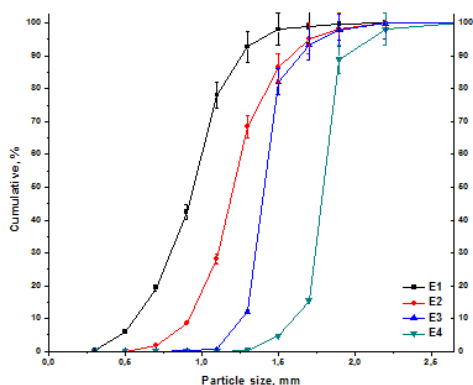


Fig. 2. Cumulative particle size distribution of formulations E1-E4; mean \pm SD; n=3.

Pellet shape

The bead shape was evaluated based on the aspect ratio. An aspect ratio of 1.0 indicates a perfect shape. However, an aspect ratio ≥ 0.8 has been considered good for pharmaceutical pellets. This specification was not achieved only for formulation E1 (AR=0.647) because of the swelling of the hydrophilic polymers sodium alginate and PEO, causing the formation of a tacky wet mass with extremely high plasticity resulting in the formation of an extrudate, which broke unevenly and resisted rounding up completely in the spheronizer. Formulations E2-E3 possessed high value of AR (above 0.8), which meant that they had

the desired nearly spherical shape, demonstrating the success of spheronization under these conditions. The improved sphericity associated with increased amount of ethanol in the kneading liquid was caused by the partial melting and dissolution of EC under the influence of evaporating ethanol, which led to self-layering and rounding.

Table 3. Parameters of pellet formulations E1-E4

Formulation No	d_{av} , mm	Span	Aspect ratio	MDT, h
E1	1.029	0.69	0.647	0.04231
E2	1.327	0.49	0.881	0.20830
E3	1.529	0.18	0.889	2.36971
E4	1.901	0.13	0.920	4.39490

Pellet Morphology

The shape and surface characteristics of the prepared pellet formulations E1-E2 at 40 \times and 250 \times magnifications are illustrated in Fig. 3. As it was mentioned before, the final beads of formulation E1 showed heterogeneity in shape - only some of them possessed the desired spherical form. The texture of the pellets of formulation E1 at higher magnification (250 \times) showed that the surface of the beads was rough, porous and marked with irregularities for both spherical and dumb-bell shape pellets. SEM observations of formulations E2-E4 estimated that pellets were spherical in shape. A smoothing on the surface of pellets was observed with the increase in ethanol concentration. This was due to the fact that some of EC was partially dissolved in ethanol forming film pieces [8].

Drug release studies and analysis of release data

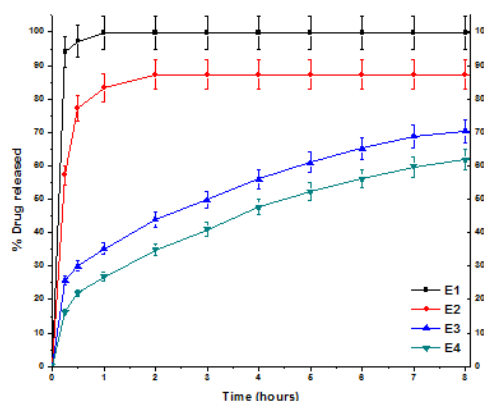


Fig. 4. *In vitro* release profiles of pellet formulations E1-E4; mean \pm SD; n=6.

Fig. 4 and Table 3 show the results from the release studies of the obtained formulations. The increased amount of ethanol in the kneading liquid

T. M. Popova et al.: Characterization and drug release from extended-release matrix pellets with montelukast sodium significantly delayed the release rate and increased MDT of API. As a result an immediate release product was obtained from formulations E1 and E2, whereas formulations E3 and E4 demonstrate extended release of montelukast sodium. The presence of both sodium alginate and PEO, as hydrophilic water-soluble polymers, resulted in the formation of pores on the pellets surface [6,7].

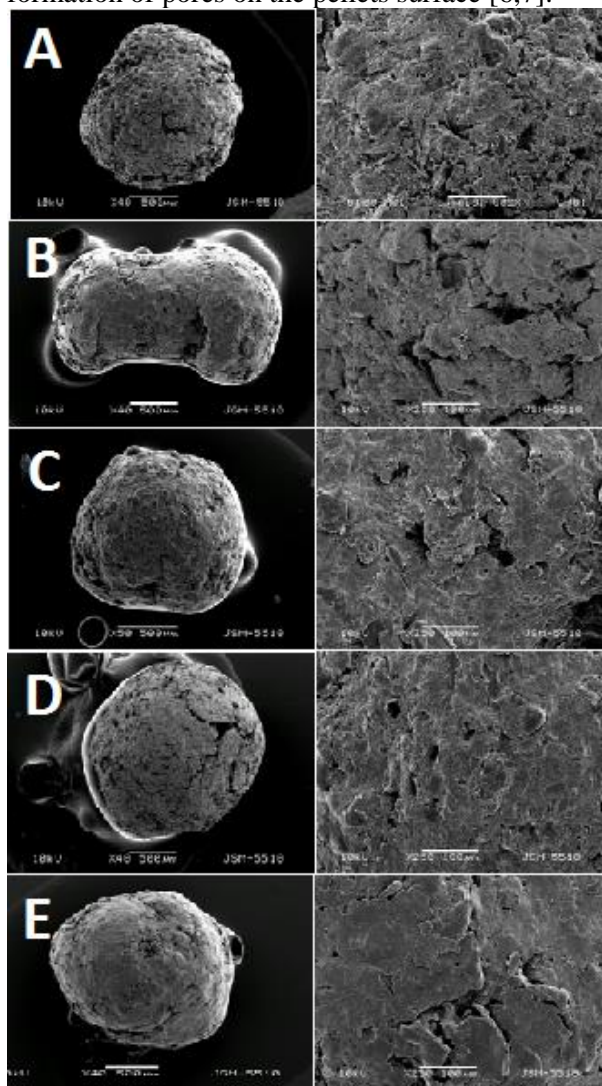


Fig. 3. SEM micrographs of pellets at magnifications 40 \times (right) and 250 \times (left): A. Formulation E1 – spherical pellet; B. Formulation E1 – dumb-bell shape pellet; C. Formulation E2; D. Formulation E3; E. Formulation E4.

The increase in ethanol concentration in the kneading liquid increased the amount of dissolved EC which led to obtaining of a thicker hydrophobic EC film, to increased MDT value and to a slower release rate of montelukast sodium [8].

CONCLUSION

The results from our studies demonstrated that the choice of a kneading liquid had a decisive impact on the size and size distribution, shape, surface morphology, as well as on the release behavior of the obtained pellets. Except for formulation E1, all the other batches (E2-E4) in the study were highly spherical and exhibited an extended release rate of montelukast sodium, which suggested that the composition and process conditions were optimal. Evaporation of ethanol during spheronization induced a change of thermo-mechanical properties of EC causing its partial melting and dissolution. These led to agglomeration, rounding and smoothing and reflected in the formation of a very strong hydrophobic film around the particles during the drying period. Due to this an increase in the ethanol concentration resulted in obtaining pellets with narrower particle size distribution, higher dimensions, better sphericity and MDT and slower release rate of montelukast sodium.

REFERENCES

1. C. Vervaet, L. Baert, J. P. Remon, *International Journal of Pharmaceutics*, **116**, 131 (1995).
2. S. Ramu, G. Ramakrishna, M. Balaji, K. Kondal Rao, S. Haranadreddy, D. Pavankumar, *American Journal of Advanced Drug Delivery*, **1**, 2013-011-021 (2013).
3. A. Dukis-Ott, M. Thommes, J. R. Remon, P. Kleinebudde, C. Vervaet, *Eur. J. Pharm. Biopharm.*, **71**, 38 (2009).
4. J. M. Newton, *Encyclopedia of Pharmaceutical Technology*, Marcel Dekker Inc., New York and Basel, 2002, p. 1220.
5. R. Mallipeddi, K. Saripella, S. Neau, *SPJ*, **22**, 360 (2014).
6. R. Mallipeddi, K. Saripella, S. Neau, *International Journal of Pharmaceutics*, **385**, 53 (2010).
7. P. Sriamornsak, J. Nunthanid, M. Luangtana-anan, Y. Weerapol, S. Puttipipatkachorn, *Eur. J. Pharm. Biopharm.*, **69**, 274 (2008).
8. E. Hamedelniei, J. Bajdik, K. Pintye-Hódi, *Chem. Eng. Process.*, **49**, 120 (2010).
9. T. F. Reiss, P. Chervinsky, R. J. Dockhorn, S. Shingo, B. Seidenberg, *Arch. Intern. Med.*, **158**, 1213 (1998).
10. M. Davidovich-Pinhas, S. Barbut, A. G. Marangoni, *Cellulose*, **21**, 3243 (2014).
11. D. Q. M. Craig, M. Reading, *Thermal Analysis of Pharmaceuticals*, CRC Press, 2007.
12. A. M. Agrawal, R. V. Manek, W. M. Kolling, S. H. Neau, *PharmSciTech*, **4**, Article 60 (2003).

ОХАРАКТЕРИЗИРАНЕ И ЛЕКАРСТВЕНО ОСВОБОЖДАВАНЕ ОТ МАТРИЧНИ ПЕЛЕТИ С УДЪЛЖЕНО ОСВОБОЖДАВАНЕ НА МОНТЕЛУКАСТ НАТРИЙ

Т. М. Попова^{1*}, Ст. А. Иванова², М. В. Димитров¹

¹ *Медицински университет – София, Фармацевтичен факултет, Катедра по фармацевтична технология и биофармация, ул. Дунав 2, София 1000, България*

² *Медицински университет – София, Фармацевтичен факултет, Катедра по фармацевтична химия, ул. Дунав 2, София 1000, България*

Постъпила на 20 февруари, 2018 г.; приета на 20 март, 2018 г.

(Резюме)

Безспорните ползи от пелетите, свързани с подобрена бионаличност, ги правят идеални за изготвяне на лекарствени форми с удължено освобождаване. За съжаление, независимо от многото предимства на влажната екструзия и сферонизация, трудно се постига удължено освобождаване, дори с обикновено използваните агенти за модифициране на освобождаването, като целулозни деривати, полиетилен оксид, натриев алгинат и др. За решаване на този проблем ние включихме етанол в свързващата течност и изследвахме влиянието му върху свойствата на етилцелулозни пелети и освобождаването на монтелукаст натрий. Чрез диференциална сканираща калориметрия на етилцелулозата (ЕС) е установено повишаване на топлинния капацитет, свързано с увеличаването на количеството на етанол. Това показва, че етанолът променя термомеханичните свойства на ЕС. Освен това, изпаряването на етанол по време на сферонизацията предизвиква частично стапяне и разтваряне на ЕС, водещи до агломерация, закръгляне и заглаждане и образуване на хидрофобен филм около частиците. В резултат на повишаването на концентрацията на етанол в свързващата течност се получават по-големи частици с по-тясно разпределение по размери, подобрена сферичност, по-продължително средно време за разтваряне и по-бавно освобождаване на монтелукаст натрий.

X-ray photoelectron spectroscopy investigations of lignocellulosic materials

I. A. Avramova^{1*}, T. Hr. Radoykova², I. V. Valchev², D. R. Mehandjiev³

¹*Institute of General and Inorganic Chemistry, Bulgarian Academy of Sciences, Acad. G. Bontchev, str., Bl. 11, Sofia 1113, Bulgaria*

²*University of Chemical Technology and Metallurgy, 8, Kl. Ohridski blvd, Sofia 1756, Bulgaria*

³*Institute of Catalysis, Bulgarian Academy of Sciences, Acad. Georgi Bontchev str, Bl. 11, Sofia 1113, Bulgaria*

Received December 15, 2017; Revised March 15, 2018,

Hydrolyzed plant biomass from willow, paulownia and straw was studied by using XPS and IR spectroscopy method in order to understand in depth their chemical composition and the nature of the functional groups on their surfaces. The surface concentration and the presence or absence of some functional groups and their amount on the surface of these materials were studied by the XPS method. The calculated O/C ratio shows that the surface of lignin, paulownia and willow samples was lignin rich, while the surface of straw sample was cellulose rich.

Key words: Hydrolyzed lignocellulosic materials, X-ray photoelectron spectroscopy

INTRODUCTION

In recent years there is increased interest toward the use of waste lignocellulosic materials as adsorbents for water purification from heavy metals [1-6].

The lignocellulosic biomass could be straw, grass, corn-stover, reed, wood, agricultural waste, forestry residues, paper and household waste. The low cost and absence of competition with food industry is the main advantage of using such type of materials. Lignocellulosic biomass contains mainly cellulose, hemicelluloses, lignin, proteins; lipids and ash, which together form a complex solid structure. The ratios of these components in various lignocellulosic materials depend on the source of the biomass (softwood or hardwood, grass and annual plants, energy crops, agricultural waste-straw, husks, bagasse).

One of the questions that arise when studying the adsorption properties of such materials concerns the mechanism of adsorption and the existing adsorption sites.

In ref. [7] through examination of the EPR and EXAFS the conclusion is made that Cr(III) ions are in octahedral position. In ref. [8] it is stated that in relation to its adsorption ability, the lignin isolated from the black fluid has affinity toward metal ions in the following order: Pb(II) > Cu(II) > Cd(II) > Zn(II) > Ni(II). According to the authors, the adsorption sites are phenol and carboxyl OH-groups, the phenol ones having higher affinity towards metal ions.

In our former study we showed that hydrolyzed waste lignocellulosic materials are effective adsorbents of heavy metal ions from aqueous solutions [9].

Agricultural by-products are mostly composed of lignin and cellulose, as well as of other polar functional group-containing compounds, which include alcohols, aldehydes, ketones, carboxylates, phenols and ethers.

These groups are able to bind heavy metals through replacement of hydrogen ions with metal ions in solution or by donation of an electron pair from these groups to form complexes with metal ions in solution [10]. The use of these materials as adsorbents requires detailed investigation of their surface chemical composition.

The biosorption mechanism is difficult to be determined, due to many mechanisms that can contribute to the overall process according to the material used as a biosorbent, environmental factors, presence or absence of metabolic processes in case of presence of living organisms. Biosorbents include various components with a highly complex structure, whose various building elements comprise a plurality of different molecules, which in turn show several binding sites.

One widely used method for this purpose is IR spectroscopy. Nevertheless, infrared analysis of wood surfaces is not considered to be sufficiently surface-sensitive because the depth of infrared radiation into the sample is of the order of 100 μm . Consequently, the changes in infrared features as a result of changes of surface chemistry are often masked by spectral features coming from the bulk [11]. In X-ray photoelectron spectroscopy (XPS) analysis the electrons are ejected from the core levels of atoms in the surface and their binding energies are determined from their kinetic energy and the energy of the incidence beam. Simultaneously, the binding energy of a given atom

* To whom all correspondence should be sent:

E-mail: iva@svr.igic.bas.bg

is influenced by its chemical environment and the sample depth of the XPS is around 5-10 nm.

Therefore, the aim of this work is to demonstrate the ability of this method in studying waste lignocellulosic material in case of their further application as adsorbents or carriers of catalysts. As a result, the hydrolysis of woody chips (willow and paulownia) and wheat straw, that are the subject of this investigation, were studied by X-ray photoelectron spectroscopy.

EXPERIMENTAL

Sample preparation Procedures

In the present study we used hydrolyzed plant biomass from willow, paulownia and wheat straw (denoted as w; p; and s; respectively) as raw materials.

The sample named LC was produced after high-temperature hydrolysis with dilute sulphuric acid of softwood and hardwood chips to sugars under factory conditions, which were further subjected to yeast fodder production. The LC was washed and milled. The 0.1 - 0.3 mm fraction was used.

The samples pLC(w) and pLC(p) were obtained by steam explosion treatment for hydrolysis facilitation, followed by enzymatic hydrolysis with cellulose enzyme complex combined with β -glycosidase of willow and paulownia, respectively. The steam explosion was performed in a 2 L stainless steel laboratory installation at hydromodul ratio of 1:10; initial temperature 100°C; maximal temperature 190°C; pressure 12.8 bar; heating time 60 min and time at maximal temperature 10 min. The cellulosic hydrolysis was carried out in polyethylene bags in a water bath previously heated to the desired temperature. Enzymatic treatment conditions were as follows: temperature 50°C, reaction time 24 h, lignocellulosic content 10 wt.%, $\text{pH}_{\text{initial}}$ 5.5 - 6.0, pH_{final} 4.2 - 4.6 and 5 wt.% charge of the cellulose enzyme complex NS 22086 in combination with 0.5 wt.% of β -glycosidase NS 22118.

The sample hLC(s) was obtained by hydrothermal treatment for hydrolysis facilitation, followed by enzymatic hydrolysis with cellulose enzyme complex combined with β -glycosidase of wheat straw. The hydrothermal hydrolysis of the agricultural lignocellulosic raw materials was performed in 1000 mL stainless steel laboratory autoclaves rotated at constant rate under the following conditions: biomass/water ratio of 1:10; initial temperature 100°C; max. temperature 190°C; heating time 60 min, time at maximum temperature 30 min.; Enzymatic treatment conditions were as follows: temperature 50°C, reaction time 72 h,

lignocellulosic content 10 wt.%, $\text{pH}_{\text{initial}}$ 5.5 - 6.0 and 5 wt.% charge of the cellulose enzyme complex NS 22086 in combination with 0.5 wt.% of β -glycosidase NS 22118 of Novozymes AS. All amounts and experimental conditions were used according to the Novozymes Application Sheet.

Sample characterization

The cellulose content in the studied lignocellulosic materials was determined according to [12]; the lignin content (acid-insoluble lignin in wood and pulp, TAPPI standard test method T 222 om-11) and ash (ash in wood, pulp, paper and paperboard: combustion at 525°C, TAPPI standard T 211 om-02).

An elemental analyzer Eurovector EA 3000 was used for analysis of C, N, S and H. The oxygen content of the samples was calculated by the difference between 100% and the sum of carbon, hydrogen, nitrogen, sulphur and ash.

Infrared spectra were measured on a Varian 660 IR spectrometer. The spectra were collected in the mid-infrared region (4000-400 cm^{-1}). The samples were prepared by the standard KBr pellet method.

XPS investigations were carried out by means of ESCALAB MKII spectrometer with Al $K\alpha$ (unmonochromatized) source at 1486.6 eV with a total instrumental resolution of ~ 1 eV, under a base pressure of 10^{-8} mbar. The C1s, O1s, N1s, photoelectron lines were recorded and calibrated to the C1s line at 285.0 eV. XPSPEAK 4.0 fitting program was used for deconvolution of the photoelectron peaks. All data were recorded at 45° take-off angle.

RESULTS AND DISCUSSION

The used waste hydrolyzed lignocellulosic materials were obtained after different pre-treatment methods for hydrolysis facilitation and enzymatic hydrolysis with cellulose enzyme complexes with different activity. For these reason, part of the hardly hydrolyzable polysaccharides was not hydrolyzed. In Table 1 the data for the chemical and the elemental composition of the investigated materials are presented. The data show that the samples substantially differ as regards the lignin and cellulose contents. The highest lignin content is observed in sample LC - 78 %, in the other samples it is lower and slightly changes from 37.4 (pLC(p)) to 44.1 % (pLC(w)). Concerning the cellulose content, the lowest amount is observed in LC - 12.8 %, while in the other samples it is higher and slightly changes from 50.4 in hLC(s) to 58.6 in pLC(p).

Table 1. Chemical and elemental composition data of the investigated hydrolyzed materials

Samples	Elemental Composition					Chemical Composition		
	H, %	C, %	O, %	N, %	S, %	Cellulose, %	Lignin, %	Mineral substances, %
LC	6.3	58.6	25.3	-	0.7	12.8	78.0	9.1
pLC(p)	6.6	58.7	30.5	0.9	-	58.6	37.4	3.4
pLC(w)	6.3	54.9	35.5	0.6	-	52.3	44.1	2.7
hLC(s)	6.2	48.3	38.4	0.6	-	50.4	42.9	6.5

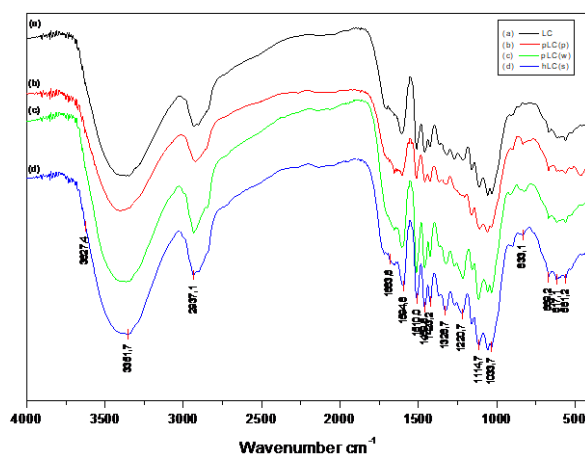


Figure 1. IR spectra of LC, pLC(p), pLC(w) and hLC(s) samples.

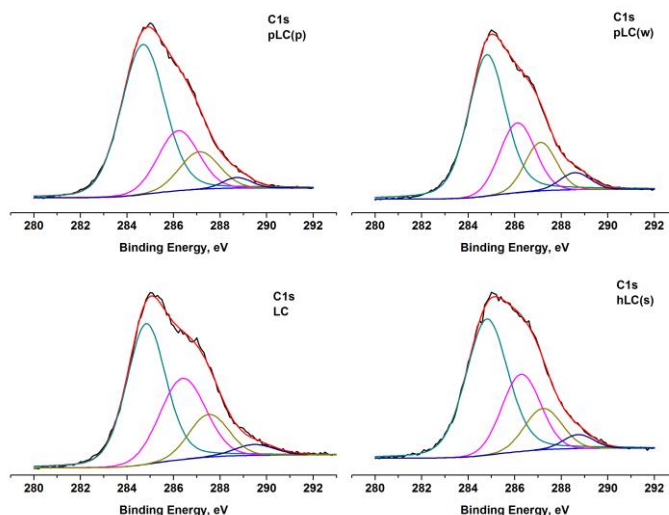


Figure 2. C1s photoelectron lines for the studied lignocellulosic samples.

The carbon, hydrogen and oxygen contents in all samples do not substantially differ from each other. The samples, obtained after hydrolysis of wheat straw (hLC(s)) contained the highest quantity of oxygen and the lowest quantity of carbon. Based on these observations, the structure of hLC(s) is probably condensed to a lower scale and has contained a larger number of free groups. Only LC

contains sulphur because of the use of sulphuric acid as a catalyst of the hydrolysis process, and does not contain nitrogen. The information concerning the nature of the functional groups and ions playing the role of adsorption sites in the hydrolyzed biomass is obtained by using IR spectroscopy. The data of the studied materials are presented on fig. 1.

It is seen that the FTIR spectra of the hydrolyzed lignocellulosic materials are identical. The broad bands in the range of 3500-3100 cm^{-1} are due to stretching vibrations of the hydrogen bonding alcohol and phenol hydroxyl groups. The range 1663-1720 cm^{-1} is characteristic for the carbonyl absorption, which is related with ketones and acids. The bands at 3000-2850 cm^{-1} are referred to symmetrical and asymmetrical stretching vibrations of the C-H bonds in methyl and methylene groups. The IR bands that appear at 1600 and 1510 cm^{-1} for skeleton vibrations of the aromatic rings were characteristic for all materials which contained lignin. It is thought that the bands at 1460 cm^{-1} and at 1424 cm^{-1} are related to CH deformation vibrations in the methyl and methylene groups. The presence of different functional groups such as -OH, -COOH, -C-O-C-, etc., as well as the shapes of the spectral bands are complex and broad due to the hydrogen bonds and conformational structure of the materials. It is obvious that the IR spectroscopy method provides information about the presence of functional groups in these materials, but their quantity on the surface is difficult for evaluation.

A surface-sensitive technique such as XPS is useful to examine the carbon and oxygen content of various organic materials in order to determine the type and relative amount of chemical groups at

their surfaces. In most XPS spectra of organics materials, we would expect to find four functional groups and the presence of more than one relative to another would be evidence of a chemical change at the surface.

The recorded C1s photoelectron spectra of wasted wood samples were further subjected to a fitting procedure for better evaluation of the amount of different functional groups on their surface (see figure 2).

Obviously, there are four peaks as a result of the above mentioned procedure applied. The first one named C1 and situated at around 285 eV we associated with $\underline{\text{C}}-\text{C}$ and $\underline{\text{C}}-\text{H}$ bonds. The second C2 peak at ~ 286.5 eV was related to $\underline{\text{C}}-\text{OH}$ or $\underline{\text{C}}-\text{O}-\text{C}$ bonds. The next C3 peak situated at ~ 288.0 eV corresponds to a $\text{C}=\text{O}$ bond and the last C4 to a $\text{O}-\text{C}=\text{O}$ bond at 289.5 eV. Shake-up peaks ($\pi-\pi^*$ at 290-292 eV) were not detected. The quantitative results from the fitting are summarized in Table 2. The change in the relative amount of those components as a function of oxygen ratio shows the change in the surface composition of the studied lignin and waste wood samples. As a result, only the change in the presence of C-O/C-OH functional groups on the surface is remarkable.

Table 2. Evaluated functional groups on the surface of the studied products by X-ray photoelectron spectroscopy.

Sample	Carbon functional groups,%				Oxygen functional groups, %		Surface concentration of elements, at.%			
	C1	C2	C3	C4	O1	O2	C	O	N	O/C
LC	51.3	31.2	13.9	3.6	27.5	72.5	79.7	27.3	-	0.37
pLC(p)	62.2	22.0	13.2	2.6	41.2	58.8	76.0	21.9	2.1	0.35
pLC(w) (00)	57.3	23.3	14.4	5.0	33.6	66.4	78.1	20.3	1.6	0.26
hLC(s)*	56.6	26.3	13.4	3.7	26.9	73.1	60.9	32.0	1.7	0.53

* On the surface a small quantity of silicon (5.7 at.%) was detected

A higher amount was evaluated for the lignin sample. The oxygen photoelectron lines were subjected to a fitting procedure too (see figure 3). Two peaks are necessary to fit the O1s photoelectron spectra. The O1 component situated at 532 eV is due to the presence of C=O bond, while the O2 component at 533.5 eV was associated to C-O/C-OH groups. The evaluation of the presence of different oxygen groups on the wood surfaces is also shown in Table 2.

The calculated O/C ratio is also shown in the table. The latter clearly indicates if the surface is lignin- or cellulose-rich [13].

Simultaneously, the calculated surface concentration of the studied wood waste materials permits to classify them as lignin or cellulose. The lignin, paulownia and willow samples have O/C ratios equal or slightly lower than the theoretically

calculated one (between 0.33-0.36) typical for lignin. Higher is only the O/C ratio for the sample from straw, equal to 0.53. This shows that the surface is lignin-rich for lignin, paulownia and willow samples, while the surface of the straw sample is cellulose-rich. The observed difference between the bulk phase composition and that on the surface of the studied woods could be due to the migration of lignin to the surface for paulownia and willow, while opposite migration of lignin to the bulk of wood was observed for the straw sample. The reason for that could be the specific way of wood treatment. Similar observation was already reported [14]. On the surface of paulownia, willow and straw samples small amount of nitrogen was detected. These observations coincide with the bulk chemical analysis results.

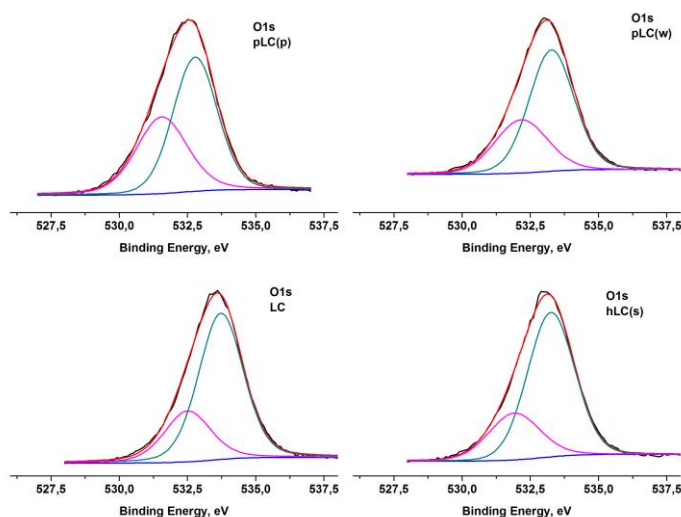


Figure 3. O1s photoelectron lines for the studied lignocellulosic samples.

CONCLUSIONS

The results demonstrate the capability of the XPS method for evaluation of surface characteristics such as chemical composition and existing functional groups in lignocellulosic products. Moreover, obtaining of such data may help clarify issues of the mechanism of adsorption, such as adsorption sites and oxidation state and evaluate the coordination of adsorbed ions. Also, the way to increase the absorption capacity should be held in mind, considering that these lignocellulosic waste materials may be used as carriers for catalytically active components.

REFERENCES

1. J. Hristov, C. Nenkova, M. Karsheva, *European Meeting on Chemical Industry and Environment, Chemical Industry and Environment III*, **2**, 555 (1999).
2. G. Harman, R. Patrick, T. Spittler, *Industrial Biotechnology*, **3(4)** 366 (2008).
3. S. Nenkova, E. Tzolova, *J. Univ. Chem. Tech. Met.*, **38(1)**, 11 (2003).
4. J. E. Penaranda, A. Marcos, A. Sabino, *Polym. Bull.*, **65**, 495 (2010).
5. N. Tazrouti, M. Amrani, *BioResources*, **4(3)**, 740 (2009).
6. N. T. Abdel-Ghani, M. Hefny, G. A. F El-Chaghaby, Removal of lead from aqueous solution using low

- cost abundantly available adsorbents, *Int. J. Environ. Sci. Tech.*, **4** (1), 67 (2007).
7. K. Flogeac, E. Guillon, E. Marceau, M. Aplincourt, *New J. Chem.*, **27**, 714 (2003).
 8. X. Guo, S. Zhang, X. Shan, *J. of Hazard. Materials*, **151**, 134 (2008).
 9. T. Hr. Radoykova, S. V. Dimitrova, K. I. Aleksieva, S. K. Nenkova, I. V. Valchev, D. R. Mehandjiev, *J. of Environ. Prot. and Ecol.*, **16**, 23 (2015).
 10. S. O. Lesmana, N. Febriana, F. E. Soetaredjo, J. Sunarso, S. Ismadji, *Biochem. Eng. J.*, **44**, 19 (2009).
 11. Roger M. Rowell, *Handbook of wood chemistry and wood composites*, Second ed., CRC Press, 2012.
 12. A. V. Obolenskaya, V. P. Sheglov, G. L. Akim, E. L. Akim, N. L. Kossovich, I. Z. Emelianova, *Practical training works in wood and cellulose chemistry*, Lesnaya promishlennost, Moscow, 1965.
 13. P. J. Mjoberg, *Cellul. Chem. Technol.*, **15**, 481 (1981).
 14. M. Ł. Mamiński, M. Król, A. G. McDonald, D. N. McIlroy, I. B. Niraula, J. Czechowska, P. Parzuchowski, *Wood Sci. Technol.*, **47**, 1019, (2013).

ИЗСЛЕДВАНЕ НА ЛИГНО-ЦЕЛУЛОЗНИ МАТЕРИАЛИ ПОСРЕДСТВОМ РЕНТГЕНОВА ФОТОЕЛЕКТРОННА СПЕКТРОСКОПИЯ

И. А. Аврамова^{1*}, Т. Хр. Радойкова², И. В. Вълчев², Д. Р. Механджиев³

¹*Институт по обща и неорганична химия, Българска академия на науките, ул. Акад. Г. Бончев, бл. 11, 1113
София, България*

²*Химикотехнологичен и металургичен университет, бул. Кл. Охридски 8, 1756 София, България*

³*Институт по катализ, Българска академия на науките, ул. „Акад. Г. Бончев“, бл. 11, 1113 София,
България*

Постъпила на 15 декември, 2017 г.; коригирана на 15 март, 2018 г.

(Резюме)

Изследвана е хидролизирана растителна биомаса, получена от върба, пауловния и пшенична слама с помощта на РФС и ИЧ спектроскопски методи с цел изясняване както на техния химичен състав, така и на природата на повърхностните функционални групи в тях. Повърхностната концентрация, присъствието или отсъствието на някои функционални групи и тяхното количество на повърхността на тези материали са определени чрез РФС метода. Отношението О/С показва, че повърхността на пробите от лигнин, пауловния и върба се обогатява на лигнин, докато повърхността на пробата от слама е богата на целулоза.

The effect of iron and manganese oxyhydroxide soil fraction on the occurrence of Cr(VI)

Ts. Voyslavov, S. Tsakovski, V. Simeonov*, S. Arpadjan

Faculty of Chemistry and Pharmacy, Sofia University "St. Kl. Ohridski", 1, J. Bourchier Blvd., 1164 Sofia, Bulgaria

Received March 19, 2018; Accepted April 17, 2018

The objective of the present paper was to study the effect of soil natural oxidants (Fe/Mn oxides) on the occurrence of Cr(VI) in soil in order to better understand and predict the fate, mobility and toxicity of chromium in the environment. Thirty five surface soil samples were examined for Cr(VI) content in their aqueous and alkaline leachates. The reducible iron and manganese oxides in soils, that could promote the oxidation of Cr(III), were extracted using acidified hydroxylamine hydrochloride solution (BCR procedure). Liquid phase extraction was used for redox speciation of Cr. The results obtained indicated that the Cr(III) oxidation in soils occurs *via* interactions with iron and manganese oxides. Cr(VI) was the predominant form in aqueous leachates (44–145 $\mu\text{g kg}^{-1}$ Cr). For the main part of the samples the dissolved alkaline Cr(VI) presented 80 – 89 % of the total soil chromium dissolved in 0.1 mol l⁻¹ NaOH.

Key words: Chromium (VI), Soils, Reducible soil fraction, Chemometrics

INTRODUCTION

Chromium is a common trace element in rocks and soils, found as amorphous Cr(III) hydroxides, eskeolaite (Cr₂O₃) and chromite [FeCr(III)₂O₄], all Cr(III) forms [1, 2]. They exhibit very low solubility and of the mobile, toxic and carcinogenic Cr(VI) species in the environment is typically associated with anthropogenic activities [3–7]. But a significant number of studies in the scientific literature have reported geogenic origin of hexavalent chromium in soil and groundwater. The natural oxidation of Cr(III) to Cr(VI) proceeds in the presence of Mn(III/IV) hydroxides or oxides and bacteria [8–12]. Oxides and oxyhydroxides of iron and manganese constitute an appreciable fraction of the soils. Under common environmental conditions Mn-oxides are considered to be the only environmentally relevant Cr(III) oxidant [13, 14]. Manganese oxides and hydroxides can oxidize Cr(III) in soils transforming it to more mobile Cr(VI) species [12, 15–17].

The importance of the high surface reactivity and redox chemistry of Fe oxides/oxyhydroxides (Fe-oxide) [18] was evaluated in terms of i) development of Fe amendment technologies during treatment of polluted soils and sediments [19–21] and ii) sorption of the reduced form of Cr on the Fe-oxide as a sorbent [22, 23]. To the best of our knowledge, the potential oxidative reactivity of Fe oxides to generate Cr(VI) in soils is not studied yet. How the presence of both oxides (Fe/Mn oxides) in soils would affect the actual potential of chromium(VI) release in soils is not known. In order to better understand and predict the fate,

mobility and toxicity of chromium in the environment, it is important to elucidate the oxidation potential of the soil fraction containing Fe/Mn oxides.

The purpose of the present paper was to study the effect of soil natural oxidants on the occurrence of Cr(VI) in soil. The soil oxidation capacity was investigated using the soil extract obtained in the second step (leaching of reducible Fe/Mn-oxides with acidified hydroxylamine hydrochloride solution) of the modified BCR four-step sequential extraction procedure [24, 25]. The following experiments were performed: i) extraction and separation of the Fe/Mn-oxide fraction in soils and determination of Fe and Mn content; ii) determination of chromium in aqueous and alkaline soil extracts as total chromium [Cr(III) + Cr(VI)] and Cr(VI); iii) chemometrical interpretation of the data.

EXPERIMENTAL

Samples, reagents and instrumentation

Thirty five soil samples were collected in the surroundings of a former steel mill Kremikovtsi located about 20 km northeast of the Bulgarian capital, Sofia. The sampling was performed on grassland from soils not treated by fertilizers. Soil types were Luvisols (Chromic) and Fluvisols (Arenic). The samples were collected from the top soil layer (0–10 cm) according to ISO 10381-2002. The samples were air-dried, then gently crushed, cleaned from extraneous material, sieved to < 2 mm and stored at 4 °C. The examined soils had a pH in the range of 6.8–7.1, equivalent calcium carbonate content was between 0.1 and 22%, total organic matter (TOM) – from 5 to 11 %.

* To whom all correspondence should be sent:
E-mail: VSimeonov@chem.uni-sofia.bg

Ts. Voyslavov et al.: The effect of iron and manganese oxyhydroxide soil fraction on the occurrence of Cr(VI)

All reagents used were of analytical reagent grade (Merck). High-purity water (Milli-Q 50, Millipore) was used throughout. For Cr(III), Fe(III) and Mn(II) ready for use standard solutions for AAS (Merck) were used for preparation of calibration solutions. The stock standard solution with concentration of 1 g l^{-1} Cr(VI) was prepared from $(\text{NH}_4)_2\text{CrO}_4$ delivered from Sigma-Aldrich.

The applied instrumentation was: inductively coupled plasma optical emission spectrometer (Perkin Elmer ICP-OES 6000, MiraMist nebulizer) for measurement of *aqua regia* soluble content of Cr, Fe and Mn in soils; flame (Perkin Elmer, Analyst 400) and electrothermal atomic absorption spectrometer (ETAAS) (Perkin Elmer Zeeman 3030, HGA-600) for determination of elements (Cr, Fe, Mn) in the extracts.

Extraction procedures

The procedure for extraction and determination of Cr(VI) in soils is described in our previous work [26]. In brief, one gram of soil sample was shaken with 20 ml of Milli-Q water or 20 ml of 0.1 mol l^{-1} NaOH for 2 h at 150 rpm. After centrifugation the samples were filtered through $0.45 \mu\text{m}$ syringe filter for determination of total dissolved chromium [Cr(III)+Cr(VI)]. Then an appropriate volume (from 1.0 to 5.0 ml) of the filtrate was placed into an extraction tube. After dilution to 10 ml with Milli-Q water, 2.0 ml of 2% solution of Aliquat 336 in xylene was added and the extraction was performed by up and down shaking for 8 min. In the organic phase Cr(VI) was determined by ETAAS. The certified reference material CRM041-30G Chromium VI–Soil (Fluka, Sigma-Aldrich) was used for proving the reliability of the procedure.

The content of iron and manganese oxides/oxyhydroxides in soils was evaluated using the leachate from the second step of the BCR three-step sequential extraction procedure [24] which represents the reducible (Fe/Mn associated with Fe/Mn oxyhydroxides) soil fraction. The soil residue obtained after the first procedural step was treated with a mixture of 0.5 mol l^{-1} $\text{NH}_2\text{OH}\cdot\text{HCl}$ and 0.05 mol l^{-1} HNO_3 . The reduction of insoluble Fe(III)/Mn(IV) oxyhydroxides leads to formation of soluble Mn(II) and Fe(II) species. The concentration of the dissolved Fe and Mn corresponds to the reducible Fe/Mn oxyhydroxide content in the soil. The accuracy of the procedure was controlled with CRM BCR–701.

Aqua regia soil extracts (ISO 11466) were used for determination of total element contents. With each run two CRMs (Stream Sediments STSD-1 and STSD-3) were analyzed in parallel.

In all cases recoveries in the range of 94–105 % were classified as satisfactory.

Chemometric methods

Cluster analysis is a widely used chemometric approach. In order to cluster objects characterized by a set of variables, one has to determine their similarity. A preliminary step of data scaling is necessary (e.g., autoscaling or z — transform) to avoid dimension impact on the clustering. Then, the similarity between the objects in the variable space can be determined using, for instance, the Euclidean distance or squared Euclidean distance. Typical method for linkage of similar objects into clusters is the Ward's method offering a very stable procedure of clustering. The graphical presentation of the results of the clustering is normally a treelike hierarchical scheme called dendrogram. The cluster significance is determined by the Sneath's index.

Principal components analysis (PCA) is a multivariate method, which allows estimating the data structure. PCA uses the formation of linear combination of the original columns in the data matrix - responsible for the description of the input variables. These linear combinations represent a type of abstract variables being better descriptors of the data structure than the original variables. Usually, the new abstract variables are called latent factors. Just a few of the latent variables account for a large part of the data set variation. Thus, the data structure in a reduced variable space can be observed and interpreted. The initial PCs represent the direction in the data, containing the largest variation. The projections of the data on the plane of PC 1 and PC 2 can be computed and shown as a plot (score plot) where similarity groups could be distinguished. It is important to note that PCA very often requires scaling of the input raw data to eliminate dependence on the scale of the original values. For better representation of the results a mode called Varimax rotation is applied.

All multivariate statistical calculations were performed by STATISTICA (data analysis software system), StatSoft, Inc. (2007) version 8.0. www.statsoft.com.

RESULTS AND DISCUSSION

Iron and manganese species in soils. The *aqua regia* soluble content of iron and manganese in soils (Table 1) varied remarkably between the 35 samples. The concentration of iron ranged from 22 to 301 g kg^{-1} Fe, and that of manganese from 1.2 to 14.7 g kg^{-1} Mn. The variation in metal concentrations could be assigned to geogenic, as well as to anthropogenic origin. The results for the reducible part of Fe and Mn are presented in Table

Ts. Voyslavov et al.: The effect of iron and manganese oxyhydroxide soil fraction on the occurrence of Cr(VI)

1. The reducible part of Fe presents 0.28–10.4 % of the total Fe. The reducible Mn species were found to be in the range 31–74.4 % of the *aqua regia* soluble soil manganese. Chromium species in the soils. The ranges of chromium species content in soils are shown in Table 2. The total soil chromium was less than the permissible level of Cr in agricultural (200 mg kg⁻¹ Cr) and urban (250 mg kg⁻¹ Cr) soils according to the national regulatory standard [27]. The studied soil samples could be considered as not contaminated with Cr.

The aqueous and the alkaline leachates were analyzed for both total Cr and Cr(VI). The difference between the two values approximates the amount of soluble Cr(III) present in a given sample. The results show that only a negligible part of total soil Cr can be dissolved in water or sodium hydroxide. As expected, the aqueous soluble Cr was mainly in the form of Cr(VI) species. Cr(VI) in the soil usually exists in the form of HCrO₄⁻ and

CrO₄²⁻ depending on pH of the surrounding aqueous environment. At a pH above 7, most of the Cr(VI) exists in the form of CrO₄²⁻, whereas at lower pH, Cr(VI) tends to be in the form of HCrO₄⁻ [7]. The less negatively charged anions are stronger adsorbed on the soil surface, because the surface of the most natural soils is negatively charged. Thus, CrO₄²⁻ is weaker adsorbed on the soil compared to HCrO₄⁻ [28].

The presence of Cr(III) in the aqueous extracts could be explained with probable desorption of Cr(OH)₂⁺ or Cr(OH)₂⁺ species from the soil surface [29] or dissolution of Cr(III) complexes with soil fulvic acids dissolved at soil pH. The solubility of chromium increased in NaOH still remaining in the µg kg⁻¹ range (Table 2). The higher Cr concentrations under alkaline conditions could be explained with Cr-silicate mineral dissolution which could lead to higher rates of Cr(VI) generation [30, 31].

Table 1. Iron and manganese in soils as *aqua regia* soluble (Fe_{total}, Mn_{total}) and as reducible oxides (Fe_{OX}, Mn_{OX}). SD: standard deviation (n=3)

	Unit	Min	Max	Mean	SD
Fe _{total}	g kg ⁻¹	22	301	66.6	58
Fe _{OX}	g kg ⁻¹	0.06	6.42	2.66	1.40
Fe _{OX} / Fe _{total}	%	0.3	10.4	4.7	1.9
Mn _{total}	g kg ⁻¹	1.2	14.7	4.9	4.3
Mn _{OX}	g kg ⁻¹	0.54	5.42	2.07	1.45
Mn _{OX} / Mn _{total}	%	31	74	46.5	10.7

Table 2. Soil chromium species: *aqua regia* soluble Cr (Cr_{total}), total aqueous soluble Cr (Cr_{H2O}), aqueous soluble Cr(VI) (Cr(VI)_{H2O}), total alkaline soluble Cr (Cr_{OH}), alkaline soluble hexavalent Cr (Cr(VI)_{OH}). SD: standard deviation (n=3).

Chromium species	Unit	Valid N	Min	Max	Mean	SD
Cr _{total}	mg kg ⁻¹	35	24	189	89	38
Cr _{H2O}	µg kg ⁻¹	35	44	145	88	28
Cr(VI) _{H2O}	µg kg ⁻¹	35	41	142	85	27
Cr _{OH}	µg kg ⁻¹	35	57	548	210	111
Cr(VI) _{OH}	µg kg ⁻¹	35	45	502	174	105
Cr(VI) _{H2O} /Cr _{H2O}		35	1.04	0.96	0.80	0.05
Cr(VI) _{OH} /Cr(III) _{OH}		32	1.1	12.2	3.2	3.2
Cr(VI) _{OH} /Cr _{OH}		35	0.52	0.99	0.82	0.12
Cr(VI) _{OH} /Cr(VI) _{H2O}		35	0.85	4.83	1.99	1.01

The trivalent chromium species in alkaline soil extracts (evaluated as difference between total and hexavalent Cr) represented less than 20 % (for 22 samples) of the total alkaline soluble Cr. The occurrence of Cr(III) was most probably connected

with the dissolution of its complexes with soil humic acids at pH 13 (0.1 mol l⁻¹ NaOH).

In most of the studied sites (22 samples) the content of Cr(VI) in the alkaline extracts was 1.1 to 2.3 times higher than in aqueous soil leachates. It

Ts. Voyslavov et al.: The effect of iron and manganese oxyhydroxide soil fraction on the occurrence of Cr(VI) could be explained with the higher solubility of hexavalent chromium species in alkaline media. For 3 samples the difference between aqueous and alkaline Cr(VI) was not significant. For two samples the ratio between Cr(VI) in alkaline and aqueous extracts was 0.85. This is probably due to partial reduction of Cr(VI) in presence of soil organic substances dissolved at pH 13.

For the main part of the samples the dissolved alkaline Cr(VI) represented 80 – 89 % of the total chromium dissolved in 0.1 mol l⁻¹ NaOH. In nine samples the dissolved hexavalent chromium species were 91 – 99 % of all dissolved chromium species. For 6 samples Cr(VI) was 70 ± 2 % of total alkaline dissolved Cr.

The equilibrium ratio between Cr(VI) and Cr(III) in the alkaline extracts ranged from 1.07 to 66 (Table 2). But for the half of the sites (17 samples) this ratio was between 1.1 and 5, for 15 samples – between 5 and 12. For two samples the Cr(VI)/Cr(III) ratio was 20 and 30, and for one single sample – 66. The latter three samples were not included in the calculation of the average values and of the standard deviation.

Chemometric analysis

Correlation analysis. In Table 4 the correlation matrix for the data set is presented. The statistically significant correlation coefficients are marked. Two levels of significance are highlighted: strong correlation indicated by bold and significant

correlation marked by italics. The rest of the correlation coefficients are statistically non significant.

It could be readily seen that Cr(VI) content in the alkaline leachates (Cr(VI)_{OH}) is strongly correlated with the content of Mn(IV) (*r=0.80*) and Fe(III) (*r=0.89*) species in the soils. These results confirm the oxidizing role of Mn oxyhydroxides reported in previous studies. The present paper shows for the first time the potential of soil iron oxides to generate Cr(VI) species. Even Cr(VI) in aqueous soil extracts is significantly well correlated (*r=0.44*) with Fe(III) species and does not correlate with Mn(IV).

The correlation between the content of the hexavalent chromium in both aqueous and alkaline soil leachates and the total Cr dissolved in these extracts is extremely strong. It agrees with the results from the redox speciation analysis for Cr, presented in Table 2.

This consideration is a solid preliminary background for searching more detailed relationships between the variables of interest.

Cluster analysis. As already mentioned above, the cluster analysis was performed after z-transform of the raw input data, squared Euclidean distances as similarity measures and Ward's method of linkage. The cluster significance was determined according to Sneath's criterion.

Table 3. Correlation matrix [*–strong correlation ($\rho < 0.01$); **–significant correlation ($\rho < 0.05$)]

	TOM	Fe(III) species	Mn(IV) species	Cr _{tot}	Cr _{H2O}	Cr(VI) _{H2O}	Cr _{OH}
Fe(III) species	-0.10						
Mn(IV) species	-0.18	0.60*					
Cr _{tot}	-0.11	0.04	-0.15				
Cr _{H2O}	-0.27	<i>0.40**</i>	0.25	0.24			
Cr(VI) _{H2O}	-0.29	<i>0.44**</i>	0.28	0.24	0.98*		
Cr _{OH}	-0.16	0.88*	0.80*	0.01	<i>0.50**</i>	<i>0.52**</i>	
Cr(VI) _{OH}	-0.13	0.89*	0.80*	-0.03	<i>0.47**</i>	<i>0.50**</i>	0.97*

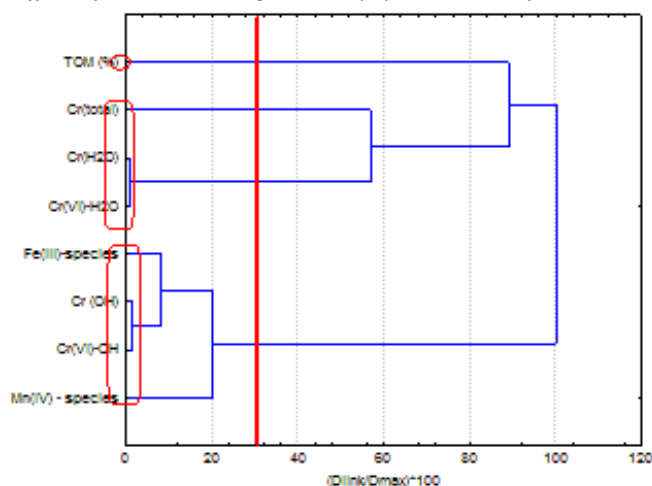


Fig. 1. Hierarchical dendrogram for clustering of 8 variables

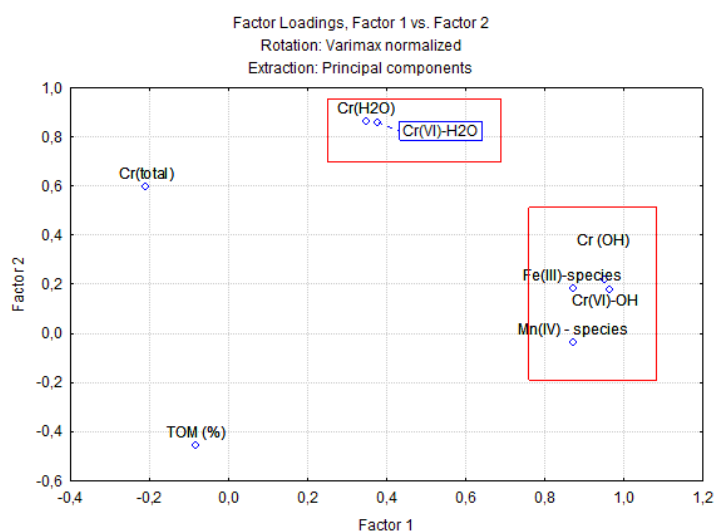


Fig. 2. Biplot PC1 vs. PC2 for factor loadings

In Fig. 1 the hierarchical dendrogram showing the clustering of the variables is presented.

Two major clusters are formed:

K1 [Mn(IV), Cr(VI)- OH, Cr (OH), Fe(III)]

K2 [Cr(VI)-H2O, Cr(H2O), Cr(total)]

TOM is a typical outlier which differs from the rest of variables.

In K2 Cr(total) also slightly differs from the other members of the cluster K2. In general, the results from the hierarchical clustering of variables confirm those from correlation analysis. *Principal components analysis*. In order to confirm the results from correlation analysis and hierarchical cluster analysis the input data were subjected to principal components analysis (PCA). It was found that two principal components explain over 75 % of the total variance. It means that two significant factors are responsible for the data structure. In Fig. 3 the biplot for the factor loadings PC1 vs. PC2 is presented. As in cluster analysis, there is close relationship between chromium species with water

extraction, on one hand, and between chromium species after OH-extraction along with Fe(III) and Mn(IV) species, on the other. It can be concluded that the two latent factors determining the data structure are conditionally “water extraction” and “alkaline extraction”. Again, total Cr and TOM are not closely related to the other soil features. It is obvious that TOM negatively correlated to all other species.

CONCLUSION

The Cr(III) oxidation in soils occurs *via* interactions with iron and manganese oxides. Multivariate statistical analysis revealed information about the probable mechanism for Cr(III) oxidation in soils: the soil fraction containing Fe(III) and Mn(IV) species is the phase that promotes the oxidation of Cr(III). The BCR sequential extraction procedure and the isolation of the soil fraction bound to amorphous Fe/Mn oxyhydroxides can be a useful tool for evaluating the oxidation capacity of the soils.

Acknowledgements: The authors gratefully acknowledge the financial support from the Bulgarian National Science Fund (Grant EO2/7).

REFERENCES

1. K. Shiraki, *Resour. Geol.*, **47**, 319 (1997).
2. F. C. Richard, A. M. Bourg, *Water Resources*, **25**, 807 (1991).
3. D. S. Becker, E. R. Long, D. M. Proctor, T. C. Ginn, *Environ. Toxicol. Chem.*, **25**, 2576 (2006).
4. W. J. Berry, W. S. Boothman, J. R. Serbst, P. A. Edwards, *Environ. Toxicol. Chem.*, **23**, 2981 (2004).
5. W. Ding, D. I. Stewart, P. N. Humphreys, S. P. Rout, I. T. Burke, *Sci. Total Environ.*, **541**, 1191 (2016).
6. J. F. Papp, *Mineral Commodity Summaries: Chromium*, U.S. Department of the Interior, U.S. Geological Survey, Washington, DC, 2001.
7. C. H. Wang, C. P. Huang, P. F. Sanders, *Pract. Period. Hazard. Toxic Radioact. Waste Manag.*, **6**, 6 (2002).
8. S. E. Fendorf, R. J. Zasoski, *Environ. Sci. Technol.*, **26**, 79 (1992).
9. P. S. Nico, R. I. Zasoski, *Environ. Sci. Technol.*, **34**, 3363 (2000).
10. C. D. Palmer, P. R. Wittbrodt, *Environ. Health Persp.*, **92**, 25 (1991).
11. L. M. Zhang, F. Liu, W. F. Tan, X. H. Feng, Y. G. Zhu, J. Z. He, *Soil Biol. Biochem.* **40**, 1364 (2008).
12. Z. Stepniewska, K. Bucior, R. P. Bennicelli, *Geoderma*, **122**, 291 (2004).
13. L. E. Eary, D. Rai, *Environ. Sci. Technol.*, **21**, 1187 (1987).
14. S. E. Fendorf, *Geoderma*, **57**, 65 (1995).
15. B. R. James, J. C. Petura, R. J. Vitale, G. R. Mussoline, *J. Soil Contam.*, **6**, 569 (1997).
16. C. Yingxu, C. Yiyi, L. Qi, H. Ziqiang, H. Hong, W. Jianyang, *Pedosphere*, **7**, 185 (1997).
17. M. Debra, D. M. Hausladen, S. Fendorf, *Environ. Sci. Technol.*, **51**, 2058 (2017).
18. R. M. Cornell, U. Schwertmann, *The iron oxides: structure, properties, reactions, occurrences and uses*, John Wiley & Sons, 2006.
19. A. B. Cundy, L. Hopkinson, R. L. Whitby, *Sci. Total Environ.*, **400**, 42 (2008).
20. M. Komárek, A. Vaněk, V. Ettler, *Environ. Pollut.*, **172**, 9 (2013).
21. J. Kumpiene, A. Lagerkvist, C. Maurice, *Waste Manag.*, **28**, 215 (2008).
22. E. C. Butler, L. Chen, C. M. Hansel, L. R. Krumholz, A. S. E. Madden, *Environ. Sci.: Processes Impacts*, **17**, 1930 (2015).
23. D. Fandeur, F. Juillot, G. Morin, L. Olivi, A. Cognigni, J. P. Ambrosi, F. Guyot, E. Fritsch, *American Mineralogist*, **94**, 710 (2009).
24. G. Rauret, J. F. Lopez-Sanchez, A. Sahuquillo, E. Barohona, M. Lachica, A. M. Ure, C. Davidson, A. Gomez, D. Luck, J. Bacon, M. Yli-Halla, H. Muntau, Ph. Quevauviller, *J. Environ. Monit.*, **2**, 228 (2000).
25. J. M. Serafimovska, S. Arpadjan, T. Stafilov, K. Tsekova, *J. Soils Sed.*, **13**, 294 (2013).
26. C. Voyslavov, S. Tsakovski, S. Arpadjan, *Turkish J. Chem.*, **40**, 944 (2016).
27. Regulation № 3 /01/08/2008 on the allowable limits of toxic substances in the soils. www.government.bg/bg/legislation/soil/normipochv_i.doc.
28. K. R. Krishna, L. Philip, *J. Hazard. Mat.*, **21**, 109 (2005).
29. E. I. Hawley, R. A. Deeb, M. C. Kavanaugh, J. R. G. Jacobs, *Chromium(VI) Handbook. Chapter 8: Treatment Technologies for Chromium (VI)*, CRC Press, Florida, 2004, p. 273.
30. C. Oze, D. K. Bird, S. Fendorf, *Proc. Nat. Acad. Sci. USA*, **104**, 6544 (2007).
31. A. U. Rajapaksha, M. Vithanage, Y. S. Ok, C. Oze, *Environ. Sci. Technol.*, **47**, 9722 (2013).

ВЛИЯНИЕ НА ПОЧВЕНАТА ФРАКЦИЯ, СЪДЪРЖАЩА ЖЕЛЕЗНИ И МАНГАНОВИ ОКСИДИ, ВЪРХУ НАЛИЧИЕТО НА Cr(VI)

Ц. Воиславов, С. Цаковски, В. Симеонов*, С. Арпаджан

Факултет по химия и фармация, Софийски университет „Св. Кл. Охридски“, 1164 София, бул. Дж. Баучер 1, България

Постъпила на 19 март, 2018 г.; коригирана на 17 април, 2018 г.

(Резюме)

Целта на настоящата работа е да се изучи влиянието на природните окислителни в почвата (Fe/Mn оксиди) върху наличието на Cr(VI) в почвата с оглед по-доброто разбиране и предсказване на промените, мобилността и токсичността на хрома в околната среда. Водни и алкални извлеци от 35 образци от повърхностния слой на почвата са изследвани за съдържанието на Cr(VI). Редуцируемите железни и манганови оксиди в почвата, които биха могли да промотират окислението на Cr(III), са екстрахирани с използване на подкислен разтвор на хидроксиламин хидрохлорид (BCR процедура). Течна екстракция е използвана за определяне на редокс формите на Cr. Установено е, че окислението на Cr(III) в почвите се извършва посредством взаимодействие с железните и мангановите оксиди. Cr(VI) е преобладаващата форма във водните извлеци (44–145 $\mu\text{g kg}^{-1}$ Cr). За по-голямата част от образците, разтворимият в алкален разтвор Cr(VI) представлява 80 – 89 % от тоталния почвен хром, разтворен в 0.1 mol l⁻¹ NaOH.

Transformation from α - to β - phase in vinylidene fluoride–hexafluoropropylene copolymer nanocomposites prepared by co-precipitation method

L. H. Borisova, D. S. Kiryakova*, A. N. Atanassov

Department of Materials Science, Prof. Assen Zlatarov University, Y. Yakimov Str. 1, Burgas 8010, Bulgaria

Received September 7, 2015; Revised March 16, 2018

Nanocomposite materials on the basis of vinylidene fluoride–hexafluoro-propylene copolymer with Cloisite®15A were obtained by a co-precipitation method from dimethylsulfoxide solution. The addition of organically modified nanoclay was found to facilitate the transformation of the polymer crystals from α - to β - phase. The amount of β - phase calculated for the materials containing 6.0 mass % of modified nanoclay was more than 95%. At lower Cloisite®15A content, the β - phase also increased compared to that in the initial copolymer and was in the range 47–82%. The increase of the tensile strength and elongation at break of the nanocomposites was higher at lower content of nanoclay Cloisite®15A (38–39 MPa and 820–850% at 0.75–1.0 mass %, respectively). The reinforcing effect was lower for the nanocomposites with higher clay content owing to some clay platelets being partially exfoliated and stacked. This was confirmed by transmission electron micrographic observations of the nanomaterials obtained.

Keywords: nanoclay, nanocomposites, vinylidene fluoride-hexafluoropropylene copolymer, co-precipitation, phases

INTRODUCTION

Poly(vinylidene fluoride) (PVDF) and copolymers on its basis have been some of the most researched polymers, due to their ferroelectric properties. These polymers have different unit cells of varying polarity, because of their different crystal modifications. At least four different crystal modifications of PVDF with different molecular conformations and lattice parameters are known [1–3]. The most common, easily obtainable phase is the α - phase. It does not show net lattice polarization. In the β - phase, the molecules are configured in *all-trans* conformation. This imparts spontaneous lattice polarization to the β - phase crystals which results in ferroelectricity observed in PVDF. The γ - phase is a combination of alternating conformational units from the α - and β - phases, and the δ - phase is a polar version of the α - phase.

The crystal forms of PVDF are retained in many copolymers of VDF containing small amounts of comonomers [4]. The fluorine atoms in the copolymers produce steric hindrance which prevents the molecular chains from assuming conformations similar to the non-electroactive α - phase of PVDF. Many of the copolymers directly crystallize into the polar electroactive β - phase [3] which is responsible for the ferro-, pyro-, and piezoelectric behavior in PVDF and its copolymers [3, 5].

It is well known that films of vinylidene fluoride–hexafluoropropylene copolymer (VDF–HFP) with different HFP contents indicate

prominent piezo-, pyro-, and ferroelectricity comparable to that in PVDF [6–9]. It was also found that these properties are highly dependent on the crystal structure and polymer chain orientation of the VDF–HFP copolymer [10].

Over the past decade, many researchers have reported a possibility to stabilize the β - phase in PVDF and its copolymers with HFP in the presence of layered silicates well scattered within the polymer matrix. The addition of nanoclays is a prerequisite for the improvement of the mechanical, piezo-, pyro- and ferroelectric properties [11, 12].

The aim of the present work is to obtain nanocomposite materials on the basis of vinylidene fluoride–hexafluoropropylene copolymer with organically modified nanoclay Cloisite®15A by a co-precipitation method from dimethylsulfoxide solution and to study some properties of the nanocomposites obtained.

EXPERIMENTAL

Materials

Vinylidene fluoride–hexafluoropropylene copolymer referred to as VDF–HFP is a copolymer (15 mol% of HFP comonomer) with melting temperature of 117°C and melt index of 6.52 g/10 min (220°C, load 98 N) in the form of powder, kindly supplied by Arkema, France. Cloisite®15A, organically modified montmorillonite nanoclay from Southern Clay Products Inc. was used. Cloisite®15A is a Na⁺ montmorillonite clay modified with dimethyl, dehydrogenated tallow, quaternary ammonium (2M2HT) with d_{001} spacing of 31.5 Å and density of 1.66 g/cm³. The modifier concentration of Cloisite®15A was 125 meq/100 g.

* To whom all correspondence should be sent:
E-mail: dskiryakova@abv.bg

The solvent used for the compositions was dimethylsulfoxide (DMSO), Sigma Aldrich. All the materials described above were used directly without any further modification or treatment.

Sample preparation

The co-precipitation method was used to prepare VDF–HFP copolymer nanocomposites containing 0.5, 0.75, 1.0, 1.5, 3.0 and 6.0 mass % of nanoclay Cloisite®15A. To obtain the nanoclay contents in the VDF–HFP copolymer mentioned, two premixes were made: one for the nanoclay and the other for the VDF–HFP, using DMSO as a solvent. The two premixes were sonicated using a Branson 8510 ultrasonication bath at 30–40°C for approximately 5 min. The final 10% solution was prepared by adding the contents of the nanoclay premix to the VDF–HFP copolymer premix and the product was sonicated again for 20 min. To the mixture obtained, 150 ml of deionized water were added. A stringy, white, translucent precipitate formed immediately. Then, the precipitate was removed and dried in a vacuum oven until constant weight. For most physical testings, the precipitated samples were pressed into films on a laboratory press PHI (England) between aluminum foils under the following conditions: sample thickness about 0.3 mm, temperature 200°C, melting period at 200°C – 3 min, pressing pressure – 12 MPa; cooling rate – 40°C/min.

Fourier transform infrared spectroscopy (FT–IR)

Samples prepared as films were analyzed using a spectrophotometer produced by “Bruker” (Germany) in the interval 4000–400 cm^{-1} with Tensor 27. To determine the relative quantity of the β - phase, the heights of the series of peaks were determined by simulation of the spectrum observed. This was done using OPUS – 65 software which automatically corrects the baseline. For each sample, the fraction of the β - crystalline phase (F_{β}^{IR}) was calculated by the formula: $F_{\beta}^{\text{IR}} = A_{\beta} / (1.26A_{\alpha} + A_{\beta})$, where: A_{α} and A_{β} are the heights of the peaks at 764 and 840 cm^{-1} , respectively, and the coefficient 1.26 represents the ratio of the absorption coefficients at 764 and 840 cm^{-1} [13].

Differential scanning calorimetry (DSC) measurements

The behavior under melting and crystallization in nitrogen atmosphere of samples with a mass of

ca. 4 mg was analyzed using a simultaneous thermal analyzer „STA 449F3 Jupiter” (Netzsch, Germany) under the following conditions: first heating from 20 to 240°C at a rate of 10°C/min, isothermal period of 1 min at 240°C (to remove any traces of crystalline structure) followed by cooling to 20°C and second heating to 240°C at the same rate. The degree of crystallinity of the samples was calculated at $\Delta H_{100\%} = 104.7 \text{ J/g}$ for 100% crystalline VDF–HFP copolymer [14].

Tensile properties

The tensile strength, elongation at break and the other characteristics of the initial VDF–HFP copolymer and the materials based on it were measured on a dynamometer INSTRON 4203 (England) at a speed of 100 mm/min and room temperature.

Transmission electron microscopy (TEM)

For the TEM experiments, JEOL JEM 2100 microscope was used. The observations were performed at 200 kV acceleration voltage. The samples were prepared by dropping and evaporating particle suspensions on a standard copper grid.

RESULTS AND DISCUSSION

Figs 1 A) and B) show DSC thermograms of heating and cooling of the initial VDF–HFP copolymer and the nanomaterials on its base with Cloisite®15A, prepared by the co-precipitation method in the temperature range from 80 to 160°C, at a scanning rate of 10°C/min in nitrogen atmosphere. The large endothermic peak present in all samples obtained from solution is related to the melting of α - and/or β - phase crystals (Fig. 1 A) while the exothermic peak observed at cooling was attributed to crystallization (Fig. 1 B). Table 1 shows the thermal characteristics, such as the temperature of melting T_m , the degree of crystallinity α for both heating processes of the initial VDF–HFP copolymer and the nanocomposites based on it with modified Cloisite®15A obtained by co-precipitation from DMSO solution.

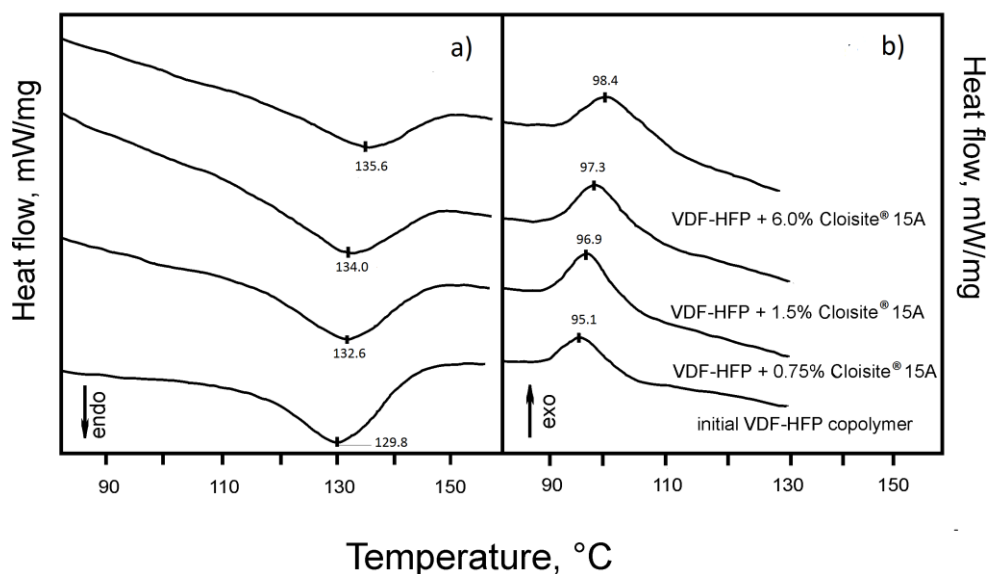


Fig. 1. DSC thermograms at: (A) heating and (B) cooling of the initial VDF–HFP copolymer and nanocomposite materials on its basis containing Cloisite®15A.

Table 1. DSC- thermogram values of the initial PVDF–HFP and its nanocomposites

Content of Cloisite®15A, mass %	Content of β - phase, %
0	26
0.5	47
0.75	54
1.0	54
1.5	57
3.0	82
6.0	95

It can be seen that the temperatures of melting T_m slightly increased during the first and second melting (by ca. 5°C) with the increase of organically modified nanoclay Cloisite®15A content from 0.5 to 6 mass %. For the initial copolymer, these temperatures were 129.8 and 129.7°C while for the materials with 6 mass % Cloisite®15A they were 135.6 and 133.2°C, respectively, during the first and second melting. The temperature of crystallization T_c also increased with the content of nano-filler in the compositions to reach 98.4°C. As it has been reported by Buckley *et al.* [15], the increase of the temperatures of melting and crystallization of the nanomaterials based on VDF–HFP copolymer is related to the formation of β - phase. The degree of crystallinity α of the series of samples based on VDF–HFP copolymer with nanoclay was found to decrease by 4–5% compared to these of the initial copolymer, due to the formation of a higher amount of β - phase [16].

The FT–IR spectra of the initial copolymer, organically modified nanoclay (Cloisite®15A) and films of VDF–HFP (15 mol%) copolymer coprecipitated from DMSO solution with different contents of Cloisite®15A are presented in Figure 2. The spectrum of the modified montmorillonite-Cloisite®15A showed the characteristic vibrational bands at 3633 cm^{-1} attributed to O–H silicate stretching [17]; 1640 cm^{-1} (related to O–H bending), 1042 cm^{-1} (owing of stretching vibration of Si–O–Si in silicate) and 917 cm^{-1} (from Al–OH–Al deformation of aluminates) [18]. The bands at 2921, 2851 and 1469 cm^{-1} were assigned to C–H vibrations of methylene groups (asymmetric stretching, symmetric stretching and bending, respectively) belonging to the surfactant chemical structure. The bands at 465, 521, 626, 722 and 796 cm^{-1} were attributed to the Si–O–Al bending vibrations [17], 847 cm^{-1} corresponds to Al–O–H and 1469 cm^{-1} – to the presence of ammonium salts [19]. The characteristic vibration bands of the initial VDF–HFP copolymer observed at 410, 489 ($-\text{CF}_2$ -wagging), 510 ($-\text{CF}_2$ -bending), 532, 614, 764, 797, 976, 1190 and 1406 cm^{-1} are a strong evidence for the existence of α - phase of VDF crystals [20]. The peak at 840 cm^{-1} is characteristic for $-\text{CF}_2$ symmetric stretching in the *all-trans* β - phase. It can be seen from Fig. 2 that the intensity at 840 cm^{-1} increases with the increase of Cloisite®15A content in the compositions.

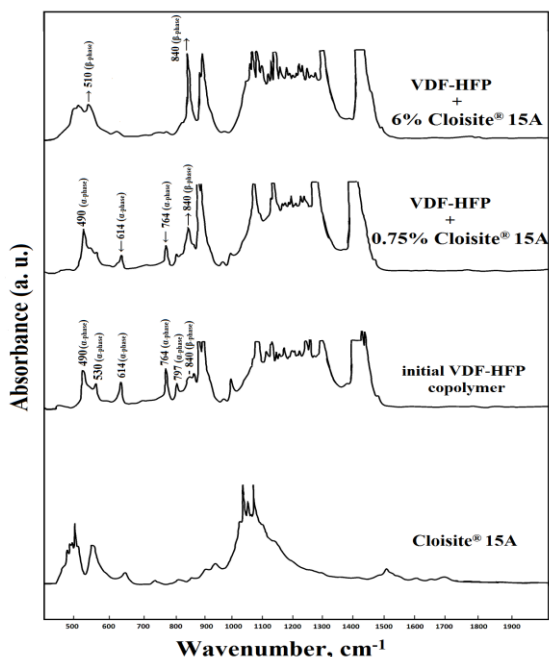


Fig. 2. IR-spectra of the initial copolymer, organically modified nanoclay (Cloisite®15A) and nanocomposite materials on their basis.

Another peak indicating for the change in conformation was registered at 764 cm^{-1} , which is characteristic of $-\text{CF}_2$ and $\text{C}-\text{C}-\text{C}$ bending in the trans-gauche α - phase. Obviously, the intensity of this peak decreases with the increase of the amount of Cloisite®15A. Comparing the initial VDF-HFP copolymer with the materials containing Cloisite®15A, a new peak was observed at 510 cm^{-1} which confirms the crystal transformation from α - to β - phase. It should be noted that γ - phase was present in the materials containing 0.5–3 mass % of nanoclay Cloisite®15A, which indicates the transformation of the structure to a more polar

phase. This can be explained with the inclusions of γ - together with β - phase.

The absorption bands at 764 and 796 cm^{-1} are mainly related to the presence of α - phase. According to [21], when the absorption bands of the γ - phase at 776 and 812 cm^{-1} are absent, the band at 840 cm^{-1} can be solely attributed to the presence of β - phase. Therefore, the relative fractions of the α - and β - crystalline phases can be calculated using the absorptions at 764 and 840 cm^{-1} , respectively.

The initial VDF-HFP copolymer mainly contains α - phase. With the addition of Cloisite®15A to the copolymer, the α - phase was fully transformed into β - phase. Furthermore, the amount calculated for nanomaterials with 6.0 mass % modified nanoclay was higher than 95%. At a Cloisite®15A content less than 6.0 mass %, the β - phase also significantly increased compared to that in the initial copolymer (47–82%) – Table 2. The tensile strength, elongation at break and *Young* modulus of the materials based on VDF-HFP copolymer with Cloisite®15A are shown in Table 3. It can be seen that the increase of the values of tensile strength (to 38.7 MPa) and elongation at break (to 848%) was higher at lower content of Cloisite®15A nanoclay (0.75–1.0 %, mass%), compared to that of initial VDF-HFP copolymer.

The reinforcing effect was lower for the nanocomposites with higher clay content owing to some clay platelets being only partially exfoliated and stacked (Fig. 3 B). The formation of β - phase in the compositions studied is also beneficial to the improvements of mechanical properties of the materials obtained (Table 3 and Fig. 2).

Table 2. Content of β - phase in the crystalline phase of initial VDF-HFP copolymer and its nanocomposites with Cloisite®15A prepared by co-precipitation method

Content of cloisite®15A, mass %	First melting		Second melting		Crystallization	
	$T_m, ^\circ\text{C}$	$\alpha, \%$	$T_m, ^\circ\text{C}$	$\alpha, \%$	$T_c, ^\circ\text{C}$	$\alpha, \%$
0	129.8	18.6	129.7	17.0	95.1	28.7
0.5	131.6	17.0	130.0	16.9	96.4	28.5
0.75	132.6	16.5	130.5	15.8	96.9	28.3
1.0	133.5	15.9	130.7	15.1	97.0	27.8
1.5	134.0	15.4	130.8	14.9	97.3	27.2
3.0	134.4	14.2	132.0	13.6	97.7	26.4
6.0	135.6	13.8	133.2	12.9	98.4	23.4

Table 3. Tensile parameters of the initial VDF-HFP copolymer and its nanocomposites.

Content of Cloisite®15A, mass %	Tensile strength, MPa	Elongation at break, %	Young modulus, MPa
0	27.2	795	125
0.5	34.8	831	143
0.75	37.9	848	170
1.0	38.7	823	215
1.5	36.2	807	190
3.0	35.2	805	156
6.0	33.6	750	154

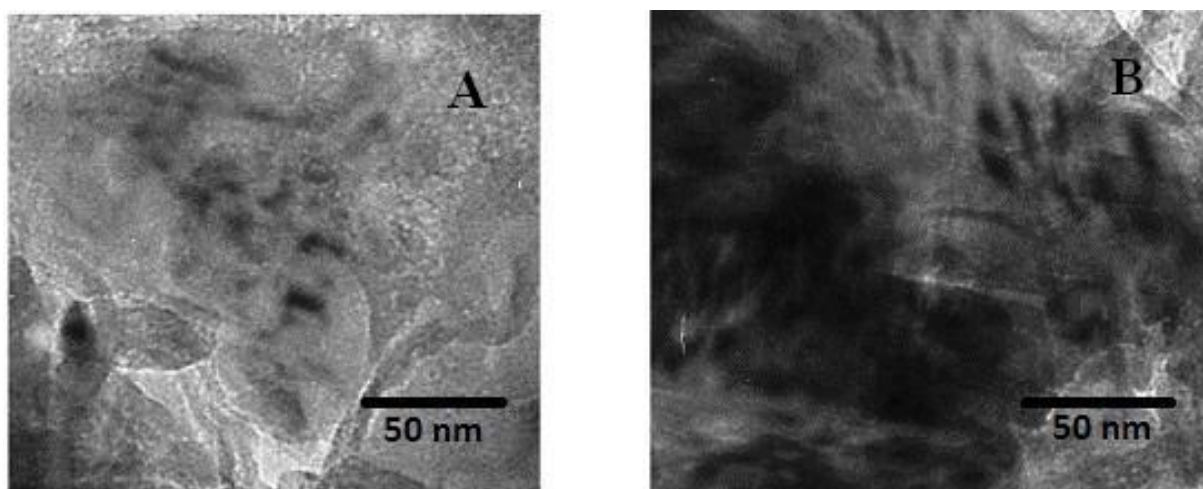


Fig. 3. TEM images of the nanocomposite materials based on VDF–HFP copolymer with 1.0 mass % (A) and 6.0 mass % (B) Cloisite®15A

CONCLUSIONS

Polymer nanocomposite materials containing up to 6.0 mass % of organically modified montmorillonite nanoclay Cloisite®15A were prepared by the co-precipitation method. The FT–IR analysis showed that the initial copolymer mainly contains the non-polar α - phase. The intensity of the peak at 840 cm^{-1} characteristic of $-\text{CF}_2$ symmetric stretching in the *all-trans* β - phase, increases with the Cloisite®15A content in the compositions. The intensity of the peak at 764 cm^{-1} which is characteristic of $-\text{CF}_2$ and C–C–C bending in the *trans-gauche* α - phase decreases with the increase of the nanoclay content. This proved the transformation of polymer crystals conformation from α - to β - phase. The highest content of β - phase (more than 95%) was calculated to be in the materials containing 6.0 mass % of Cloisite®15A. It was found that the values of the tensile strength and elongation at break of the nanomaterials obtained were higher at lower nanoclay content (0.75–1.0 mass %) and decreased to 33.6 MPa and 750%, respectively at 6.0 mass % of Cloisite®15A owing

to poor exfoliation of the clay layers in the copolymer matrix.

REFERENCES

1. J. S. Humphrey, R. Amin-Sanayei, in: Encyclopedia of polymer science and technology, Wiley, New York, 2006, p. 510.
2. A. J. Lovinger, in: D. C. Bassett (ed.) Developments in crystalline polymers, Applied Science Publishers Ltd, Englewood, New Jersey, 1982, p. 195.
3. H. S. Nalwa, Ferroelectric Polymers: Chemistry, Physics, and Applications, Marcel Dekker Inc., New York, 1995.
4. Yu. A. Panshin, S. G. Malkevich, Z. S. Dunaevskaya, Ftoroplasty (Fluoroplastics), Khimiya, Leningrad, 1978.
5. H. Lefebvre, F. Bauer, L. Eyraud, *Ferroelectrics*, **171**, 259 (1995).
6. F. Wang, Z. Xia, X. Qiu, J. Shen, X. Zhang, Z. An, *IEEE Trans. Dielectr. Electr. Insul.*, **13**, 1132 (2006).
7. A. C. Jayasuriya, J. I. Scheinbeim, *Appl. Surf. Sci.*, **175**, 386 (2001).
8. M. Wegener, W. Künstler, R. Gerhard-Mulhaupt, *Integr. Ferroelectr.*, **60**, 111 (2004).

- L. H. Borisova et al.: Transformation from α - to β - phase in vinylidene fluoride–hexafluoropropylene copolymer... Washington, N. Wolchover, *Polymer*, **47**, 2411 (2006).
9. F. Wang, P. Frubing, W. Wirges, R. Gerhard, M. Wegener M, *IEEE Trans. Dielectr. Electr. Insul.*, **17**, 1088 (2010).
 10. X. He, K. Yao, B. K. Gan, *J. Appl. Phys.*, **97**, 084101 (2005).
 11. A. Kellarakis, S. Hayrapetyan, S. Ansari, J. Fang, L. Estevez, E. P. Giannelis, *Polymer*, **51**, 469 (2010).
 12. V. K. Tiwari, P. K. Kulriya, D. K. Avasthi, Pralay Maiti, *J. Phys. Chem. B*, **113**, 11632 (2009).
 13. H. Sobhani, M. Razavi-Nouri, A. A. Yousefi, *J. Appl. Polym. Sci.*, **104**, 89 (2007).
 14. S. Rudzhiah, N. Muda, S. Ibrahim, A. A. Rahman, N. S. Mohamed, *Sains. Malays.*, **40**, 707 (2011).
 15. J. Buckley, P. Cebe, D. Cherdark, J. Crawford, B. S. Ince, M. Jenkins, J. Pan, M. Reveley, N.
 16. T. U. Patro, M. V. Mhalgi, D. V. Khakhar, A. Misra, *Polymer*, **49**, 3486 (2008).
 17. J. M. Yeh, S. J. Liou, Y. Lin, Ch-Y. Cheng, Ya-W. Chang, *Chem. Mater.*, **14**, 154 (2002).
 18. M. Bora, J. N. Ganguli, D. K. Dutta, *Thermochim. Acta*, **346**, 169 (2000).
 19. H. Balakrishnan, M. Ibrahim, M. U. Wahit, A. Hassan, *Polym. Compos.*, **32**, 1927 (2011).
 20. Ye. Bormashenko, R. Pogreb, O. Stanevsky, Ed. Bormashenko, *Polym. Test.*, **23**, 791 (2004).
 21. R. Gregorio, *J. Appl. Polym. Sci.*, **100**, 3272 (2006).

ТРАНСФОРМАЦИЯ НА α - В β - ФАЗА ПРИ ВИНИЛИДЕНФЛУОРИД-ХЕКСАФЛУОРОПРОПИЛЕНОВИ СЪПОЛИМЕРНИ КОМПОЗИТИ, ПОЛУЧЕНИ ПО МЕТОДА НА СЪУТАЯВАНЕТО

Л. Х. Борисова, Д. С. Кирякова*, А. Н. Атанасов

Катедра по минералознание, Университет „Асен Златаров“, ул. Проф. Я. Якимов 1, Бургас 8010, България

Постъпила на 7 септември, 2015 г.; коригирана на 16 март, 2018 г.

(Резюме)

Нанокompatитни материали на основата на винилиденфлуорид-хексафлуоропропиленов съполимер с Cloisite®15A са получени по метода на съутаяването из разтвор на диметилсулфоксид. Установено е, че добавянето на органично модифицирана наноглина улеснява трансформацията на полимерните кристали от α - в β - фаза. Количеството на β - фаза, изчислено за материалите, съдържащи 6.0 мас. % модифицирана наноглина е над 95%. При по-ниско съдържание на Cloisite®15A, β - фазата нараства в сравнение с тази в изходния съполимер и е в интервала от 47–82%. Повишаването на издръжливостта на опън и удължението при счупване на нанокompatитите е по-високо при по-ниско съдържание на наноглина Cloisite®15A (съответно 38–39 МПа и 820–850% при 0.75–1.0 мас. %). Усилващият ефект е по-слаб за нанокompatити с по-високо съдържание на глина поради частичното екслолиране и слепване на някои от глинестите плочки, доказано чрез трансмисионна електронна микрография на получените наноматериали.

Sol-gel hydrothermal preparation of $\text{Bi}_4\text{Ti}_3\text{O}_{12}$ ceramic

M. Afqir^{1,2*}, A. Tachafine², D. Fasquelle², M. Elaati¹, J-C. Carru², A. Zegzouti¹, M. Daoud¹

¹Laboratoire des Sciences des Matériaux Inorganiques et leurs Applications, Faculté des Sciences Semlalia, Université Cadi Ayyad, Marrakech, Maroc

²Unité de Dynamique et Structure des Matériaux Moléculaires, Université du Littoral- Côte d'Opale, Calais, France

Received November 28, 2017; Revised May 15, 2018

This manuscript reports a modified method of preparation of $\text{Bi}_4\text{Ti}_3\text{O}_{12}$ ceramic powder by a sol-gel approach, followed by hydrothermal treatment of the obtained gel. Bismuth acetate and titanium isopropoxide were used as metallic sources to prepare the precursor gel, and it was successfully converted into bismuth-titanium oxide by hydrothermal treatment at 400 °C and 600 °C for 24 h. Multiple characterizations, namely XRD, FTIR, SEM measurements were used to validate the structural features.

Keywords: $\text{Bi}_4\text{Ti}_3\text{O}_{12}$; Sol-gel; Hydrothermal; Characterization.

INTRODUCTION

Aurivillius oxides prepared through a soft chemical route such as hydrothermal or co-precipitation method attracts much attention. These methods constitute an environment-friendly medium for syntheses contrary to solid state methods, which need relatively high processing temperature (above 1100 °C).

Aurivillius phases have the general formula $(\text{Bi}_2\text{O}_2)^{2+}(\text{A}_{n-1}\text{B}_n\text{O}_{3n+1})^{2-}$, where $n=1-8$, A stands for a divalent cation (*e. g.* Ca^{2+} , Ba^{2+}), B for a tetravalent or pentavalent ion (*e. g.* Nb^{5+} , Ti^{4+}) and form a perovskite block $\text{A}_{n-1}\text{B}_n\text{O}_{3n+1}$ [1]. The bismuth-titanium oxide $\text{Bi}_4\text{Ti}_3\text{O}_{12}$ belongs to this family with $\text{A}=\text{Sr}$, $\text{B}=\text{Ti}$ and $n=3$. The bismuth layer-structured ferroelectric materials have attracted increasing attention for non-volatile ferroelectric random access memory (FeRAM) applications [2][3].

$\text{Bi}_4\text{Ti}_3\text{O}_{12}$ compounds have been prepared by various methods, which require more or less higher temperatures to be achieved. Preparation of powders by conventional processing, *i. e.* solid state reaction method (sintering temperature $\sim 1150^\circ\text{C}$ [4]), often leads to commotional and structural inhomogeneities in the produced ceramics. However, a sol-gel technology has been used to prepare $\text{Bi}_4\text{Ti}_3\text{O}_{12}$ nanopowders at $\sim 900^\circ\text{C}$ [5]. A hydrothermal method has been developed for the synthesis of $\text{Bi}_4\text{Ti}_3\text{O}_{12}$ powder without treatment at high temperature [6,7].

To our knowledge, practical physical issues such as the structure-property relationship and the

physical nature leading to the change of the properties for $\text{Bi}_4\text{Ti}_3\text{O}_{12}$ ceramics are not resolved, and from the viewpoint of physics there is lack of novelty. In this regard, this paper describes a novel method for synthesizing bismuth-titanium oxide. The effect of heat on sample' microstructure morphology was studied by XRD, FTIR and SEM.

EXPERIMENTAL

The details of the sol-gel process used to prepare the appropriate alkoxide solution of bismuth and titanate have been published elsewhere [8,9]. A flowchart of the sol-gel procedure used is shown in Fig. 1. Stoichiometric amounts of a bismuth (III) acetate (Alfa, 99%) aqueous solution and a titanium (IV) isopropoxide (Sigma-Aldrich, 97%) solution stabilized by acetylacetone to form a titanium solution were mixed, and then dried to obtain a gel.

For hydrothermal treatment, the gel was kept under stirring in a solution of KOH (1 M) for 1 h, and then put into an autoclave (filling ratio above 80%) and heated at 180 °C for 12 h. After filtration and drying, the sample was thermally treated at 400 °C and 600 °C for 24 h.

The formation and quality of the powder were verified by X-ray diffraction (Philips X'Pert Pro). IR spectrum of the prepared powder at 600 °C was recorded on a Bruker, Vertex 70 DTGS FT-IR instrument using KBr pellet technique. Microstructure studies were performed by scanning electron microscopy with 10 kV of accelerating voltage at high vacuum.

*To whom all correspondence should be sent:

E-Mail: mohamed.afqir@yahoo.fr

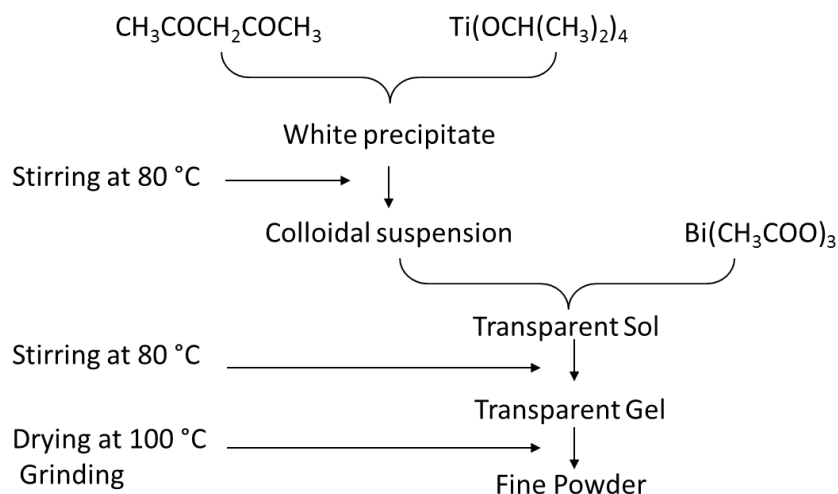


Fig. 1. Flowchart for preparation of powder by a sol-gel procedure.

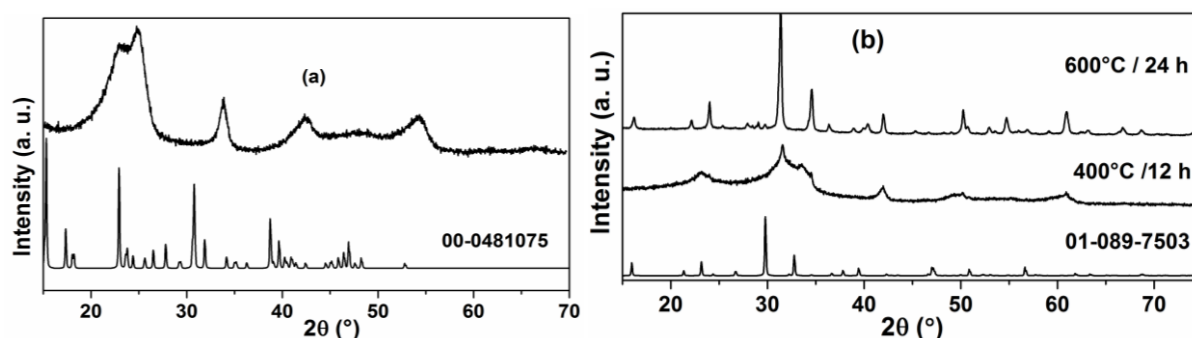


Fig. 2. XRD patterns of $\text{Bi}_4\text{Ti}_3\text{O}_{12}$ without (a) and with hydrothermal treatment (b).

RESULTS AND DISCUSSION

Fig. 2 shows the X-ray diffraction patterns of dry gel (a) and ceramic powders obtained by hydrothermal treatment (b) of $\text{Bi}_4\text{Ti}_3\text{O}_{12}$. The XRD peaks were identified as bismuth acetate for the precursor gel before the hydrothermal treatment, according to the standard pattern $\text{Bi}(\text{CH}_3\text{COO})_2$ (00-048-1075) (Fig. 2a).

The hydrothermally synthesized ceramic powders from the precursor gel at 400 °C during 12 h were still quite amorphous, as expected. The XRD peaks became notably narrower with an annealing temperature of 600 °C for 24 h, indicating that this sample can be indexed using JCPDS-ICDD pattern number 01-089-7503 corresponding to $\text{Bi}_4\text{Ti}_3\text{O}_{12}$ tetragonal symmetry (space group $A2_1am$). As it can be seen from figure 3b, the XRD curves extracted using HighScore software of the sample annealed at 600 °C are remarkably similar to those obtained from the JCPDS-ICDD. However, the mismatch between the reference and experimental patterns is bigger than 0.05 2 θ . This mismatch in peak positions may be explained by inaccuracies in the fitting software, offering inefficient curve fitting.

The average size for the sample sintered at 600 °C was estimated using Scherrer's formula:

$$D = \frac{0.9\lambda}{\beta \cos\theta} \quad (1)$$

where D is the crystallite size, λ the $\text{CuK}\alpha$ wavelength (1.5406 Å) and β the full width at half maximum (FWHM) [10], which was found to be 40 nm.

Fig. 3 shows the FTIR spectrum of the ceramic powder sintered at 600 °C. The bands at 3440 cm^{-1} and 1633 cm^{-1} are due to water molecules. The bands located at 23870 cm^{-1} can be attributed to CO_2 . The bands at 2853 cm^{-1} and 2929 cm^{-1} indicate the presence of residual organics. The band range 500-820 cm^{-1} and the band at 936 cm^{-1} are related to the crystallization of the phase $\text{Bi}_4\text{Ti}_3\text{O}_{12}$ [6-7]. The SEM micrographs of $\text{Bi}_4\text{Ti}_3\text{O}_{12}$ ceramic are shown in Fig. 4. The tow images taken at different locations, consist of plate-like and rod-like grains with random distribution comparing to plate-like morphology which is characteristic of the Aurivillius type [10-13]. The obtained samples are micro- to nanograined and contain, therefore, very developed grain boundaries and free surfaces. It has been recently demonstrated that the physical

properties of pure and doped fine-grained oxides strongly depend on the presence of defects like interphase boundaries and grain boundaries [14,15].

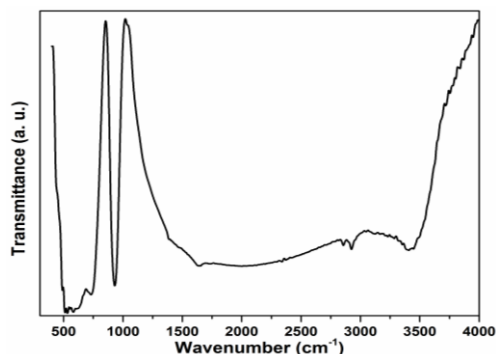


Fig. 3. FTIR micrograph of $\text{Bi}_4\text{Ti}_3\text{O}_{12}$ ceramic powder.

There is a high degree of inhomogeneity in size and shape of grains, and the average particle size is $1\ \mu\text{m} - 0.2\ \mu\text{m}$. Thus, the hybrid hydrothermal – co-precipitation process can be used for manufacturing ultrafine-grained materials, differently from the solid-state method, which shows microcrystalline grains of plate-like shape.

The crystallite size (40 nm) estimated from XRD data does not correlate with the size of the grains, observed in the SEM image. Though, both XRD and SEM show nanoscale particle size. However, up-micro and the boundary of the particle are not proven so far by XRD [16].

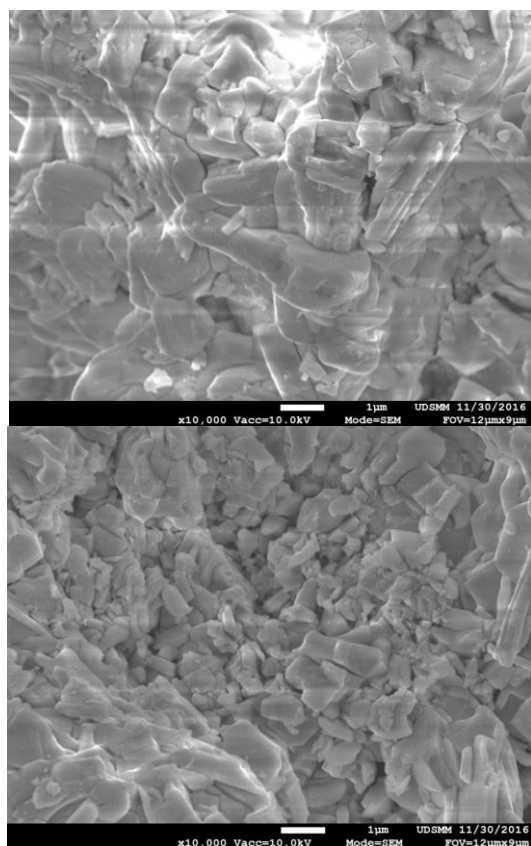


Fig. 4. SEM micrographs of $\text{Bi}_4\text{Ti}_3\text{O}_{12}$ ceramic.

CONCLUSION

The mentioned method was already used for other oxide powders preparation, but we presented a new version. After hydrothermal treatment the powder was still amorphous and supplementary thermal treatment at 400 and finally at 600 °C was required. This process seems to afford a means of environmentally friendly and inexpensive aqueous synthesis.

REFERENCES

1. E. P. Kharitonova V. I. Voronkova, *Inorg. Mater.* **43**, 1340 (2007).
2. T. Takenaka, *Piezoelectric Acoust. Mater. Transducer Appl.* 103 (2008).
3. P. H. Pang, C. R. Robbins, B. Aurivillius, *Phys. Rev.* **126**, 1957 (1962).
4. Y. Chen, S. Xie, H. Wang, Q. Chen, Q. Wang, J. Zhu, Z. Guan, *J. Alloys Compd.* **696**, 746 (2017).
5. C. Ma, X. Lin, L. Wang, Y. Yan, *Adv. Mater. Res.* **997**, 359 (2014).
6. D. Chen X. Jiao, *Mater. Res. Bull.* **36**, 355 (2001).
7. Z. Chen, Y. Yu, J. Hu, A. Shui, X. He, *J. Ceram. Soc. Japan* **117**, 264 (2009).
8. X. Du, Y. Xu, J. Wang, X. Li, *J. Am. Ceram. Soc.* **90**, 1382 (2007).
9. A. V. P. Rao, A. I. Robin, S. Komarneni, *Mater. Lett.* **28**, 469 (1996).
10. R. Singh, V. Luthra, R. S. Rawat, R. Tandon, *Ceram. Int.* **41**, 4468 (2015).
11. P. Fang, Z. Xi, W. Long, X. Li, S. Qiu, *J. Sol-Gel Sci. Technol.* **71**, 241 (2014).
12. T. Jardiel, A. Caballero, M. Villegas, *J. Ceram. Soc. Japan* **116**, 511 (2008).
13. X. Tian, S. Qu, Y. Zhou, B. Xu, Z. Xu, *J. Inorg. Organomet. Polym. Mater.* **23**, 877 (2013).
14. B. B. Straumal, A. A. Mazilkin, S. G. Protasova, S. V. Stakhanova, P. B. Straumal, M. F. Bulatov, G. Schutz, T. Tietze, E. Goering, B. Baretzky, *Rev. Adv. Mater. Sci.* **41**, 61 (2015).
15. B. B. Straumal, S. G. Protasova, A. A. Mazilkin, E. Goering, G. Schütz, P. B. Straumal, B. Baretzky, *Beilstein J. Nanotechnol.* **7**, 1936 (2016).
16. M. Afqir, A. Tachafine, D. Fasquelle, M. Elaati, J. C. Carru, A. Zegzouti, M. Daoud, *Mater. Lett.* **205**, 178 (2017).

ЗОЛ-ГЕЛ ХИДРОТЕРМАЛНО ПОЛУЧАВАНЕ НА Bi₄Ti₃O₁₂ КЕРАМИКА

М. Афкир^{1,2*}, А. Ташафин², Д. Фаскел², М. Елатмани¹, Ж.-С. Карю², А. Зегзуги¹, М. Дауд¹

¹ *Лаборатория по изследвания на неорганични материали и техните приложения, Научен факултет Семлалия, Университет „Кади Аяд”, Маракеш, Мароко*

² *Отдел по динамика и структура на молекулни материали, Университет на Литорал-Кот д'опал, Кале, Франция*

Постъпила на 28 ноеври, 2017 г.; коригирана на 15 май, 2018 г.

(Резюме)

Представен е модифициран зол-гел метод за получаване на Bi₄Ti₃O₁₂ керамичен прах с последваща хидротермална обработка на получения гел. Бисмутов ацетат и титанов изопропоксид са използвани като източници на металите за получаване на прекурсорния гел, който успешно е превърнат в бисмут-титанов оксид чрез хидротермална обработка при 400 °С и 600 °С за 24 h. Продуктът е охарактеризиран посредством XRD, FTIR, SEM за определяне на неговите свойства и структурни характеристики.

A metal-organic framework of Co(II): synthesis and supercapacitive properties

H. L. Bai^{1,3}, F. L. Meng², Y. Fan^{3*}, P. Zhang^{3*}

¹College of Chemistry, Changchun Normal University, Changchun, 130032, Jilin, P. R. China

²Institute of Agricultural Quality Standard and Testing Technology, Jilin Academy of Agricultural Sciences, Changchun, 130033, Jilin, P. R. China

³College of Chemistry, Jilin University, Changchun, 130012, Jilin, P. R. China

Received November 11, 2017; Accepted March 7, 2018

A metal-organic framework based on pytpy and H4abtc as secondary ligands, namely Co₂(pytpy)(abtc)₂ was solvothermally synthesized and structurally characterized. The supercapacitive behavior of MOFs was determined. There are reduction and oxidation peaks when cyclic voltammetry is performed at different scan rates, which shows typical faradic redox characteristics. The specific capacitances slowly decrease along with the increase in scan rates, which signifies that the material has a good high-rate capability. The results show that the loss of specific capacitance of Co-MOF is not remarkable and it has an excellent cycle life after 1000 cycles test.

Keywords: Metal-organic framework; Supercapacitive properties; Co(II)

INTRODUCTION

At present, there are a lot of materials based on carbon and transition metal oxides which are mainly used as supercapacitor materials. MOF material is prospectful to be applied in a supercapacitor, because its porosity provides a larger number of active sites, which is beneficial to the penetration of the electrolyte and the ion transport [1,2]. Recently, some MOFs of cobalt and nickel have been reported as supercapacitor electrode materials [3-8], and there are several teams which have investigated on this topic in our country [9-13], but the specific capacitance values of overall MOF materials as supercapacitor electrode materials need to be improved. In addition, due to the low stability and poor electrical conductivity of MOF materials, direct reports on using MOF materials in supercapacitor electrode materials are very limited. In this paper, we used pytpy and H4abtc ligands to synthesize a new MOF under solvothermal conditions, and analyzed the structure of the compound, which determines the supercapacitor properties of the compound.

EXPERIMENTAL

Materials and Methods

All starting materials were of analytical grade and were used as received without further purification. Powder X-ray diffraction (PXRD) data were recorded on a Rigaku D/M-2200T automated diffractometer. Electrochemical properties were determined in a CHI 760D electrochemical workstation.

Co₂(pytpy)(abtc)₂ (1): A mixture of HNO₃/DMA was prepared by mixing 2.2 mL of HNO₃ and 10 mL of DMA in a 20 mL vial, and was ultrasonicated for 5 min. Compound 1 was prepared by solvothermal reaction of Co(NO₃)₂·6H₂O (11.6 mg, 0.04 mmol), pytpy (12.4 mg, 0.04 mmol), H₄abtc (14.3 mg, 0.04 mmol), DMA (0.5 mL), ethanol (0.5 mL), H₂O (0.5 mL), HNO₃/DMA (0.2 mL) at 100°C for 3 days. The mixture was sealed with tin foil paper in a 20 mL vial. After gradually being cooled to room temperature colorless crystals of 1 were obtained.

X-ray Crystallography

Single-crystal XRD data for compound 1 were recorded on a Bruker Apex II diffractometer with graphite monochromatized Mo K α radiation ($\lambda = 0.71073 \text{ \AA}$) at 285(2) K. Absorption corrections were applied by using multiscan technique. All structures were solved by the direct method of SHELXS-97 and refined by the full-matrix least-squares technique using the SHELXL-97 program within WINGX. No-hydrogen atoms were refined with anisotropic temperature parameters. The hydrogen atoms of the organic ligands were refined as rigid groups. The detailed crystal data and structure refinement parameters for the compound 1 are summarized in Table 1.

RESULTS AND DISCUSSION

Structure of [Ca₂(BTEC)(DMF)(H₂O)₃] (1)

Compound 1 crystallizes in triclinic crystal system of *P*-1. In the asymmetric unit there are two crystallographically unique Co(II) atoms, two pytpy

* To whom all correspondence should be sent:

E-mail: baihelong2000@126.com

anions and a H₄abtc ligand (Fig. 1). In the asymmetric unit, the two metal centers Co1 and Co2 are not in the same environment. Coordination mode of H₄abtc ligand is different. Some oxygen atoms in the carboxyl have monofunctional coordination. Some oxygen atoms in the carboxyl have chelated coordination. Some oxygen atoms in the carboxyl are in the form of O, O. The Co1 atom is coordinated by four oxygen atoms from two H₄abtc ligands, two nitrogen atoms from two different H₄abtc ligands and two nitrogen atoms from two different pytpy ligands. The Co2 atom is the same as the Co1 atom, but the direction of the pyridine ring which connects nitrogen atom is opposite. Both Co1 and Co2 anions are connected by H₄abtc ligands in the *ab* plane extended into a 2D layer structure (Fig. 2). Each 2D layer structure is connected by a pytpy ligand extended into a 3D framework (Fig. 3), which shows the 3D framework in the *x* plane for 1 (Fig. 4).

PXRD Analysis

Fig. 5 shows the simulated and experimental PXRD patterns of compound 1. The experimental peak positions match well to the simulation of the single crystal data, and the results indicate that the synthesized compound is of good phase purity.

Table 1. Crystal data and structure refinement for the compound 1

Compound	1
Empirical formula	C ₅₆ H ₃₄ Co ₂ N ₁₀ O ₈
Formula weight (g/mol)	1092.79
Temperature (K)	296(2) K
Crystal system	Triclinic
Space group	P-1
a (Å)	13.646(3)
b (Å)	16.705(3)
c (Å)	16.783(3)
α (°)	100.01(3)
β (°)	103.30(3)
γ (°)	108.23(3)
V (Å ³)	3409.0
Z	2
Calculated density (g/cm ³)	1.065
Absorption coefficient (mm ⁻¹)	1.408
Theta range for data collection (°)	3.17-27.43
	-7<=h<=8
Limiting indices	-27<=k<=27
	-17<=l<=17
F(000)	1116
Reflections collected	24245
Completeness	99.1 %
Data/restraints/parameters	4167/0/266
Goodness-of-fit on F ²	1.054
R1a/wR2b [I>2σ(I)]	0.0768/0.2492
R1/wR2 (all data)	0.1127/0.2829
Largest diff. peak and hole (e ⁻ ·Å ⁻³)	0.796/-0.443

$${}^a R_1 = \frac{\sum ||F_o| - |F_c||}{\sum |F_o|} \quad {}^b wR_2 = \frac{\sum [w(F_o^2 - F_c^2)]}{\sum [w(F_o^2)]^{1/2}}$$

$${}^b wR_2 = \frac{\sum [w(F_o^2 - F_c^2)]}{\sum [w(F_o^2)]^{1/2}}$$

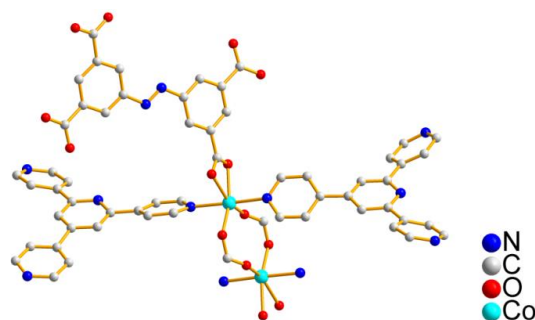


Fig. 1. Coordination environment of Co(II) atom in 1

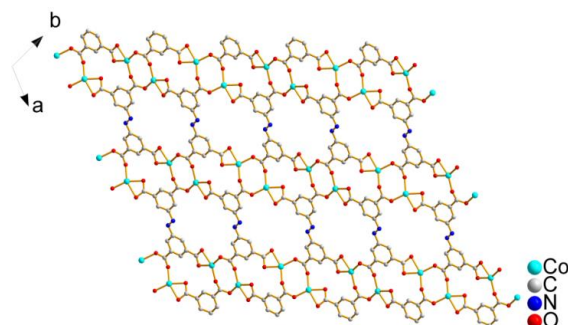


Fig. 2. View of 2D planar layer in the *ab* plane

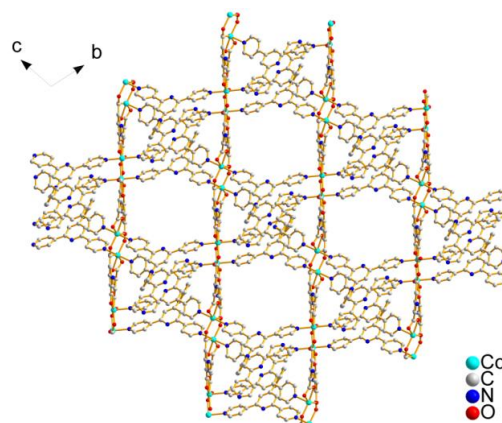


Fig. 3. Perspective view of the 3D framework for 1

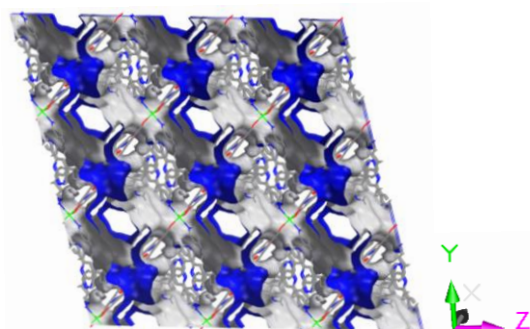


Fig. 4. View of the 3D framework in the *x* plane for 1

All electrochemical experiments were performed according to the standard three-electrode system at room temperature. The saturated calomel

electrode was the reference electrode and the platinum electrode – the auxiliary electrode. For working electrode, a mixture containing 80% of active substance, 10% of acetylene black and 10% of polyvinylidene fluoride was mixed well, and a suspension made from N-methyl-2-pyrrolidone (Aldrich) was smeared on the nickel foam current collector (1 cm × 1 cm), and dried at 100 °C for 10 h. Cyclic voltammetry (CV) and galvanostatic charge-discharge (GC) were performed on an electrochemical workstation (CHI 760D).

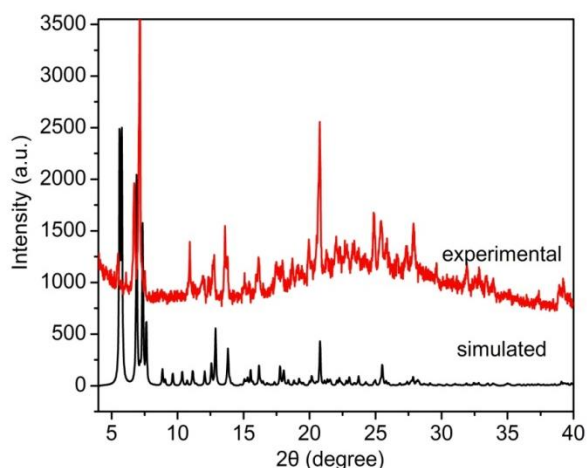


Fig. 5. Simulated and experimental XRPD patterns for 1

Fig. 6 shows the cyclic voltammetry (CV) curves of the Co-MOF electrode at various scan rates (5~50 mVs⁻¹). As depicted in Fig. 6, it clearly exhibits a couple of redox peaks at +0.33V (oxidation) and +0.23V (reduction) at a low scan rate of 5 mV s⁻¹, indicating that the pseudocapacitive behavior resulted from the surface faradic redox reactions. Electrochemical capacitor properties of Co₂(pytpy)(abtc)₂ may be due to Faraday redox reaction of Co(II) ion in the framework (Co²⁺/Co³⁺), and OH⁻ of alkaline electrolyte may be mediated. Similar to most of the capacitor electrode materials, the symmetry of the scan curve of the cyclic voltammetry is good between positive and negative, which indicates that the electrode material has reversibility and good capacitance characteristics. With the increase in scan rate, the potential of the anodic peak gradually increases and the cathodic peak gradually decreases, which shows that the electrode material has good rate capability. The galvanostatic charge-discharge curves at different current density are shown in Fig. 7. As can be seen, the curve shape of charge and discharge is very similar, and there are potential platforms. It shows the typical pseudocapacitor characteristic, which is consistent with the cyclic voltammetry curve. According to Fig. 7 we can calculate the specific capacitance at different current densities. The specific capacitance of the activated crystalline electrode is 101.65, 94.19, 88.19, 79.52, 74.55 and 72.06 F g⁻¹ when the

current density is 0.5, 1, 2, 4, 6 and 8 A g⁻¹, respectively.

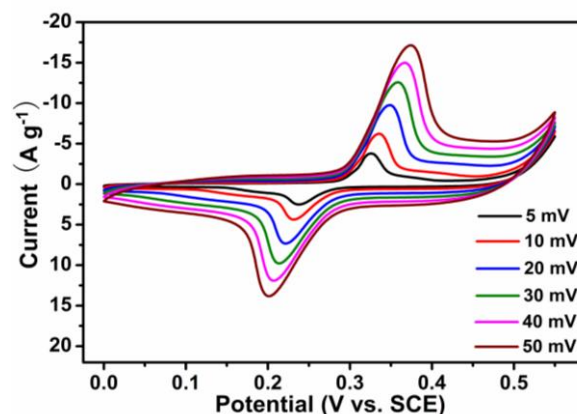


Fig. 6. Cyclic voltammetry curves at different scan rates

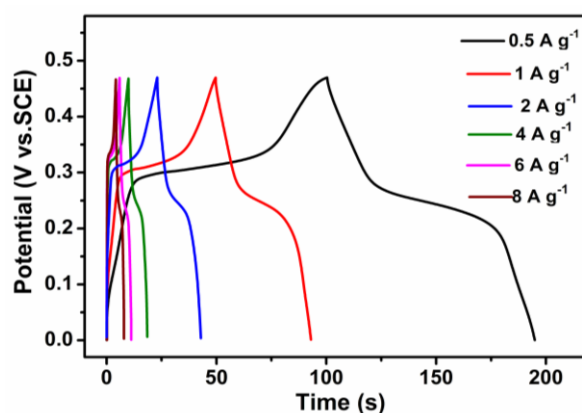


Fig. 7. Galvanostatic charge-discharge curves at different current densities

We obtained the curve of the specific capacitance of electrode as a function of the change in current density (Fig. 8). It can be seen from the figure that the specific capacitance slowly descends with current density decrease, the electrode materials have good rate capability. In addition, its value is similar to some typical supercapacitors of cobalt oxide, such as CoMoO₄ nanorods (62.8 F g⁻¹/1 A g⁻¹), MnMoO₄ nanorods (9.7 F g⁻¹/1 A g⁻¹) [11], but not as good as the supercapacitor of NiO@ CoMoO₄ nanomaterials [12] and the electrode of CoMoO₄-3D graphene hybrid (NSCGH) [13]. It is the key factor that cycle life of supercapacitor applies to practice. It was found that the capacitance retention was kept at 78% of its highest value after 1000 cycles, indicating that this kind of Co-based MOF material not only has large specific capacitance and good rate capability but also has excellent cycling stability (Fig. 9). This might be attributed to the fact that the charge transfer resistance slightly increased after long cycles. The results showed that the compound 1 has a good application prospect as a supercapacitor electrode material.

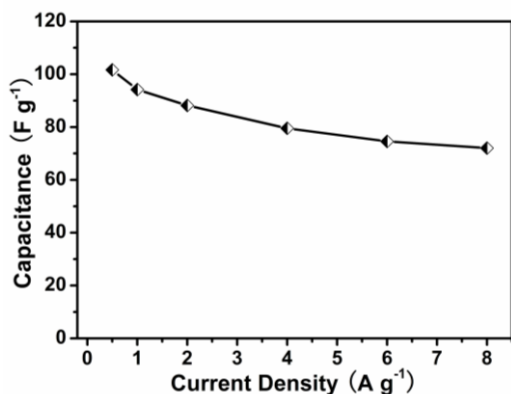


Fig. 8. Curve of specific capacitance change along with the current density

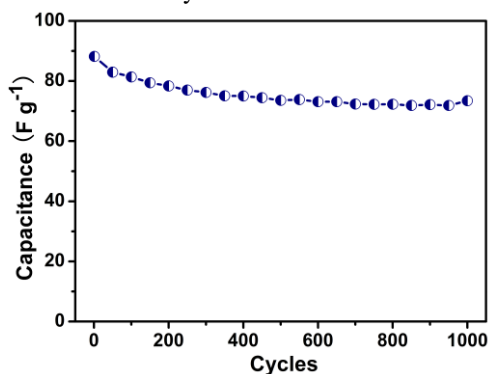


Fig. 9. Curve of cycling stability in 2 A g⁻¹

CONCLUSION

We used pytpy and H₄abtc ligand to synthesize a new MOF under solvothermal conditions. The structure and supercapacitive behavior were characterized.

Reduction and oxidation peaks are observed when cyclic voltammetry is performed at different scan rates, which show typical faradic redox characteristics. The specific capacitance slowly decreases along with the increase in scan rate, which means that the material has a good high-rate capability. The results show that the loss of specific

capacitance (Co-MOF) is not remarkable and the sample has excellent cycle life after 1000 cycles test.

Acknowledgements: The authors gratefully acknowledge the financial support of the Natural Science Foundation of China (Grant No. 21301009); the Science & Technology Foundation of Henan Province (15A150031) and the Science & Technology Foundation of Jilin Province (20170520029JH).

REFERENCES

1. F.S. Ke, Y.S. Wu, H.X. Deng, *Journal of Solid State Chemistry*, **223**,109 (2015).
2. L.Wang, Y. Han, X. Feng, *Coordination Chemistry Reviews*, **307**, 361 (2016).
3. J.Yang, P.Xiong, C. Zheng, *J. Mater. Chem. A*, **2**,16640 (2014).
4. Z.F. Wang, C.W. Gao, Y.S. Liu, *Materials Letters*, **193**, 216 (2017).
5. R. Díaz, M.G. Orcajo, J.A. Botas, *Materials Letters*, **68**,126 (2012).
6. L.Y. Chen, Q. Zhang, H. Xu, *J. Mater. Chem. A*, **3**,1847 (2015).
7. K.M. Choi, H.M. Jeong, J.H. Park, *ACS Nano*, **8**,7451 (2014).
8. X.X. Liu, C.D. Shi, C.W. Zhai, *ACS Appl. Mater. Interfaces*, **8**, 4585 (2016).
9. Y. Jiao, J. Pei, D.H. Chen, *J. Mater. Chem. A*, **5**, 1094 (2017).
10. M. Du, E. Csanudo, E. Jimenez, *J. Mater. Chem. A*, **2**, 9828 (2014).
11. L. Wang, X. Feng, L. Ren, *J. Am. Chem. Soc.*,**137**, 4920(2015).
12. J. Yang, P.X. Xiong, C. Zheng, *J. Mater. Chem. A*, **2**,16640 (2014).
13. J. Yang, Z.H. Ma, W.X. Gao, M.D. Wei, *Chem. Eur. J.*, **23**, 631 (2017).

МЕТАЛ-ОРГАНИЧНА МРЕЖА НА Co(II): СИНТЕЗ И СУПЕРКАПАЦИТИВНИ СВОЙСТВА

Х. Л. Бай^{1,3}, Ф. Л. Менг², Й. Фан^{3*}, П. Жанг^{3*}

¹ Колеж по химия, Чангчунски университет, Чангчун, 130032, Джилин, Н. Р. Китай

² Институт по стандарти за качество на селскостопанска продукция и технологии за проверка, Джилинска академия по селскостопански науки, Чангчун, 130033, Джилин, Н. Р. Китай

Постъпила на 11 ноември, 2017 г.; приета на 7 март, 2018 г.

(Резюме)

Метал-органична мрежа Co₂(pytpy)(abtc), основаваща се на pytpy и H₄abtc₂ като вторични лиганди, е синтезирана солвотермично, охарактеризирана е структурно и са определени суперкапацитивните свойства на MOF. При циклична волтаперометрия с различни скорости на сканиране се наблюдава редукционен и окислителен пик, които са с типични фарадееви редокс характеристики. Специфичният капацитет бавно намалява с нарастването на скоростта на сканиране, което свидетелства за добрите отнасяния на материала при високи скорости. Установено е, че загубата на специфичен капацитет на Co-MOF не е съществена и материалът има отлични показатели след 1000 цикъла.

Promotional effect of Au on γ -Al₂O₃ supported cobalt based catalyst for total oxidation of methane

M. Kumar^{1,2*}, G. Rattan¹, R. Prasad³

¹Dr. S. S. Bhatnagar University Institute of Chemical Engineering & Technology, Panjab University, Chandigarh 160014, India

²Department of Chemical Engineering, Chandigarh University, Mohali, Punjab, India

³Department of Chemical Engineering, IIT-BHU, Varanasi, U.P, India

Received November 13, 2017; Revised February 16, 2018,

Effect of gold loading (within the range of 4 mass % - 16 mass %) on the behavior of the catalyst (Co/ γ -Al₂O₃) for CH₄ oxidation is studied. Gold promoted CoO_x/ γ -Al₂O₃ catalysts were prepared *via* deposition precipitation method and calcined at 550°C. A significant improvement in activity was observed (T_{100%}=380 °C) toward CH₄ oxidation with increase in gold loading, though a plateau was reached at ca. 13.45 wt. % Au content. The catalytic activity is studied on a fixed catalyst weight (500 mg) in an air flow containing 1 % of CH₄ introduced to the reactor at a total feed rate of 150 mL/min. The catalyst characterization is done using XRD, TGA/DSC and SEM. The best catalysts according to the catalytic activity obtained are as follows: Au (13.45>10.44>16.27>07.21>04.06>0 wt. %)-CoO_x/ γ -Al₂O₃. It is found that the catalyst containing 13.45 wt. % of Au loaded on 18 wt. % Co/ γ -Al₂O₃ is the most active catalyst as it decreases the temperature (T_{100%}=380 °C) by 110°C required for methane oxidation in comparison to the catalyst that does not contain gold, i.e., 18wt.%Co/ γ -Al₂O₃ (T_{100%}=490 °C).

Keywords: Methane, Oxidation, Catalysts, Gold, Cobalt, Alumina

INTRODUCTION

With the exponential growth of vehicles on road, fossil fuels have led to an alarming level of exploitation. Thus the need arises for substitution of both, the vehicles and the fuel in pursuit of green and clean environment. In comparison to gasoline and diesel, compressed natural gas (CNG) as a fuel is an attractive choice with significant environmental advantages as it is available in abundance, is cheaper and highly efficient.

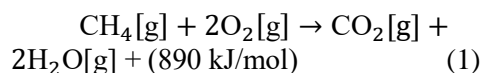
According to Jahirul *et al.* [1] it suitably mixes with air and burns effectively, due to its high octane number, engine operates smoothly without knocking, the formation of non-methane hydrocarbons and other air pollutants in CNG fueled engines is one-tenth of that in gasoline engines. The formation of CO and NO_x is by 80% lower than in gasoline engines because of the simple chemical structure of compressed natural gas (primarily CH₄), it contains single carbon in comparison to diesel (C₁₅H₃₂) and gasoline (C₈H₁₈). In terms of economy CNG fueled engines are by 20% more economical than gasoline and diesel engines [2].

However, the inevitable methane emission from vehicles using CNG as the fuel has a very harmful effect on the environment, as methane is a potent greenhouse gas and its global warming potential is 21 times that of CO₂ at equivalent emissions [3,

27].

Further, compared to low-emitting diesel, the CNG exhaust has higher levels of six toxic air contaminants (TAC) listed by the California Air Resources Board (ARB), namely: acetaldehyde, acrolein, benzene, formaldehyde, methyl ethyl ketone, and propionaldehyde. Formaldehyde emission is very high with CNG vehicles. It is also classified as a toxic air contaminant and is known as carcinogenic [4].

Therefore, the challenge before the researchers around the globe is to abate harmful chemicals from CNG exhaust, especially methane emission. This task can be achieved with the help of a catalytic convertor [5] fitted before the exhaust of vehicle. The convertor has the properties of reducing harmful chemicals to less harmful chemicals (CO₂, H₂O). The oxidation and reduction reactions take place due to the catalyst present on the interior of the surface of convertor. Catalyst present in the interior oxidizes the unburnt methane from vehicular exhaust and converts it into less harmful products (Eq. 1).



Gold based catalysts have been studied by numerous researchers for oxidation of methane. Numerous PhD degrees have been awarded [6], various patents have been granted [7-8], a number of research [9-16] and review [17-19] articles has been published on gold based catalysts for methane

* To whom all correspondence should be sent:
E-mail: maninderbhatoy@gmail.com

M. Kumar et al.: Promotional effect of Au on γ -Al₂O₃ supported cobalt based catalyst for total oxidation of methane oxidation/combustion reactions.

EXPERIMENTAL

Catalyst preparation

Table 1 depicts some of the advances made on gold based catalysts and is strictly devoted to gold based catalysts. A number of conclusions can be drawn from this table such as preparation methods of the catalyst, type of the reactor used, amount of catalyst used for reaction, flow conditions and at last but not least the T_{100%} which denotes the temperature required for 100% conversion of methane. It is interesting to note that from all the reported work, the minimum temperature for 100% conversion of CH₄ is 350 °C [12] and the maximum hovers around 680 °C [20]. However, all the other works report an average temperature of 500 °C. Keeping in view the literature accumulated it was observed that the combination of gold, cobalt and γ -alumina has not been investigated over the whole composition range. Hence, the present work is devoted to the promotional effect of gold on alumina supported cobalt based catalyst.

The Au-Co/ γ -Al₂O₃ mixed oxide catalysts were prepared by a deposition precipitation method [5]. All chemicals used were of analytical grade (AR). Stoichiometric amount of gold (HAuCl₄) and cobalt (Co(NO₃)₂·6H₂O) salts were first dissolved in doubly distilled water followed by addition of γ -alumina powder. The formed suspension was stirred vigorously at 70°C. Sodium carbonate solution was added dropwise to this suspension maintaining pH of 7, hence the formation of precipitates takes place. The precipitate was washed several times with deionized water. The formed solid was heated overnight in an oven at 110 °C. Further it was pressed (mortar and pestle) and finally the fine powder was calcined at 550 °C for 4 h.

Table 1. Parameters in some publications related to gold based catalysts

Catalyst, Prepn. Method	Exp. Operating Parameters	Remark	Reference
Au/Co ₃ O ₄ -CeO ₂ Co-precipitation, Calc. temp. 600 °C.	50 mg, U-shaped quartz, 0.3 vol.% CH ₄ , 2.4 vol.% O ₂ in He. WHSV=60,000 mL/ gh.	AuCo ₃ O ₄ T _{100%} =550°C.	[11]
Au/CoO _x , Au/MnO _x Co-precipitation, Calc. temp. 400 °C	50 mg, fixed-bed S. S. tubular flow, 50 mL/min, GHSV = 15,000 h ⁻¹ , alkane/air (molar ratio) of 0.5/99.5	Au/CoO _x T _{100%} = 350 °C.	[12]
Au/MgO, Impregnation, Calc. temp. 850 °C.	200 mg, microreactor of quartz glass, CH ₄ (46%, O ₂ 8%, He 46%. GHSV=750 h ⁻¹ .	Enhanced activity when gold was employed	[21]
Au-Pt/Co ₃ O ₄ Co-precipitation technique Calc. temp. 400 °C.	0.10 g, fixed-bed microreactor, 1 vol.% CH ₄ , 5 vol.% O ₂ , and rest N ₂ , space velocity of 10,000 h ⁻¹	Activity of Au/Co ₃ O ₄ enhanced when Pt, e.g. 0.2 wt.% was added, and conv. temp. decreased by 50°C.	[22]
Au/MO _x /Al ₂ O ₃ where M is Cr, Mn, Fe, Co, Ni, Cu, and Zn, Homogeneous deposition precipitation, Calc. temp. 400 °C	Lab-scale fixed-bed, 0.8 vol.% CH ₄ and 3.2 vol.% O ₂ in He, 30 mL/min.	Au/Al ₂ O ₃ T _{100%} = 655°C	[23]
Au/TiO ₂ , Au/SiO ₂ , Au/CeO ₂ , Au/ZrO ₂ , Au/Al ₂ O ₃ , Deposition precipitation, Calc. temp. 400 °C	Quartz tubular fixed bed, 50 mL/min. (20% CH ₄ and 5% O ₂ , rest is He).	Au/TiO ₂ T _{80%} = 400°C, Au/Al ₂ O ₃ T _{20%} =400°C.	[10]
Au/Fe ₂ O ₃ Deposition precipitation	0.1 g, fixed-bed quartz, 1 vol.% CH ₄ in air, flow rate=100 mL/min, GHSV = 51,000 h ⁻¹ .	Au/Fe ₂ O ₃ prep. by HDP T _{50%} =375°C, T _{100%} =500°C.	[24]
AuO _x /Ce _{0.6} Zr _{0.3} Y _{0.1} O ₂ Co-precipitation, Calc. temp. 700 °C	0.12 mg, quartz fixed-bed microreactor, 5% CH ₄ /95% He (v/v, 40 mL/min) + O ₂ (8 mL/min) + He (52 mL/min), SV= 50,000 h ⁻¹ .	Catalyst with 6% AuO _x T _{50%} =590°C T _{100%} =680°C	[20]

Table 2. Composition of gold on different catalysts with catalyst ID.

Catalyst ID	G50	G51	G52	G53	G54	G55
Gold (wt.%)	00.00	04.06	07.21	10.44	13.45	16.27
Co:Au	5:0	5:1	5:2	5:3	5:4	5:5

Au-CoO_x/ γ -Al₂O₃ samples contained {00.00, 04.06, 07.21, 10.44, 13.45, 16.27 wt. % Au} and {18 wt.% Co}. The compositions of gold and cobalt are expressed in weight percent throughout the paper and are also presented in Table 2, each catalyst having a unique ID. The resulting powder was finally stored in air-tight triplex vials for further experiments and characterization.

Catalytic Activity Measurement

The catalytic activities of all prepared catalysts (Table 2) towards methane oxidation were tested in a compact scale fixed-bed, down-flow tubular reactor [5]. The reactor was placed vertically in a split open furnace. 500 mg of the catalyst was diluted with 1 ml of alumina and placed in the reactor. The reactant gas mixture consisted of 1% CH₄ in air maintaining a total flow rate of 150 mL/min, corresponding to a WHSV about 36000 mLh⁻¹g⁻¹. The reaction was carried out in temperature range of ambient to a temperature at which 100% CH₄ conversion was attained. It was also ensured that the gas does not contain any moisture or CO₂ by passing it through CaO and KOH pellet drying towers. Digital flow meters were used for measuring the flow rate of both methane and air. The catalytic experiments were carried out under steady-state conditions. The steady-state temperature was controlled with the help of a microprocessor-based temperature controller with precision of $\pm 0.5^\circ\text{C}$. The products and reactants were analyzed by means of an online gas chromatograph (Nucon 5765) using a Porapak Q-column, methaniser and FID detector for the concentrations of CH₄ and CO₂. The fractional conversion of methane was calculated on the basis of the values of concentration of CH₄ in the product stream using Eq. (2). Only one chromatogram peaks corresponding to CH₄ was recorded for inlet, whereas the chromatogram of reactor outlet gases contains an additional peak of CO₂ with unreacted CH₄.

$$X_{CH_4} = \left\{ |C_{CH_4}|_{in} - |C_{CH_4}|_{out} \right\}_i / |C_{CH_4}|_{in} \quad (2)$$

where the change in concentration of CH₄ due to oxidation at any instant $\left\{ |C_{CH_4}|_{in} - |C_{CH_4}|_{out} \right\}_i$ is proportional to the decrease in the area of the chromatogram of CH₄ at that instant. Experimental

data were collected at every measurement point after stabilizing for 20 min.

Catalyst Characterization

Characterization of the catalysts was done by XRD (X-Ray Diffraction), TGA/DSC (thermo gravimetric analysis) and SEM (scanning electron microscopy). XRD pattern was recorded in an X'PERT PRO diffractometer using CuK α radiation source. Operating current and operation voltage were 40mA and 45KV, respectively. The scanning range 2θ was $5.00 - 99.98^\circ$ with a divergence slit of 0.8709° . The continuous scanning was done with a step size of 0.0170° and with scan step time of 30.36 s. The TGA/DSC analysis was carried out in air on a thermo gravimetric analyzer. The temperature of the cycle was programmed from 40 to 700°C increasing at the rate of 10°C per minute. In order to observe the microstructure of the prepared catalysts, SEM micrographs were obtained using a JEOL JSM-6700F instrument.

RESULTS & DISCUSSION

Effect of gold addition to CoO_x/ γ -Al₂O₃

In Figure 1, the methane conversion is plotted as a function of the operating temperature for each catalyst. It was observed that the methane conversion increases by increasing temperature. This evidence can be explained by considering that with increase in temperature, the activation energy required for the reaction is attained in that temperature region. It can be seen that with increase in gold content, the activity of the catalyst increases. The plot (figure 1) can be divided into two branches: methane conversion below 50% and methane conversion above 50%. It can be seen that below 50% the ignition temperature for methane oxidation is almost the same for each of the catalysts. But with increase in temperature each curve proceeds *via* different oxidation route.

Reaching 50% methane conversion, each curve differs by 25-30 $^\circ\text{C}$, as far as methane conversion above 50% is concerned. The difference of conversion temperature is minimised with increase in temperature. Each catalyst has the ability for 100% methane conversion. Further, it can be seen that almost each catalyst has traced an S-type curve. It is observed that the catalyst having 13.45% Au loaded on 18 wt.% CoO_x/ γ -Al₂O₃ exhibits the highest activity among all prepared catalysts. The

M. Kumar et al.: Promotional effect of Au on γ -Al₂O₃ supported cobalt based catalyst for total oxidation of methane catalyst without gold has the worst activity among all catalysts.

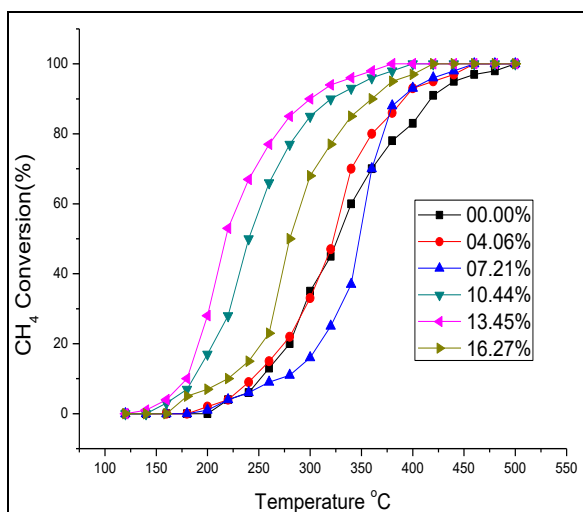


Figure 1. Temperature dependence of methane conversion over different amounts of gold loaded on 18wt.% Co/ γ -Al₂O₃.

A significant influence of the gold loading on the activity of different catalysts is evident. It is interesting to note that the catalyst (G50) without gold shows high activity than the catalyst (G52) between the span of 260-340°C temperature. It is very clear from figure 2 that with increase in gold content the activity of catalyst increases up to 13.45%, however, on further increase in gold content the activity decreases. This can be attributed to the bulk dispersion or aggregated particles of gold with further increase in gold content. The activity of the highly active catalyst (G54) can be attributed to the uniform dispersion of gold and cobalt on γ -alumina.

X-Ray diffractograms (XRD)

The XRD patterns of Au-CoO_x/ γ -Al₂O₃, as well as of CoO_x/ γ -Al₂O₃ are shown in figure 3 and figure 4, respectively. The formation of crystalline phase can be seen from the patterns of powders calcined at 550°C. The peaks at $2\theta=45.65^\circ$ and 67.18° (JCPDS 04-0783) are attributed to alumina in all catalysts [25,6].

The intense peaks further correspond to 38.2° the (111) lattice planes of metallic cobalt phase [26]. Narrow peaks indicate large particles and broad peaks correspond to small particles.

Characterization of the pure Co₃O₄/ γ -Al₂O₃ catalysts in comparison with catalyst having Au

loadings by powder X-ray diffraction showed that Au phases could be observed, although the Au loading in the catalyst (G55) was 16.27 wt.%, and only Co₃O₄/ γ -Al₂O₃ was determined, indicating that Au was amorphous or highly dispersed.

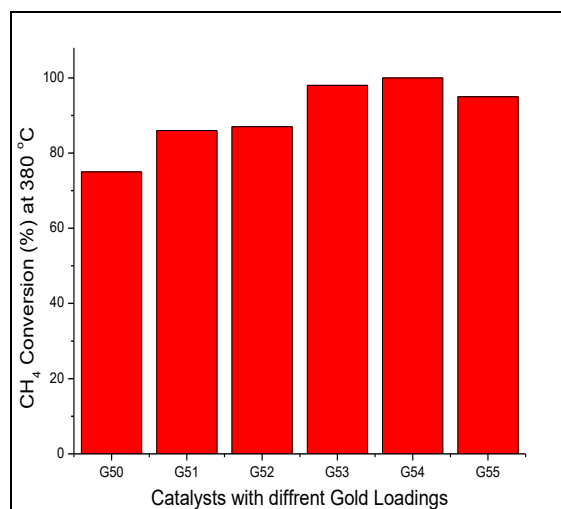


Figure 2. Methane conversion at 380°C for all catalysts.

Thermo Gravimetric Analysis (TGA/DSC)

The result of the TGA/DSC analysis of G53 catalyst is shown in figure 5. There is approx. 12wt.% reduction in weight of the catalyst. It can be seen that weight loss occurs in three intervals, i.e. 40-270; 270-550; 550-690 °C.

From 40-270 °C the weight loss is significant and may be attributed to the loss of water present with the precursor with an endothermic peak at 270°C. With further increase in the temperature there is a tremendous decrease in weight loss in the temperature range of 270-550 °C. This is due to the decomposition of nitrates and chlorides present in the precursor on contact with oxygen. However, the weight loss between 550-690 °C is negligible which means that anhydrous salts are completely decomposed. Figure 6 represents the thermograms of G54 catalyst. The weight loss is around 12 wt%, a little more than G53. This may be due to the high concentration of gold. The weight loss trend is similar to G53 catalyst. However, much of the weight loss is in the range of 40-270 °C with the endothermic peak again at 270°C. After 550 °C the loss in weight is negligible.

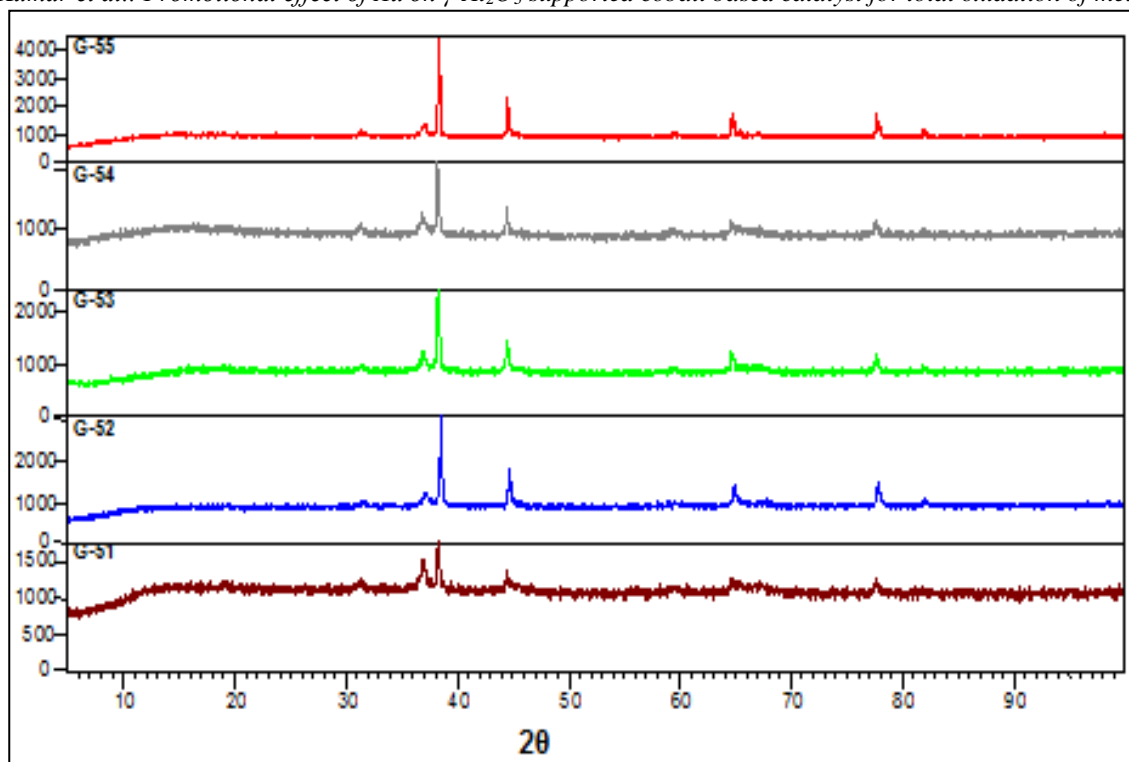


Figure 3. XRD patterns of catalysts having different gold loadings.

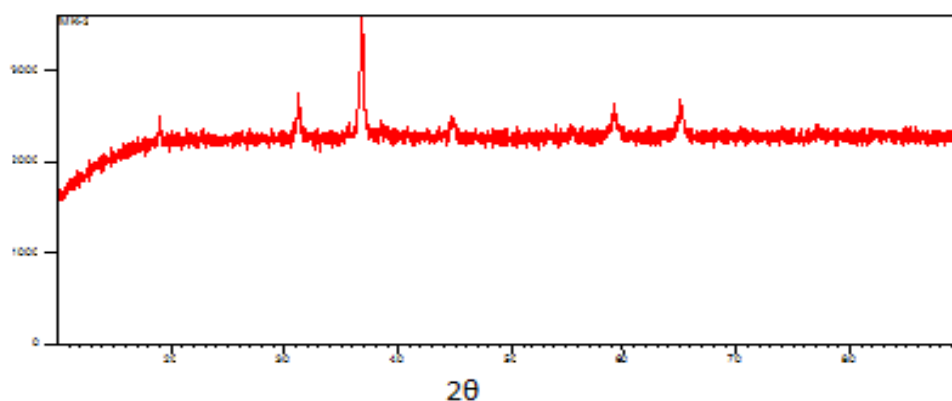


Figure 4. XRD pattern of 18wt.% Co/ $\gamma\text{-Al}_2\text{O}_3$

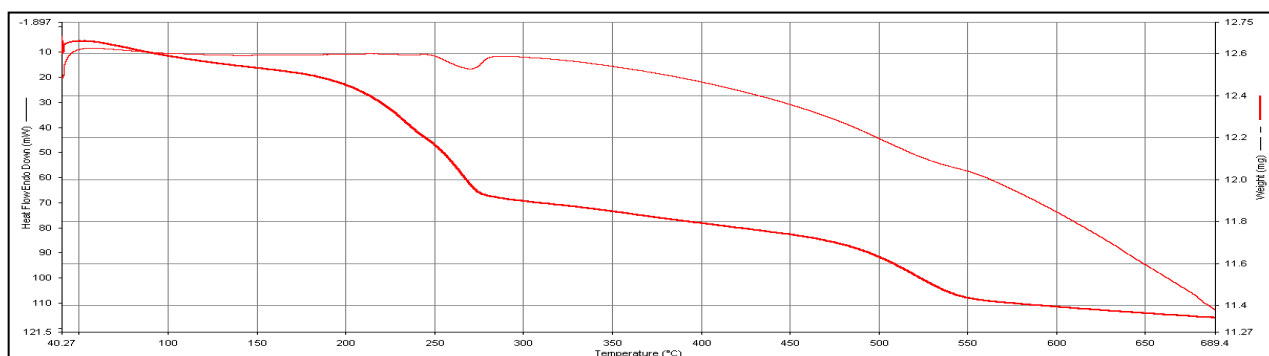


Figure 5. Graphical representation of TGA/DSC thermograms of the precursors of 10.44wt.% Au supported on 18wt.%Co/ $\gamma\text{-Al}_2\text{O}_3$

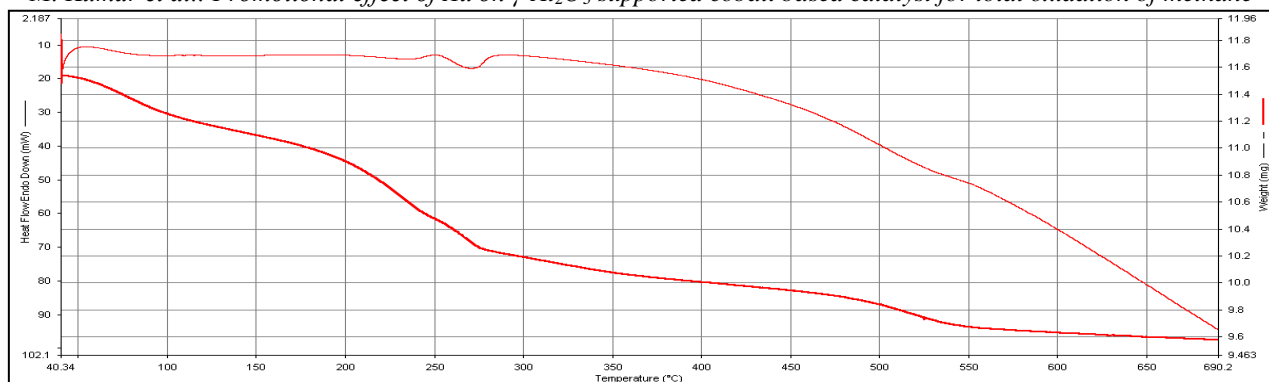


Figure 6. Graphical representation of TGA/DSC thermograms of the precursors of 13.45wt.% Au supported on 18wt.%Co/ γ -Al₂O₃

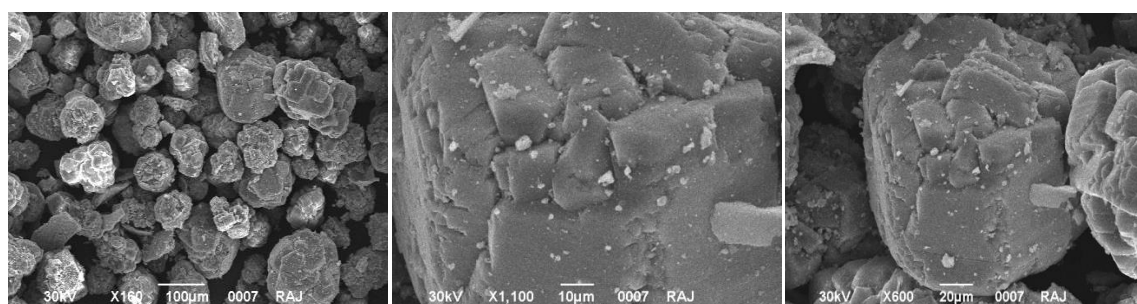


Figure 7. SEM micrographs of G51 catalyst.

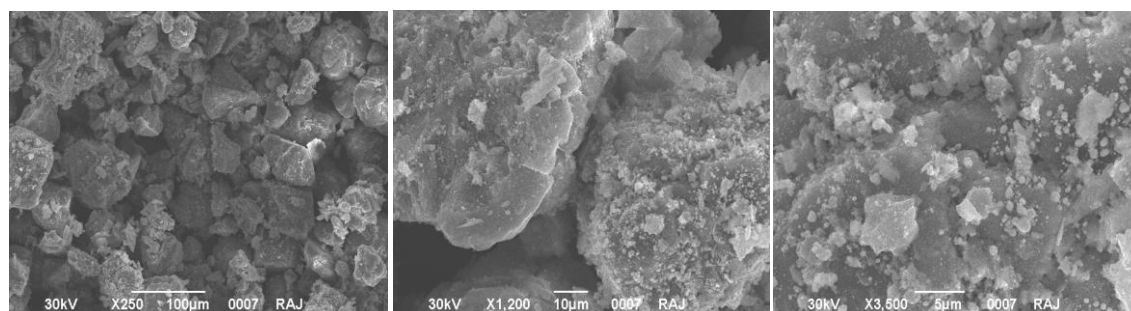


Figure 8. SEM micrographs of G52 catalyst.

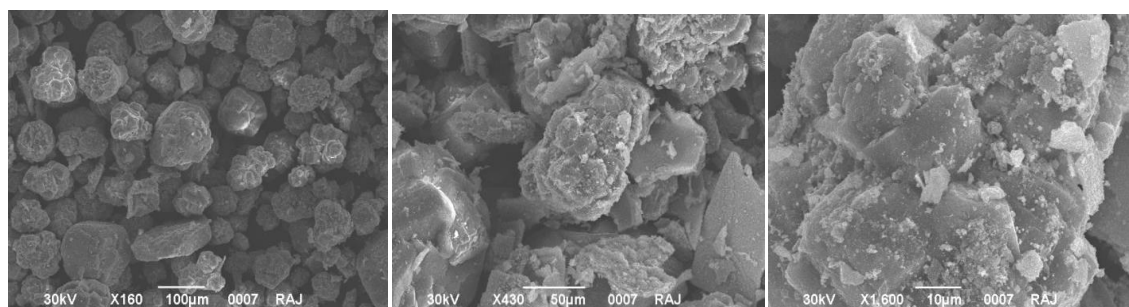


Figure 9. SEM micrographs of G53 catalyst.

SEM analysis

The SEM micrographs of all catalysts are shown in figures 7-11. Figure 7 shows the G51 catalyst, the flakes and spheres of cobalt are dispersed on alumina; separate cobalt oxide particles are also present. It can be seen that the gold particles are also dispersed on cobalt oxide, as well as on

alumina. Figure 8 represents the SEM micrographs of catalyst G52 at various resolutions. It can be seen that the density of the gold particles is very high in comparison to G51, which is due to the high concentration of gold in comparison to G51. Larger spheres of gold are dispersed on cobalt and alumina.



Figure 10. SEM micrographs of G54 catalyst.

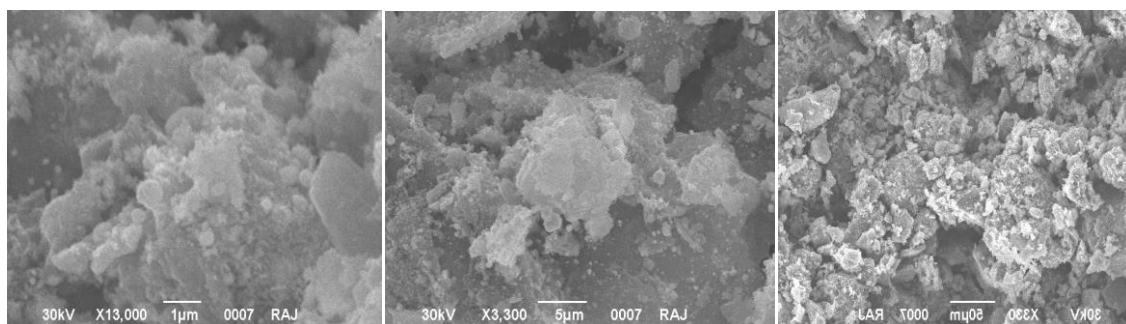


Figure 11. SEM micrographs of G55 catalyst.

Figure 9 represents the SEM images of G53 catalysts. Huge blocks or particles of both gold and cobalt are dispersed on alumina which is in good agreement with the catalytic activity of the catalyst. The SEM micrographs of the highly active catalyst G54 are presented in figure 10. It can be seen that the gold particles are dispersed on cobalt species which are further embedded in alumina particles and this reflects the reason behind the high activity of the catalyst. This morphology helps in oxidation/combustion of methane and also provides very high surface area per gm of the catalyst. However, figure 11 shows that agglomeration of gold particles takes place due to their high concentration.

CONCLUSIONS

Six catalyst samples having different gold composition and a constant amount of cobalt and alumina were prepared by a deposition/precipitation method and tested for methane oxidation. Table 3 represents the temperature required for {100, 50 and 10}% conversion of methane for each catalyst. The catalytic performance for the said reaction (1) and the morphology of the catalysts strongly depend upon the gold content in the catalyst. The activation energy required for reaction is different for each catalyst and is also a function of gold content. The catalyst having 13.45% gold shows the best catalytic performance, this is ascribed to the uniform dispersion of gold species in the catalyst. The catalyst sample having 4.06 wt.% gold exhibits poor activity. The catalyst without gold shows the

worst activity among all catalysts. Figure 12 shows the promotional effect of gold. It is clearly seen that light off temperature is tremendously increased with addition of gold. The catalytic activity of the tested samples is as follows: Au (13.45>10.44>16.27>07.21>04.06>0 wt. %) - CoO_x/ γ -Al₂O₃. All six catalysts are active for CH₄ oxidation and do not show deactivation of catalytic activity for 50 h of continuous run at 380 °C at different levels of methane conversions.

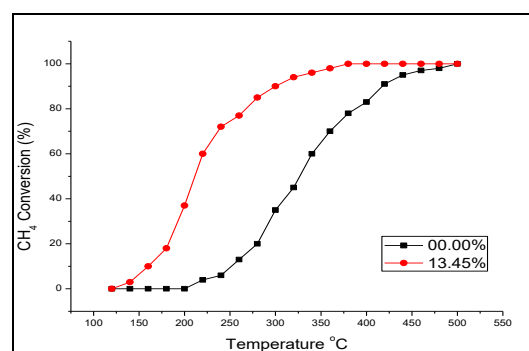


Figure 12. Promotional effect of gold (catalyst with 0, 13.45% Au) on methane conversion.

Table 3. Promotional effect of Au loading on light off temperatures of different catalysts prepared by a deposition precipitation method

Catalyst ID	Gold (wt.%)	Co:Au	Temperature (°C)		
			T _{10%}	T _{50%}	T _{100%}
G50	00.00	5:0	260	350	490
G51	04.06	5:1	245	325	460
G52	07.21	5:2	270	345	450
G53	10.44	5:3	195	240	400
G54	13.45	5:4	180	215	380
G55	16.27	5:5	220	280	415

REFERENCES

1. M. I. Jahirul, H. H. Masjuki, R. Saidur, M. A. Kalam, M. H. Jayed, M. A. Wazed, *Applied Thermal Engineering*, **30**, 14-15, 2219 (2010).
2. A. M. Hochhauser, W. J. Koehl, J. D. Benson, V. R. Burns, J. C. Knepper, W. R. Leppard, L. J. Painter, *SAE*, 952507 (1995).
3. A. R. Moss, J.-P. Jouany, J. Newbold, *Annales de Zootechnie*, **49**, 3, 231 (2000).
4. S. Kumar, M. Nayek, A. Kumar, A. Tandon, P. Mondal, P. Vijay, U. D. Bhangale, D. Tyagi, *American Chemical Science Journal*, **1**, 1 (2011).
5. M. Kumar, G. Rattan, *Journal of Chemical Technology and Metallurgy*, **51**, 63 (2016).
6. W. Guido, Ph.D. Thesis, Technical University of Denmark, Center for Nanotechnology at DTU, (2008)
7. Anderson, C.; Kupe, J.; LaBarge, W. J., U.S. Patent No. 7,094,730. Washington, DC: U.S. Patent and Trademark Office, (2006).
8. Fajdala, Kyle L.; Jia, Jifei; Truex, Timothy J., Engine Exhaust Catalysts Containing Palladium-Gold. U.S. Patent 7,709,414, 2010.
9. R. D. Waters, J. J. Weimer, J. E. Smith, *Catalysis Letters*, **30**, 181 (1994).
10. B. P. C. Hereijgers, B. M. Weckhuysen, *Catalysis Letters*, **141**, 10, 1429 (2011).
11. L.F. Liotta, G. Di Carlo, A. Longo, G. Pantaleo, A. M. Venezia, *Catalysis Today*, **139**, 3, 174 (2008).
12. B. E. Solsona, T. Garcia, Ch. Jones, S. H. Taylor, A. F. Carley, G. J. Hutchings, *Applied Catalysis A: General*, **312**, 67 (2006).
13. G. C. Bond, *Gold Bulletin*, **5**, 1, 11 (1972).
14. V.R. Choudhary, B.S. Uphade, S.G. Pataskar, *Fuel*, **78**, 8, 919 (1999).
15. L. F. Liotta, G. Di Carlo, G. Pantaleo, G. Deganello, *Applied Catalysis B: Environmental*, **70**, 1, 314 (2007).
16. L. F. Liotta, G. Di Carlo, G. Pantaleo, G. Deganello, *Catalysis Communications*, **6**, 5, 329 (2005).
17. T. V. Choudhary, S. Banerjee, V. R. Choudhary, *Applied Catalysis A: General*, **234**, 1, (2002).
18. G. Patrick, E. Van der Lingen, C. W. Corti, R. J. Holliday, D. T. Thompson, *Topics in Catalysis*, **30**, 1, 273 (2004).
19. M. Kumar, G. Rattan, R. Prasad, *Can. Chem. Trans.*, **3**, 4, 381 (2015).
20. Yu. Zhang, J. Deng, L. Zhang, W. Qiu, H. Dai, H. He, *Catalysis Today*, **139**, 1, 29 (2008).
21. K. Blick, Th. D. Mitrelias, J. S. J. Hargreaves, G. J. Hutchings, R. W. Joyner, Ch. J. Kiely, F. E. Wagner, *Catalysis Letters*, **50**, 3, 211 (1998).
22. Sh. Miao, Y. Deng, *Applied Catalysis B: Environmental*, **31**, 3 (2001).
23. R. J. H. Grisel, B. E. Nieuwenhuys, *Catalysis Today*, **64**, 1, 69 (2001).
24. V. R. Choudhary, V. P. Patil, P. Jana, B. S. Uphade, *Applied Catalysis A: General*, **350**, 2, 186 (2008).
25. S. Damyanova, C. A. Perez, M. Schmal, J. M. C. Bueno, *Applied Catalysis A: General*, **234**, 1, 271 (2002).
26. S. Storsæter, B. Tøtdal, J. C. Walmsley, B. S. Tanem, A. Holmen, *Journal of Catalysis*, **236**, 1, 139 (2005).
27. Th. W. Hesterberg, Ch. A. Lapin, W. B. Bunn, *Environmental Science & Technology*, **42**, 17, 6437 (2008).

ПРОМОЦИОНАЛЕН ЕФЕКТ НА Au ВЪРХУ γ -Al₂O₃ НАНЕСЕН КАТАЛИЗАТОР НА БАЗАТА НА КОБАЛТ ЗА ПЪЛНО ОКИСЛЕНИЕ НА МЕТАН

М. Кумар^{1,2*}, Г. Ратан¹, Р. Прасад³

¹Институт по инженерна химия и технология „Д-р С. С. Бхатнагар“, Панджабски университет, Чандигар 160014, Индия

²Департамент по инженерна химия, Университет на Чандигар, Мохали, Панджаб, Индия

³Департамент по инженерна химия, ИТ-ВНУ, Варанаси, У.П., Индия

Постъпила на 13 ноември, 2017 г.; коригирана на 16 февруари, 2018 г.

(Резюме)

Изучено е влиянието на съдържанието на злато в интервала от 4 мас. % - 16 мас. % върху отнасянията на катализатора Co/ γ -Al₂O₃ при окислението на CH₄. Промотираните със злато CoO_x/ γ -Al₂O₃ катализатори са получени чрез утаително нанасяне и калциниране при 550°C. При повишаване на съдържанието на злато се наблюдава значително повишаване на активността (T_{100%}=380 °C) при окисляване на CH₄, като при около 13.45 тегл. % Au се достига до плато. Каталитичната активност е изучена при постоянно тегло на катализатора (500 mg) в поток от въздух, съдържащ 1 % CH₄, внасян в реактора със скорост от 150 mL/min. Катализаторите са охарактеризирани чрез XRD, TGA/DSC и SEM. Каталитичната активност на катализаторите е в реда: Au (13.45>10.44>16.27>07.21>04.06>00.00 тегл. %)-CoO_x/ γ -Al₂O₃. Установено е, че катализаторът, съдържащ 13.45 тегл. % Au, нанесено върху 18 wt. % Co/ γ -Al₂O₃ е най-активен и понижава температурата (T_{100%}=380 °C) на редукция на метан със 110°C в сравнение с катализатор несъдържащ злато, т.е., 18 тегл.% Co/ γ -Al₂O₃ (T_{100%}=490 °C).

Synthesis and spectral properties of new piperazine derivatives and a structural study

Z. Gokmen*, N. G. Deniz, M. E. Onan, C. Sayil

Istanbul University-Cerrahpasa, Engineering Faculty, Department of Chemistry, Division of Organic Chemistry, 34320 Avcilar, Istanbul, Turkey

Received May 15, 2017; Accepted April 18, 2018

In this study, new piperazine derivatives were synthesized by the reactions of *S*-substituted-3-nitro-1,3-butadienes with some piperazine derivatives: (1-(2-furoyl)-, 1-(4-fluorobenzyl)-, 1-(3-fluorophenyl)- and 1-(1-tetrahydro-2-furyl)piperazine) in CHCl₃ at room temperature. The structures of the new compounds were characterized by micro analysis, FT-IR, MS spectrometry, ¹H- and ¹³C-NMR. The crystal structure analysis was performed on the synthesized compound **5d** by using the X-ray diffraction method. The compound **5d** crystallizes in the monoclinic space group P2₁/c with a = 12.5503(2) Å, b = 11.2039(2) Å, c = 14.1007(4) Å, Z = 4. The structure was solved by direct methods (SIR92) and refined to the residual index R₁ = 0.031.

Keywords: Piperazine derivatives; X-ray study; Organic synthesis; Vinylic substitution

INTRODUCTION

Polyhalo-substituted-1,3-butadienes possess a broad spectrum of useful properties: they are employed as monomers for the preparation of valuable polymers and copolymers resistant to heat, light and chemical corrosion, and exhibit algicidal, bactericidal and fungicidal activities [1]. Moreover, the precursor perchloronitrobutadiene **1** proved to be active against cancer cells [2].

Piperazine analogues have drawn great interest for their biological activities in a number of different therapeutic areas [3]. These include anticancer, antifungal [4,5], antibacterial, antimalarial and antipsychotic agents [6], as well as HIV protease inhibitors and antidepressants. Also, the N-carbonyl piperazine moieties exhibit cardiovascular properties [7].

EXPERIMENTAL

General

Melting points were measured on a Büchi B-540 melting point apparatus. FTIR spectra (cm⁻¹) were recorded as KBr pellets in nujol mulls on a Shimadzu IR Prestige 21 model Diamond spectrometer (ATR method). ¹H and ¹³C NMR spectra were recorded on a Varian Unity Inova spectrometer at 499.83 MHz for ¹H and 125.48 MHz for ¹³C using CDCl₃ as a solvent and TMS as an internal standard. Mass spectra were obtained on a hybrid triple quadrupole linear ion trap mass spectrometer (4000 QTRAP, ABSciex). The 4000 QTRAP was operated in the triple quadrupole mass spectrometer mode by use of electrospray ionization (ESI) source. The crystal structure of compound **5d** was determined on Rikagu R-Axis

Rapid-S X-Ray Single Crystal diffractometer. Micro analyses (C, H, N, S) were conducted using the Thermo Finnigan Flash EA 1112 elemental analyzer. Products were isolated by column chromatography on silica gel (Fluka Silica gel 60, particle size 63–200 µm). Kieselgel 60 F-254 plates (Merck) were used for thin layer chromatography (TLC). All chemicals were of reagent grade and were used without further purification. Moisture was excluded from the glass apparatus with CaCl₂ drying tubes.

General Method 1 for the synthesis of S-substituted-3-nitrobutadiene Compounds (3a-d)

4-(Hexadecylsulfanyl)-1,1,2,4-tetrachloro-3-nitro-1,3-butadiene (**3a**) [8], 4-(cyclopentylsulfanyl)-1,1,2,4-tetrachloro-3-nitro-1,3-butadiene (**3b**) [9], 4-(octadecyl-sulfanyl)-1,1,2,4-tetrachloro-3-nitro-1,3-butadiene (**3c**) [8] and 4-(ethylsulfanyl)-1,1,2,4-tetrachloro-3-nitro-1,3-butadiene (**3d**) [10] were synthesized by the reactions of **1** with **2a-d** according to the literature [8-10].

General method 2 for the synthesis of piperazine derivatives

The *S*-substituted-3-nitro-1,3-butadienes **3a-d** and equimolar amounts of the piperazine derivatives were stirred in chloroform (25 mL) for 8 h. Chloroform (30 mL) was added to the reaction mixture. The organic layer was washed with water (4×30 mL), and dried with Na₂SO₄. After the solvent was evaporated the residue was purified by column chromatography on silica gel.

[4-(1-(2-Furoyl)piperazin-1-yl)-4-(4-hexadecylsulfanyl)-1,1,2-trichloro-3-nitro-1,3-butadiene (5a): Compound **5a** was synthesized by the reaction

* To whom all correspondence should be sent:
E-mail: : gokm@istanbul.edu.tr

of **3a** (0.1 g, 0.2 mmol) with 1-(2-furoyl)piperazine **4** (0.036 g, 0.2 mmol) according to general method 2.

Yellow oil, yield: 0.062 g, 49%. R_f: 0.64 [PET:EtAc (2:1)]. FT-IR (KBr, cm⁻¹): ν = 2952, 2853 (C-H), 1649 (C=O_{Amide}), 1570 (C=C), 1529, 1487, 1274 (NO₂). ¹H NMR (CDCl₃, ppm): δ = 0.86-0.92 (t, 3H, CH₃), 1.24-1.32 (m, 24H, CH₂), 1.37-1.43 (m, 2H, CH₂), 1.65-1.72 (m, 2H, CH₂), 2.97-3.10 (s, 2H, S-CH₂), 3.40-3.85 (sbr, 4H, CH₂_{piper.}), 4.05-4.32 (s, 4H, CH₂_{piper.}), 6.53-6.57 (m, 1H, H_{arom.}), 7.15-7.17 (d, 1H, H_{arom.}), 7.52-7.55 (s, 1H, H_{arom.}). ¹³C NMR (CDCl₃, ppm): δ = 14.14 (CH₃), 23.71, 28.73, 29.04, 29.37, 29.39, 29.53, 29.62, 29.67, 29.70, 29.75 (CH₂), 31.94 (S-CH₂), 35.66, 52.91 (C_{piper.}), 111.79, 118.00, 118.83, 125.04, 126.53, 144.31 (C_{butad.}, C_{arom.}), 147.28 (C_{furoyl}), 169.30 (C=O). MS [+ESI]: m/z (%) 638 (100) [M+H]⁺. Micro analysis: C₂₉H₄₄C₁₃N₃O₄S, (M_A = 637.1 g/mol). Calculated: C, 54.67; H, 6.96; N, 6.60; S, 5.03%; Found: C, 54.69; H, 7.00; N, 6.62; S, 5.02%.

[4-(1-(2-Furoyl)piperazin-1-yl)-4-(4-octadecyl-sulfanyl)-1,1,2-trichloro-3-nitro-1,3-butadiene (5c): Compound **5c** was synthesized by the reaction of **3c** (0.1g, 0.2 mmol) with 1-(2-furoyl)piperazine **4** (0.035 g, 0.2 mmol) according to general method 2. Yellow oil, yield: 0.053 g, 42%. R_f: 0.30 [PET:EtAc (2:1)]. FT-IR (KBr, cm⁻¹): ν = 2952, 2853 (C-H), 1649 (C=O_{Amide}), 1570 (C=C), 1529, 1487, 1274 (NO₂). ¹H NMR (CDCl₃, ppm): δ = 0.87-0.90 (t, 3H, CH₃), 1.25-1.32 (m, 28H, CH₂), 1.39-1.42 (m, 2H, CH₂), 1.67-1.70 (m, 2H, CH₂), 2.97-3.00 (d, 2H, S-CH₂), 3.99 (sbr, 8H, CH₂_{piper.}), 6.53-6.54 (s, 1H, H_{arom.}), 7.13-7.14 (s, 1H, H_{arom.}), 7.51-7.52 (s, 1H, H_{arom.}). ¹³C NMR (CDCl₃, ppm): δ = 14.12 (CH₃), 22.69, 28.72, 29.02, 29.36, 29.38, 29.52, 29.61, 29.66, 29.70, 29.74 (CH₂), 31.92 (S-CH₂), 35.63, 52.89 (C_{piper.}), 111.75, 117.94, 118.86, 125.00, 126.54, 144.28, 158.99 (C_{butad.}, C_{arom.}), 147.27 (C_{furoyl}), 169.63 (C=O). MS [+ESI]: m/z (%) 688 (100) [M+Na]⁺. Micro analysis: C₃₁H₄₈C₁₃N₃O₄S, (M_A = 665.15 g/mol). Calculated: C, 55.98; H, 7.27; N, 6.32; S, 4.82%; Found: C, 55.99; H, 7.29; N, 6.35; S, 4.86%.

[4-(1-(2-Furoyl)piperazin-1-yl)-4-(ethyl-sulfanyl)-1,1,2-trichloro-3-nitro-1,3-butadiene (5d) [11]: Compound **5d** was synthesized by the reaction of **3d** (0.1g, 0.34 mmol) with 1-(2-furoyl)piperazine **4** (0.057 g, 0.32 mmol) according to general method 2. Yellow solid, yield: 0.057 g, 46%. M.p.: 135.8-136.0°C.

[4-(1-(4-Fluorobenzyl)piperazin-1-yl)-4-(4-hexadecyl-sulfanyl)-1,1,2-trichloro-3-nitro-1,3-butadiene (7a): Compound **7a** was synthesized by

the reaction of **3a** (0.1g, 0.2 mmol) with 1-(4-fluorobenzyl)piperazine **6** (0.039 g, 0.2 mmol) according to general method 2. Yellow solid, yield: 0.042 g, 32%. R_f: 0.63 [PET:EtAc (2:1)]. M.p.: 75°C. FT-IR (KBr, cm⁻¹): ν = 2924, 2853 (C-H), 1620, 1510 (C=C), 1530, 1279 (NO₂). ¹H NMR (CDCl₃, ppm): δ = 0.86-0.92 (t, 3H, CH₃), 1.24-1.32 (m, 24H, CH₂), 1.37-1.43 (m, 2H, CH₂), 1.65-1.72 (m, 2H, CH₂), 2.55-2.75 (sbr, 2H, Ph-CH₂), 2.97-3.10 (s, 2H, S-CH₂), 3.50-3.80 (s, 4H, CH₂_{piper.}), 3.90-4.12 (sbr, 4H, CH₂_{piper.}), 7.05-7.07 (t, 2H, H_{arom.}), 7.32-7.35 (s, 2H, H_{arom.}). ¹³C NMR (CDCl₃, ppm): δ = 14.14 (CH₃), 23.71, 28.73, 29.04, 29.37, 29.39, 29.53, 29.62, 29.67, 29.70, 29.75, 31.94 (CH₂), 35.66 (S-CH₂), 52.40, 61.50 (C_{piper.}), 115.36, 115.53, 126.83 (C_{butad.}, C_{arom.}). MS [+ESI]: m/z (%) 652 (100) [M+H]⁺. Micro analysis: C₃₁H₄₇Cl₃FN₃O₂S, (M_A = 651.15 g/mol). Calculated: C, 57.18; H, 7.28; N, 6.45; S, 4.92%; Found: C, 57.20; H, 7.26; N, 6.46; S, 4.90%.

[4-(1-(4-Fluorobenzyl)piperazin-1-yl)-4-(4-cyclopentyl-sulfanyl)-1,1,2-trichloro-3-nitro-1,3-butadiene (7b): Compound **7b** was synthesized by the reaction of **3b** (0.1g, 0.3 mmol) with 1-(4-fluorobenzyl)piperazine **6** (0.058 g, 0.3 mmol) according to general method 2. Orange solid, yield: 0.074 g, 51%. R_f: 0.41 [PET:EtAc (2:1)]. M.p.: 124°C. FT-IR (KBr, cm⁻¹): ν = 3052, 2961, 2871, 2805, 2768 (C-H), 1602 (C=C), 1529, 1278 (NO₂). ¹H NMR (CDCl₃, ppm): δ = 1.52-1.76 (m, 4H, CH₂_{cyclo.}), 1.65-1.73 (s, 4H, CH₂_{cyclo.}), 2.55 (sbr, 3H, S-CH_{cyclo.} and Ph-CH₂), 3.45 (s, 4H, CH₂_{piper.}), 3.50-3.91 (sbr, 4H, CH₂_{piper.}), 6.90-7.00 (t, 2H, CH_{arom.}), 7.19-7.21 (m, 2H, CH_{arom.}). ¹³C NMR (CDCl₃, ppm): δ = 24.61, 48.26 (C_{cyclo.}), 52.52, 53.35 (C_{piper.}), 115.26, 115.43, 118.12, 124.6, 126.88, 130.7, 130.53, 132.82, 161.26 (C_{butad.}, C_{arom.}), 163.21 (C_{Farom.}). MS [+ESI]: m/z (%) 494 (100) [M]⁺. Micro analysis: C₂₀H₂₃Cl₃FN₃O₂S, (M_A = 494.84 g/mol). Calculated: C, 48.54; H, 4.68; N, 8.49; S, 6.48%; Found: C, 48.59; H, 4.69; N, 8.51; S, 6.47%.

[4-(1-(4-Fluorobenzyl)piperazin-1-yl)-4-(4-octadecyl-sulfanyl)-1,1,2-trichloro-3-nitro-1,3-butadiene (7c): Compound **7c** was synthesized by the reaction of **3c** (0.1g, 0.19 mmol) with 1-(4-fluorobenzyl)piperazine **6** (0.037 g, 0.19 mmol) according to general method 2. Oil, yield: 0.055 g, 43%. R_f: 0.59 [PET:EtAc (2:1)]. FT-IR (KBr, cm⁻¹): ν = 2924, 2853 (C-H), 1610 (C=C), 1529, 1278 (NO₂). ¹H NMR (CDCl₃, ppm): δ = 0.78-0.82 (t, 3H, CH₃), 1.15-1.25 (m, 28H, CH₂), 1.28-1.35 (m, 2H, CH₂), 1.50-1.60 (m, 2H, CH₂), 2.55-2.75 (sbr, 2H, Ph-CH₂), 2.85-2.93 (t, 2H, S-CH₂), 3.45-3.58 (s, 4H, CH₂_{piper.}), 3.62-3.83 (sbr, 4H, CH₂_{piper.}), 6.96-6.99 (t, 2H, CH_{arom.}), 7.23-7.29 (sbr, 2H,

CH_{arom.}). ¹³C NMR (CDCl₃, ppm): δ=14.15 (**CH₃**), 22.71, 28.69, 29.0, 29.38, 29.52, 29.62, 29.68, 29.71, 29.76, 31.94 (**CH₂**), 35.51 (**S-CH₂**), 61.48 (**Ph-CH₂**), 115.58, 128.02, 130.50, (**C_{butad.}**, **C_{arom.}**). MS [+ESI]: m/z (%) 680 (100) [**M+H**]⁺. Micro analysis: C₃₃H₅₁Cl₃FN₃O₂S, (M_A = 679.2 g/mol). Calculated: C, 58.36; H, 7.57; N, 6.19; S, 4.72%; Found: C, 58.38; H, 7.58; N, 6.20; S, 4.75%.

[4-(1-(3-Fluorophenyl)piperazin-1-yl)-4-(4-hexadecyl-sulfanyl)-1,1,2-trichloro-3-nitro-1,3-butadiene (9a): Compound **9a** was synthesized by the reaction of **3a** (0.1g, 0.2 mmol) with 1-(3-fluorophenyl)piperazine **8** (0.037 g, 0.2 mmol) according to general method 2. Orange solid, yield: 0.036 g, 28%. R_f: 0.33 [PET:EtAc (9:1)]. M.p.: 82-83°C. FT-IR (KBr, cm⁻¹): ν= 2919, 2850 (C-H), 1615, 1518 (C=C), 1533, 1277 (NO₂). ¹H NMR (CDCl₃, ppm): δ= 0.88-0.92 (t, 3H, **CH₃**), 1.23-1.33 (s, 24H, **CH₂**), 1.38-1.44 (m, 2H, **CH₂**), 1.67-1.73 (s, 2H, **CH₂**), 2.97-3.10 (s, 2H, **S-CH₂**), 3.35-3.45 (s, 4H, **CH₂**_{piper.}), 3.65-4.05 (sbr, 4H, **CH₂**_{piper.}), 6.66-6.72 (m, 3H, **H_{arom.}**), 7.22-7.29 (t, 1H, **H_{arom.}**). ¹³C NMR (CDCl₃, ppm): δ=14.15 (**CH₃**), 22.71, 28.55, 28.71, 29.04, 29.26, 29.38, 29.53, 29.62, 29.67, 29.71, 31.94, 35.63 (**CH₂**), 39.23, 48.79 (**C_{piper.}**), 107.3, 111.65 (**C_{butad.}**, **C_{arom.}**). MS [+ESI]: m/z (%) 638 (100) [**M+H**]⁺. Micro analysis: C₃₀H₄₅Cl₃FN₃O₂S, (M_A = 637.12 g/mol). Calculated: C, 56.55; H, 7.12; N, 6.60; S, 5.03%; Found: C, 56.54; H, 7.13; N, 6.63; S, 5.07%.

[4-(1-(3-Fluorophenyl)piperazin-1-yl)-4-(4-cyclopentyl-sulfanyl)-1,1,2-trichloro-3-nitro-1,3-butadiene (9b): Compound **9b** was synthesized by the reaction of **3b** (0.1g, 0.3 mmol) with 1-(3-fluorophenyl)piperazine **8** (0.053 g, 0.3 mmol) according to general method 2. Orange solid, yield: 0.049 g, 35%. R_f: 0.53 [PET:EtAc (2:1)]. M.p.: 128.5°C. FT-IR (KBr, cm⁻¹): ν= 2962, 2868, 2826 (C-H), 1613 (C=C), 1529, 1273 (NO₂). ¹H NMR (CDCl₃, ppm): δ= 1.48-1.52 (s, 2H, **CH₂**_{cyclo.}), 1.57-1.64 (s, 2H, **CH₂**_{cyclo.}), 1.67-1.78 (s, 2H, **CH₂**_{cyclo.}), 2.00-2.10 (m, 2H, **CH₂**_{cyclo.}), 3.20-3.30 (s, 1H, **S-CH₂**_{cyclo.}), 3.50-4.00 (m, 8H, **CH₂**_{piper.}), 6.49-6.52 (m, 2H, **CH_{arom.}**), 6.67-6.64 (d, 1H, **CH_{arom.}**), 7.13-7.20 (t, 1H, **CH_{arom.}**). ¹³C NMR (CDCl₃, ppm): δ= 24.64, 48.36 (**C_{cyclo.}**), 48.75, 52.72 (**C_{piper.}**), 103.26, 103.46, 107.27, 107.44, 111.64, 111.66, 124.94, 126.69, 130.50, 130.58 (**C_{butad.}**, **C_{arom.}**), 151.60 (**N-C_{phenyl}**), 162.82, 164.76 (**C-F_{arom.}**). MS [+ESI]: m/z (%) 480 (100) [**M**]⁺. Micro analysis: C₁₉H₂₁Cl₃FN₃O₂S, (M_A = 480.81 g/mol). Calculated: C, 47.46; H, 4.40; N, 8.74; S, 6.67%; Found: C, 47.50; H, 4.43; N, 8.70; S, 6.69%.

[4-(1-(3-Fluorophenyl)piperazin-1-yl)-4-(4-octadecyl-sulfanyl)-1,1,2-trichloro-3-nitro-1,3-butadiene (9c): Compound **9c** was synthesized by the reaction of **3c** (0.1g, 0.3 mmol) with 1-(3-fluorophenyl)piperazine **8** (0.034 g, 0.3 mmol) according to general method 2. Orange solid, yield: 31%. R_f: 0.52 [PET:EtAc (4:1)]. M.p.: 96-97°C. FT-IR (KBr, cm⁻¹): ν= 2926, 2854 (C-H), 1615 (C=C), 1528, 1265 (NO₂). ¹H NMR (CDCl₃, ppm): δ= 0.77-0.84 (t, 3H, **CH₃**), 1.18-1.24 (d, 30H, **CH₂**), 1.50 (s, 2H, **CH₂**), 2.90 (s, 2H, **S-CH₂**), 3.30 (s, 4H, **CH₂**_{piper.}), 3.65-4.10 (sbr, 4H, **CH₂**_{piper.}), 6.50-6.64 (m, 2H, **H_{arom.}**), 7.14-7.20 (m, 2H, **H_{arom.}**). ¹³C NMR (CDCl₃, ppm): δ= 14.15 (**CH₃**), 22.71, 28.71, 29.04, 29.36, 29.53, 29.63, 29.68, 29.71, 29.80, 31.94, 35.63 (**CH₂**), 48.79 (**C_{piper.}**), 103.29, 103.48, 107.47, 111.65, 130.53 (**C_{butad.}**, **C_{arom.}**). MS [+ESI]: m/z (%) 688 (100) [**M+Na**]⁺. Micro analysis: C₃₂H₄₉Cl₃FN₃O₂S, (M_A = 665.17 g/mol). Calculated: C, 57.78; H, 7.42; N, 6.32; S, 4.82%; Found: C, 57.80; H, 7.44; N, 6.35; S, 4.83%.

[4-(1-(Tetrahydro-2-furyl)piperazin-1-yl)-4-(4-hexadecyl-sulfanyl)-1,1,2-trichloro-3-nitro-1,3-butadiene (11a): Compound **11a** was synthesized from the reaction of **3a** (0.1g, 0.19 mmol) with 1-(1-tetrahydro-2-furyl)piperazine **10** (0.037 g, 0.19 mmol) according to general method 2. Yellow oil, yield: 0.043 g, 34%. R_f: 0.67 [PET:EtAc (1:1)]. FT-IR (KBr, cm⁻¹): ν= 2952, 2853 (C-H), 1659 (C=O), 1529, 1273 (NO₂). ¹H NMR (CDCl₃, ppm): δ=0.88-1.03 (t, 3H, **CH₃**), 1.22-1.26 (m, 28H, **CH₂**), 1.30-1.48 (m, 2H, **CH₂**), 1.58-1.65 (m, 2H, **CH₂**_{furyl}), 2.95-2.98 (s, 2H, **S-CH₂**), 3.60-3.82 (m, 2H, **CH₂**_{furyl}), 3.84-3.97 (m, 8H, **CH₂**_{piper.}), 4.57-4.59 (t, 1H, **CH_{furyl}**). ¹³C NMR (CDCl₃, ppm): δ= 14.12 (**CH₃**), 22.69, 25.58, 25.79, 27.90, 28.70, 29.02, 29.35, 29.51, 29.60, 29.65, 29.67, 29.71, 29.70, 29.75, 31.92 (**CH₂**), 35.61 (**S-CH₂**), 41.75, 44.73, 47.51 (**C_{furyl}**), 51.77, 53.49 (**C_{piper.}**), 69.18 (**C_{furyl}**), 118.77, 124.97, 126.56 (**C_{butad.}**), 169.88 (C=O). MS [+ESI]: m/z (%) 664 (100) [**M+Na**]⁺. Micro analysis: C₂₉H₄₈Cl₃N₃O₄S, (M_A = 641.13 g/mol). Calculated: C, 54.33; H, 7.55; N, 6.55; S, 5.00%; Found: C, 54.37; H, 7.56; N, 6.58; S, 5.02%.

[4-(1-(Tetrahydro-2-furyl)piperazin-1-yl)-4-(4-octadecyl-sulfanyl)-1,1,2-trichloro-3-nitro-1,3-butadiene (11c): Compound **11c** was synthesized by the reaction of **3c** (0.1g, 0.19 mmol) with 1-(1-tetrahydro-2-furyl)piperazine **10** (0.353 g, 0.19 mmol) according to general method 2. Yellow solid, yield: 0.065 g, 51%. R_f: 0.42 [PET:EtAc (1:1)]. M.p.: 120°C. FT-IR (KBr, cm⁻¹): ν= 2952, 2853 (C-H), 1659 (C=O), 1613 (C=C), 1529, 1273 (NO₂). ¹H NMR (CDCl₃, ppm): δ= 0.79-0.83 (t, 3H,

CH₃), 1.15-1.25 (m, 2H, **CH₂**), 1.28-1.35 (m, 2H, **CH₂**), 1.57-1.63 (m, 2H, **CH₂**), 1.84-2.00 (m, 4H, **CH₂**_{furyl}), 2.85-2.97 (s, 2H, S-**CH₂**), 3.40-3.70 (sbr, 4H, **CH₂**_{piper.}), 3.75-3.81 (m, 2H, **CH₂**_{furyl}), 3.83-3.98 (m, 4H, **CH₂**_{piper.}), 4.47-4.57 (t, 1H, **CH**_{furyl}). ¹³C NMR (CDCl₃, ppm): δ=14.14 (**CH₃**), 22.71, 25.79, 27.88, 28.70, 29.04, 29.37, 29.39, 29.53, 29.62, 29.67, 29.71, 29.76, 31.94 (**CH₂**), 35.61 (S-**CH₂**), 41.75, 44.74 (**C**_{furyl}), 52.63, 53.51 (**C**_{piper.}), 69.21 (**C**_{furyl}), 118.73, 124.98, 126.57 (**C**_{butad.}), 169.84 (**C=O**). MS [+ESI]: m/z (%) 692 (100) [M+Na]⁺. Micro analysis: C₃₁H₅₂Cl₃N₃O₄S, (M_A= 669.19 g/mol). Calculated: C, 55.64; H, 7.83; N, 6.28; S, 4.79%; Found: C, 55.69; H, 7.86; N, 6.32; S, 4.84%.

[4-(1-(3,4-Dichlorophenyl)piperazin-1-yl)-4-(4-cyclopentyl-sulfanyl)-1,1,2-trichloro-3-nitro-1,3-butadiene (**13b**): Compound **13b** was synthesized by the reaction of **3b** (0.1g, 0.3 mmol) with 1-(3,4-dichlorophenyl)piperazine **12** (0.069 g, 0.3 mmol) according to general method 2. Orange solid, yield: 0.064 g, 41%. R_f: 0.53 [PET:EtAc (2:1)]. M.p.: 172-173°C. FT-IR (KBr, cm⁻¹): ν= 3054, 2986, 1610 (C=C), 1526, 1265 (NO₂). ¹H NMR (CDCl₃, ppm): δ=1.50-1.53 (s, 2H, **CH₂**_{cyclo.}), 1.55-1.64 (s, 2H, **CH₂**_{cyclo.}), 1.67-1.77 (s, 2H, **CH₂**_{cyclo.}), 2.00-2.10 (m, 2H, **CH₂**_{cyclo.}), 3.20 (s, 1H, S-**CH**_{cyclo.}), 3.45-4.20 (m, 8H, **CH₂**_{piper.}), 6.67-6.71 (d, 1H, **CH**_{arom.}), 6.89 (d, 1H, **CH**_{arom.}), 7.24-7.28 (d, 1H, **CH**_{arom.}). ¹³C NMR (CDCl₃, ppm): δ= 24.63, 48.36 (**C**_{cyclo.}), 48.82, 52.57 (**C**_{piper.}), 115.96, 117.90, 123.91, 126.61, 130.80, 131.17, 143.37 (**C**_{butad.}, **C**_{arom.}). MS [+ESI]: m/z (%) 532 (100) [M]⁺. Micro analysis: C₁₉H₂₀Cl₃N₃O₂S, (M_A = 531.71 g/mol). Calculated: C, 42.92; H, 3.79; N, 7.90; S, 6.03%; Found: C, 42.93; H, 3.81; N, 7.92; S, 6.04%.

[4-(1-(3,4-Dichlorophenyl)piperazin-1-yl)-4-(4-octadecyl-sulfanyl)-1,1,2-trichloro-3-nitro-1,3-butadiene (**13c**): Compound **13c** was synthesized frbyom the reaction of **3c** (0.1g, 0.3 mmol) with 1-(3,4-dichlorophenyl)piperazine **12** (0.044 g, 0.3 mmol) according to general method 2. Orange solid, yield: 0.035 g, 26%. R_f: 0.48 [PET:EtAc (5:1)]. M.p.: 75-76°C. FT-IR (KBr,cm⁻¹): ν= 2921, 2852 (C-H), 1593 (C=C), 1528, 1272 (NO₂). ¹H NMR (CDCl₃, ppm): δ= 0.77-0.84 (t, 3H, **CH₃**), 1.15-1.25 (m, 26H, **CH₂**), 1.28-1.35 (m, 2H, **CH₂**), 1.47-1.53 (s, 2H, **CH₂**), 1.55-1.67 (m, 2H, **CH₂**), 2.87-2.97 (s, 2H, S-**CH₂**), 3.20-3.30 (s, 4H, **CH₂**_{piper.}), 3.50-4.00 (sbr, 4H, **CH₂**_{piper.}), 6.65-6.70 (d, 1H, **H**_{arom.}), 6.90 (d, 1H, **H**_{arom.}), 7.25-7.30 (d, 1H, **H**_{arom.}). ¹³C NMR (CDCl₃, ppm): δ= 14.15 (**CH₃**), 22.71, 28.71, 29.04, 29.36, 29.53, 29.63,

29.68, 29.71, 29.80, 31.94, 35.63 (**CH₂**), 48.79 (**C**_{piper.}), 103.29, 103.48, 107.47, 111.65, 130.53 (**C**_{butad.}, **C**_{arom.}). MS [+ESI]: m/z (%) 738 (100) [M+Na]⁺. Micro analysis: C₃₂H₄₈Cl₃N₃O₂S, (M_A = 716.07 g/mol). Calculated: C, 53.67; H, 6.76; N, 5.87; S, 4.48%; Found: C, 53.72; H, 6.79; N, 5.88; S, 5.89%.

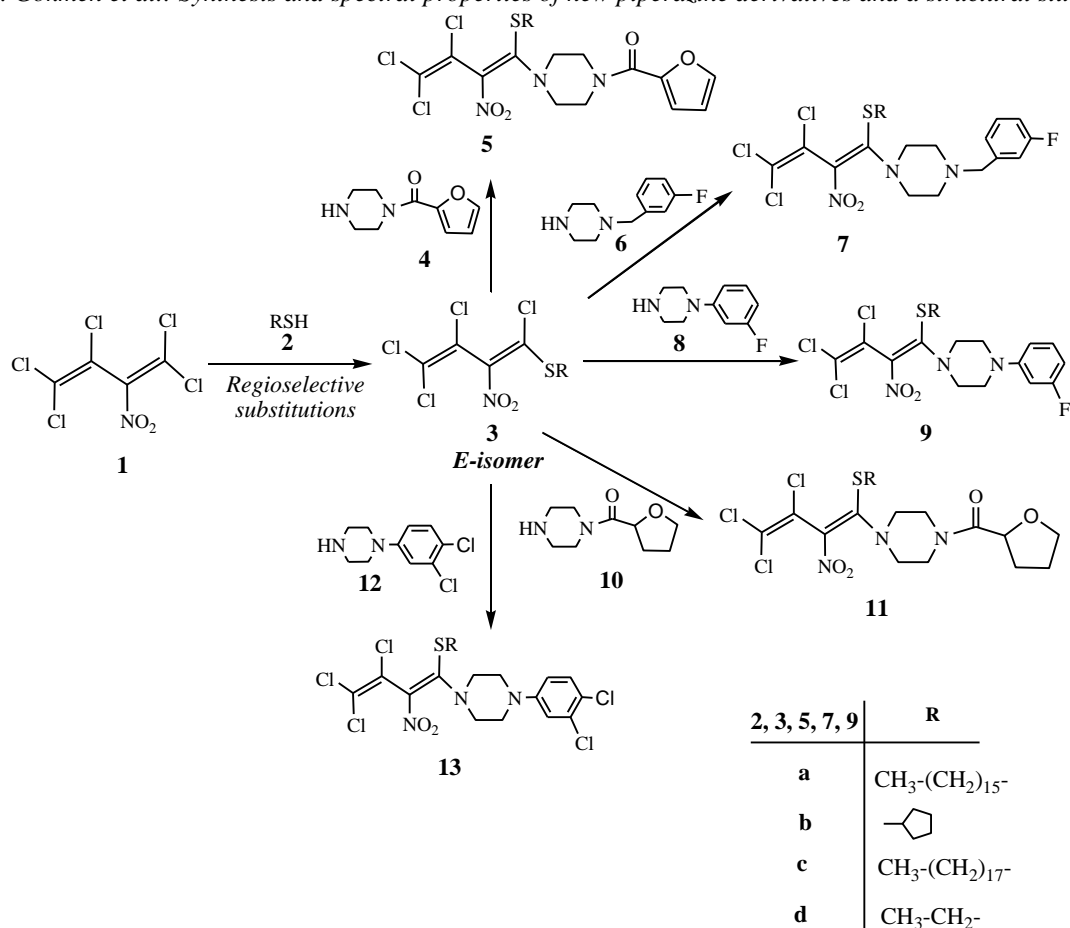
X-Ray Crystallography

Yellow crystals of compound **5d** suitable for X-ray diffraction analysis were obtained by slow evaporation of an ethanol/chloroform (10:1) solution at room temperature. The compound **5d**, C₁₅H₁₆Cl₃N₃O₄S₁, having approximate dimensions of 0.60 × 0.30 × 0.20 mm, was mounted on a glass fiber. All measurements were made on a Rigaku R-Axis Rapid-S imaging plate area detector with graphite monochromated Mo-Kα radiation (λ = 0.71073 Å). The crystal structures were solved by SIR 92 [12] and refined with CRYSTALS [13]. The non-hydrogen atoms were refined anisotropically. H atoms were located in geometrically idealized positions C-H = 0.95(6) Å and treated as riding and U_{iso}(H) = 1.2U_{eq}(C). Drawing was performed with the program ORTEP-III [14] with 50% probability displacement ellipsoid. Crystallographic data (excluding structure factors) for the structures reported in this paper have been deposited with the Cambridge Crystallographic Data Centre as supplementary publication numbers. CCDC-1544558 for compound **5d** [15].

RESULTS AND DISCUSSION

The aim of this study was to synthesize new piperazine derivatives **5a**, **5c-d**, **7a-c**, **9a-c**, **11a**, **11c** and **13b-c** and to determine the exact structures of the new compounds by using spectroscopic techniques (¹H NMR, ¹³C NMR, FTIR, MS) and X-ray diffraction method. In this work, the *S*-substituted-3-nitro-1,3-butadienes were obtained by direct reactions of pentachloro-3-nitrobutadiene with some *S*-nucleophiles [hexadecylthiol-, cyclopentylthiol, octadecylthiol and ethylthiol] [8-10].

The novel piperazine derivatives **5a**, **5c**, **5d** [11], **7a-c**, **9a-c**, **11a**, **11c** and **13b-c** were synthesized by the reaction of the *S*-substituted-3-nitro-1,3-butadienes (**3a** [8], **3b** [9], **3c** [8] and **3d** [10]) with (1-(2-furoyl)piperazine **4**, 1-(4-fluorobenzyl)piperazine **6**, 1-(3-fluorophenyl)piperazine **8**, 1-(1-tetrahydro-2-furyl)piperazine **10**, and 1-(3,4-dichlorophenyl)piperazine **12** in CHCl₃, respectively, as shown in Scheme 1.

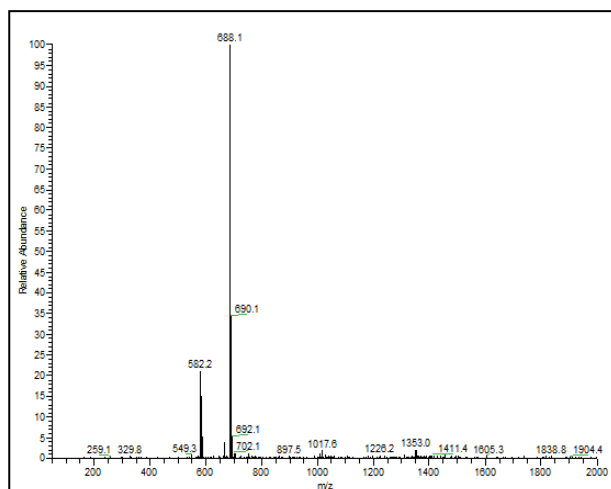


Scheme 1. Synthesis of piperazine derivatives.

The FT-IR spectra of compounds **5a** and **5c**, **11a** and **11c** showed the absorption bands of the amide carbonyl group at 1649 and 1659 cm⁻¹, respectively. The proton NMR data of compounds **5a**, **5c**, **7a-c**, **9a-c** and **13b-c** showed the aromatic protons within the range 6.42-7.55 ppm. In the ¹³C NMR spectra of all compounds signals were observed at 49-62 ppm for the methylene carbon atom of the piperazine ring. Due to the aromatic ring of furoyl, in the carbon NMR spectra of compounds **5a** and **5c** signals were observed at $\delta = 147$ ppm for the furoyl (C-O) carbons. The (C-O) signals of the tetrahydrofuroyl units were observed at 69 ppm in the carbon NMR spectra of **11a** and **11c**. The carbon NMR shift of the carbonyl groups of compounds **5a**, **5c**, **11a** and **11c** appeared around $\delta = 169$ -170 ppm. The (+ESI) mode mass spectra of **5c** revealed at *m/z* (%) 688 (100) [M+23]⁺ which corresponds to the addition of one sodium ion. The (+ESI) mass spectrum of **5c** is shown in Fig. 1.

X-ray study

The crystals used in the X-ray diffraction study were obtained by recrystallization of compound **5d** from a solution of ethanol-chloroform (10:1). The crystal structure of compound **5d** is shown in Fig. 2.

Fig. 1. MS[+ESI] spectrum of compound **5c**

The butadiene unit is not planar as would be if the two double bonds were fully conjugated. Non-coplanar structures of the butadiene fragments of these molecules and the clear C2-C3 single bonds indicate the lack of delocalization of π -electron density in the butadiene chains, which is apparently one of the major reasons for the inertness of

polychlorobutadienes and their functional derivatives with non-planar molecular structure relative to 1,4-addition. Crystal data and refinement parameters are summarized in Table 1 and the selected bond distances, bond and torsion angles are listed in Table 2 for compound **5d**.

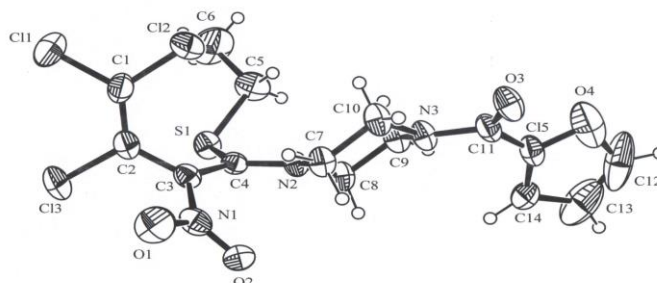


Fig. 2. Molecular structure of compound **5d**. Displacement ellipsoids are plotted at the 40% probability level (symmetry transformations used to generate equivalent atoms: (i) $-x, -y, -z$).

Table 1. Main crystallographic parameters of compound **5d**

Empirical formula	$C_{15}H_{16}Cl_3N_3O_4S_1$
Crystal colour, habit	Yellow, chunk
Crystal size (mm)	$0.60 \times 0.30 \times 0.20$
Wavelength (\AA)	0.71073
Crystal system	Monoclinic
Space group	P21/c
Cell dimensions	$a = 12.5503(2)\text{\AA}$ $b = 11.2039(2)\text{\AA}$ $c = 14.1007(4)\text{\AA}$
Cell volume (\AA^3)	1924.60(7)
Cell formula units (Z)	4
Density ($\text{g}\cdot\text{cm}^{-3}$)	1.521
μ [cm^{-1}]	0.610
F_{000}	904.00
h,k,l. ranges	$-17 \leq h \leq 17, -15 \leq k \leq 15, -20 \leq l \leq 17$
Reflections collected	112600
Independent reflections	5845 [$R_{\text{int}} = 0.086$]
Data/restraints/parameters	4293/0/251
Goodness of fit indicator	1.115
Final R indices [$I > 2\sigma(I)$]	$R_1 = 0.081$ $wR_2 = 0.031$
Largest diff. peak and hole	0.035 and -0.035 $\text{e}\cdot\text{\AA}^{-3}$
CCDC deposition number	1544558

Table 2. Selected bond distances (\AA), bond and torsion angles ($^\circ$) for compound **5d**

Bond distances		Bond angles		Torsion angles	
C1-C2	1.330(4)	C1-C2-C3	124.4(3)	C1-C2-C3-C4	-60.2(5)
C2-C3	1.459(4)	C2-C3-C4	124.0(3)	N2-C8-C9-N3	52.4(3)
C3-C4	1.398(4)	O1-N1-O2	122.3(3)	N2-C7-C10-N3	-56.4(3)
C4-S1	1.734(3)	C7-N2-C8	112.1(2)	C2-C3-C4-S1	-38.2(3)
C4-N2	1.338(4)	C9-N3-C10	112.5(3)	C2-C3-C4-N2	140.2(3)
C11-O3	1.204(4)	C11-C1-Cl2	113.5(2)	C1-C2-C3-N1	118.1(4)

The nitro group is nearly coplanar with the butadiene unit to which it is attached, with torsion angles of (O1-N1-C3-C2) and (O1-N1-C3-C4) - $11.3(4)^\circ$ and $167.0(3)^\circ$, respectively. The four

carbon atoms of the piperazine ring (C7-C8-C9-C10) are planar with a maximum deviation of $0.0102(1)\text{\AA}$ and they adopt a chair conformation; the perpendicular distances of the two chair atoms

in the para positions (N2 and N3) from the plane of the other four atoms of the six-membered piperazine ring are 0.6066(1) and -0.6332(1) Å, respectively. The two ethyl groups, at N2 and N3, adopt an *anti* conformation. The furan ring (C12-C13-C14-C15-O4) is planar with a maximum deviation of 0.0296(1)Å. The dihedral angle between the piperazine ring and the furan ring is 142.4(1)°.

CONCLUSIONS

In this study, new piperazine derivatives were obtained by the reaction of *S*-substituted-3-nitro-1,3-butadienes with some piperazine derivatives in CHCl₃ at room temperature. The substitution reaction proceeds by an addition-elimination mechanism (nucleophilic vinylic substitution (S_NVin)). First, an addition of the attacking reagent to the C,C double bond occurs and in a second step the intermediate product is stabilized by elimination of hydrogen chloride. The novel piperazine derivatives were obtained in good yields, and are yellow solids or oils. They are soluble in organic solvents such as chloroform, petroleum ether. The crystal structure of compound **5d** was solved by X-ray diffraction method. The crystal structure showed that piperazinyl-substituted-3-nitrobutadienes were *E*-isomers.

Acknowledgement: The authors would like to express their gratitude to the Scientific Research Projects Coordination Unit of Istanbul University for financial support (Project Number: 49993).

REFERENCES

1. L. M. Kalatskaya, A. A. Malama, *Mikrobiologiya*, **55**, 618 (1986).
2. P.E. Blower, J. H. Chung, J. S. Verducci, S. Lin, J. K. Park, Z. Dai, C. G. Liu, T. D. Schmittgen, W. C. Reinhold, C. M. Croce, J. N. Weinstein, W. Sadee, *Mol. Cancer Ther.*, **7**, 1 (2008).

3. M. Berkheij, L. van der Sluis, C. Sewing, D. J. den Boer, J. W. Terpstra, H. Hiemstra, W. I. I. Bakker, A. van den Hoogenband, J. H. van Maarseveena, *Tetrahedron Lett.*, **46**, 2369 (2005).
4. R. S. Upadhayaya, N. Sinha, S. Jain., N. Kishore, R. Chandra, S.K. Arora, *Bioorg. Med. Chem.*, **12**, 2225 (2004).
5. Z. Gokmen, N. G. Deniz, M. E. Onan, M. Stasevych, V. Zvarych, O. Komarovska-Porokhnyavets, V. Novikov, *Wulfenia*, **22**(12), 371 (2015).
6. P. Chaudhary, R. Kumar, A. K. Verma, D. Singh, V. Yadav, A. K. Chhillar, G. L. Sharma, R. Chandra, *Bioorg. Med. Chem.*, **14**, 1819 (2006).
7. D. Dauzonne, J. M. Gillardin, F. Lepage, R. Pointet, S. Risse, G. Lamotte, P. Demerseman, *Eur. J. Med. Chem.*, **30**, 53 (1995).
8. C. Ibis, C. Sayil, *Rev. Roum Chim.*, **46** (3), 211 (2001).
9. N. G. Deniz, C. Ibis, *Heteroatom Chem.*, **26**, 51 (2015).
10. C. Ibis, C. Sayil, *Phosphorus, Sulfur, and Silicon*, **92**, 39 (1994).
11. Z. Gokmen, N. Hanay, N. G. Deniz, *J. Chem. Soc. Pak.*, **38**, 1159 (2016).
12. A. Altomare, G. Cascarano, C. Giacovazzo, A. Guagliardi, M. Burla, G. Polidori, M. Camalli, *J. Appl. Cryst.*, **27**, 435 (1994).
13. D. J. Watkin, C. K. Prout, J. R. Carruthers, J. R. Betteridge, *Crystals*, **10**, P. W. Chemical Crystallography Laboratory: Oxford, UK, (1996).
14. L. J. Farrugia, *J. Appl. Crystallogr.*, **30**, 565 (1997).
15. Crystallographic data (excluding structure factors) for the structures in this paper have been deposited in the Cambridge Crystallographic Data Centre as supplementary publication number CCDC-1544558 for **5d**. Copies of the data can be obtained free of charge, via www.ccdc.cam.ac.uk/conts/retrieving.html or from the Cambridge Crystallographic Data Centre, CCDC, 12 Union Road, Cambridge CB2 1EZ, UK; fax: +44 1223 336033. E-mail: deposit@ccdc.cam.ac.uk.

СИНТЕЗ И СПЕКТРАЛНИ СВОЙСТВА НА НОВИ ПИПЕРАЗИНОВИ ПРОИЗВОДНИ И СТРУКТУРЕН АНАЛИЗ

З. Гокмен*, Н. Г. Дениз, М. Е. Онан, Ц. Саил

Истанбулски университет Церахпашиа, Инженерен факултет, Департамент по химия, Отдел по органична химия, 34320 Авчилар, Истанбул, Турция

Постъпила на 15 май, 2017 г. ; приета на 18 април, 2018 г.

(Резюме)

Синтезирани са нови производни на пиперазина чрез реакции на *S*-заместени-3-нитро-1,3-бутадиеми с някои производни на пиперазина: (1-(2-фурил)-, 1-(4-флуоробензил)-, 1-(3-флуорофенил)- и 1-(1-тетрахидро-2-фурил) пиперазин) в CHCl₃ при стайна температура. Структурите на новите съединения са охарактеризирани чрез микроанализ, FT-IR, маспектрометрия, ¹H- и ¹³C-NMR. Кристалната структура на синтезираното съединение **5d** е определена по метода на рентгеновата дифракция. Съединението **5d** кристализира в моноклинната пространствена група P2₁/c с a = 12.5503(2) Å, b = 11.2039(2) Å, c = 14.1007(4) Å, Z = 4. Структурата е определена чрез директен метод (SIR92) и е прецизирана спрямо остатъчния индекс R₁ = 0.031.

Molecular modeling of galanthamine derivatives comprising peptide moiety: methods, targets and accuracy of results

Zh. Velkov^{1*}, D. Tsekova², V. Karadjova², L. Vezenkov²

¹ South-West University "Neofit Rilski", 2700 Blagoevgrad, Bulgaria

² University of Chemical Technology and Metallurgy, Sofia 1756, Bulgaria

Received May 21, 2018; Revised June 6, 2018

Using parametrical and semi-empirical quantum-chemical methods, three important descriptors of a series of peptides, linked to the molecule of galanthamine, were calculated. Studied compounds are planned as drugs for the prevention and treatment of Alzheimer's disease. The descriptors: polarizability, hydration energy and log P, undoubtedly have a bearing on the ability of the compounds to form strong enzyme-inhibitory complexes. Optimal geometries of the investigated peptides, as well as the intramolecular hydrogen bonds that define their structure were found. The most reliable structures defined on the basis of calculated descriptors are suggested.

Keywords: Alzheimer's disease, Galanthamine, Nicotinic acid, Isonicotinic acid, Cholinesterase inhibitor

INTRODUCTION

The Alzheimer's disease (AD) is a neurodegenerative illness which, due to brain disturbances, affects millions of people worldwide. In 1991, it was suggested that β -amyloid protein plays as a key factor in the development of AD [1,2]. Galanthamine (Gal) (Fig. 1) is one of the most useful in medicinal practice inhibitors of the β -amyloid aggregation and the toxicity of the β -amyloid peptide [3]. It is an inhibitor with moderate acetylcholinesterase (AcChE) and low butyrylcholinesterase (BuChE) inhibition activity.

Nicotinic acid is a β -secretase inhibitor, it also increases the levels of good cholesterol (HDL cholesterol) and improves the penetration through blood brain barrier (BBB) [4,5].

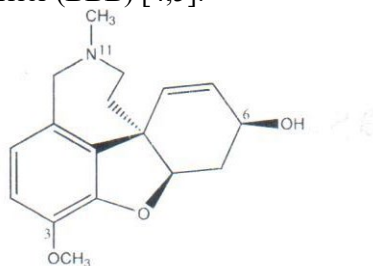


Fig. 1. (-) Galanthamine structure

Galanthamine derivatives containing either in position 6 or in position 11 di- and tripeptides modified with N-(3,4-dichlorophenyl)-D,L-Ala or shortened analogues of β -secretase inhibitor OM 99-2 were synthesized and investigated in our previous study [6-8].

The aim of this study is the modeling of unsynthesized hybrid molecules composed by the galanthamine, a peptide fragment,

Boc-group or nicotinic/isonicotinic acid moiety in position P4 or P5. Thus, we can suggest the creation of new molecules possessing more than one important part for the AD treatment.

Peptides are not agreeable subjects for quantum-chemical investigation. The reasons are several. Firstly, the peptides have many single bonds around which rotation happens, which leads to the existence of many local minima in the hyper-surface of the potential energy of the molecule, evoking high probability to miss the global one and not to find the most likely spatial structure. On the other hand, optimization procedures taking into account the influence of the environment, typical for the living organisms, should be performed. This further complicates the task, although the solvent influence (most commonly water) through only one additional term in the Hamiltonian of the system, rather than by explicit methods, could be expressed. Last but not least, peptides usually contain many atoms, making it impossible to use more precise quantum-chemical methods.

Therefore, the use of purely parametric and semi-empirical quantum-chemical methods is imperative in most of the cases.

In order to optimize the synthetic jobs of new peptide inhibitors of acetylcholinesterase (AChE) and butyrylcholinesterase (BCH), we decided to perform some preliminary quantum chemistry studies and calculate a series of molecular descriptors for these peptides.

The main question arising here is which descriptors should be calculated so to receive an appropriate information for the peptides possessing the mentioned above inhibitory activity.

* To whom all correspondence should be sent:
E-mail: jivko_av@abv.bg

Inhibitory activity of the compounds primarily depends on the spatial and functional congruence with enzymes and, as a consequence, from the forces of attraction inside the enzyme-inhibitory complexes. Since the intermolecular interactions primarily depend on the polarizability of the molecules, it was the first descriptor chosen to be computed [9].

The new drugs design is a process of optimization of both the interaction between ligand and receptor and the ability of the drug to reach its receptor. This makes lipophilicity an important descriptor that correlates well with the biological activity of different substances [10]. Obviously, the next important descriptor worthy to be computed is log P. The calculation of log P of a compound is much easier, quicker and cheaper than determining it by conventional experimental "shakeflask" [11,12] or chromatographic methods [12-14]. There are different approaches to its theoretical calculation [15]. The most common among them is classified as a "fragment constant" method in which the structure of a molecule is divided into fragments (atoms or groups), and the contribution of each group is summed up (sometimes a factor of structural correction is added) [16]. The routine application of these approaches, however, requires careful verification of their validity through comparisons with other experimental or theoretical data. The many QSARs found are proof of the significance of this descriptor. Though recent attempts have been made to calculate log P by using a series of quantum chemical molecular descriptors [17] the parametric computational methods are without a serious alternative.

Another descriptor we decided to calculate was the "hydration energy" that is related to the stability of the found conformations of the investigated peptides. The implemented in Hyperchem 8.0 hydration energy calculation method was created for peptides and proteins [18]. The calculations are based on the "solvent-accessible surface energy" of the molecules, calculated by the approximate method of Still and co-workers [19,20].

The only data for the inhibitory activity of peptides resembling ours are given in [8]. Four peptides show a marked inhibitory activity against BuChE. The biological activity, as well as the calculated polarizability, hydration energy and log P values of these compounds are shown in Table 1. Ultimately, the above descriptors were firstly calculated for peptides already tested for inhibitory activity. Comparison of the descriptors values of the active peptides with the values of those to be synthesized can provide valuable information as to

which of them could be promising enzyme inhibitors.

25 hybrid compounds were investigated in this study. By the proximity of their descriptors and spatial structure with those of the active peptides studied earlier, we will judge whether a compound is promising.

EXPERIMENTAL

All calculations in this work were done using the program package Hyperchem 8.0 Professional edition [21]. This package was chosen because of convenience: it provides an easy creation of the input geometries, amino acid data base and the QSAR module for the calculation of important molecular descriptors. AM1 Hamiltonian is implemented [22] in HyperChem 8.0. We chose a gradient norm limit of 0.01kcal/Å for the geometry optimization.

The polarizability was calculated using the semi-empirical quantum-chemical method AM1. Calculation of log P and hydration energy were carried out using atomic parameters derived by Ghose, Pritchett and Crippen [23,24].

RESULTS AND DISCUSSION

Descriptors given in Table 1 were calculated for the already tested compounds that have shown good inhibition activities towards BuChE. They are our *lead compounds*, because all other investigated structures (from Table 2 and 3) were compared with them.

It was not possible to present here all the spatial structures found. That is why we will describe here the most important intramolecular interactions in each of them.

The first peptide is **(I)** 6-O-[Boc-Val-Asn-Leu-Ala-Gly]-Galantamine (Table 2.) The spatial structure found for this peptide is characterized by three hydrogen bonds: the first is between the hydrogen from the amino group of Gly and the oxygen from Leu (2.222 Å), the second is between the oxygen from Ala and the hydrogen from the amino group of Val (2.191Å), and the third is between N-H of the α -amino group of Asn and the oxygen from Val (2.318 Å). The mean polarizability of the peptide is 383.855 au, less than that of the lead compounds. It is significantly more hydrophilic (log P = -3.53) than the most active peptides. Only the hydration energy is close to that of the most active peptide (-9.54 kcal/mol).

In the next peptide Val is added between Ala and Gly in the first peptide: **(II)** 6-O-[Boc-Val-Asn-Leu-Ala-Val-Gly]-Galantamine. Here the molecular shape is almost linear until to the Leu.

Table 1. Calculated descriptors of compounds reported earlier [8] possessing good inhibition activities towards BuChE

№	Compounds	Polarizability	Hydration energy	Log P	IC50
		au	kcal/mol		μM
(A)	6-O-[Boc-Asn-Leu-Ala-Gly]-Galanthamine	383.204	-10.19	-2.57	17.87
(B)	6-O-[Boc-Val-Asn-Leu-β-Ala-Val-Gly]-Galanthamine	433.162	-8.71	-2.60	6.70
(C)	11-N-demethyl-11-N-N[Boc-Asp(Asn-Leu-Ala-Val-NH-Bzl)]-Galanthamine	513.172	-16.21	-2.29	5.96
(D)	11-N-demethyl-11-N-N-[Boc-Asp(Val-Asn-Leu-β-Ala-Val-NH-Bzl)]-Galanthamine	549.590	-19.35	-2.78	9.31

The β-amide group of the Asn is turned to the Val and forms two relatively strong hydrogen bonds that determine the found spatial structure, as it is shown on Figure 2.

Inclusion of Val is a reason for the increase of the mean polarizability (441.683 au) and the lipophilicity (-3.20). The addition of Val changes these two descriptors in the appropriate direction, but the hydration energy is still high (-15.12 kcal/mol).

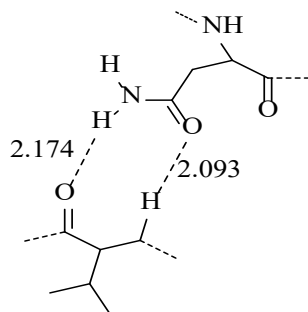


Fig. 2. Hydrogen bonds in 6-O-[Boc-Val-Asn-Leu-Ala-Val-Gly]-Galanthamine.

(III) 11-N-Demethyl-11-N-N-[Boc-Asp(Asn-Leu-β-Ala-Val-NH-Bzl)]-Galanthamine. Its spatial structure is more compact than the foregoing. The reason is most probably related to the increased number of groups which can participate in hydrogen bonds: the urethane group of Boc-protection groups, the β-amide group of Asn, and the Val-NHBzl group at the last position. It is also significant that the peptide bond between Boc-Asp and Asn is formed through the β-carboxyl group of the first amino acid. This leads to the initial right turn of a chain followed by another turn to the left. More significant hydrogen bonds: between C=O from urethane protecting group and H-N from

amino group of Asn (2.07 Å), C=O from α-peptide group of Asn and H-N from β-Ala (2.24 Å), and C=O from benzyl amide and H-N from β-amid group of Asn (2.15 Å). Mean polarizability is 520.103 au, log P is -2.28 and hydration energy is -13.67 kcal/mol. Here, the calculated descriptors are very close to those of the lead compounds. High polarizability, significantly lower hydrophilicity and approximately the same hydration energy as the previous peptide. The primary structures of the peptides in the next group of compounds are obtained by some changes in the primary structure of the previous peptides. In all of them, the N-terminal amino group of the amino acid Asp is linked to nicotinic or isonicotinic acid through an amide link.

(I) 11-N-Demethyl-11-N-N-[nicotinoyl-Asp(Val-Asn-Leu-Ala-Val-NH-Bzl)]-Galanthamine.

This peptide has an interesting β-turn structure with hearpin at Val and Asn. There are relatively weak hydrogen bonds between carbonyl oxygen from the ester function between Asn and NorGal, and the H-atom from the Leu. The mean polarizability is 571.270 au, log P is -3.62, and hydration energy is -19.35 kcal/mol. This peptide has appropriate polarizability, hydration energy, but it is too hydrophilic.

(2) 11-N-Demethyl-11-N-N-[nicotinoyl-Asp(Val-Asn-Leu-β-Ala-Val-NH-Bzl)]-Galanthamine.

In this peptide Ala in peptide 1 is replaced by β-Ala. Several intramolecular hydrogen bonds define the spatial structure of this peptide, the most significant of which is between oxygen of Leu and hydrogen from the amino group of the C-

Table 2. Calculated descriptors of new analogues of compounds reported earlier [8]

№	Compounds	Polarizability	Hydration energy	Log P
		Au	kcal/mol	
(I)	6-O-[Boc-Val-Asn-Leu-Ala-Gly]-Galanthamine	383.855	-9.54	-3.53
(II)	6-O-[Boc-Val-Asn-Leu-Ala-Val-Gly]-Galanthamine	441.683	-15.12	-3.20
(III)	11-N-Demethyl-11-N-N-[Boc-Asp(Asn-Leu-β-Ala-Val-NH-Bzl)]-Galanthamine	520.103	-13.67	-2.28

terminal Val. Mean polarizability 575.2 au, log P -3.97 , hydration energy -20.49 kcal/mol.

(12) 11-N-Demethyl-11-N-N-[isonicotinoyl-Asp(Val-Asn-Leu-Ala-Val-NH-Bzl)]-Galanthamine. Here isonicotinic acid moiety instead of nicotinic acid was included. Its mean polarizability (570.953 au), log P (-3.74), and the hydration energy (-19.46 kcal/mol) are almost the same as in **(1)** 11-N-Demethyl-11-N-N-[nicotinoyl-Asp(Val-Asn-Leu-Ala-Val-NH-Bzl)]-Galanthamine (Table 3) peptide. Here again the lipophilicity is very low, and the hydration energy is slightly larger. Replacing nicotinic acid by isonicotinic acid does not lead to dramatic changes in the chosen descriptors and in the spatial structure.

(13) 11-N-Demethyl-11-N-N-[isonicotinoyl-Asp(Val-Asn-Leu- β -Ala-Val-NH-Bzl)]-Galanthamine. Polarizability: 573.581 au; log P: -3.59 ; hydration energy: -19.73 kcal/mol.

(3) 11-N-Demethyl-11-N-N-[nicotinoyl-Asp(NVal-Asn-Leu- β -Ala-Val-NH-Bzl)]-Galanthamine. In this peptide Val in peptide **2** is replaced by NVal in position P_3 . No strong hydrogen bonds. Polarizability is 571.23 au, log P is -3.98 and hydration energy is -20.18 kcal/mol.

(4) 11-N-Demethyl-11-N-N-[nicotinoyl-Asp(NVal-Asn-Leu- β -Ala-NVal-NH-Bzl)]-Galanthamine. In peptide **3** Val in position P_2 was replaced by NVal. The mean polarizability is almost the same (571.785 au), log P is -3.98 , slightly reduced comparing to the previous, but the hydration energy (-20.10 kcal/mol) is slightly increased compared to the previous one.

(5) 11-N-Demethyl-11-N-N-[nicotinoyl-Asp(NVal-Asn-Leu-Ala-NVal-NH-Bzl)]-Galanthamine. Here β -Ala in peptide **4** is replaced by Ala. The structure is similar to that of the previous peptides. There is a hearpin at NVal and Asn and two important H-bonds at the same atoms as in previous peptides. Mean polarizability: 579.048 au, log P: -3.12 , hydration energy: -18.97 kcal/mol. The polarizability and hydration energy are appropriate but the peptide is too hydrophilic.

(14) 11-N-Demethyl-11-N-N-[isonicotinoyl-Asp(NVal-Asn-Leu- β -Ala-NVal-NH-Bzl)]-Galanthamine. Here nicotinic acid in peptide **4** was replaced by isonicotinic acid. There is one more significant hydrogen bond between the urethane carbonyl oxygen and the Ala N-H and at least two weaker ones. Mean polarizability is higher relative to the previous peptide (571.201 au) as well as log P (-3.75) and the hydration energy is slightly decreased (-19.42 kcal/mol).

(6) 11-N-Demethyl-11-N-N-[nicotinoyl-Asp(Tle-Asn-Leu- β -Ala-Val-NH-Bzl)]-Galanthamine.

In this peptide Val in peptide **2** is replaced by Tle in position P_3 . The only stronger hydrogen bond (2.25 Å) in this peptide is between the oxygen of the Leu and hydrogen from the C-terminal benzylamide. Polarizability is (578.35 au), log P is (-3.47) and hydration energy is -19.56 kcal/mol.

(7) 11-N-Demethyl-11-N-N-[nicotinoyl-Asp(Tle-Asn-Leu-Ala-Val-NH-Bzl)]-Galanthamine. Polarizability here is 575.535 au; log P is -3.11 , and the hydration energy is -18.77 kcal/mol.

(15) 11-N-Demethyl-11-N-N-[isonicotinoyl-Asp(Tle-Asn-Leu- β -Ala-Val-NH-Bzl)]-Galanthamine. Polarizability of this peptide is 577.463 au; log P is -3.47 ; and the hydration energy is -19.57 kcal/mol.

(16) 11-N-Demethyl-11-N-N-[isonicotinoyl-Asp(Tle-Asn-Leu-Ala-Val-NH-Bzl)]-Galanthamine. Its polarizability is 575.913 au, log P is -3.23 , and hydration energy is -18.86 kcal/mol.

Several optimized structures were considered for each of the last peptides by variation of the input geometry. The only descriptor for which different values were obtained is the polarizability. The difference between them does not exceed 7 au, which is about 1%. In this case the average values of polarizability are shown in tables 3 and 4.

In the next group of compounds the Val residue in position P_3 was removed.

(8) 11-N-Demethyl-11-N-N-[nicotinoyl-Asp(Asn-Leu-Ala-Val-NH-Bzl)]-Galanthamine. As a result of this change, the average polarizability decreased to 520.479 au, the hydration energy to -18.12 kcal/mol and log P increased in hydrophilic direction -4.07 . Compared with the previous compounds, this peptide is too hydrophilic.

Replacement of Ala with β -Ala gives the next peptide.

(9) 11-N-Demethyl-11-N-N-[nicotinoyl-Asp(Asn-Leu- β -Ala-Val-NH-Bzl)]-Galanthamine. The spatial structure of the β -Ala analogue is interesting. After initial rotation to the right at Leu, the direction of rotation changes to the left. The structure is fixed by the presence of three relatively strong hydrogen bonds. First is between the oxygen of the amide group of nicotinic acid and the hydrogen from the β -amide group between Asp and Asn; the second is between the oxygen of the peptide bond between Asn and Leu, and the third is between the hydrogen from the Asn β -amide group and the oxygen from the benzylamide group at the end of the peptide. The values of the descriptors do not differ significantly from those of peptide 11-N-Demethyl-11-N-N-[nicotinoyl-Asp(Asn-Leu-Ala-Val-NH-Bzl)]-Galanthamine. This peptide has a mean polarizability 519.703 au, log P -4.43 and

hydration energy -18.31 kcal/mol. The peptide is slightly more hydrophilic than **(8)** 11-N-Demethyl-11-N-N-[nicotinoyl-Asp(Asn-Leu-Ala-Val-NH-Bzl)]-Galanthamine.

(17) 11-N-Demethyl-11-N-N-[isonicotinoyl-Asp(Asn-Leu-Ala-Val-NH-Bzl)]-Galanthamine. Mean polarizability is 519.682 au, $\log P$ is -4.07 , and hydration energy is -18.06 kcal/mol. The peptide is too hydrophilic.

(18) 11-N-Demethyl-11-N-N-[isonicotinoyl-Asp(Asn-Leu- β -Ala-Val-NH-Bzl)]-Galanthamine. Mean polarizability is 518.606 au, $\log P$ is -4.43 , and hydration energy is -18.63 kcal/mol.

Replacement of Asn with Asp gives the next peptides:

(10) 11-N-Demethyl-11-N-N-[nicotinoyl-Asp(Asp-Leu-Ala-Val-NH-Bzl)]-Galanthamine.

Surprisingly, the optimal geometry we obtained for this peptide significantly differs from that of the previous peptides. Three strong hydrogen bonds are identified for it: between the oxygen of the nicotinic acid and the hydrogen from the amide group between Asp and Asp (2.09 Å), the oxygen from the peptide bond between Asp and Leu (2.15 Å) and the carboxyl hydrogen of Asp and the oxygen from the benzamide group. The mean polarizability is 518.322 au, $\log P$ is -3.21 , and the hydration energy is -19.38 kcal/mol. The only

desired change here concerns $\log P$ toward lower hydrophilicity.

The optimized structure of the next peptide **(11)** 11-N-Demethyl-11-N-N-[nicotinoyl-Asp(Asp-Leu- β -Ala-Val-NH-Bzl)]-Galanthamine is similar to the structure of the previous peptide, but hydrogen bonds are stronger. Its average polarizability is 517.134 au, $\log P$ is -3.56 , and its hydration energy is -20.14 kcal/mol.

The following two peptides are analogues of the previous two in which nicotinic acid is replaced by isonicotinic acid. This change does not lead to noticeable differences in spatial structures compared to the previous peptides, or to noticeable differences in the calculated descriptors. It has only to be said that the substitution of β -amide group by the carboxyl group significantly reduces the value of $\log P$ of the corresponding peptide.

(19) 11-N-Demethyl-11-N-N-[Iso-nicotinoyl-Asp(Asp-Leu- β -Ala-Val-NH-Bzl)]-Galanthamine. Mean polarizability: 516.246 au, $\log P$: -3.56 , and hydration energy: -20.50 kcal/mol.

The last peptides are too hydrophilic compared to the previous ones.

(20) 11-N-Demethyl-11-N-N-[Iso-nicotinoyl-Asp(Asp-Leu-Ala-Val-NH-Bzl)]-Galanthamine. Mean polarizability: 517.364 au, $\log P$: -3.21 , and hydration energy: -19.76 kcal/mol.

Table 3. Calculated descriptors of galanthamine derivatives containing peptide fragment and nicotinic acid.

№	Compounds	Polarizability	Hydration energy	Log P
		au	kcal/mol	
(1)	11-N-Demethyl-11-N-N-[nicotinoyl-Asp(Val-Asn-Leu-Ala-Val-NH-Bzl)]-Galanthamine	571.270	-19.35	-3.62
(2)	11-N-Demethyl-11-N-N-[nicotinoyl-Asp(Val-Asn-Leu- β -Ala-Val-NH-Bzl)]-Galanthamine	575.2	-20.49	-3.97
(3)	11-N-Demethyl-11-N-N-[nicotinoyl-Asp(NVal-Asn-Leu- β -Ala-Val-NH-Bzl)]-Galanthamine	571.23	-20.18	-3.98
(4)	11-N-Demethyl-11-N-N-[nicotinoyl-Asp(NVal-Asn-Leu- β -Ala-NVal-NH-Bzl)]-Galanthamine	571.785	-20.10	-3.98
(5)	11-N-Demethyl-11-N-N-[nicotinoyl-Asp(NVal-Asn-Leu-Ala-NVal-NH-Bzl)]-Galanthamine	579.048	-18.97	-3.12
(6)	11-N-Demethyl-11-N-N-[nicotinoyl-Asp(Tle-Asn-Leu- β -Ala-Val-NH-Bzl)]-Galanthamine	578.35	-19.56	-3.47
(7)	11-N-Demethyl-11-N-N-[nicotinoyl-Asp(Tle-Asn-Leu-Ala-Val-NH-Bzl)]-Galanthamine	575.535	-18.77	-3.11
(8)	11-N-Demethyl-11-N-N-[nicotinoyl-Asp(Asn-Leu-Ala-Val-NH-Bzl)]-Galanthamine	520.479	-18.12	-4.07
(9)	11-N-Demethyl-11-N-N-[nicotinoyl-Asp(Asn-Leu- β -Ala-Val-NH-Bzl)]-Galanthamine	519.703	-18.31	-4.43
(10)	11-N-Demethyl-11-N-N-[nicotinoyl-Asp(Asp-Leu-Ala-Val-NH-Bzl)]-Galanthamine	518.322	-19.38	-3.21
(11)	11-N-Demethyl-11-N-N-[nicotinoyl-Asp(Asp-Leu- β -Ala-Val-NH-Bzl)]-Galanthamine	517.134	-20.14	-3.56

Table 4. Calculated descriptors of galanthamine derivatives containing peptide fragment and isonicotinic acid.

№	Compounds	Polarizability	Hydration energy	Log P
		au	kcal/mol	
(12)	11-N-Demethyl-11-N-N-[isonicotinoyl-Asp(Val-Asn-Leu-Ala-Val-NH-Bzl)]-Galanthamine	570.953	-19.46	-3.74
(13)	11-N-Demethyl-11-N-N-[isonicotinoyl-Asp(Val-Asn-Leu-β-Ala-Val-NH-Bzl)]-Galanthamine	573.581	-19.73	-3.59
(14)	11-N-Demethyl-11-N-N-[isonicotinoyl-Asp(NVal-Asn-Leu-β-Ala-NVal-NH-Bzl)]-Galanthamine	571.201	-19.42	-3.75
(15)	11-N-Demethyl-11-N-N-[Isonicotinoyl-Asp(Tle-Asn-Leu-b-Ala-Val-NH-Bzl)]-Galanthamine	577.463	-19.57	-3.47
(16)	11-N-Demethyl-11-N-N-[Isonicotinoyl-Asp(Tle-Asn-Leu-Ala-Val-NH-Bzl)]-Galanthamine	575.913	-18.86	-3.23
(17)	11-N-Demethyl-11-N-N-[Isonicotinoyl-Asp(Asn-Leu-Ala-Val-NH-Bzl)]-Galanthamine	519.682	-18.06	-4.07
(18)	11-N-Demethyl-11-N-N-[isonicotinoyl-Asp(Asn-Leu-β-Ala-Val-NH-Bzl)]-Galanthamine	518.606	-18.63	-4.43
(19)	11-N-Demethyl-11-N-N-[isonicotinoyl-Asp(Asp-Leu-β-Ala-Val-NH-Bzl)]-Galanthamine	516.246	-20.50	-3.56
(20)	11-N-Demethyl-11-N-N-[isonicotinoyl-Asp(Asp-Leu-Ala-Val-NH-Bzl)]-Galanthamine	517.364	-19.76	-3.21

CONCLUSIONS

We have chosen three important descriptors, characterising the primary and spatial structure of investigated compounds. These descriptors were calculated for the so called „lead compounds“, compounds possessing inhibitory activity toward BuChE and the values obtained were used for comparison to the planned for synthesis compounds. High polarizability (between 500 and 515 au), hydration energy of about $-16 \div -17$ kcal/mol and log P lower than -3.53 were calculated as important data.

The closest lipophilicity to the lead compounds possess peptides 5, 7, 10, 16 and 20. The rest of the peptides are too hydrophilic (log P higher than -3.23).

Several peptides have close polarizability (lower than 520 au): 9, 10, 11 and 17, 18, 19 and 20. The remaining peptides are of too polarizable.

All planned peptides have higher hydration energy than the lead compounds (higher than 18 kcal/mol).

Assuming that the slightly higher polarizability is not necessarily undesirable

feature, and comparing by the log P it becomes clear that peptides **10** (11-N-Demethyl-11-N-N-[nicotinoyl-Asp(Asp-Leu-Ala-Val-NH-Bzl)]-Galanthamine) and **20** (11-N-Demethyl-11-N-N-[Isonicotinoyl-Asp(Asp-Leu-Ala-Val-NH-Bzl)]-Galanthamine) are the most suitable for synthesis.

Acknowledgments: This study is supported by the Scientific Research Fund of Bulgaria through the project DH 03/8, “Galanthamine’s and 4-aminopyridine’s derivatives containing peptide motif with expected effect on the Alzheimer’s disease and multiple sclerosis”.

REFERENCES

- 1.J. Hardy, D. Allsop, *Trends in Pharmacological Sciences*, **12**(10), 383(1991).
- 2.A. Mudher, S. Lovestone, *Trends in Neurosciences*, **25**(1), 22 (2002).
- 3.B. Matharua, B.G. Gibsona, R. Parsons, T.N. Huckerby, S.A. Moore, L.J. Coopereb, R.M.D. Allsop, B. Austena, *J. Neurol. Sci.*, **280** (1-2), 49 (2009).
- 4.L.V. Hankes, H.H. Coenen, E. Rota, K.J. Langen, H. Herzog, W. Wutz, G. Stoecklin, *Adv. Exp. Med. Biol.*, **294**, 675 (1991)

5. J. Chen, M. Chopp, *The Open Drug Discovery Journal*, **2**, 181 (2010).
6. L. T. Vezenkov, M. G. Georgieva, D. L. Danalev, Tch. B. Ivanov, G. I. Ivanova, *Protein & Peptide Letters*, **16**, 1024 (2009).
7. L. Vezenkov, M. Georgieva, D. Danalev, Tch. Ivanov, A. Bakalova, K. Hristov, V. Mitev, 2011, EP2123328-B1.
8. L. T. Vezenkov, L. Ilieva, D. L. Danalev, A. Bakalova, N. Vassilev, N. Danchev, I. Nikolova, *Protein & Peptide Letters*, **22**, 913 (2015).
9. H. Adams, V. P. Whittaker, *Biochimica Et Biophysica Acta*, **4**, 543 (1950).
10. X. Liu, B. Testa, A. Fahr, *Pharm Res*, **28** (5), 962 (2011).
11. K. B. Lodge, *J. Chem. Eng. Data*, **44**, 1321 (1999).
12. D. J. Edelbach, K. B. Lodge, *Phys. Chem. Chem. Phys.*, **2**, 1763 (2000).
13. C. V. Eadsforth, P. Moser, *Chemosphere*, **12**, 1459 (1983).
14. A. Finizio, M. Vighi, D. Sandroni, *Chemosphere*, **34**, 131 (1997).
15. P. Buchwald, N. Bodor, *Current Medicinal Chemistry*, **5**, 353 (1998).
16. E. Benfenati, G. Gini, N. Piclin, A. Roncaglioni, M. R. Vari, *Chemosphere*, **53**, 1155 (2003).
17. Ou. Ouattara, N. Ziao, *Computational Chemistry*, **5**, 38 (2017).
18. T. Ooi, M. Oobatake, G. Nemethy, H. A. Scheraga, *Proc. Natl. Acad. Sci. USA*, **84**, 3086 (1987).
19. W. Hasel, T. F. Hendrickson, W. C. Still, *Tet. Comput. Meth.*, **1**, 103 (1988).
20. W. C. Still, A. Tempczyk, R. C. Hawley, T. Hendrickson, *J. Am. Chem. Soc.*, **112**, 6127 (1990).
21. Hyperchem (Molecular Modeling System) Hypercube, Inc., 1115 Nw, 4th Street, Gainesville, FL 32601; USA, 2007.
22. J. S. Dewar Michael, Eve G. Zoebisch, Eamonn F. Healy, James J. P. Stewart, *J. Am. Chem. Soc.*, **107**, 13, (1985).
23. A. K. Ghose, A. Pritchett, G. M. Crippen, *J. Comp. Chem.*, **9**, 80 (1988).
24. V. N. Viswanadhan, A. K. Ghose, G. N. Revankar, R. K. Robins, *J. Chem. Inf. Compt. Sci.*, **29**, 163 (1989).

МОЛЕКУЛНО МОДЕЛИРАНЕ НА ПРОИЗВОДНИ НА ГАЛАНТАМИН, СЪДЪРЖАЩИ ПЕПТИДНА ЧАСТ: МЕТОДИ, ЦЕЛИ И ТОЧНОСТ НА РЕЗУЛТАТИТЕ

Ж. Велков^{1*}, Д. Цекова², В. Караджова², Л. Везенков²

¹ Югозападен университет „Неофит Рилски“, 2700 Благоевград, България

² Химикотехнологичен и металургичен университет, 1756 София, България

Постъпила на 21 май, 2018 г.; коригирана на 6 юни, 2018 г.

(Резюме)

С използване на чисто параметрични и полуемпирични квантово-химични методи са изчислени три важни дескриптора на серия от пептиди, свързани с молекулата на галантамина. Изследваните съединения са планирани като лекарства за превенция и лечение на болестта на Алцхаймер. Дескрипторите поляризуемост, енергия на хидратация и log P несъмнено имат отношение към способността на съединенията да образуват здрави ензим-инхибиращи комплекси. Установени са оптималните геометрии на изследваните пептиди, както и вътремолекулните водородни връзки, които определят структурата им. Предложени са най-достоверните структури, дефинирани на основата на изчислените дескриптори.

Newly characterized butyrate producing *Clostridium* sp. strain 4a1, isolated from chickpea beans (*Cicer arietinum* L.)

S.P. Hristoskova¹, L.D. Yocheva^{2*}, D.S. Yankov¹, S.T. Danova^{3*}

¹ Institute of Chemical Engineering, Bulgarian Academy of Sciences, Acad. G. Bontchev Str. 103, 1113 Sofia, Bulgaria

² Department of Biology, Medical Genetics and Microbiology, Faculty of Medicine, Sofia University "St. Kliment Ohridski", 15 Tsar Osvooboditel Blvd., 1504 Sofia, Bulgaria

³ The Stephan Angeloff Institute of Microbiology, Bulgarian Academy of Sciences, 26, Acad. G. Bontchev Str., 1113 Sofia, Bulgaria

Received February 1, 2018; Revised February 15, 2018

Butyric acid is a valuable chemical with wide application in various industries. The interest in its biotechnological production is revived in view to the application in the production of alternative fuels from biomass feedstocks. Microorganisms of genus *Clostridium* are well known as producers of butyric acid. *Clostridium* species was found to dominate the system in the spontaneous chickpea fermentation. In the present study a *Clostridium* sp. strain 4a1 from chickpea beans fermentation was selected as a good producer of butyric acid. Some process parameters as initial pH of the medium (7.5), temperature (37 °C), medium composition and glucose concentration (20 g/l) were determined. The strain was identified as *Clostridium beijerinckii* (97% similarity) on the basis of classical and modern polyphasic taxonomy methods.

Keywords: Butyric acid, Chickpea beans, Fermentation, *Clostridium*, Polyphasic taxonomy.

INTRODUCTION

Butyric acid (C₄H₈O₂, IUPAC name butanoic acid) is a chemical with wide application in several industries like food, pharmaceutical, chemical industry, etc. Among the main applications of butyric acid is the production of plastics for textile fibers, of butyrate esters as food and perfume additives, and of biodegradable biopolymers. Because of its ability to neutralize the activity of food carcinogens [1], to lower cholesterol levels [2] and to inhibit tumor cells [3] butyric acid is subject to increased research interest. Derivatives of butyric acid are used for the production of anti-thyroid drugs and vasopressors [4], as well as of antioxidants. In the recent years, butyric acid is used in the production of biobutanol, not only as an intermediate in acetone-butanol-ethanol (ABE) fermentation, but as a co-fermenting substrate, leading to significant enhancement of butanol yield [5, 6].

Butyric acid can be produced *via* chemical or biotechnological routes. Bacteria involved in the production of butyric acid are divided into two groups – producing acid as a final product and producing mostly butanol. The ABE fermentation is one of the oldest industrial fermentations and in the first half of the twentieth century it has become one of the largest biotechnological processes [7]. Later on, the fermentative production of butyric acid could not compete to the low price of acid produced

via petrochemical route and nowadays butyric acid is mainly produced *via* oxidation of butyraldehyde derived from propylene by an oxo process. The annual production of butyric acid is estimated to be around 50,000 t [8].

In the last 20 years, the interest towards the fermentative production of butyric acid has revived. This is due to the increasing demand for butyric acid from microbial fermentation, on one hand because of strong demand for bio-based products and decreasing resources of crude oil and environmental issues on the other hand. The development of *in-situ* separation processes, helping to overcome low final product concentration and product inhibition problems, as well as the possibility of using agricultural and industrial byproducts and wastes as substrates also play an important role.

According to Zhang *et al.* [7] there are more than 10 butyrate-producing bacteria species from at least seven genera with butyric acid-producing capacity being investigated for potential industrial application. The microorganisms belong to the genera *Clostridium*, *Butyrivibrio*, *Butyribacterium*, *Eubacterium*, *Fusobacterium*, *Megasphaera*, and *Sarcina* and all of them are anaerobic [9]. In view of industrial application, the strains of *Clostridium* (*Cl. butyricum*, *Cl. tyrobutyricum* and *Cl. thermobutyricum*) have been largely studied for the production of butyric acid. However, because acetic acid is also produced as a byproduct, genetic engineering and process development have been

* To whom all correspondence should be sent:

E-mail: lyubomirayocheva@abv.bg;

stdanova@yahoo.com

attempted to increase butyric acid yield and selectivity [10].

Chickpea (*Cicer arietinum* L.) is one of the most important legumes in the world. It is known from ancient times and now is grown in many countries – in the Balkans, Mediterranean, Middle East, Indian subcontinent, and Americas. There are two distinct types of cultivated chickpea, Desi, and Kabuli – they differ by size and color [11]. Chickpea is utilized either in whole or paste form as a main or side dish after cooking or as a snack food after roasting. In some Mediterranean countries, fermented chickpea is being used as a leavening agent to make traditional bread and rusks [12]. By the addition of fermented chickpea beans in the wheat flour, besides the enhancement of the nutritional quality, the product's shelf life is also expanded [13]. In the most of the Mediterranean countries, fermented chickpea is used as a leavening agent to make baked products [14]. Bread prepared with chickpea yeast ("simmits") is a very popular product in Bulgaria, some of the Balkans countries and the Near East [15].

The data for the microbial community in fermented chickpea are very limited in the scientific literature. There are only a few published research results. According to Tangüler [16] in studies done in Turkey, lactic acid bacteria such as *Lb. plantarum*, *Lb. pentosus*, *Lb. bifermantans*, *Str.thermophilus*, *Lc. ssp. lactis*, *Lb. brevis*, *Lb. plantarum*, *Lb. pentosus*, coccobacillus *Weissella confusa* and yeasts such as *S. cerevisiae* were identified. Katsaboxakis and K. Mallidis [17] studied the microflora of soak water during natural fermentation of coarsely ground chickpea seed at different temperatures. A gas-producing *Clostridium* species was found to dominate this fermentation system, particularly at higher temperatures. Gram-negative bacteria and yeasts were not found. *Bacillus* species, as well as *Lactobacillus*, *Corynebacterium*, *Micrococcus* and *Pediococcus* spp. were isolated. Kyyaly et al. [18] investigated the major bacteria genera in the soaked fermented chickpea and isolated the following species: *Clostridium sartagoforme*, *Bacillus thuringiensis* and *Enterococcus faecium*. Only *Clostridium* sp. produced gas from sugar and hydrolysed gluten during dough fermentation. In a study of changes in numbers and kinds of bacteria during a chickpea submerged fermentation used as a leavening agent for bread production Hatzikamari et al. [12, 19] isolated only representatives of bacilli (*B. cereus*, *B. thuringiensis* and *B. licheniformis*) and clostridia (*Cl. perfringens* and *Cl. beijerinckii*). *B. cereus* and *C. perfringens* predominantly growing during fermentation do not

seem to form any toxins. Antonova-Nikolova et al. [15] studied the dynamics of the development of chickpeas fermentation microflora. They found only representatives of the genera *Bacillus* and *Clostridium* and suggested additional studies to prove the possible participation of lactic acid bacteria. On the basis of phenotypic characteristics and numerical taxonomy clostridial strains were related in 3 clusters of *Cl. acetivum*, *Cl. acidurici* and *Cl. polysaccharolyticum* and bacilli in 8 groups of *B. lentus*, *B. pumilus*, *B. subtilis*, *B. coagulans*, *B. sphaericus*, *B. alvei*, *B. polymyxa* and *B. cereus* [20].

Fermentation of chickpea beans (*Cicer arietinum* L.), as it was shown in previous investigations [15, 20, 21], was caused by members of the genus *Clostridium*. Therefore, it could be used as a source for isolation of desirable clostridial strains. With this aim 14 new strains were isolated from four samples of chickpea crops harvested from different geographical regions of North and South Bulgaria during 1996 and 1997. Initial characterization of the metabolic activity of these 14 pure cultures isolated from chickpea beans fermentation showed the strain 4a1 as a promising isolate [22].

In the present study, the *Clostridium* sp. strain 4a1 from chickpea beans was characterized as a good butyric producing strain and was identified according to the modern polyphasic taxonomy.

MATERIALS AND METHODS

Chickpea beans fermentation

Coarsely ground chickpea beans were put in a bottle with a narrow long neck and washed twice with boiled and slightly salted water. They were poured on to the bottle neck and kept at about 40° C until thick foam was rising and started to overflow, and the fermentation liquid clarified [23]. The duration of fermentation varied between 8 and 18 h.

Microorganisms, media and culture conditions

A protocol for *Clostridium* sp. isolation from different samples with fermented chickpea beans was designed including steps of initial enrichment followed by cultivation and pure cultures isolation [23]. The isolation of pure cultures and their maintenance were carried out on nutrient agar with 3% (w/v) glucose. A chickpea infusion medium was used as enrichment medium and for determination of gas and butyric acid formation. It was prepared as 1 part of coarsely ground chickpeas was poured with 5 parts of tap water. After autoclaving (1 atm/30 min) the mixture was

filtered through cheesecloth and the filtrate was centrifuged at 4000 rpm for 30 min. The separated supernatant was adjusted to pH 7.5 with 1N NaOH and sterilized again at 0.8 atm for 20 min. All isolates were sub-cultured on blood agar (BulBio, Bulgaria) and the hemolysis was monitored.

Disinfectants examinations were performed using PY (peptone – yeast extract) broth, PYG (peptone – yeast extract – glucose) broth, PYG broth with 1% fructose or 20% bile, yolk agar, nutrient agar with 6.5 % NaCl, gelatin, starch agar by procedures described in Bergey's manual [24] using Winogradsky's N-free selective medium for anaerobic nitrogen fixation.

The isolates were lyophilized in protective medium (10% skimmed milk, 1.5% gelatin and 10% sucrose) and stored at 4°C until tests [25].

The morphological, physiological and biochemical characterizations of the isolated strains were carried out under anaerobic conditions in an anaerobic jar (Anaerocult, Merck) at 40 °C according to [24].

Phenotypic characterization

The presumptive colonies of *Clostridium spp.* were described macroscopically on blood agar and characterized microscopically by using Gram's staining. Starch inclusions and spore-formation were confirmed by staining [26]. Motility of the strains was examined by the classical hanging drop method. Bacterial growth at different temperatures was determined after 3 days at 40 °C and 55 °C, after 5 days at 22 °C, and after 21 days at 4 °C in nutrient agar with 1% glucose. The growth in nutrient agar with 6.5% sodium chloride was recorded on the 5th day. Nitrogen fixation was observed after 24-48 h, as a positive reaction was gas formation.

Biochemical characterization

Several biochemical tests such as carbohydrate fermentation test, methyl red and Voges-Proskauer (MR-VP) tests, indole reaction, starch, gelatin and esculin hydrolysis, enzyme activity (catalase, lecithinase, lipase, urease, reductase), bile susceptibility, H₂S and butyric acid production, hemolysis were performed according to the procedures described in [26].

Numerical taxonomy

Using the K-mean method, a program was set up for clustering of isolated clostridial strains on the basis of similarity to the type of clostridial cultures.

A butyrate producing strain was identified to the species level, according to the modern polyphasic taxonomy. Isolation of genomic DNA from a pure exponential culture of the selected *Clostridium* strain was performed according to the method of Delley *et al.* [27] in modification. The obtained DNA sample was analyzed by 1% v/v agarose gel electrophoresis and the concentration and purity were checked. The DNA, stored at -20°C, was used as a target in the PCR assay and following sequencing analysis. Amplification of 16S rDNA gene was carried out with the following pairs of primers: forward primer fD1 (5'-AGA GTT TGA TCC TGG CTC AG-3') and reverse primer rD1 (5'-AAG GAG GTG ATC CAG CC-3'). Amplification reactions were performed with 2×PCR TaqMixture kit (HiMedia, India), primers rD1 and fD1 (0.6 μM each) and 1 ng of DNA/μl. They were conducted on the above-mentioned apparatus under the following amplification conditions: initial denaturation at 94 °C for 3 min, 40 °C for 5 min, 72 °C for 5 min, 32 cycles of denaturation at 94 °C for 5 min, followed by 35 cycles of denaturation at 94 °C for 1 min, annealing at 56.5 °C for 75 s, elongation at 72 °C for 75 s, and a final synthesis at 72 °C for 5 min. The amplified products of approximately 1550 bp were purified and sequenced using a 3730×1 DNA analyzer (Thermo Fisher Scientific, USA) by Macrogen Inc. (Belgium). The obtained sequences were analyzed with *Chromas 2.3* programme (*Technelysium Pty Ltd., Australia*) and species identification of the strain was performed by BLASTN analysis.

Butyric acid production

In view to investigate the influence of different parameters on butyric acid production nutrient medium CM with composition (g/l): yeast extract - 5; K₂HPO₄ - 1; KH₂PO₄ - 1; CaCl₂·2H₂O - 0.01; (NH₄)₂SO₄ - 0.1; FeSO₄·7H₂O - 0.005; MgSO₄·7H₂O - 0.1 was used. The medium was sterilized for 20 min at 121°C. Glucose (20 g/l) was used as a substrate and the fermentations were carried out without pH control (initial pH was 7.5).

Analytical methods

The concentrations of glucose and butyric acid were determined by HPLC. Samples were analyzed on a chromatographic system consisting of a pump Smartline S-100, Knauer, RI detector - Perkin - Elmer LC- 25RI, column Aminex HPX- 87H, Biorad, 300×7.8 mm and specialized software EuroChom, Knauer. 0.01 N H₂SO₄ was used as mobile phase at a flow rate of 0.6 ml/min.

Clostridia and its role in the fermentation of various non-milk substrates are relatively poorly studied. At the same time, the interest in the so-called "functional foods" with beneficial properties increases. The use of butyrate-producing microorganisms for food production is also among the weakly studied issues. Therefore, a key part of the study of spontaneous chickpea fermentation was the characterization of the species involved.

Butyric acid production by newly isolated bacteria from chickpea beans

In the present work a newly isolated strain from spontaneous fermented chickpea beans was characterized as a butyrate producer and was identified. This strain is a part of a group of 21 newly isolated bacteria from laboratory made spontaneous fermentations of chickpea beans in water. A pre-selection between isolates was made on the base of classical microbiological characteristics. Thus, 14 strains were characterized as belonging to the genus *Clostridium* and were estimated as butyrate producers. The strain 4a1 showed the highest butyric acid production. In addition, optimization of some process parameters was carried out.

Optimization of some process parameters - pH of the medium and temperature

The influence of pH on the growth and butyric acid production was investigated in the interval 4.5 -10.0. As it can be seen on Fig.1 the maximum production of butyric acid (~6 g/l) was observed at initial pH=7.5.

The temperature influence was studied at four levels – 4, 22, 37 and 55 °C. The best growth and maximal production was observed at 37 °C (Fig. 2).

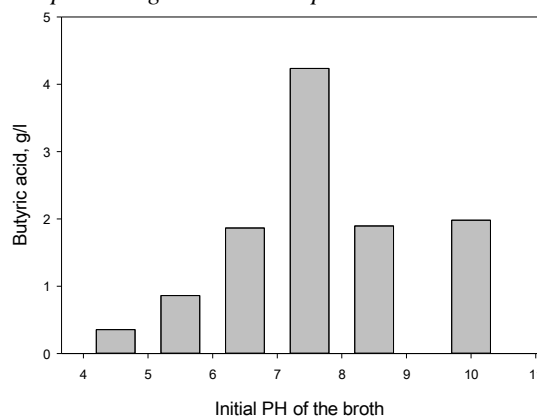


Fig. 1. Influence of the initial pH on the butyric acid production by 4a1 strain.

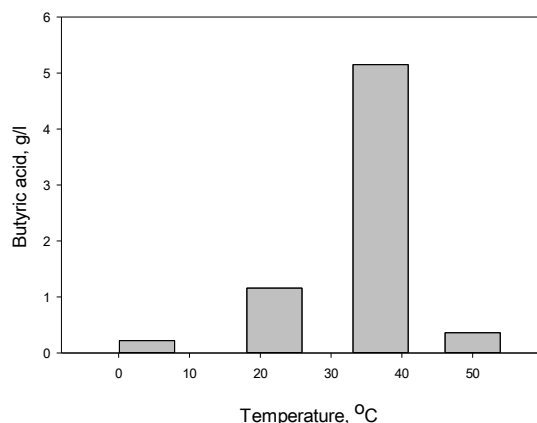


Fig. 2. Influence of temperature on butyric acid production by 4a1 strain.

Effect of medium composition

Seven medium compositions with different amounts of various nitrogen sources and microelements were tested (Table 1). The composition CM7 was found as optimal for maximal butyric acid production.

Identification of pre-selected butyric acid producing strain 4a1

All strains with industrial potential and especially for food-associated application have to be identified to the species level, according to the

Table 1. Media composition for butyric acid production by 4a1 strain

	Glucose	Peptone	Yeast Extract	Meat Extract	KH ₂ PO ₄	K ₂ HPO ₄	MgSO ₄ ×7H ₂ O	CaCl ₂ ×2H ₂ O	FeSO ₄ ×7H ₂ O	NaCl		
CM1	5	10	3	10	-	-	-	-	-	5		
CM2	5	-	1	-	0.5	0.5	0.21	0.001	-	-		
CM3	5	2	5	-	1	1	0.1	0.01	0.005	-		
	Glucose	Peptone	Yeast Extract	Tryptone	KH ₂ PO ₄	K ₂ HPO ₄	MgSO ₄ ×7H ₂ O	CaCl ₂ ×2H ₂ O	FeSO ₄ ×7H ₂ O	MnCl ₂ ×4H ₂ O	CoCl ₂ ×6H ₂ O	Na ₂ MoCl ₄ ×2H ₂ O
CM4	5	2	5	2	1	1	0.025	0.015	0.01	0.002	0.025	0.025
CM5	10	2	6	2	1.2	5.5	0.025	0.015	0.01	0.002	0.025	0.025
CM6	15	5	6.5	2	1.2	3.5	0.025	0.015	0.01	0.002	0.025	0.025
CM7	20	2	6	2	2	5.5	0.025	0.015	0.01	0.002	0.025	0.025

modern polyphasic taxonomy. Initial taxonomic characterization was carried out according to Bergey's Manual of systematic bacteriology [24]. The strain Aa1 was initially identified as *Clostridium* sp. on the base of morphological characteristics, as Gram-positive staining, catalase-negative and spore-forming, motile, rod-shaped bacteria, with polymorphism of cells (Fig. 3a). Subterminal spores are oval and swell vegetative cells. The strain 4a1 forms round, large, white, glossy non-hemolytic colonies, convex, with regular edge and uniform consistency after anaerobic growth for 72 h on blood agar (BulBio, Bulgaria) (Fig.3b).

Several biochemical tests, usually applied for Gram-positive bacteria from the genus *Clostridium* were carried out and the results are summarized in Table 2.

The investigated strain does not grow under aerobic conditions. The most abundant growth is observed at 37 °C, showing that the strain belongs to mesophilic clostridia.

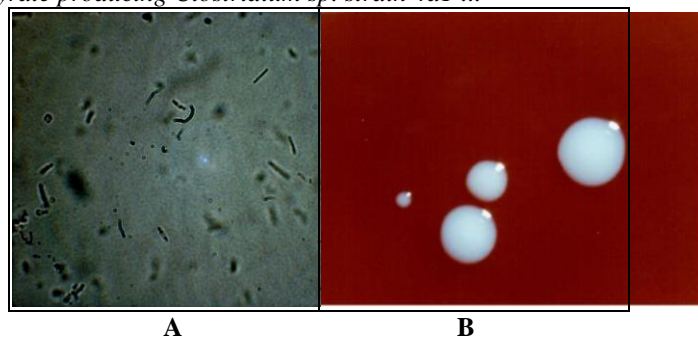


Fig. 3. Cell-morphology (A) and colony appearance on Blood agar (B) of the *Clostridium* strain 4a1
*Light microscopy Boecko microscope, magnitude 1000×

The strain 4a1 is susceptible to high concentration of bile but can grow weakly at 6.5% NaCl. It ferments glucose with acid production but does not hydrolyze gelatin and casein. In the opposite, it can hydrolyze polysaccharides as esculin and starch. The strain 4a1 can fix molecular nitrogen when is grown in Winogradski's N₂-free liquid medium. It does not produce indole, acetoin and H₂S, as well as the enzymes lecithinase, lipase and urease. A weak carbolytic activity had to be pointed when the fermentation of 19 carbohydrates by isolated pure culture was examined.

Table 2. Physiological and biochemical characterization of the investigated strain 4a1

Characteristics		Results	Characteristics		Results
Aerobic growth		-	Acid from glucose		+
Hemolysis		-	Gelatin hydrolysis		-
Catalase		-	Nitrogen fixation		+
Growth at:	4 °C	+	Production of	Indole	-
	22 °C	+		H ₂ S	-
	37 °C	+++		Lecithinase	-
	55 °C	+		Lipase	-
	6.5% NaCl	+/-		Urease	-
	20% bile	-			
Nitrate reduction		-	Voges-Proskauer reaction		-
Methyl red test		-	Neutral red reduction		-
Hydrolysis of Esculin		+	Hydrolysis of Starch		+
Acid production from	Arabinose	-	Acid production from	Mannitol	-
	Galactose	-		Manose	-
	Sucrose	+/-		Starch	-
	Inositol	-		Rhamnose	+
	Inulin	-		Raffinose	-
	Xylose	-		Ribose	+
	Lactose	+/-		Sorbitol	-
	Melibiose	-		Fructose	-
	Maltose	-		Cellobiose	-
Milk coagulation		+/-	Casein hydrolysis		-
Milk reaction-methylene blue reduction					+

Legend: (+) – weak growth; positive biochemical activity
 (+/-) – doubtful growth; doubtful biochemical activity
 (+++) – abundant growth
 (-) – absence of growth; negative biochemical activity

The strain ferments glucose, rhamnose and ribose and weakly or no utilizes sucrose and lactose. On the basis of two characteristics (acid formation from glucose and gelatin hydrolysis), the clostridia are grouped into four groups: 1) non-carbolytic and non-proteolytic; 2) carbolytic and non-proteolytic; 3) non-carbolytic and proteolytic, and 4) carbolytic and proteolytic [24]. Using the methods of numerical taxonomy, the strain 4a1 was related to the group of carbolytic and non-proteolytic clostridia with type strain *Cl. Saccharolyticum* (at similarity of 50%), together with *Cl. butyricum*, *Cl. tyrobutiricum*, *Cl. beijerinckii* (Fig. 4). As it was mentioned above,

these clostridial species are good producers of butyric acid. Some differences were established when the phenotypic characteristics of the investigated strain 4a1 and the type strains were compared. The differences between strain 4a1 and *Cl. butyricum* and *Cl. beijerinckii* were mainly found in the utilization of sugars, whereas differences between strain 4a1 and *Cl. saccharolyticum* and *Cl. tyrobutiricum* were in nitrate reduction, indole production, nitrogen-fixation and absence of motility. Therefore, it was not possible to make a definitive identification on the basis of phenotypic features alone.

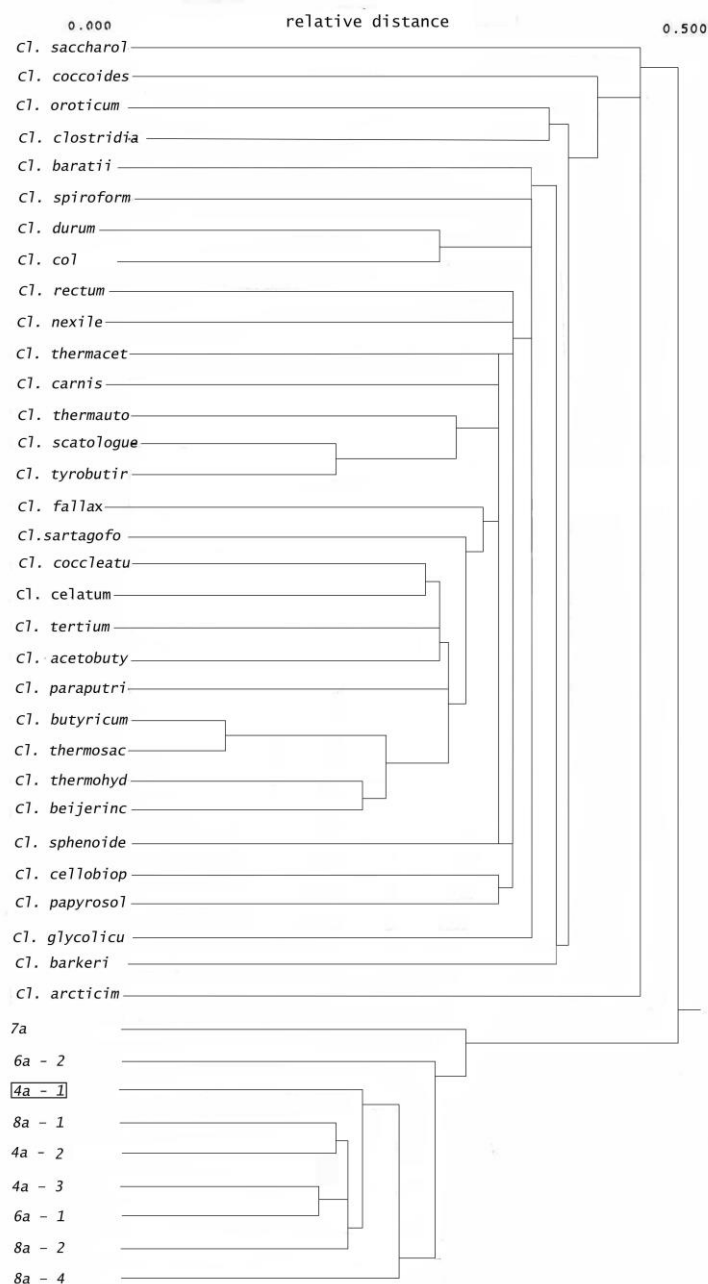


Fig. 4. Dendrogram for location of the *Clostridium* strain 4a1 depending on the relative distance in the group of clostridia, producing acid of glucose (0) and non-hydrolyzing gelatin (1).

The *Clostridium* has long been recognized as a phenotypically heterogeneous genus. Therefore, molecular – based methods have to be applied for species identification. One of the main stages in the study of newly isolated strains is to determine their species by a sequence analysis of parts of the ribosomal operon. This approach was successfully applied for the genus *Clostridium* [28-30].

In order to identify to the species level selected strain 4a1, additionally, molecular – genetic approach was applied. A total DNA from exponential *Clostridium* culture was extracted by the modified method of Delley *et al.* [27] and subjected to PCR amplification with universal primers for 16S rRNA gene of ribosomal operon (*fD1* и *rD1*), according to Weisburg *et al.*, [31]. The amplified PCR product (~ 1550 bp) was sequenced in Macrogen (The Netherlands) using ABIPRISM®310 DNA Genetic Analyzer, (PE Applied Biosystems). The golden 16S rDNA sequence analysis was applied. Obtained sequences were edited by Chromas. The comparative analysis of the obtained partial 16S rDNA sequence for unidentified strain 4a1, with the extensive GenBank database was used to assign the isolate to the species. The strain was identified as *Cl. beijerinckii* with 97% similarity. The sequence was deposited to the NCBI - GenBank - JN244676 and a phylogenetic tree was constructed (Fig. 5).

Clostridium beijerinckii species are ubiquitous in nature and routinely isolated from soil samples. It was reported as a species during a chickpea submerged fermentation by M. Hatzikamari *et al.* [19].

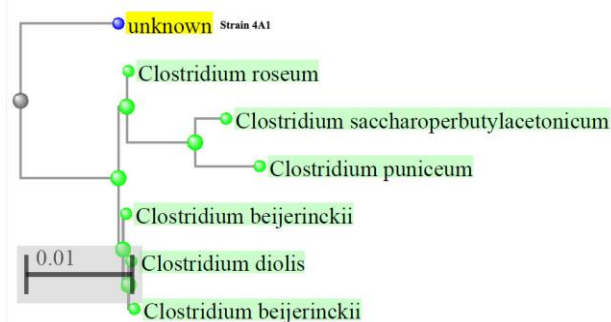


Fig. 5. A phylogenetic tree showing the interrelationships within a cluster formed by the newly identified *Clostridium beijerinckii* strain 4a1 and other *Clostridium* species. Tree was constructed on the base of 16S rDNA sequences, using BLAST pairwise alignments (NCBI), by Newburgh Joining tree method at max. sequences distances 0.75. (Tree Viewer 1.17.0 (October 24, 2017)).

A newly isolated strain 4a1 from chickpea beans fermentation was identified as *Clostridium beijerinckii* according to modern polyphasic taxonomy, combining classical phenotypic and molecular-genetic methods. It is capable to produce butyric acid from glucose in a relatively broad temperature interval (from 4°C to 55°C). The optimum initial pH (7.5), temperature (37 °C) and optimized fermentation medium for butyric production with good yield were determined. However, further optimization of the process parameters is necessary and is still in progress.

Acknowledgement: This work was supported by Grant E02/16 of the Fund for Scientific Research, Republic of Bulgaria.

REFERENCES

1. F. Van Immerseel, R. Ducatelle, M. De Vos, N. Boon, T. Van de Wiele, K. Verbeke, P. Rutgeerts, B. Sas, P. Louis, *Journal of Medical Microbiology*, **59**(2), 141 (2010).
2. G. Porcellati, D. Giorgini, E. Toja, *Lipids*, **4**(3), 190 (1969).
3. J. R. Lupton, *Journal of Nutrition*, **134**(2), 479 (2004).
4. M. J. Playne, in: *Comprehensive biotechnology*, M. Moo-Young (ed.), vol. 3, Pergamon Press, Oxford, 1985, p. 731
5. S.-M. Lee, M. O. Cho, Ch. H. ee Park, Y.-Ch. Chung, J. i H. Kim, B.-I. Sang, Y. Um, *Energy & Fuels*, **22**, 3459 (2008)
6. D. Sh. Lin, H.W. Yen, W.Ch. Kao, Ch.L. Cheng, W.M. Chen, Ch.Ch. Huang, J.Sh. Chang, *Biotechnol. Biofuels*, **8**, Article 168, DOI 10.1186/s13068-015-0352-6 (2015).
7. Ch. Zhang, H. Yang, F. Yang, Y. Ma, *Curr. Microbiol.*, **59**, 656 (2009).
8. M. Sauer, D. Porro, D Mattanovich, P, Branduardi, *Trends in Biotechnology*, **26**(2), 100 (2008).
9. J. Zigorová, E. Šturdík, *J. Ind. Microb. Biotechn.* **24**, 153 (2000).
10. M. Kim, K.-Y. Kim, K. M. Lee, S. H. Youn, S.-M. Lee, H. M. Woo, M.-K. Oh, Y. Um, *Biores. Techn.*, **218**, 1208 (2016).
11. A. K. Jukanti, P. M. Gaur, C. L. L. Gowda, R. N. Chibbar, *Brit. J. .Nutrit.*, **108** S1, S11 (2012).
12. M. Hatzikamari, D.A. Kyriakidis, N. Tzanetakis, C.G. Biliaderis, E. Litopoulou-Tzanetaki. *Eur. Food Res. Techn.*, **224**, 715 (2007).
13. M.C. Tulbek, C.A. Hall, J.G. Schwarz, The use of fermented chickpea on dough rheology and white pan bread quality, in: IFT Annual Meeting, Chicago, July 13–16, 2003
14. A.M. Saad, R.A. Elmassry, K.M.M. Wahdan, M. F. Ramadan, *Acta Periodica Technologica*, **46**, 91 (2015).

15. S. Antonova-Nikolova, R. Vassileva, L. Yocheva, *Compt. rend. de l'Acad. bulgare des Sci.*, **55**(8), 79 (2002).
16. H. Tangüler, *Turk. J. Agric. - Food Sci. Techn.*, **2**(3), 144 (2014).
17. K. Katsaboxakis, K. Mallidis, *Lett. Appl. Microb.*, **23**, 261 (1996).
18. R. Kyyaly, M. Lawand, F. Khatib, *Int. J. Acad. Sci. Res.*, **59**(4), 77 (2017).
19. M. Hatzikamari, M. Yiangou, N. Tzanetakis, E. Litopoulou-Tzanetaki, *Int. J. Food Microb.*, **116**, 37 (2007).
20. L. Yocheva, R. Vassileva, S. Antonova-Nikolova, In: Traditional foods from Adriatic to Caucasus. Tekirdağ, Turkey, April 15-17, 2010.
21. S. Antonova-Nikolova, L. Yocheva, R. Vassileva, in: Book of Abstracts of the Microbiologia Balkanica, First Balkan Conference of Microbiology. Plovdiv, Bulgaria, October 5-9 1999, p. 237.
22. S. P. Hristoskova, L. D. Yocheva, D. S. Yankov, *Sci. Works Univ. Food Techn.*, **63**(1) 171 (2016)
23. R. Vasileva, S. Antonova-Nikolova, L. Yocheva, *Sci Works Agric. Acad.*, **4**(3), 14 (1997), in Bulgarian.
24. Bergey's Manual of Systematic Bacteriology, vol. 3 The firmicutes, P. Vos, G. Garrity, D. Jones, N.R. Krieg, W. Ludwig, F.A. Rainey, K.-H. Schleifer, W.B. Whitman, (eds), Springer-Verlag, New York, 2009
25. S. Antonova-Nikolova, Tzv. Kalcheva, R. Vassileva, L. Yocheva, *J. Biotechn. Biotechnol. Equip.*, Suppl. 2003, 129 (2003).
26. I.A. Merchant, R.A. Packer, Veterinary Bacteriology and Virology, 7th ed. The Iowa State University Press, Ames, Iowa, 1967.
27. M. Delley, B. Mollet, H. Hottinger, *Appl. Environ. Microbiol.*, **56**, 1967 (1990)
28. A.G. Freifeld, K.A. Simonsen, C.S. Booth, †X. Zhao, S. E. Whitney, T. Karre, P.C. Iwen, H. J. Viljoen, *J. Molec. Diagn.*, **14**(3), 274 (2012).
29. Y. Song, Ch. Liu, S. M. Finegold, *Appl. Environ. Microbiol.*, **70**(11), 6459 (2004).
30. D. Szymanowska-Powalowska, D. Orczyk, K. Leja, *Braz. J. Microbiol.*, **45**(3), 892 (2014)
31. W.G. Weisburg, S.M. Barns, D.A. D.J. Pelletier, Lane, *J. Bacteriol.*, **173**(2), 697 (1991).

НОВООХАРАКТЕРИЗИРАН ЩАМ *CLOSTRIDIUM* SP. 4A1, ИЗОЛИРАН ОТ ЗЪРНА НАХУТ (*CICER ARIETINUM* L.), ПРОИЗВЕЖДАЩ БУТИРАТ

С. П. Христоскова¹, Л. Д. Йочева^{2*}, Д. С. Янков¹, С. Т. Данова^{3*}

¹ *Институт по инженерна химия, Българска академия на науките, ул. Акад. Г. Бончев 103, 1113 София, България*

² *Катедра по биология, медицинска генетика и микробиология, Медицински факултет, Софийски университет „Св. Кл. Охридски“, бул. Цар Освободител 15, 1504 София, България*

³ *Институт по микробиология „Стефан Ангелов“, Българска академия на науките, ул. Акад. Г. Бончев 26, 1113 София, България*

Постъпила на 1 февруари, 2018 г.; коригирана на 15 февруари, 2018 г.

(Резюме)

Бутировата киселина е ценно съединение с широко приложение в различни клонове на индустрията. Интересът към нейното биохимично производство се възражда с оглед на приложението ѝ за получаване на алтернативни горива от биомаса. Микроорганизмите от вида *Clostridium* са добре известни като производители на бутирова киселина. Установено е, че те доминират при спонтанната ферментация на зърна от нахут. В настоящото изследване щамът *Clostridium* sp. 4a1 от ферментацията на зърна от нахут е избран като производител на бутирова киселина. Определени са някои параметри на процеса като първоначално рН на средата (7.5), температура (37 °C), състав на средата и концентрация на глюкозата (20 g/l). С помощта на класически и съвременни полифазни таксономични методи щамът е идентифициран като *Clostridium beijerinckii* с 97% подобие.

Determination of the drying characteristics of cherry laurel (*Laurocerasus officinalis* Roem.) puree in a freeze-dryer

M. Talih*, S.N. Dirim

Department of Food Engineering, Ege University, 35100 Bornova, Izmir, Turkey

Received December 6, 2017; Revised January 18, 2018

This study aims at the determination of the effect of thickness on the freeze drying behavior of cherry laurel (*Laurocerasus officinalis* Roem.) puree, together with the determination of the physical, chemical, and powder properties of the obtained powders and the calculation of the energy efficiency of the drying process. The samples were dried at 3, 5, and 7 mm thicknesses. Among the twelve thin-layer drying models used, the Page (3 and 5 mm) and Logarithmic models (7 mm) were found to satisfactorily describe the drying behavior. The drying times were 8, 10, and 11 h with increasing the moisture extraction rate (MER) and specific moisture extraction rate (SMER), and decreasing specific energy consumption (SEC) values for the increasing thicknesses. The effective moisture diffusivity (D_{eff}) values were between $4.70\text{--}7.78\text{E-}08$ m²/s. The average total phenolic compounds and the vitamin C content values were 710 mg GAE/100g (db) and 23 mg/100g (db), respectively. The bulk density values were between 99.75 and 113.88 kg/m³, and the flowability and cohesiveness values were at fair-bad, and intermediate-high levels, respectively.

Keywords: Cherry laurel puree, Freeze drying, Thin layer modeling, Effective moisture diffusivity, Energy consumption, Powder properties.

INTRODUCTION

Cherry laurel (*Laurocerasus officinalis* Roem.) which belongs to the Rosaceae family is generally grown in the Black Sea Region in Turkey [1]. Cherry laurel contains high amounts of minerals (K (7938.7 ppm), Mg (1242.2 ppm), Ca (1158.9 ppm) etc.), vitamin C (3.7–6.8 mg/100 g wb), phenolic (3129.2 mg GAE/100 g db) and antioxidant compounds (2575 μmol Trolox/g wb) [2–4]. Besides being consumed fresh and in dried form, it is also used for making jams, molasses, marmalade, fruit juice, and pickle.

The consumption of cherry laurel is quite limited due to the short harvest time and the high perishability of the fruits. Considering the high nutritional properties of this fruit, freezing and drying might be suitable techniques for prolonging the consumption period, increasing the areas of utilization and increasing the post-harvest stability. Among these techniques drying constitutes an alternative way to increase the shelf life and consumption of cherry laurel. Freeze drying is a method in which drying takes place at very low temperatures and by this way a high quality product is provided. The water in the product (in solid phase) is removed by vacuum protecting the shape and texture and the volume loss of the product is prevented. In addition, the loss of minerals, vitamins, flavor, and aroma compounds of food is minimized [5].

Freeze drying has been used for several kinds of

fruits such as strawberry [6], guava [7], pumpkin [8], mango [9], kiwi [10], watermelon [11], etc.

The aim of this study covers the determination of the effect of different thicknesses of cherry laurel puree on the freeze drying behavior, the determination of the physical, chemical, and powder properties of the obtained products and the calculation of the energy efficiency of the drying process.

MATERIAL AND METHOD

Material

Fully matured fresh fruits were obtained from a local supermarket in Kocaeli, Turkey. They were washed and grinded with a home-type blender (Tefal Smart, MB450141, Turkey) after the removal of the stones.

Drying Experiments

The experiments were performed in a pilot scale freeze dryer (Armfield, FT 33 vacuum freeze drier, England) at three thicknesses of 3, 5, and 7 mm in a vacuum (13.33 Pa absolute pressure), at a -48°C condenser temperature. The temperature of the heating plate was set to 10°C .

The weight of the samples was determined at 1 h intervals by using a digital balance with 0.01 precision (Ohaus AR2140, USA) until the weight of the sequent samples reached a constant value. The dried material was grinded for one minute in a home-type blender (Tefal Smart, MB450141, Turkey), then, the powders were stored in

* To whom all correspondence should be sent:
E-mail: meryem_talih07@hotmail.com

M. Talih, S. N. Dirim: Determination of the drying characteristics of cherry laurel (*Laurocerasus officinalis roem.*)... aluminum-laminated polyethylene (ALPE) packaging materials. Verma, and Logistic), commonly used in drying processes, were employed [17,18].

Physical and Chemical Analyses

The moisture content of the samples was determined according to AOAC [12]. The soluble solid contents (TSS), water activity, pH and color values of the samples were measured by using ATAGO 1T (England), Testo-AG 400 (Germany), Inolab WTW pH 720 (Germany), and Minolta CR-400 Colorimeter (Japan), respectively.

Total color changes (ΔE) of the powders with respect to cherry laurel puree were calculated by using Eq. (1) [13]:

$$\Delta E = \sqrt{\Delta L^{*2} + \Delta a^{*2} + \Delta b^{*2}} \quad (1)$$

In addition, Chroma value was calculated by using Eq. 2 [13]:

$$\text{Chroma} = (a^{*2} + b^{*2})^{1/2} \quad (2)$$

For the determination of the chemical properties of the samples; extracts were obtained according to the methods of Cemeroglu [14]. The obtained extracts were stored at -24°C in the dark until analysis.

The total phenolic content (TPC) of the samples was determined according to Franke *et al.* [15] and the results were given as gallic acid equivalents per 100 grams of dry sample.

The total antioxidant activities of the samples were determined using the method based on the principle of the activity of DPPH radicals. The % inhibition of samples was calculated by using Eq. (3):

$$\% \text{ inhibition} = \frac{(A_{\text{DPPH}} - A_{\text{extract}})}{A_{\text{DPPH}}} * 100 \quad (3)$$

The total antioxidant activity was expressed as $\mu\text{mol Trolox equivalent per g sample (db)}$ [14]. The vitamin C content of the samples was determined according to Hıslıl [16] as $\text{mg vitamin C/100 g sample (db)}$.

Mathematical Modeling of Drying Data

The moisture ratio (MR) values of the samples were calculated throughout the freeze drying operation by using Eq. (4):

$$\text{MR} = \frac{M_t - M_e}{M_0 - M_e} \quad (4)$$

where, M_0 , M_t and M_e represent the initial, any time and equilibrium moisture contents (kg water/kg dry matter), respectively.

Twelve thin layer drying models (Lewis, Page, Modified Page, Henderson and Pabis, Logarithmic, Midilli, Two Term, Two Term Exponential, Approximation of Diffusion, Wang and Singh,

The coefficient of determination (R^2), root mean square error (RMSE) and the reduced chi-square (χ^2) values were determined according to Ergun *et al.* [10]. The higher values of the coefficient of determination (R^2) and the lower values of root mean square error (RMSE), and reduced chi-square (χ^2) were chosen for assessing the goodness of fit.

For the determination of the effective moisture diffusivity (D_{eff}) values of the cherry laurel, Fick's diffusion model as given in Eq. (5) was used:

$$\text{MR} = \frac{8}{\pi} \sum_{i=1}^{\infty} \frac{1}{(2i-1)^2} \exp\left[-(2i-1)^2 \pi^2 \frac{D_{\text{eff}}}{4L^2} t\right] \quad (5)$$

where, t is the time (s), D_{eff} is the effective moisture diffusivity (m^2/s) and L (m) is the thickness of sample. For long drying times ($\text{MR} < 0.6$) [19], a limiting case of Eq. (5) was obtained, and expressed in logarithmic form as given in Eq. (6):

$$\ln \text{MR} = \ln\left(\frac{8}{\pi^2}\right) - \left(\frac{\pi^2 D_{\text{eff}}}{4L^2}\right) t \quad (6)$$

The effective diffusivity is typically calculated by plotting the experimental moisture ratio *versus* the drying time. From Eq. (6), a plot of $\ln \text{MR}$ *versus* the drying time gives a straight line with the slope given in Eq. (7):

$$\text{Slope} = \frac{\pi^2 D_{\text{eff}}}{4L^2} \quad (7)$$

Determination of Energy Efficiency of Freeze Drying Operation

The total energy consumption of the freeze-drying process was measured by a power measurement device (Makel M310.2218, Turkey). In order to determine the effectiveness of freeze drying, the moisture extraction rate (MER), specific energy consumption (SEC), and specific moisture extraction rate (SMER) values were calculated by the following equations (Eqs. 8-10) [20, 21]:

$$\text{MER} = \frac{\text{Amount of water removed during drying (kg)}}{\text{Drying time (h)}} \quad (8)$$

$$\text{SEC} = \frac{\text{Total energy supplied in drying process (MJ)}}{\text{Amount of water removed during drying (kg)}} \quad (9)$$

$$\text{SMER} = \frac{\text{Amount of water removed during drying (kg)}}{\text{Energy consumption (kWh)}} \quad (10)$$

Determination of the Powder Properties

The bulk and tapped density values, flowability (Carr Index) and cohesiveness (Hausner Ratio), the average wettability times, dispersibility, hygroscopicity (%) and caking degree of the powders were determined by using the methods of Chegini and Ghobadian [22], Jinapong *et al.* [23],

M. Talih, S. N. Dirim: Determination of the drying characteristics of cherry laurel (*Laurocerasus officinalis roem.*)... Gong *et al.* [24], Pisecky [25], and Jaya and Das [26], respectively.

Determination of the Morphological Properties by Scanning Electron Microscopy (SEM)

The powder samples were placed on aluminum stubs using a double-sided adhesive tape. The samples were then coated with gold and were examined with a scanning electron microscope (Carl Zeiss 300 VP, Germany) operating at 3 kV accelerating voltage.

Determination of the Glass Transition temperature by Differential Scanning Calorimeter (DSC)

The glass transition temperature of the powder was determined by a differential scanning calorimeter (TA DSC Q2000, New Castle, DE USA) equipped with a thermal analysis station between -30°C to 100°C at 10°C/min for formation of glassy state in the powder and equilibrated for 10 min. DSC thermograms presenting the heat flow (W/g) and temperature relationship were used to analyze the thermal transitions in samples during heating and cooling. TA Instruments Universal analyses software was used to analyze the onset, mid and end points of the glass transition. The glass transition temperature (T_g) was calculated as the average of the onset and end point values [27].

Statistical Analyses

The data were analyzed using statistical software SPSS 16.0 (SPSS Inc., USA). The data

were also subjected to analysis of variance (ANOVA) and Duncan's multiple range test ($\alpha=0.05$) to determine the difference between means. The drying experiments were replicated twice and all the analyses were triplicated.

RESULTS AND DISCUSSION

The experimental results showed that freeze-drying technique was effectively used in the drying of cherry laurel puree, as supported by the acceptable values for the analyzed properties. The efficiency of the process was calculated based on the solid content of puree (98.44-98.68%) and only slight losses due to handling were observed.

Some of the physical properties of cherry laurel powders are given in Table 1. Moisture content is the critical quality parameter for the powder products. The total soluble solid content (TSS) (°Bx) of cherry laurel puree was measured as 14.1°Bx, with a moisture content value of 81.15±0.28% (wb) which is similar to the value presented by Kolaylı *et al.* [2] (80.00±4.10% for cherry laurel). The moisture content values must be below 10% for the protection of the properties of powder products [28, 29] and suitable values of moisture content of the powders were obtained in this study. The final moisture content of the powders ranged between 7.05 and 9.42% (wb) and they could be classified as microbiologically safe for long-term storage. It was observed that the moisture content of the dried powders was affected by the drying thicknesses (P<0.05).

Table 1. Physical properties of the powders.

Properties	Cherry Laurel Powders Dried at Different Thicknesses		
	3 mm	5 mm	7 mm
Moisture Content (% wb)	7.70±0.86 ^a	7.05±0.19 ^a	9.42±0.17 ^b
Water activity	0.248±0.011 ^a	0.261±0.008 ^a	0.270±0.039 ^a
pH	4.527±0.022 ^a	4.509±0.022 ^a	4.499±0.022 ^a
Color			
L*	45.09±0.35 ^c	40.20±1.67 ^b	37.95±0.65 ^a
a*	20.54±0.66 ^a	23.14±0.96 ^b	24.27±0.53 ^b
b*	3.16±0.65 ^a	3.95±0.86 ^a	3.88±0.78 ^a
ΔE	17.77±0.11 ^b	14.71±0.48 ^a	13.69±0.74 ^a
Chroma	20.79±0.75 ^a	23.74±0.79 ^b	24.58±0.43 ^b

^{a-c} Differences in the statistical evaluation are shown with different letters in the same row (P<0.05)

The water activity values of cherry laurel powders reached the range of 0.248 to 0.270 at the end of drying as in the acceptable limits for the safe storage of the powders. The measured water activity values were in the same range with freeze dried kiwi, pumpkin, quince and persimmon puree powders (between 0.225 and 0.273) [30, 31]. According to Table 1, it can be stated that the water activity values of the powders increased with the increasing drying thicknesses although no statistical difference was observed ($P>0.05$).

The pH value of the cherry laurel puree was measured as 4.424 ± 0.001 , similar to the pH values of 4.500 ± 0.500 reported by Kolaylı *et al.* [2]. The pH values of the reconstituted powders (4.499-4.527) were found to be slightly higher compared to the puree and at 3 mm thickness it was observed to be the highest one. Considering the results in Table 1, the change in the drying thicknesses caused no significant effect on pH values ($P>0.05$). The increase in the pH values might be due to the loss of some acidic compounds in the structure during the drying process. In addition, since the powders were diluted to the initial moisture content before the measurements, the pH values might be affected by differences in the moisture content of the powders, hence, by the amount of water added.

The color values of the powders are given in Table 1 and it can be seen that significant differences were registered for L^* and a^* values between the powders ($P<0.05$) dried at different thicknesses. The color values (L^* , a^* , and b^*) of the cherry laurel puree were measured as 28.38 ± 0.17 , 14.63 ± 0.23 , and 2.44 ± 0.08 , respectively. Kasım *et al.* [32] reported the color values of cherry laurel as 21.14-24.21, 5.63-17.72, and 0.22-3.97 for L^* , a^* , and b^* , respectively, for 12 natural genotypes. These differences in the color values can be due to differences in the maturation degree and harvesting time. The color values were affected by the freeze drying process and higher values were observed for the powder products. The lightness values of the powders decreased depending on increasing drying thicknesses ($P<0.05$), which can be explained with the long drying times. The greenness/redness value of the sample dried at 3 mm thickness was statistically different from the other sample thicknesses ($P<0.05$) and there was no statistical difference in blueness/yellowness values of the powders depending on the increase of the drying thicknesses ($P>0.05$). The calculated values of ΔE for the powders with respect to the cherry laurel puree were significantly affected by the change of the drying thicknesses ($P<0.05$). The Chroma value of the cherry laurel puree was calculated as $14.83\pm$

0.24. This value is similar to that reported by Kasım *et al.* [32] and Halilova and Ercisli [33] (5.35-18.15 and 8.39-19.07, respectively). The Chroma values of the powders significantly increased depending on the increasing drying thicknesses ($P<0.05$).

The results obtained from the chemical analysis of the powders are given in Table 2. According to Table 2 the total phenolic content values of cherry laurel puree and its powders were determined as 1083.11 and between 697.27 and 719.81 mg GAE/100g (db), respectively. The values of phenolic content of cherry laurel reported in the literature [4, 33, 34] ranged between 2436 and 7527 mg GAE/100 g (db) showing a large variation between the samples. No significant differences were observed in the phenolic content values of the powders for the change of the drying thicknesses ($P>0.05$). Dirim and Caliskan [8] reported a decrease of 3% (db) in total phenolic content of pumpkin puree in freeze drying. In another study, Chinese ginger was dried by five different drying methods (hot air, freeze, infrared, microwave, and intermittent microwave-convective drying). The phenolic content of fresh and dried Chinese ginger was found as 11.97, 9.69, 13.83, 11.35, 8.41, and 11.28 mg GAE/g (db), respectively. According to these values, the freeze drying method better preserved the phenolic content than the other methods [35].

The antioxidant activity of the cherry laurel puree and its powders was determined as 186.20 and 46.54-83.68 $\mu\text{mol Trolox/g}$ (db), respectively. According to results, the antioxidant activity of the powders was affected by the change in drying thickness ($P<0.05$). The phenolic content affects the amount of antioxidant substances in foods, but color pigments are also a major parameter for the amount of antioxidant in foods. The values of the antioxidant activity of cherry laurel reported in the literature [36, 37] ranged between 21.20 and 35.9 $\mu\text{mol Trolox/g}$ (wb). The degree of maturation, genotypes, and conditions of the growth area can be the reason for the different chemical properties of cherry laurel. In a study by Valadez-Carmona *et al.* [38], cacao pod husk was dried by convective, microwave, and freeze drying methods and the antioxidant activity of powders was found to be 35.8, 59.3, and 70.8 $\mu\text{mol Trolox/g}$ (db), respectively, indicating better antioxidant activity preservation with freeze drying.

The vitamin C content of the cherry laurel puree was determined as 177.44 mg/100 g (db) and values ranging between 2.96 and 204.00 mg/100g (wb) for cherry laurel were reported in the literature [2, 37]. According to the results, the vitamin C values of the freeze dried cherry laurel powders decreased

M. Talih, S. N. Dirim: Determination of the drying characteristics of cherry laurel (*Laurocerasus officinalis roem.*)... depending on increasing drying thickness ($P < 0.05$). The vitamin C losses can be due not only to the freeze drying process, but to the operations before freeze drying such as handling, storage conditions, and mashing of cherry laurel. In general, vitamin C loss in freeze drying is lower when compared to other drying methods, since the process is performed at low temperatures with application of vacuum [39]. In their studies, Dirim and Caliskan [8] and Marques *et al.* [40] reported losses of vitamin C as 18% (db) for pumpkin and 13.0-69.3% (db) for acerola, respectively. However, in our study a considerable loss was observed.

The drying characteristics of the samples during the freeze drying process were determined from the mass loss in the samples of the known initial moisture content ($81.15 \pm 0.28\%$, wb). The drying process was carried out by following the weight of the samples at one-hour intervals until constant weight. Most of the moisture in the samples was removed at the beginning of the drying process and at a slower rate until the end of the drying process. Moisture ratio with respect to drying time was

calculated by using the moisture content data and fitted into the thin layer drying models. As a result of calculation of model parameters, five of the most suitable model equations and the statistical evaluations are given in Tables 3-5 for 3, 5 and 7 mm thicknesses, respectively.

The R^2 values of the different thin layer model equations were found to be above 0.9 for the three drying thicknesses (Tables 3-5). The experimental data and the model equations for the three most suitable drying curves of drying cherry laurel puree are given in Fig. 1.

The highest R^2 values were obtained for Page, Midilli and Two-Term Exponential model; Page, Midilli and Logistic model; and Logarithmic, Midilli, and Approximation of Diffusion model for 3, 5, and 7 mm, respectively. According to Tables 3-5, when RMSE and χ^2 values were examined, Page (3 and 5 mm thicknesses) and Logarithmic (7 mm thickness) models were chosen as the most suitable models for determining freeze drying characteristics of the samples.

Table 2. Chemical properties of the powders.

Properties	Cherry Laurel Powders Dried at Different Thicknesses		
	3mm	5mm	7mm
Total Phenolic Content (mg GAE/ 100g db)	715.30±14.24 ^a	697.27±19.37 ^a	719.81±8.72 ^a
Antioxidant Activity (µmol Trolox/g db)	63.31±1.00 ^b	83.68±1.25 ^c	46.54±0.80 ^a
Vitamin C (mg /100 g db)	28.26±1.24 ^b	22.84±1.45 ^a	20.01±1.55 ^a

^{a-c} Differences in the statistical evaluation are shown with different letters in the same row ($P < 0.05$).

Table 3. Model equations and statistical results for the samples of 3 mm thickness (R^2 , RMSE, and χ^2).

Models	Equations	R^2	RMSE	χ^2
Page	MR= $e^{-0.471 t^{1.333}}$	0.997	0.0183	0.0004
Midilli	MR= $0.999e^{-0.470t^{1.329}} + 0.001t$	0.997	0.0183	0.0006
Two-Term Exponential	MR= $1.908e^{-0.876t} + (1 - 1.908)e^{-1.908(0.876)t}$	0.997	0.0197	0.0004
Approximation of Diffusion	MR= $29.885e^{-0.371t} + (1 - 29.885)e^{-0.371(0.984)t}$	0.992	0.0289	0.0125
Logistic	MR= $1.542/(1 + 0.543e^{1.000t})$	0.997	0.6064	0.5516

Table 4. Model equations and statistical results for the samples of 5 mm thickness (R^2 , RMSE, and χ^2).

Models	Equations	R^2	RMSE	χ^2
Page	MR= $e^{-0.308t^{1.300}}$	0.987	0.0390	0.0019
Midilli	MR= $0.989e^{-0.304t^{1.275}} - 0.002t$	0.987	0.0374	0.0022
Approximation of Diffusion	MR= $-65.415e^{-0.751t} + (1 + 65.415)e^{-0.751(0.989)t}$	0.985	0.0399	0.0022
Verma	MR= $26.767e^{-0.240t} + (1 - 26.767)e^{-0.235t}$	0.985	0.4054	0.2260
Logistic	MR= $1.516/(1 + 0.537e^{0.701t})$	0.987	0.5882	0.4758

Table 5. Model equations and statistical results for the samples of 7 mm thickness (R^2 , RMSE, and χ^2).

Models	Equations	R^2	RMSE	χ^2
Logarithmic	$MR= 1.066e^{-0.293t} - 0.071$	0.986	0.0368	0.0018
Midilli	$MR= 0.986e^{-0.291t^{1.073}} - 0.004t$	0.986	0.0374	0.0021
Approximation of Diffusion	$MR= -56.567e^{-0.536t} + (1 + 56.567)e^{-0.536(0.991)t}$	0.985	0.0406	0.0022
Verma	$MR= 0.141e^{-17.605t} + (1 - 0.141)e^{-0.423t}$	0.984	0.3433	0.1620
Logistic	$MR= 1.934/(1 + 0.984e^{0.485t})$	0.984	1.1675	1.8170

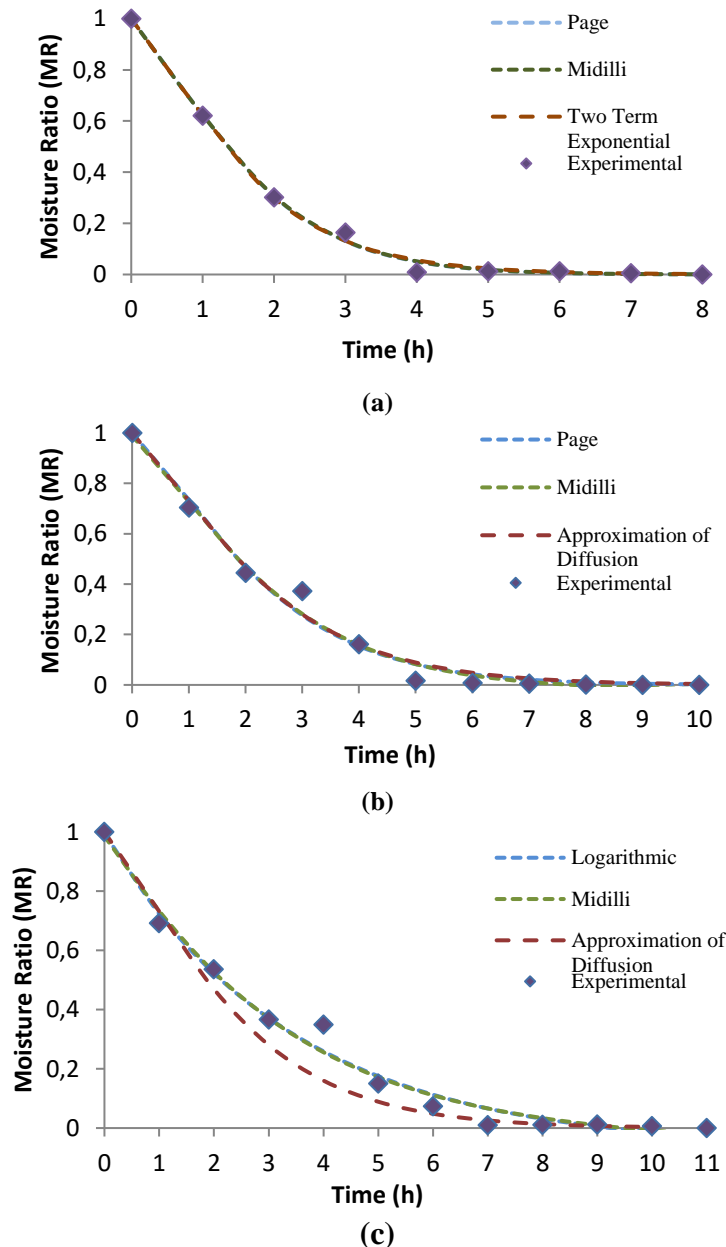


Fig. 1. Experimental data and computed moisture ratio values obtained by the selected models for different drying thicknesses: (a) 3 mm, (b) 5 mm, and (c) 7 mm.

Oztekin *et al.* [41] studied the drying of cherry laurel (250 g) using microwave and hot air and mathematical modeling of the drying behavior and found that Midilli and Verma models are the best models in describing the microwave (180-900W) and hot air (60-70°C) drying, respectively.

Although there is no study in the literature about freeze drying of cherry laurel puree, there are lots of mathematical modeling studies for freeze drying of foods, e.g., Ergun *et al.* [10], Souza *et al.* [42], and Caliskan *et al.* [43] who reported the drying models as Two-term Exponential model for kiwi

M. Talih, S. N. Dirim: Determination of the drying characteristics of cherry laurel (*Laurocerasus officinalis roem.*)... (*Actinidia deliciosa*) slices, Page model for avocado (*Persea americana Mill.*) pulp, and Logarithmic model for kiwi (*Actinidia deliciosa*) puree as the best representative model, respectively. The moisture transfer during drying was modeled by using the Fick's law of diffusion model. Plots of natural logarithm of MR (lnMR) against drying time (s) for different drying thicknesses (3, 5, and 7 mm) yielded straight lines with relatively high correlation coefficients (0.983, 0.985, and 0.988, respectively) indicating goodness of fit (data and plots are not given here). The effective moisture diffusivity (D_{eff}) of the cherry laurel was calculated by using the equations 6 and 7 by taking into consideration that the MR values are lower than 0.6 for 80% of the total drying operation. The calculated values were $7.06E-08$, $7.78E-08$, and $4.70E-08$ m^2/s , respectively for 3, 5, and 7 mm thicknesses. Kaya and Aydın [44] reported the effective diffusivity values of hot air-dried cherry laurel (35, 45, 55, and 65°C, 0.2-20.0 m/s air velocity and 10-95% relative humidity) as varying between $1.896E-10$ and $3.252E-10$ m^2/s indicating both higher D_{eff} results for freeze drying and difference in the genotypes. Caliskan and Dirim [31] reported the effective diffusivity value of persimmon puree as $7.302E-10$ m^2/s at freeze drying. Erbay and Icier [17] observed that the efficiency of moisture diffusivity in the drying of food materials was in the range of $10E-12$ to $10E-06$ m^2/s according to the literature. Also, 75% of the diffusivity values accumulated in the range of $10E-10$ to $10E-08$ m^2/s and the results of our study are in a good agreement with this fact.

The MER, SEC, and SMER values were used to determine the efficiency of the dryers and the results are given in Fig. 2 for different drying thicknesses.

As can be seen from Fig. 2 the MER and SMER values of the samples increased and SEC values of the samples decreased depending on increasing drying thickness related with amount. Oztekin *et al.* [41] reported that the energy consumption for drying of laurel berry samples was 0.92-1.44 kWh/kg sample for microwave dryer (0.2-1.1 h) and 6.12-9.26 kWh/kg sample for hot air dryer (12.0-28.0 h). In our study, the total energy consumptions of the equipment for drying were measured as 351.18- 457.67 kWh/kg sample for different drying thicknesses and these values were found to be higher than the values given by Oztekin *et al.* [47] due to the long operation time of freeze drying. Baysal *et al.* [45] studied the drying of apple slices (2 mm) at tray, heat pump and microwave freeze drying. In freeze drying, the researchers found lower SMER and MER, and

higher SEC values than other drying methods. SMER, MER, and SEC values in freeze drying of apple slices were measured as 0.01 kg/kWh, 0.02 kg/h, and 259.2 MJ/kg, respectively. In cherry laurel puree drying, MER and SEC values were lower and SMER were higher than those given by Baysal *et al.* [45]. The energy consumption for drying foods depends on the used type of drying equipment, raw material, initial moisture content and thickness of the product.

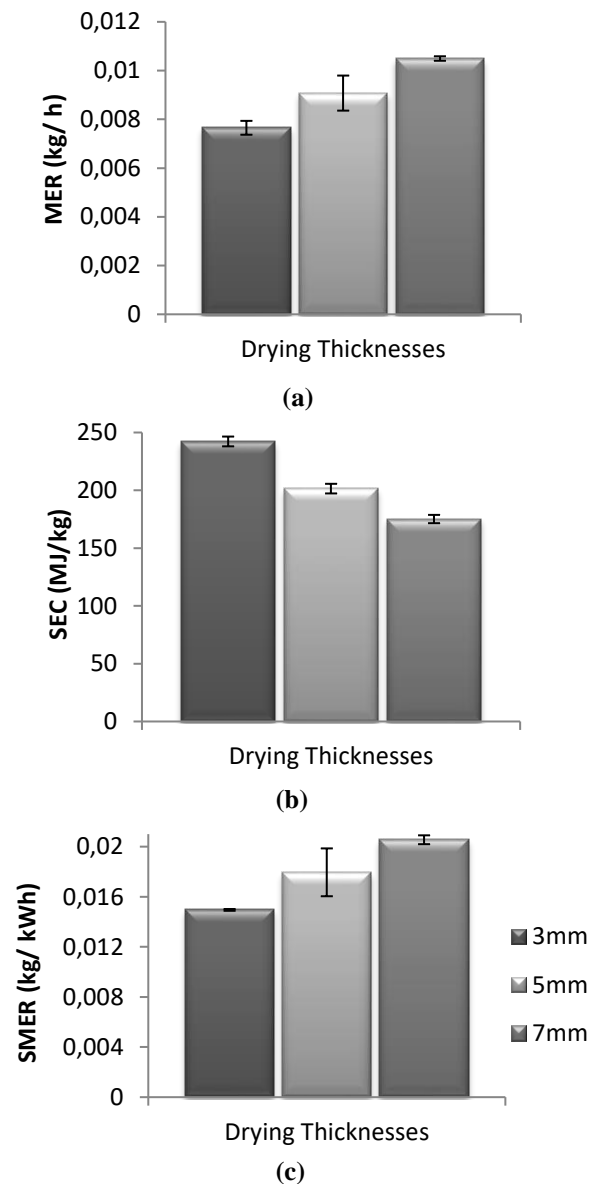


Fig. 2. Calculated values of MER (a), SEC (b), and SMER (c) for the different drying thicknesses.

The powder properties are very important for the storage, transportation and for industrial applications as dosing for powders. Some of the determined powder properties are given in Table 6. The bulk density is an important criterion for the transport and packaging of powdered foods which is influenced by the moisture content of the product, particle shape and particle size [46]. The

bulk and tapped density values of the powders ranged between 99.75-113.88 kg/m³ and, 136.20-182.40 kg/m³, respectively, as given in Table 6. The change in the drying thickness caused significant effect on the bulk and tapped density values

The flowability and cohesiveness of the powders in terms of the Carr Index and Hausner ratio were evaluated. The classification of the powder flowability and cohesiveness based on the Carr index (CI) and Hausner ratio (HR) are very good (<15), good (15–20), fair (20–35), bad (35–45), and very bad (>45), and low (<1.2), intermediate (1.2–1.4), and high (>1.4), respectively [23]. The CI and HR values of the powders ranged between 26.75-39.24, and 1.37-1.65, respectively. Drying thickness was found to affect the CI and HR values of the powders (P<0.05). It may be due to high moisture content value of the powders. Depending on these results it can be stated that the powders showed fair and bad flowability and intermediate and high cohesiveness. As indicated by Koc *et al.* [48], flowability problems may occur in powder products which have high cohesiveness values.

Wettability is the ability for absorption of water on the surface of the powder particles which is affected by several properties of the products, as surface area, density, size, and surface activities of particle and hygroscopic material content of product [49]. The average wettability times of the powders are given in Table 6 as ranging between 2.37-3.25 s. The results showed that average wettability times of the powders significantly affected from the drying thicknesses (P<0.05). Freuding *et al.* [50] reported that low tapped density products have high wettability values. Dirim *et al.* [30], reported the wettability time and tapped density of freeze dried samples (pumpkin, quince and kiwi) as 77.33, 107.50, and 186.0s, and 250, 340 and 420 kg/m³, respectively. However, in our study the wettability time values showed an inverse relationship with tapped density of the powder products.

Dispersibility is defined as the ability for the powder products to getting wet and dispersing without formation of dry lumps in water [49]. The average dispersibility values of the freeze dried powders were found to be 82.82, 75.71, and 62.52% for 3, 5, and 7mm, respectively (Table 6) and according to these results it can be stated that the average dispersibility values of the samples decreases depending on increasing drying thicknesses (P<0.05). The porous structure of the powder particles can affect the dispersibility property positively and the decrease of the pores with the increase in drying thicknesses supports this

(P<0.05), mainly due to the differences in the moisture content values. Since bulk density, flow behavior, wettability and other properties are referred to as powder properties; they are influenced by moisture content of the powders [47]. fact. Erguney *et al.* [51] reported the dispersibility values of freeze dried cherry laurel powder (without carrier agent) as 81% and Jaya and Das [52] reported the dispersibility values of foods (instant coffee, tomato soup powder, mango powder etc.) are in the range of 68.19 to 99.98%. The results of our study are consistent with the reported values.

Hygroscopicity depends on the composition (low molecular weight sugar, organic acid, and moisture content, etc.) of the product [53]. As given in Table 6, the hygroscopicity values of the powders were affected by the change of drying thicknesses (P<0.05). The results are similar to the values reported in the literature as 7.68% for grugru palm [54], 7.20% for mango powder [52] and between 4.21-6.64% for tomato soup powder [52]. Erguney *et al.* [51] determined the hygroscopicity value of cherry laurel powder as 9.2% which can be explained by the lower moisture content (2.43%) of the powder product.

The values of caking degree for the powders are given in Table 6 as ranging between 42.04-49.95%. Depending on the changes in the drying thicknesses, significant differences were observed in the caking degree of the powders (P<0.05). The caking degree values of the powders are affected by the moisture content of the products and by differences in composition and product structure.

The selected images from the SEM microstructure analysis of the freeze-dried powders are given in Fig. 3 for different drying thicknesses.

The SEM images show that the appearance of the powder particles is in the form of a flake is similar to the SEM images of freeze-dried powders in the literature [45, 49]. Considering the SEM images of the powders at 100× magnification (pictures not given here) it was observed that particle sizes of the powders dried at 3 mm are higher than the others explaining the reason for high bulk and tapped densities of the powders dried at 5 and 7 mm thicknesses.

The results obtained from DSC analysis giving the glass transition temperature of the samples of the cherry laurel puree dried at the thickness of 5 mm are shown in Fig. 4.

According to the result of the DSC analysis, there are two transitions in the thermal flow thermogram. The glass transition temperature of the powder was calculated using the onset, mid and end points of the glass transition.

Table 6. Powder properties of the powders.

Properties	Cherry Laurel Powders Dried at Different Thicknesses		
	3mm	5mm	7mm
Bulk Density (kg/m ³)	99.75± 0.79 ^a	110.83±0.62 ^b	113.88±1.53 ^c
Tapped Density (kg/m ³)	136.20± 1.03 ^a	182.40±1.32 ^c	166.35±0.97 ^b
Flowability	26.75±1.13 ^a (Fair)	39.24±0.57 ^c (Bad)	31.53±1.31 ^b (Fair)
Cohesiveness	1.37±0.02 ^a (Intermediate)	1.65±0.02 ^c (High)	1.46±0.03 ^b (Intermediate)
Wettability time (s)	3.25±0.25 ^c	2.83±0.13 ^b	2.37±0.04 ^a
Dispersibility (%)	82.82±0.71 ^c	75.51±0.69 ^b	62.52±0.97 ^a
Hygroscopicity (%)	7.18±0.06 ^b	6.36±0.52 ^a	6.78±0.12 ^a
Degree of Caking (%)	47.14±0.23 ^b	42.04±0.85 ^a	49.95±0.68 ^c

^{a-c} Different letters in the same row indicate significant difference between the drying thickness at P<0.05.

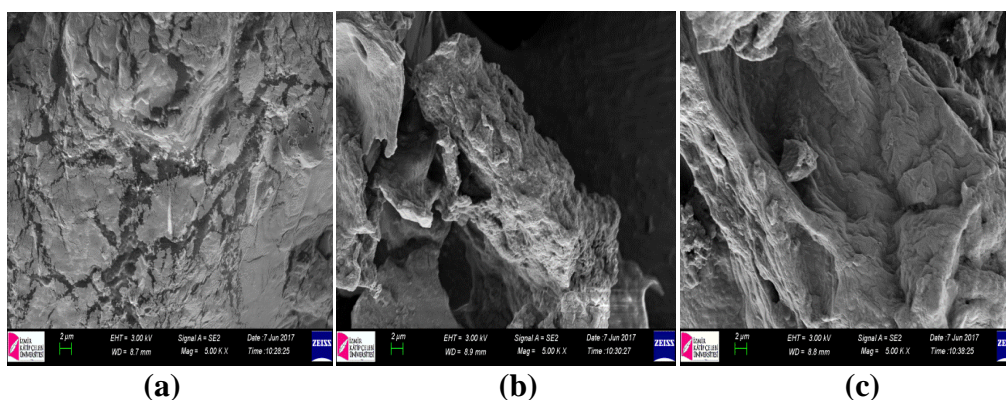


Fig. 3. Scanning electron micrographs of cherry laurel powders for the three drying thicknesses: (a) 3 mm, (b) 5mm, and (c) 7mm at 5000× magnification.

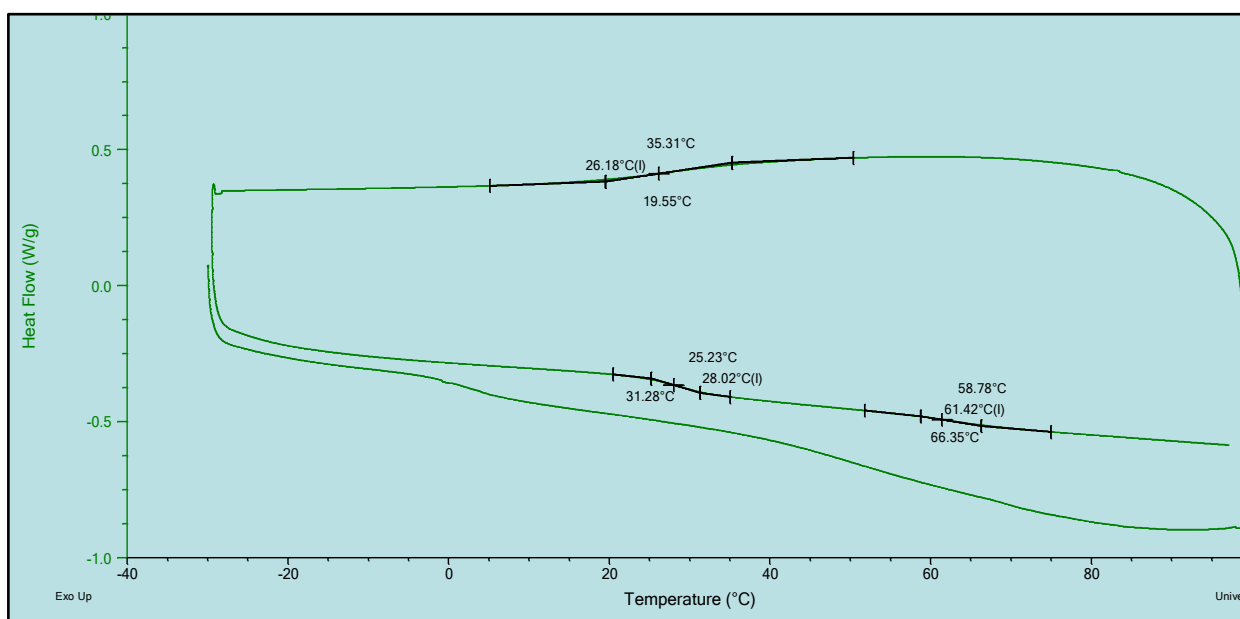


Fig. 4. Thermal flow thermogram of freeze-dried cherry laurel puree at 5 mm drying thickness

M. Talih, S. N. Dirim: Determination of the drying characteristics of cherry laurel (*Laurocerasus officinalis roem.*)...

The first transition was measured as 28.18° and the second transition was at 62.19°C. To our knowledge, no study exists in the literature for the glass transition temperature measurement of cherry laurel powder. But Can-Karaca *et al.* [27] reported the glass transition of spray-dried sour cherry powders (a very similar fruit to cherry laurel) as between 7.7 ±1.0°C and 70.6±1.0°C with the addition of different amounts of carrier agents, carrier types and different inlet temperatures. Considering the glass transition temperature of 28.18°C it should be advised that the powders should be kept at temperatures lower than this value.

CONCLUSION

In this study, we observed that freeze drying can satisfactorily be applied for drying of cherry laurel puree to produce a powder and to provide prolonged consumption period. The present work describes the changes in some physicochemical and powder properties of powders dried at different thicknesses. Page and Logarithmic model which had the highest R² and lowest χ^2 and RMSE for all drying experiments were found to satisfactorily describe the drying behavior of cherry laurel puree. The calculated values of D_{eff} ranged between 4.700E-08 and 7.784E-08 m²/s. The energy consumption was measured and it was observed that MER values and SMER of samples increased, and SEC values of samples decreased with increasing drying thickness. Moisture contents of the powders were found between 7.05 and 9.42% (wb). The measured water activity values of the powders are in acceptable limits for the safe storage of the products. The lightness value of cherry laurel puree was affected by the freeze-drying process and its value increased between 33.72% and 58.88%. ΔE values of the powders changed between 17.77±0.11, 14.71±0.48, and 13.69±0.74 for drying thickness of 3, 5, and 7 mm, respectively. The bulk density and tapped density values of the powders ranged between 99.75 and 113.88 kg/m³, and 136.20-182.40 kg/m³, respectively. Determination of flowability and cohesiveness in terms of Carr Index and Hausner ratio were evaluated as fair and bad, and intermediate and high levels, respectively. The determined average wettability times were less than 10 s. Caking degree of powders ranged between 42.04-49.95%. The results showed that average bulk and tapped density, wettability times, and caking degree of the powders significantly were affected by the drying thicknesses (P<0.05). Two transitions at 28.18°C and 62.19°C were observed with DSC analysis. The changes in tapped density, flowability, cohesiveness, hygroscopicity

and caking degree followed the same tendency with moisture content values.

Acknowledgement: The authors acknowledge the financial support by Ege University, Izmir, Turkey, Council of Scientific Research Projects (Project Number: BAP 2016/Muh/081).

REFERENCES

1. C. Alasalvar, M. Al-Farsi, F. Shahidi, *Journal of Food Science*, **70**, 1, 47 (2005).
2. S. Kolaylı, M. Küçük, C. Duran, F. Candan, B. Dincer, *Journal of Agricultural and Food Chemistry*, **51**, 7489 (2003).
3. S. Celik, I. Bakırcı, I.G. Sat, *International Journal of Food Properties*, **9**, 401 (2006).
4. E. Capanoglu, D. Boyacıoglu, R.C.H. de Vos, R.D. Hall, J. Beekwilder, *Journal of Berry Research*, **1**, 137 (2011).
5. C. Ratti, *Journal of Food Engineering*, **49**, 311 (2001).
6. F. Shishehgarha, J. Makhlof, C. Ratti, *Drying Technology*, **20**, 1, 131 (2002).
7. T. Mahendran, *Tropical Agricultural Research & Extension*, **13**, 2, 48 (2010).
8. S.N. Dirim, G. Caliskan, *Gıda*, **37**, 4, 203 (2012).
9. O.A. Caparino, J. Tang, C.I. Nindo, S.S. Sablani, J.R. Powers, J.K. Fellman, *Journal of Food Engineering*, **111**, 135–148, (2012).
10. K. Ergun, G. Caliskan, S.N. Dirim, *Heat and Mass Transfer*, **52**, 2697 (2016).
11. A. Akyıldız, S. Polat, E. Agcam, *Gıda*, **42**, 2, 169-176, (2017) (in Turkish).
12. AOAC, Gaithersburg, MD, USA: Association of Official Analytical Chemists, 2000.
13. E. Demirhan, B. Ozbek, *Chem. Eng. Comm.*, **198**, 10, 1189 (2011).
14. B. Cemeroglu, *Gıda Analizleri*, **34**, 145, 168, (2007) (in Turkish).
15. S.I.R. Franke, K. Chless, J.D. Silveria, G. Robensam, *Food Chemistry*, **8**, 45 (2004).
16. Y. Hısil, Ege University Engineering Department Academic Press. 41, 2007 (in Turkish).
17. Z. Erbay, F. İcier, *Cr. Reviews in Food Sci. and Nutrition*, **50**, 441–464 (2009).
18. I. Alibas, *J. Biol. Environ. Sci.*, **6**, 17, 161 (2012).
19. J. Crank, *The Mathematics of Diffusion*. 2nd ed. Oxford (UK), Clarendon Press, 1975.
20. K.J. Chua, S.K. Chou, J.C. Ho, M.N.A. Hawlader, *Drying Technology*, **20**, 8, 1580 (2002).
21. W. Jindarat, P. Rattanadecho, S. Vongpradubchai, *Experimental Thermal and Fluid Science*, **35**, 728 (2011).
22. G.R. Chegini, B. Ghobadian, *Drying Technology*, **23**, 657 (2005).
23. N. Jinapong, M. Suphantharika, P. Jammong, *Journal of Food Engineering*, **84**, 194 (2008).
24. Z. Gong, M. Zhang, A.S. Mujumdar, J. Sun, *Drying Technology*, **26**, 116 (2008).
25. J. Pisecky, Standards, specifications and test methods for dry milk products: in Concentration and

- M. Talih, S. N. Dirim: Determination of the drying characteristics of cherry laurel (*Laurocerasus officinalis roem.*)... Drying of Foods, Elsevier Science Publishing. 203 (1985).
26. S. Jaya, H. Das, *Journal of Food Engineering*, **63**, 125 (2004).
 27. A. Can-Karaca, O. Guzel, M.M. Ak, *J. Sci. Food Agric.* **96**, 449 (2016).
 28. Y.S. Quek, N.K. Chok, P. Swedlund, *Chemical Engineering and Processing* **46**, 386 (2007).
 29. L.T. Ng, P.H. Chong, Y.A. Yusof, N.L. Chin, R.A. Talib, T.S. Taip, M.G. Aziz, *Food Science Biotechnology*, **2**, 582 (2012).
 30. S.N. Dirim, G. Caliskan, K. Ergun, *Gıda*, **40**, 2, 85 (2015) (in Turkish).
 31. G. Caliskan, S.N. Dirim, *Gıda*, **40**, 1, 9 (2015).
 32. R. Kasim, M. Sulusoglu, M.U. Kasim, *African Journal of Plant Science*, **5**, 5, 323 (2011).
 33. H. Halilova, S. Ercisli, *Biotechnology & Biotechnological Equipment*, **24**, 3, 1970 (2010)
 34. I.T. Karabegovic, S.S. Stojicevic, D.T. Velickovic, Z.B. Todorovic, N.C. Nikolic, M.I. Lazic, *Industrial Crops and Products*, **54**, 142 (2014).
 35. K. An, D. Zhao, Z. Wang, J. Wu, Y. Xu, G. Xiao, *Food Chemistry*, **197**, 1292 (2016).
 36. S. Ercisli, F. Celik, S.O. Yilmaz, A. Hegedus, *Hort. Science*, **46**, 6, 924 (2011)
 37. H. Yildiz, S. Ercisli, H.K. Narmanlioglu, S. Guclu, M. Akbulut, Z. Turkoglu, *Genetika*, **46**, 1, 129 (2014).
 38. L. Valadez-Carmona, C.P. Plazola-Jacinto, M. Hernandez-Ortega, M.D. Hernandez-Navarro, F. Villarreal, H. Necochea-Mondragon, A. Ortiz-Moreno, G. Ceballos-Reyes, *Innovative Food Science and Emerging Technologies*, **41**, 378 (2017).
 39. L.G. Marques, J.T. Freire, *Drying Technology*, **23**, 2169 (2005).
 40. L.G. Marques, M.C. Ferreira, J.T. Freire, *Chemical Engineering and Processing*, **46**, 451 (2007).
 41. S. Oztekin, T. Erdem, S. Karaaslan, *Journal of Agricultural Machinery Science*, **6**, 2, 79 (2010).
 42. D.S. Souza, L.G. Marques, E. de B. Gomes, N. Narain, *Drying Technology*, **33**, 194 (2015).
 43. G. Caliskan, K. Ergun, S.N. Dirim, *Italian Journal Food Science*, **27**, 385 (2015).
 44. A. Kaya, O. Aydin, *Journal of Food Process Engineering*, **31**, 398 (2008).
 45. T. Baysal, N. Ozbalta, S. Gokbulut, B. Capar, O. Tastan, G. Gurlek, *J. of Thermal Science and Technology*, **35** (1), 135 (2015).
 46. D.E. Walton, *Drying Technology*, **18**, 9, 1943 (2000).
 47. A.M. Goula, K.G. Adamopoulos, *Drying Technology*, **26**, 6, 726 (2008).
 48. M. Koç, B. Koç, F. Kaymak-Ertekin, *Akademik Gıda*, **9**, 4, 60 (2011) (in Turkish).
 49. P. Schuck, Milk Powder: Physical and Functional Properties of Milk Powders, Elsevier Academic Press, London, UK, **2**, 117-124 (2011).
 50. B. Freuding, S. Hogeckamp, H. Schubert, *Chemical Engineering and Processing*, **38**, 525 (1999).
 51. E. Erguney, Z. Gulsunoglu, E. Firatgil-Durmus, M. Kılıc-Akyılmaz, *Akademik Gıda*, **13**, 2, 108 (2015) (in Turkish).
 52. S. Jaya, H. Das, *Journal of Food Processing and Preservation*, **29**, 45 (2005).
 53. C.C. Ferrari, S.P.M. Germer, I.D. Alvim, F.Z. Vissotto, J.M. de Aguirre, *International Journal of Food Science and Technology*, **47**, 1237 (2012).
 54. D.M. Oliveria, E. Clemente, M.R.A. Aonso, J.M. Correia da Costa, *American Journal of Analytical Chemistry*, **4**, 1 (2013).

ОПРЕДЕЛЯНЕ НА ХАРАКТЕРИСТИКИТЕ НА СУШЕНЕ НА ПЮРЕ ОТ ЛАВРОВА ЧЕРЕША (*LAUROCERASUS OFFICINALIS ROEM.*) В СУШИЛНЯ-ФРИЗЕР

М. Талих*, С. Н. Дирим

Департамент по хранително инженерство, Еге университет, 35100 Борнова, Измир, Турция

Постъпила на 6 декември, 2017 г.; коригирана на 18 януари, 2018 г.

(Резюме)

В статията се изследва влиянието на дебелината на слоя върху отнасянето на пюре от лаврова череша (*Laurocerasus officinalis Roem.*) при сушене чрез замразяване и са определени физичните, химичните и праховите свойства на получените прахове. Изчислена е енергийната ефективност на процеса на сушене. Пробите са сушени при дебелини на слоя от 3, 5 и 7 mm. Между дванайсетте модела на сушене на тънки слоеве, моделът на Page (3 и 5 mm) и логаритмичният модел (7 mm) описват задоволително отнасянето при сушене. Времето на сушене с повишаване на степента на изсушаване е 8, 10 и 11 ч. Специфичният разход на енергия намалява с увеличаване на дебелината. Стойностите на специфичната дифузивност на влагата (D_{eff}) са $4.70\text{--}7.78\text{E-}08\text{ m}^2/\text{s}$. Съдържанието на тотални фенолни съединения и витамин С са съответно 710 mg GAE/100g (db) и 23 mg/100g (db). Обемната плътност е между 99.75 и 113.88 kg/m³, а течливостта и сцеплението са съответно на ниво средно-лошо и междинно-високо.

Edge harmonic index of carbon nanocones and an algorithm

E. Aslan¹, Ö. K. Kürkçü^{2*}

¹ Department of Software Engineering, Manisa Celal Bayar University, Manisa, Turkey

² Department of Mathematics, Izmir University of Economics, Izmir, Turkey

Received January 16, 2017; Revised March 8, 2018

Edge harmonic index $H_e(G)$ of the (chemical) graph G is based on the end-vertex degrees of edges of the line graph $L(G)$. In this paper, the generalized formula and an algorithm (pseudocode) are given for edge harmonic index. The aim of this paper is to develop edge harmonic index for generalized carbon nanocones.

Keywords: Carbon nanocones, Edge harmonic index, Generalized formula, Graph theory.

INTRODUCTION

Graph theory has variety-applied fields, one of which is carbon nanostructure field. Carbon nanocones, which were firstly introduced by Ge and Sattler in 1994 [1], are well-founded devices in the nanostructures.

These are constructed from a graphene sheet by removing a 60° wedge and joining the edges to produce a cone with a single pentagonal defect at the apex [2]. A carbon nanocone is made up of one-polygonal and its center is surrounded by the layers of the polygonal. So, the carbon nanocones denoted by $CNC_m[n]$ consist of m -th polygonal and n th layer.

Fig. 1 illustrates the graph of one pentagonal carbon nanocone CNC_5 [6]. In recent years, several useful research articles based on the topological indices have been studied on these structures [12-22].

A topological index is the numerical quantity attributed to a (chemical) graph G . The oldest topological index is the Wiener index, which was presented by the chemist Wiener [3]. It is defined as follows:

$$W(G) = \sum_{\{u,v\} \in V(G)} d(u,v),$$

where $d(u,v)$ is the distance between atoms u and v in the chemical graph G . The topological indices are graph invariants and are used to calculate quantitative structure-activity relationships (QSAR) and quantitative structure-property relationships (QSPR) [9,10]. For the QSAR and QSPR studies, the experimental numerical results have been shown in [11]. Yang and Hua [19] have established the explicit formula and mathematical properties of the harmonic index for general connected graphs

and so they gained important results for QSAR and QSPR studies. In addition, the reader can refer to [12-22] for more information about topological indices and QSAR and QSPR.

Let us now give basic definitions. Let G be a chemical graph and its edge and vertex sets are represented by $E(G)$ and $V(G)$, respectively. In a chemical graph, the vertices of a graph are attributed to the atoms of the molecule and the edges represent the chemical bonds.

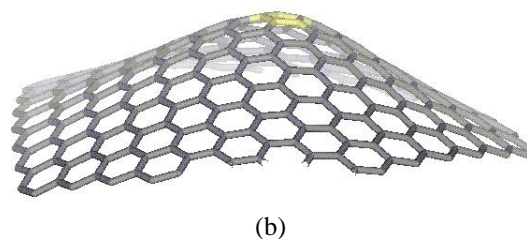
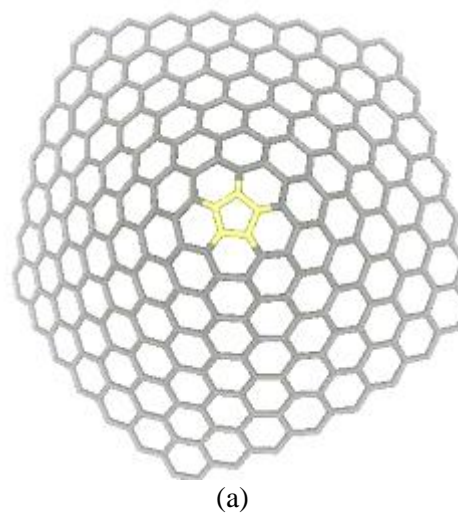


Fig. 1. (a), (b) The graph of one-pentagonal carbon nanocone CNC_5 [6] (top and side view) (color figure available online).

In 1987, the harmonic index $H(G)$ was presented by Fajtlowicz [4]. It is formulated as follows:

* To whom all correspondence should be sent:

E-mail: : omurkivanc@outlook.com

$$H(G) = \sum_{uv \in E(G)} \frac{2}{d(u) + d(v)},$$

where $d(u)$ (or $d(v)$) represents the degree of the vertex u (or v) in G . Recently, the edge harmonic index has been introduced by Nazır *et al.* [5]. It is associated with the end-vertex degrees of the edges of their line graphs. It is formulated as follows:

$$H_e(G) = \sum_{ef \in E(L(G))} \frac{2}{d(e) + d(f)},$$

where $d(e)$ and $d(f)$ are the end-vertex degrees of vertices e and f in a line graph of G .

In graph theory, a line graph is obtained by using and converting the vertices and edges of any connected graph. In order to obtain a line graph from a graph G , the vertices of G are converted to edges; the edges of G are converted to vertices. However, the neighborhoods remain the same as in G . For example, in Fig. 2, the orange-colored vertices of nanocone (a) are converted to the orange-colored edges of the line graph (b) of the nanocone and the blue-colored edges of nanocone (a) are converted to the blue-colored vertices of the line graph (b) of the nanocone (similarly as in Figs 3 and 4).

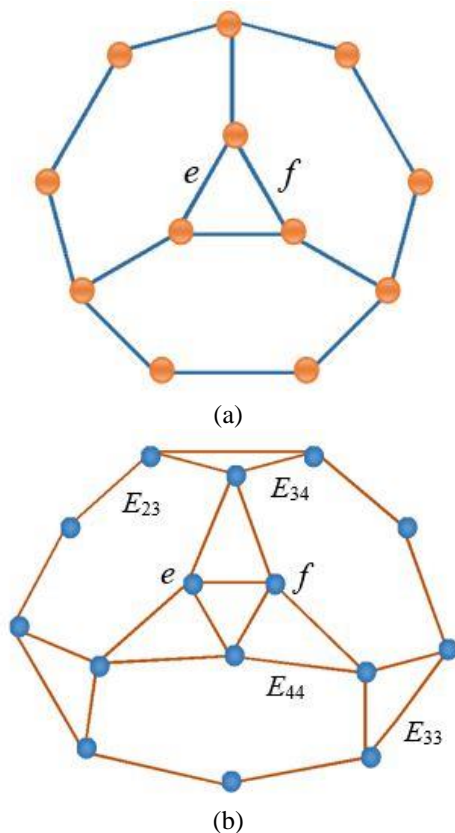


Fig. 2. The graph of carbon nanocone (a) $C_3[1]$ and its line graph (b) $L(C_3[1])$.

In this paper, we aim at developing the edge harmonic index for generalized carbon nanocones. Subsequently, we want to obtain a generalized formula for this index.

RESULTS AND DISCUSSION

Let $CNC_m[n] = C_m[n]$. Our notation is standard and mainly taken from standard books of graph theory [6-8]. Now, we give the required theorems and propositions to perform our aim.

Theorem 1. Consider the graph of carbon nanocone $C_3[n]$. Then we get

$$H_e(C_3[n]) = \frac{12}{5} + (2n-1) + \frac{12n}{7} + \frac{9n^2}{4}.$$

Proof. Let us consider the graph $C_3[n]$ and $L(C_3[n])$. $L(C_3[n])$ has $(9n^2+12n+3)$ edges and $(9n^2+15n)/2+3$ vertices for the first $n=1,2,3,\dots$ layers. On the other hand, there are 6 edges of type $(d(e)=2, d(f)=3)$, $(6n-3)$ edges of type $(d(e)=3, d(f)=3)$, $(6n)$ edges of type $(d(e)=3, d(f)=4)$ and $(9n^2)$ edges of type $(d(e)=4, d(f)=4)$. For $C_3[n]$ ($n \geq 1$), we get

$$H_e(C_3[n]) = \frac{12}{5} + (2n-1) + \frac{12n}{7} + \frac{9n^2}{4}.$$

Theorem 2. Consider the graph of carbon nanocone $C_4[n]$. Then we get

$$H_e(C_4[n]) = \frac{16}{5} + \frac{8n-4}{3} + \frac{16n}{7} + 3n^2.$$

Proof. Let us consider the graph $C_4[n]$ and $L(C_4[n])$. $L(C_4[n])$ has $(12n^2+16n+4)$ edges and $(6n^2+10n+4)$ vertices for the first $n=1,2,3,\dots$ layers. On the other hand, there are 8 edges of type $(d(e)=2, d(f)=3)$, $(8n-4)$ edges of type $(d(e)=3, d(f)=3)$, $(8n)$ edges of type $(d(e)=3, d(f)=4)$ and $(12n^2)$ edges of type $(d(e)=4, d(f)=4)$. For $C_4[n]$ ($n \geq 1$), we get

$$H_e(C_4[n]) = \frac{16}{5} + \frac{8n-4}{3} + \frac{16n}{7} + 3n^2.$$

Proposition 3. Consider the graph of carbon nanocone $C_3[1]$. Then we have

$$H_e(C_3[1]) = \frac{12}{5} + 1 + \frac{12}{7} + \frac{9}{4}.$$

Proof. The graph $C_3[1]$ and its line graph $L(C_3[1])$ are illustrated in Fig. 2. The graph $L(C_3[1])$ has 24 edges and 15 vertices. If e and f be endpoints on any edge then there exist,

6 edges (E_{23}) of type $d(e) = 2$ and $d(f) = 3$,

3 edges (E_{33}) of type $d(e) = d(f) = 3$,

6 edges (E_{34}) of type $d(e) = 3$ and $d(f) = 4$,

9 edges (E_{44}) of type $d(e) = d(f) = 4$. Hence,

$$H_e(C_3[1]) = \sum_{ef \in E(L(C_3[1]))} \frac{2}{d(e)+d(f)} = 6 \times \frac{2}{2+3} + 3 \times \frac{2}{3+3} + 6 \times \frac{2}{3+4} + 9 \times \frac{2}{4+4} = \frac{12}{5} + 1 + \frac{12}{7} + \frac{9}{4}.$$

Proposition 4. Consider the graph of carbon nanocone $C_3[2]$. Then we have

$$H_e(C_3[2]) = \frac{12}{5} + 3 + \frac{24}{7} + 9.$$

Proof. The graph $C_3[2]$ and its line graph $L(C_3[2])$ are illustrated in Fig. 3. The graph $L(C_3[2])$ has 63 edges and 36 vertices. We have:

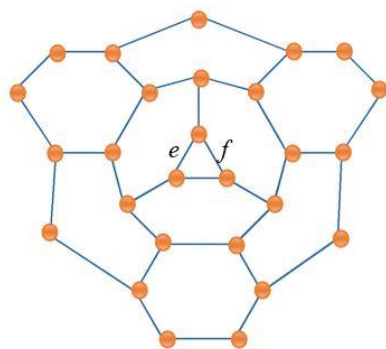
6 edges (E_{23}) of type $d(e) = 2$ and $d(f) = 3$,

9 edges (E_{33}) of type $d(e) = d(f) = 3$,

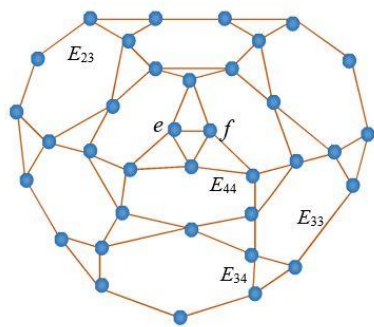
12 edges (E_{34}) of type $d(e) = 3$ and $d(f) = 4$,

36 edges (E_{44}) of type $d(e) = d(f) = 4$. Hence,

$$H_e(C_3[2]) = 6 \times \frac{2}{2+3} + 9 \times \frac{2}{3+3} + 12 \times \frac{2}{3+4} + 36 \times \frac{2}{4+4} = \frac{12}{5} + 3 + \frac{24}{7} + 9.$$



(a)



(b)

Fig. 3. The graph of carbon nanocone (a) $C_3[2]$ and its line graph (b) $L(C_3[2])$.

Proposition 5. Consider the graph of carbon nanocone $C_4[1]$. Then we have

$$H_e(C_4[1]) = \frac{16}{5} + \frac{4}{3} + \frac{16}{7} + 3.$$

Proof. The graph $C_4[1]$ and its line graph $L(C_4[1])$ are illustrated in Fig. 4. The graph $L(C_4[1])$ has 32 edges and 20 vertices. We get

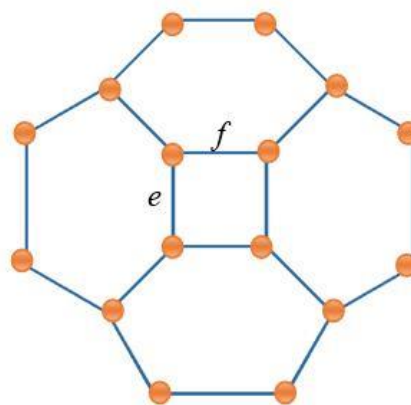
8 edges (E_{23}) of type $d(e) = 2$ and $d(f) = 3$,

4 edges (E_{33}) of type $d(e) = d(f) = 3$,

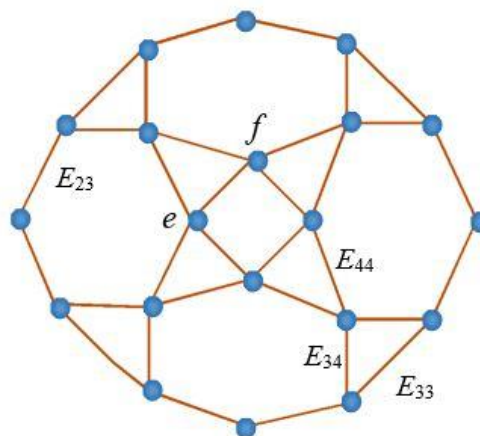
8 edges (E_{34}) of type $d(e) = 3$ and $d(f) = 4$,

12 edges (E_{44}) of type $d(e) = d(f) = 4$. Hence,

$$H_e(C_4[1]) = 8 \times \frac{2}{2+3} + 4 \times \frac{2}{3+3} + 8 \times \frac{2}{3+4} + 12 \times \frac{2}{4+4} = \frac{16}{5} + \frac{4}{3} + \frac{16}{7} + 3.$$



(a)



(b)

Fig. 4. The graph of carbon nanocone (a) $C_4[1]$ and its line graph (b) $L(C_4[1])$.

Proposition 6. Consider the graph of carbon nanocone $C_4[2]$. Then we have

$$H_e(C_4[2]) = \frac{16}{5} + 4 + \frac{32}{7} + 12.$$

Proof. The graph $L(C_4[2])$ has 84 edges and 48 vertices. Accordingly,

8 edges of type $d(e) = 2$ and $d(f) = 3$,
 12 edges of type $d(e) = d(f) = 3$,
 16 edges of type $d(e) = 3$ and $d(f) = 4$,
 48 edges of type $d(e) = d(f) = 4$. Hence,

$$H_e(C_4[2]) = 8 \times \frac{2}{2+3} + 12 \times \frac{2}{3+3} + 16 \times \frac{2}{3+4} + 48 \times \frac{2}{4+4} = \frac{16}{5} + 4 + \frac{32}{7} + 12.$$

We infer the following generalized formula from the above propositions and theorems.

Theorem 7. Let $m \geq 3$ and $n \geq 1$ be positive integers. Then, the generalized formula is of the form

$$H_e(C_m[n]) = 2m \times \frac{2}{2+3} + (2mn - m) \times \frac{2}{3+3} + 2mn \times \frac{2}{3+4} + 3mn^2 \times \frac{2}{4+4} = \frac{4m}{5} + \frac{m(2n-1)}{3} + \frac{4mn}{7} + \frac{3mn^2}{4}.$$

Proof. Let E_{23} , E_{33} , E_{34} and E_{44} orange-colored edges are subsets of $E(L(C_m[n]))$. Then, for every $E_{ij} = ef \in E(L(G))$, $s(E_{23})$, $s(E_{33})$, $s(E_{34})$ and $s(E_{44})$ are the number of E_{23} , E_{33} , E_{34} and E_{44} orange-colored edges)

$$E_{23} = \{d(e) = 2, d(f) = 3\}, s(E_{23}) = 2m,$$

$$E_{33} = \{d(e) = d(f) = 3\}, s(E_{33}) = m(2n-1),$$

$$E_{34} = \{d(e) = 3, d(f) = 4\}, s(E_{34}) = 2mn,$$

$$E_{44} = \{d(e) = d(f) = 4\}, s(E_{44}) = 3mn^2.$$

Hence,

$$H_e(C_m[n]) = \frac{4m}{5} + \frac{m(2n-1)}{3} + \frac{4mn}{7} + \frac{3mn^2}{4}.$$

The proof is completed.

Yang and Hua [19] have introduced the generalized formula of harmonic index as the following theorem.

Theorem 8. [19] The formula of the harmonic index for the generalized carbon nanocones is

$$H(C_m[n]) = \frac{m}{2} + \frac{17nm}{30} + \frac{mn^2}{2}.$$

In Tables 1 and 2, the numbers of edges of type $(d(e)=2, d(f)=3)$, $(d(e)=3, d(f)=3)$, $(d(e)=3, d(f)=4)$ and $(d(e)=4, d(f)=4)$ have been illustrated, respectively. The values of H_e index have been calculated for some $C_3[n]$, $C_4[n]$, $C_5[n]$ and $C_7[n]$. In addition, we make comparison between the edge harmonic and harmonic indices in Table 3.

Table 1. The values of H_e index for some $C_3[n]$ and $C_4[n]$

Types of nanocones	Number of edges of type $d(e)=2, d(f)=3$	Number of edges of type $d(e)=3, d(f)=3$	Number of edges of type $d(e)=3, d(f)=4$	Number of edges of type $d(e)=4, d(f)=4$	H_e index values
$C_3[1]$	6	3	6	9	7.37
$C_3[2]$	6	9	12	36	17.83
$C_3[3]$	6	15	18	81	32.79
$C_3[4]$	6	21	24	144	52.26
$C_4[1]$	8	4	8	12	9.82
$C_4[2]$	8	12	16	48	23.77
$C_4[3]$	8	20	24	108	43.72
$C_4[4]$	8	28	32	192	69.68

Table 2. The values of H_e index for some $C_5[n]$ and $C_7[n]$

Types of nanocones	Number of edges of type $d(e)=2, d(f)=3$	Number of edges of type $d(e)=3, d(f)=3$	Number of edges of type $d(e)=3, d(f)=4$	Number of edges of type $d(e)=4, d(f)=4$	H_e index values
$C_5[1]$	10	5	10	15	12.27
$C_5[2]$	10	15	20	60	29.72
$C_5[3]$	10	25	30	135	54.66
$C_5[4]$	10	35	40	240	87.10
$C_7[1]$	14	7	14	21	17.18
$C_7[2]$	14	21	28	84	41.60
$C_7[3]$	14	35	42	189	76.52

Table 3. A comparison between H_e and H for some $C_3[n]$, $C_5[n]$ and $C_7[n]$

Nanocones	$C_3[1]$	$C_3[2]$	$C_3[3]$	$C_4[4]$	$C_5[1]$	$C_5[2]$	$C_5[3]$	$C_7[1]$	$C_7[2]$	$C_7[4]$
H_e index	7.37	17.83	32.79	69.68	12.27	29.72	54.66	17.18	41.60	121.93
H index [19]	4.7	10.9	20.1	43.07	7.83	18.17	33.5	10.97	25.43	75.37

AN ALGORITHM FOR H_e INDEX

In this section, an algorithm (pseudocode) is given.

m is the number of edges of the line graph,

h_1, h_2, \dots, h_m ($h=ef$) are edges of the line graph,

Sum is the sum of H_e index for each edge.

Step 0. Start.

Step 1. Take $Sum=0, i=0$.

Step 2. $i=i+1$.

Step 3. Determine the degrees of $d(e)$ and $d(f)$

for h_i .

Step 4. $Sum=Sum + 2/(d(e)+d(f))$.

Step 5. If $i < m$ then, return to Step 2.

Step 6. Else, write the Sum .

Step 7. Stop.

CONCLUSIONS

Many topological indices have been established in the physico-chemical, pharmaceutical, toxicologic, biological models and other structure analyzing.

In this paper, we have obtained a generalized formula of edge harmonic index of carbon nanocones by using propositions and theorems.

The numerical results in Table 3 can be easily used and evaluated for QSAR and QSPR studies in [11]. For further studies, it would be interesting to use the line graphs of carbon nanocones in the investigation of their mathematical properties, QSAR, QSPR studies and other topological indices.

In addition, Theorem 7 can be easily applied to the other carbon nanocones.

REFERENCES

1. M. Ge, K. Sattler, *Chem. Phys. Lett.*, **220**, 192 (1994).
2. D. R. Nelson, L. Peliti, *J. Phys. (Paris)* **48**, 1085 (1987).
3. H. Wiener, *J. Am. Chem. Soc.*, **69**, 17 (1947).
4. S. Fajtlowicz, *Congr. Numer.*, **60**, 187 (1987).
5. R. Nazir, S. Sardar, S. Zafar, Z. Zahid, *J. Appl. Math. & Informatics*, **34**, 479 (2016).
6. D. B. West, *Introduction to Graph Theory*, Prentice Hall: Upper Saddle River, 1996.
7. N. Trinajstić, *Chemical Graph Theory*, CRC Press: Boca Raton, FL, 1983.
8. J. L. Gross, J. Yellen, *Graph Theory and Its Applications*, CRC Press: Boca Raton, FL, 2006.
9. R. Todeschini, V. Consonni, *Handbook of Molecular Descriptors*, Wiley-VCH: Weinheim, 2000.
10. M. V. Diudea, *QSPR/QSAR Studies by Molecular Descriptors*, Nova Science Publishers: Huntington, NY, 2000.
11. <http://www.moleculardescriptors.eu>.
12. A. Nejati, M. Alaeiyan, *Bulgarian Chem. Commun.*, **46**, 462 (2014).
13. S. Ediz, *Fullerenes, Nanotubes and Carbon Nanostructures*, **21**, 113 (2013).
14. M. R. Farahani, *Proc. Rom. Acad., Series B*, **15**, 83 (2013).
15. A. Khaksar, M. Ghorbani, H. R. Maimani, *Optoelectron. Adv. Mater. – Rapid Commun.*, **4**, 1868 (2010).
16. A. R. Ashrafi, F. Gholami-Nezhaad, *Current Nanoscience*, **5**, 51 (2009).

17. A. R. Ashrafi, Z. Mohammad-Abadi, *Current Nanoscience*, **8**, 180 (2012).
18. M. Ghorbani, M. Jalali, *MATCH Commun. Math. Comput. Chem.*, **62**, 353 (2009).
19. L. Yang, H. Hua, *Optoelectron. Adv. Mater. – Rapid Commun.*, **6**, 660 (2012).
20. E. Aslan, *Optoelectron. Adv. Mater. – Rapid Commun.*, **9**, 525 (2015).
21. E. Aslan, *J. Comput. Theor. Nanosci.*, **12**, 4455 (2015).
22. T. Turacı, M. Ökten, *J. Comput. Theor. Nanosci.*, **12**, 3977 (2015).

РЪБОВ ХАРМОНИЧЕН ИНДЕКС НА ВЪГЛЕРОДНИ НАНОКОНУСИ И АЛГОРИТЪМ

Е. Аслан¹, Й. К. Кюркчю^{2*}

¹ Департамент по софтуерно инженерство, Университет на Маниса Целал Баяр, Маниса, Турция

² Департамент по математика, Измирски икономически университет, Измир, Турция

Постъпила на 16 януари, 2017 г.; коригирана на 8 март, 2018 г.

(Резюме)

Ръбовият хармоничен индекс $H_e(G)$ на (химичната) графа G се основава на крайните степени на ръбовете на линейната графа $L(G)$. В настоящата статия се предлага обобщена формула и алгоритъм (псевдокод) за ръбовия хармоничен индекс. Целта на статията е да се разработи ръбов хармоничен индекс за въглеродни наноконуси.

Comparison of properties of natural rubber composites with hybrid fillers containing different modifying phase and their applicability in flexible antennas

A.G. Al-Sehemi^{1,2}, A. Al-Ghamdi³, N.T. Dishovsky^{4*}, P. A. Malinova⁴,
N.T. Atanasov^{5,6}, G. L. Atanasova^{5,6}

¹Research Center for Advanced Materials Science (RCAMS), King Khalid University, Abha 61413, P.O. Box 9004, Saudi Arabia

²Department of Chemistry, College of Science, King Khalid University, Abha 61413, P.O. Box 9004, Saudi Arabia,

³Department of Physics, Faculty of Science, King Abdulaziz University, Jeddah, Saudi Arabia

⁴Department of Polymer Engineering, University of Chemical Technology and Metallurgy, 1756 Sofia, Bulgaria

⁵Department of Telecommunications, Faculty of Telecommunications and Management, University of Telecommunications and Post, 1700 Sofia, Bulgaria

⁶Department of Communication and Computer Engineering, Faculty of Engineering, South-West University 'Neofit Rilski', 2400 Blagoevgrad, Bulgaria

Received October 19, 2017; Revised April 4, 2018

The paper presents a comparison of the effect that the chemical nature and structural specifics of the modifying oxide phase has upon dielectric and magnetic properties of natural rubber based composites. The fillers used have been prepared by impregnation of conductive carbon black with modifying oxides, SiO₂ and Fe₃O₄. The applicability of the composites as substrates in small flexible wearable antennas was investigated. It has been found that the chemical and crystallographic nature of the oxide modifying phase are the crucial factors determining the real parts of permittivity and permeability and loss angle tangents of the composites comprising the hybrid fillers. All composites developed meet the requirements of the rubber substrate antenna material. When better antenna characteristics are required, it is preferable the antenna substrate to be of a composite comprising hybrid filler with a silica phase. When focusing on the miniaturization of the antenna, it is preferable to use a hybrid filler with a magnetite modifying phase.

Keywords – dielectric properties; magnetic properties; natural rubber based composites; hybrid fillers; oxide modifying phase; flexible wearable antenna

INTRODUCTION

Recently, the markets for equipment for high-frequency wireless LAN, RFID (radio frequency identification), UWB, GPS, terrestrial digital broadcasting, home network, etc. have been dramatically expanding. In this context, a diversity of dielectric antennas are currently used. Conventional antennas often consist of a ceramic material whose relative dielectric constant cannot be arbitrarily selected. Consequently, the degree of freedom in designing antenna is low. Furthermore, these conventional antenna materials are hard and brittle, lack flexibility and are vulnerable to impact [1]. Therefore, the elastomer based composites are an alternative to conventional antenna materials used as substrates.

The requirements and typical features of **the rubber substrate antenna material** may be summarized as follows [1,2]:

- Relative dielectric constant can be selected arbitrarily (4-20). According to other authors, the dielectric constant of the various flexible substrates is in the range of 2.2-12.0 [3]. The lower dielectric

constant declines the surface wave losses which are related to the guided wave broadcast within the substrate [4].

- Low dielectric loss tangent (0.01 or lower)

Loss Tangent ($\tan\delta$) is also identified as a dissipation factor. It describes the amount of power turned into heat in the substrate material. The loss tangent in the following relation is defined as the ratio of the imaginary part to real part of the relative permittivity. The higher values of loss tangent results in additional losses in the dielectric substrate and higher losses outcomes in reduced radiation efficiency [5].

- Magnetic permeability, especially the tangent of the magnetic losses angle directly, is related to miniaturization of the antenna and its other important parameters like the geometric ones [6]. In literature [6,7] the values for these parameters, which depending on the frequency domain of the antenna, may vary between 1 and 6.5 for the real part of magnetic permeability between 0.003 and 0.5 for the tangent of magnetic losses angle.

As known, each environment is characterized by wave impedance [8] which is affected by the real and imaginary part of the

* To whom all correspondence should be sent:
dishov@uctm.edu

dielectric and magnetic permeability. Our working hypothesis is that by appropriate choice of the dielectric permittivity and magnetic permeability of the elastomer based composites used as substrates in small flexible wearable antennas one can achieve the best their performance. The last includes a minimal absorption of electromagnetic power in the human body and most of power in the free space around it. In accordance with the further development of our hypothesis, the dielectric permittivity and magnetic permeability of the tested composites can easily and accurately be adjusted using optimal quantities of hybrid fillers, whose characteristics can be controlled by introducing an inorganic modifying oxide phase into a highly conductive carbon phase. The conductive aggregates and agglomerates could be insulated by introduction of a second less conductive phase to fill the space between the aggregate and agglomerates. The second phase would have its own contribution to the formation of the dielectric and magnetic losses of the composite. For the purpose we have chosen two oxide phases differing completely in their chemical, crystallochemical and crystallographic properties, namely SiO₂ (silica) and Fe₃O₄ (magnetite) as a modifying phase.

Taking into consideration the specific features of the impregnation technologies [9] we have found them to be the most appropriate for synthesizing hybrid dual-phase fillers, containing different modifying phase.

In accordance with the working hypothesis, the paper presents a comparative study on the effect that the chemical nature and structural specifics of the modifying oxide phase has upon dielectric and magnetic properties of natural rubber based composites filled with hybrid fillers based on conductive carbon black. The applicability of these composites as substrates in small flexible wearable antennas is also investigated. The fillers have been prepared by an impregnation technology at equivalent amounts of the oxide phases.

EXPERIMENTAL

Materials

Natural rubber SVR 10 supplied by Hong Thanh Rubber Pty. Ltd. was used as a polymer matrix. The other ingredients such as zinc oxide (ZnO), stearic acid, N-tert-butyl-2-benzothiazole sulfenamide (TBBS) and sulfur (S) were commercial grades and used without further purification.

Electroconductive carbon black (CCB) Printex XE-2B (produced by Orion Engineered Carbons GmbH) was used as a substrate of the hybrid fillers.

Hybrid fillers preparation

Preparation of the conductive carbon black-magnetite (CCB/M) hybrid fillers. Conductive carbon black (90 g) and 10 g of magnetite (containing 95-100% of Fe₃O₄ and 0-5% of silica, purchased from Inoxia, UK) were loaded into a ball mill, 1500 ml of ethyl alcohol were poured and the carbon black was impregnated for 2 h. Ethyl alcohol was used to avoid eventual oxidation of magnetite. The suspension thus obtained was dried at 50°C for 2 h. Then the temperature was raised to 150°C and the drying continued for 2 more hours till the product was completely dry. The yield was ground again in a ball mill for 2 h. After that the grind was loaded into the reactor and heated under 10⁻² mm Hg vacuum at 440°C for 2 h. If necessary, the product was ground once more in a ball mill.

Preparation of conductive carbon black-silica (CCB/S) hybrid fillers. Conductive carbon black (90 g) and 32.5 ml of silicasol (containing 40% of SiO₂, pH – 9 and density 1.3 g/cm³) comprising 10 g of silica, were loaded into a ball mill and 1600 ml of distilled water were poured. The carbon black was impregnated for 2 h and the product was dried at 150 °C till the complete evaporation of water. The dried product was ground again in a ball mill for 2 h. After that the grind was loaded into the reactor and heated under 10⁻² mm Hg vacuum at 440°C for 2 h. Being removed from the reactor, the sample was ground once more in a ball mill and was ready for further experiments.

Preparation of rubber composites. The rubber compounds studied were prepared on a two-roll laboratory mill (rolls Length/Diameter 320x160 mm). Table 1 presents the compositions of the rubber compounds studied.

Table 1: Compositions of the investigated natural rubber based composites (phr)

	CCB	CCB/ /silica	CCB/ magnetite
Natural Rubber – SVR 10	100.0	100.0	100.0
Zinc Oxide	3.0	3.0	3.0
Stearic Acid	2.0	2.0	2.0
CCB	70.0	-	-
CCB/S(90:10)	-	70.0	-
CCB/M (90:10)	-	-	70.0
TBBS	1.5	1.5	1.5
Sulfur	2.0	2.0	2.0

The vulcanization of the natural rubber based compounds was carried out on an electrically heated hydraulic press using a special homemade steel mold at 150°C and 10 MPa. The optimum vulcanization time was determined by the vulcanization isotherms in accordance with ISO 3417:2002. The specimens needed for the

measurements cut from the obtained vulcanizates were 200x200x2 mm in size.

Measurements

Characterization of the studied fillers. The texture characteristics of the studied fillers were determined by low-temperature (77.4 K) nitrogen adsorption on a Quantachrome Instruments NOVA 1200e (USA) apparatus. The nitrogen adsorption–desorption isotherms were analyzed to evaluate the following parameters: specific surface area (S_{BET}) determined on the basis of the BET equation and total pore volume (V_t) estimated in accordance with the Gurvich rule [10]. The average diameter of the mesopores and their size distribution were determined by the method of Barrett-Joyner-Halenda (BJH) [11]. The volume of the micropores (V_{MI}) and the their specific surface area (S_{MI}), as well as the external specific surface area (S_{EXT}) were evaluated according to V-t-method [12]. Additionally, the pore-size distributions were calculated by the density functional theory (DFT) method using NLDFT equilibrium model [13]. All samples were outgassed for 16 hours in vacuum at 120°C before the measurements. The iodine adsorption number (IA) was determined in accordance with ISO 1304:2006; oil absorption number (OAN) – in accordance with ISO 4656:2012.

The hybrid fillers were also investigated by TEM to ascertain the distribution of carbon, silica and magnetite. The TEM investigations were performed on a TEM JEOL 2100 instrument at accelerating voltage of 200 kV. The specimens were prepared by grinding and ultrasonic dispersion in ethanol for 6 minutes. The suspension was dripped on standard holey carbon/Cu grids. The measurements of lattice-fringe spacing recorded in HRTEM micrographs were made using digital image analysis of reciprocal space parameters. The analysis was carried out by the Digital Micrograph software. TEM JEOL 2100; XEDS: Oxford Instruments, X-MAX^N 80T; CCD camera Orius 1000, 11 Mp, GATAN.

Characterization of the studied composites

Permittivity and permeability measurement. The electromagnetic parameters of the composite materials were measured by the resonant perturbation method [14]. For the rectangular cavity, the TE_{10n} modes were used for the complex permittivity and permeability measurements. The sample was placed at the position of maximum intensity of electric field, where $n=odd$ was always adopted, because the sample position could be located easily as the geometric center of the cavity is one of the maximum positions [15]. The formulas for

the real and imaginary parts of the relative permittivity areas are the following [16]:

$$\epsilon' = \left(\frac{f_c - f_s}{2f_s} \right) \left(\frac{V_c}{V_s} \right) + 1 \quad (1)$$

$$\epsilon'' = \left(\frac{V_c}{4V_s} \right) \left(\frac{1}{Q_s} - \frac{1}{Q_c} \right) \quad (2)$$

where f_c and Q_c are resonance frequency and quality factor of the cavity without an inserted sample, f_s and Q_s - are with an inserted sample, respectively; V_c is the volume of the cavity; V_s is the volume of the sample.

For permeability measurements the sample was placed at the position of maximum magnetic field, where $n=even$ was always adopted.

The formulas for the real and imaginary parts of the relative permeability areas are the following [17]:

$$\mu' = \left(\frac{f_c - f_s}{f_s} \right) \left(\frac{V_c}{V_s} \right) \left(\frac{\lambda_g^2 + 4a^2}{8a^2} \right) + 1 \quad (3)$$

$$\mu'' = \left(\frac{V_c}{V_s} \right) \left(\frac{1}{Q_s} - \frac{1}{Q_c} \right) \left(\frac{\lambda_g^2 + 4a^2}{16a^2} \right) \quad (4)$$

where $\lambda_g = 2d/L$, is the guided wavelength and $L=1,2,3,\dots$; d is cavity length and a is cavity width.

The measurements were performed at room temperature varying from 19°C to 24°C within the frequency range of 3.0 GHz to 9.5 GHz, at incident power ≤ 5 mW.

The loss tangents were calculated by the equations:

$$\tan \delta_\epsilon = \epsilon''/\epsilon' \quad (5)$$

$$\tan \delta_\mu = \mu''/\mu' \quad (6)$$

RESULTS AND DISCUSSION

Characterization of the studied fillers

Table 2 summarizes the main characteristics of the substrate carbon black and of the hybrid fillers with different modifying phase obtained.

The oil absorption number (OAN) or dibutylphthalate absorption (DBPA) of the fillers gives an idea of their ability to form different secondary structures – aggregates and agglomerates. Therefore OAN is a crucial parameter for most of the fillers used in rubber industry [18, 19]. As Table 2 shows, OAN of virgin Printex XE-2B carbon black is 420 ml/100g. The conductive carbon black/silica (CCB/S) filler obtained by impregnation has an OAN value of 505 ml/100g. That indicates the prepared hybrid filler to be more capable of forming different secondary structures than the non-modified carbon black. That is because the former filler comprises silica. As known, silica is hydrophilic – there are hydroxyl (silanol) groups interacting with each other via hydrogen bonds over its surface.

Table 2. Main properties of the studied fillers

Sample	OAN, ml/100g	IA, mg/g	S _{BET} , m ² /g	S _{MI} , m ² /g	S _{EXT} , m ² /g	V _t , cm ³ /g	V _{MI} , cm ³ /g	D _{AV} , nm
Printex XE-2B	420	1125	1000	-	-	-	-	-
Printex XE-2B/SiO ₂	505	770	870	74	817	1.67	0.025	7.6
Printex XE-2B/Fe ₃ O ₄	410	695	861	66	794	0.03	1.450	6.7

Hence, silica is more apt to agglomerate than carbon black. The hybrid filler comprising magnetite has an OAN value lower than that of the substrate carbon black because of the functional groups over its surface what favors the filler-filler interactions.

The iodine adsorption (IA) of fillers reveals their adsorption activity, towards the elastomer macromolecules, inclusive. Obviously, the adsorption ability of silica is greater than that of magnetite owing first of all to the adsorption centers and to polar functional groups available on the surface of its particles what determines its higher iodine number.

As seen from Table 2, the specific surface area (BET) of virgin carbon black (Printex XE-2B) is about 1000 m²/g. The introduction of a second phase lowers the specific surface area, as the specific surface area of the oxide phase, and particularly of magnetite, is lower.

Obviously, the difference in the properties of SiO₂ and Fe₃O₄ used for the modification is quite

significant and leads to differences in the adsorption-texture parameters of the hybrid fillers obtained. Some of those parameters (specific surface area of the micropores, external specific surface area, the average pore diameter) have close values but two of their texture characteristics differ significantly: the total pore volume of silica (1.67 cm³/g) is much higher than that of magnetite (0.03 cm³/g), while in the case of micropores volume it is on the contrary – that of magnetite (1.450 cm³/g) is higher than the one of silica. The differences are a consequence of the crystallographic and crystallochemical differences between amorphous SiO₂ and crystalline Fe₃O₄. As seen, the micropores dominate in Fe₃O₄ volume while mesopores are predominant in SiO₂.

The distribution of carbon, magnetite and silica phases within the hybrid filler obtained was investigated by scanning transmission electron microscopy (STEM) and energy dispersive X-ray spectroscopy (EDS).

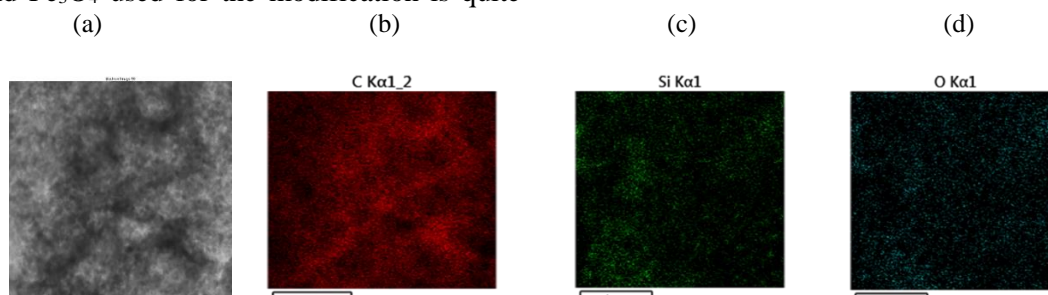


Fig. 1. a) Bright field STEM image of CCB/S hybrid filler; b) carbon map; c) silicon map; d) oxygen map

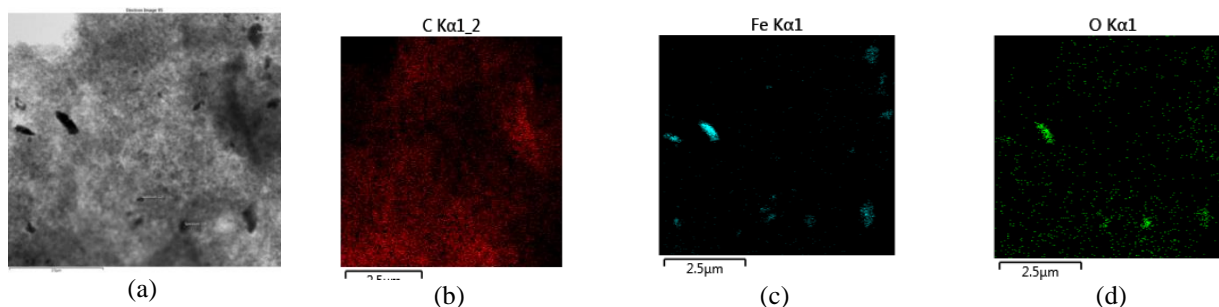


Fig. 2. a) Bright field STEM image of CCB/M hybrid filler; b) carbon map; c) iron map; d) oxygen map

Fig. 1 and Fig. 2 present the bright field STEM images and the compositional maps of the hybrid fillers investigated.

First of all figures 1 - 2 confirm the successful modification of conductive carbon black with the different oxide phases which yielded hybrid fillers of

a different type. The compositional maps of the fillers obtained demonstrate the silica phase to be distributed in the carbon one more homogeneously than the magnetite phase. Oxide phases are distributed mainly over the surface of carbon aggregates, though there are cases of greater aggregation when the oxide phase, especially magnetite, interpenetrates the aggregates. STEM is in agreement with the texture characteristics of the studied hybrid fillers and supports the data from the composition maps, confirming the fact that the oxide phases in both fillers hinder to a certain extent the contacts between carbon black aggregates and

agglomerates. That phenomenon could be a tool for tailoring the permittivity and permeability of elastomer composites by regulating the oxide phase amount and its chemical nature in the hybrid fillers used to reinforce the composites. TEM high resolution micrographs (x 400 000) are a good illustration of that effect (Fig. 3). The oxide phase distributed amongst (and probably inside) carbon black aggregates and insulating them, occurs on the image as darker and ordered structures. The effect is better pronounced for silica (Fig. 3c).

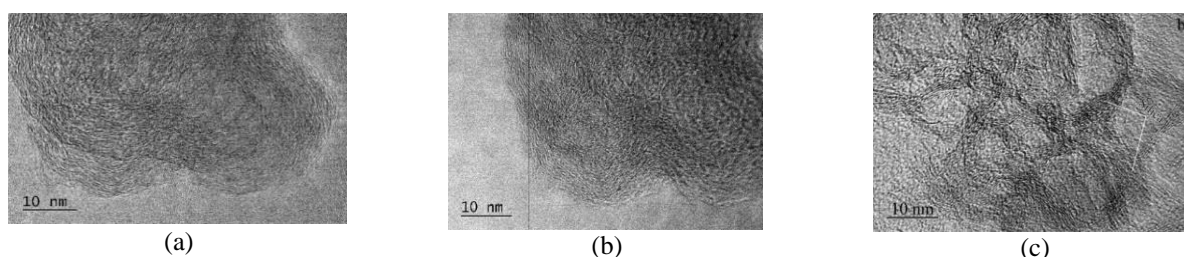


Fig. 3. High resolution TEM images of a filler comprising: a) 0 wt % magnetite; b) 10 wt % magnetite; c) 10 wt % silica

Obviously, the oxide phase having a resistance higher than that of conductive carbon black hinders the formation of electro conductive pathways. The process is more pronounced when silica is used as modifying phase.

Complex permittivity and permeability

Composites and their applicability as substrates for small flexible wearable antennas are characterized by their relative permittivity (ϵ_r^*) and permeability (μ_r^*). These properties are reported in terms of relative complex numbers: $\epsilon^* = \epsilon_r' - j\epsilon_r''$ and $\mu_r^* = \mu_r' - j\mu_r''$. They both express the interactions between composite materials and electromagnetic fields [20, 21]. The permittivity is a measure of the effect that a material has on the electric field in the electromagnetic wave and the permeability is a measure of the effect that a material has on the magnetic component of the wave. Figures 4-5 present the frequency dependences of the real part of the permittivity and the tangent of dielectric loss angle of the composites containing hybrid fillers with different oxide phase.

As seen from Fig. 4, the values of the real part of the relative permittivity for the composite comprising a hybrid filler with a silica phase are

expectedly higher than those of the composite comprising a hybrid filler with a magnetite phase. The values recorded in the 4-8 GHz range are in the 4-20 scale, i.e. those composites meet the requirements for materials with potential application as substrates for small wearable flexible antennas. The difference might be related to the difference in chemical and crystallographic nature of the two oxides.

Therefore the latter have a very different effect upon the factors determining the real part of the relative permittivity. It can be seen from Figure 5 that the tangent of the dielectric loss angle of the composite with the magnetite modifying phase is in the range of 0.7-3.5 while those for the composite comprising silica are in the 0.01-0.4 range (Fig. 5). It is obvious that composites with hybrid fillers containing silica as second modifying phase meet in higher extent the requirements to the rubber substrate antenna material [1, 2]. Figures 6-7 present the frequency dependences of the real part of the relative permeability as well as the frequency dependence of the of magnetic loss angle of the composites containing hybrid fillers with different oxide phase.

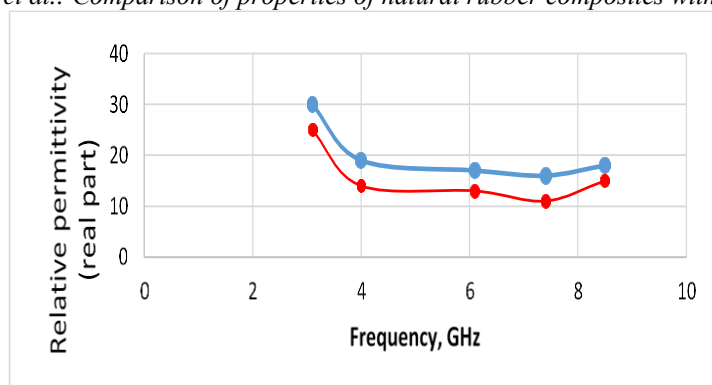


Fig. 4. Frequency dependence of the real part of the relative permittivity of composites containing hybrid fillers with different oxide phase

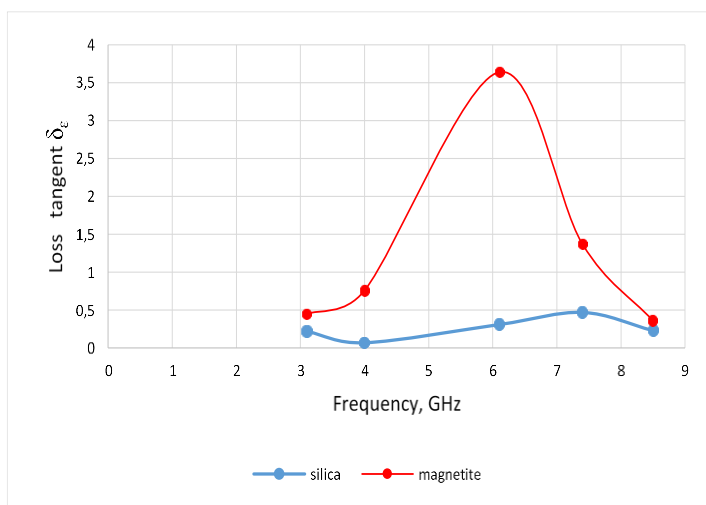


Fig. 5. Frequency dependence of the tangent of dielectric loss angle of composites containing hybrid fillers with different oxide phase

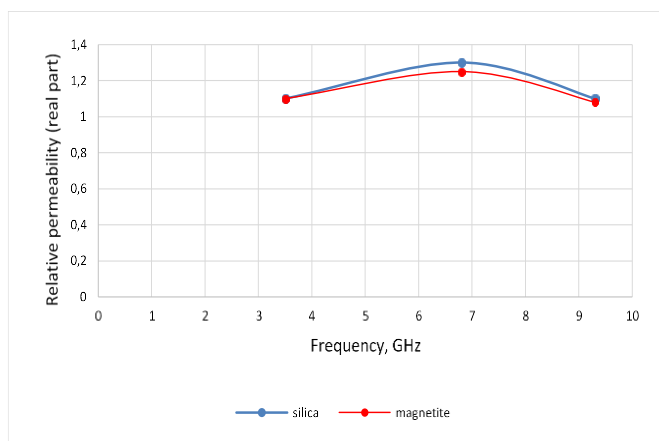


Fig. 6. Frequency dependence of the real part of the relative permeability of the composites containing hybrid fillers with a different oxide phase

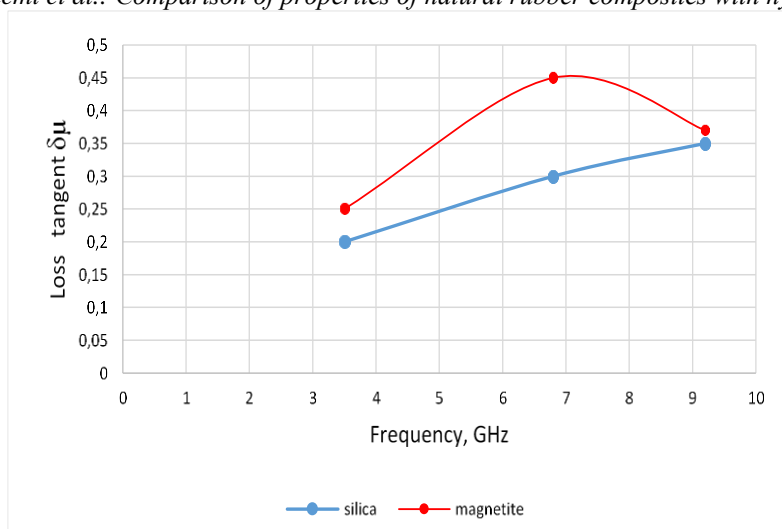


Fig. 7. Frequency dependence of the tangent of magnetic loss angle of composites containing hybrid fillers with a different oxide phase.

As seen from Figure 6, the real parts of the relative permeability for the two composites are quite close (around 1.1-1.3), while the values of the tangent of magnetic loss angle (Figure 7) for the composite with a hybrid filler comprising magnetite are higher (0.25-0.45) than the composites comprising silica (0.20-0.35) but in both cases they meet the requirements for substrates of wearable flexible antennas.

The properties of both dielectric matrix and conductive filler, as well as the morphology and structure of the composite affect the changes in the real and imaginary part of dielectric permittivity [14]. It is obvious that, the applicability of thus reinforced composites for wearable flexible antennas is affected by the modifying oxide phase in the hybrid fillers studied. It impacts mainly the imaginary part of the relative permittivity and permeability and the merit that each of the latter has to the dielectric and magnetic loss tangent. We suppose the introduction of magnetite into Printex XE2-B carbon black, which initially contains vanadium, nickel and iron, leads to the formation of different dipoles. These different dipoles have different relaxation time, giving rise to different relaxation frequencies. The different relaxation frequencies of the various dipoles formed in the composites, hopping of electrons (between Fe^{+3} and Fe^{+2}) and the relaxation due to interfacial polarization are altogether responsible for the resonant behavior of ϵ_r' and ϵ_r'' . The effects of the oxide phases are definitely related to the difference in their crystallochemical and crystallographic structure. The differences could be summarized as follows:

Magnetite, a high magnetic losses material, belongs to the spinel class and may be characterized by its low toxicity and great stability at high temperature [22]. On the other hand, magnetite crystal structure follows an inverse spinel pattern with alternating octahedral and tetrahedral-octahedral layers. The oxygen ions form a close-packed cubic lattice with the iron ions located at interstices between the oxygen ions. There are two different interstices that the metal ions can take: tetrahedral (A) sites and octahedral (B) sites – Fig. 8 [23]. It is known, that the octahedral sites in the magnetite structure contain ferrous and ferric species. The electrons coordinated with these iron species are thermally delocalized and migrate within the magnetite structure causing high conductivity exchange constants: ranging from $-28 \text{ J}\cdot\text{K}$ to $3 \text{ J}\cdot\text{K}$ between tetrahedral/octahedral sites and octahedral/octahedral sites, respectively [23]. Resultant conductivities range from 10^4 – $10^5 \text{ }\Omega^{-1}\text{m}^{-1}$. Magnetite's Curie temperature is observed at 850 K. Below the Curie temperature, the magnetic moments on tetrahedral sites, occupied by ferric species, are ferromagnetically aligned while the magnetic moments on octahedral sites, occupied by ferrous and ferric species, are antiferromagnetic and cancel each other; such a combined behavior is termed ferrimagnetic [23]. Amorphous silica (SiO_2) is an inorganic material commonly used in semiconductor circuits to isolate different conducting regions. Due to its mechanical resistance, high dielectric strength, and selectivity for chemical modification, amorphous silica has also become a key material in microelectronics. The spatial structure of amorphous silicon dioxide is presented in Fig. 9 [24].

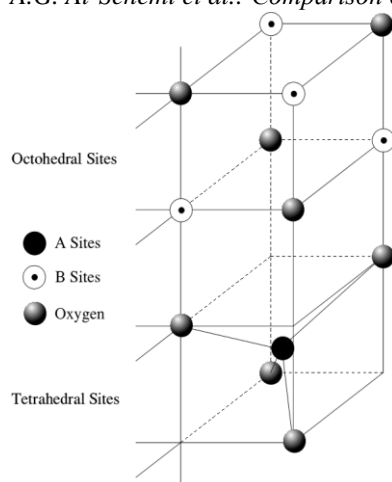


Fig. 8. Crystal structure of magnetite [23]

Comparing Fig. 8 and Fig. 9 one sees the great difference in the chemical, crystallochemical (the dependence of the crystals properties on their atom structure and type of bonds between the atoms) and crystallographic nature of the two oxide phases. That explains the different impact upon the hybrid fillers comprising them, as well as on the permittivity and permeability of the composites reinforced with the hybrid fillers. The crystallochemical factor is of particular importance in the case of magnetite. The comparison of FeO , Fe_2O_3 and Fe_3O_4 reveals that, the three compounds could be described as the densest packing of oxygen ions. However, in the case of the first oxide ferric ions occupy all the octahedral sites, in the case of the second one – $2/3$ of the octahedral sites and in the case of magnetite – half of all existing octahedral and $1/8$ of the tetrahedral sites. Meanwhile magnetite properties are much different from those of the other two ferric oxides and naturally are most favorable for applications in the manufacture of small flexible wearable antennas due to the existing magnetic losses. The magnetic losses for magnetic materials originate mainly from domain wall resonance, hysteresis loss, eddy current loss, and natural resonance [25]. The domain wall resonance normally happens at a frequency lower than 100 MHz, hence it can be neglected in the microwave range. The hysteresis loss is produced in a very strong external magnetic field, and there is no hysteresis loss in the weak magnetic field derived from microwaves. In this study the relative permeabilities were measured at a low microwave power (≤ 5 mW) and over a frequency range of 3.6 GHz to 9.3 GHz, so neither hysteresis loss nor domain wall resonance is the main contributor to magnetic loss. Therefore, the magnetic loss in the composites results from complex phenomena like eddy current loss and natural resonance. In our case,

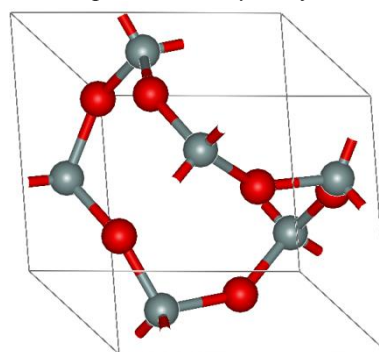


Fig. 9. Spatial structure of amorphous silicon dioxide [24]

the effect that magnetite has is doubtless. In fact, that is the major difference between magnetite and silica phases - the latter cannot produce such an effect. It is also important to note that the hybrid fillers and the changes in them due to the different oxide phase included influence on the interphase region between the rubber matrix and the filler.

Possible applications of the composites comprising hybrid fillers with different oxide phases for enhancing antenna performance

It is seen from the results obtained that both types of composites developed containing hybrid fillers with different modifying oxide phase meet the requirements to the materials which may be used as substrates in flexible antennas. Substrates containing a hybrid filler with one of the two oxide phases can be implemented when particular objectives and requirements should be met. When good characteristics are required, it is preferable the antenna substrate to be of a composite comprising hybrid filler with a silica phase. When focusing on the miniaturization of the antenna, it is preferable to use a hybrid filler with a magnetite phase. In certain cases, two-layered or three-layer substrates made of composite materials containing fillers with both phases - magnetite and silica - can also be used. Choosing one or another modifying oxide phase one can control the properties of the hybrid fillers, respectively the dielectric and magnetic properties of the composites containing them. However, the results from our further experiments have shown that composites with hybrid fillers containing silica as modifying phase are more suitable as flexible antenna substrates than composites containing hybrid fillers with magnetite. A conductive composite loaded with carbon black-silica hybrid filler described above was proposed to reduce human (head or body) effects on antenna performance and SAR values. The investigation was based on a half dipole antenna. The results show a sensible

dependence of the antenna performance and SAR reduction on the size of the composite sample and on the distance between composite sample and reference dipole. We have shown that an appropriate placement of the conductive composite loaded with carbon-silica hybrid filler next to the reference dipole can effectively reduce SAR (up to 70 %), increasing the radiation efficiency (up to 67 %) and the bandwidth (up to 110 %) of the antenna. Consequently, using this technique and such type of composite, SAR, efficiency and bandwidth of the antenna can be improved simultaneously. Other advantages of the techniques that use a conductive composite loaded with a carbon-silica hybrid filler to reduce SAR and human effects on antenna performance are the low cost of the material itself and easy implementation. The results from this work can provide useful information in designing of antennas for wireless devices and are described in details elsewhere [26].

The composites comprising hybrid fillers with different oxide phases with parameters close to those required have been used also as a substrate for manufacturing a small flexible wearable antenna in the 2.22–2.50 GHz band, with dimensions of only 58x40x4.1 mm. The fabricated prototype has good impedance matching ($VSWR < 1.4$) over the targeted frequency band, an operating bandwidth of 11.68% at 2.44 GHz and efficiency of around 19%.

CONCLUSIONS

The impregnation method allows preparing hybrid fillers with modifying oxide phases as well as tailoring the properties of the fillers via control over the oxide phase concentration and chemical nature. The effect that the modifying oxide phase in hybrid fillers based on conductive carbon black has upon the properties of natural rubber composites has been studied. It has been established that the chemical, crystallochemical and crystallographic nature of the oxide phase are the crucial factors determining the permittivity and permeability of the composites comprising the hybrid fillers. Natural rubber based composites containing hybrid fillers with silica as a modifying phase as a whole are more suitable as substrates in small flexible wearable antennas in comparison to composites containing hybrid fillers with magnetite. An appropriate placement of the conductive composite loaded with carbon-silica hybrid filler next to the reference dipole can effectively reduce SAR (up to 70 %), increasing the radiation efficiency (up to 67 %) and the bandwidth (up to 110 %) of the antenna. Consequently, using this technique and such type of composite, SAR, efficiency and bandwidth of the antenna can be improved simultaneously.

ACKNOWLEDGEMENTS. The authors would like to acknowledge the support of King Khalid University for this research through a grant RCAMS/KKU/003-16 under the Research Center for Advanced Materials Science at King Khalid University, Saudi Arabia and the University of Chemical Technology and Metallurgy, Sofia, Bulgaria.

REFERENCES

1. K. Oohira, *NTN Technical Review* **76**, 58, (2008).
2. M. Raees, S. H. Dar, J. Ahmed, *Int J Adv Comput Sci App*, **7**, 190, (2016).
3. C.A. Blannis, *Antenna Theory: Analysis and Design*, Third edition, Wiley, 2005.
4. J. Bauer, M.D. Janezic, D.C. De Groot, High Frequency Dielectric Measurements, *IEEE Instru Meas Mag*, vol. 13, (2010).
5. B. Gupta, S. Sankarlingam, S. Dhar, In: Proceeding of Mediterranean Microwave Symposium, Turkey, 2010, p. 251.
6. L. Martin, D. Staiculescu, H. Li, S. Ooi, C. Wong and M. Tentzeris, Investigation of the impact of magnetic permeability and loss of magnetic composite materials on RFID and RF Passives Miniaturization, *IEEE 2007 Workshop on Computational Electromagnetics in Time-Domain*, 15-17 Oct. 2007, 1-4.
7. K. Borah, N. Bhattacharyya, *Compos Part B-Eng*, **43**, 1309, (2012).
8. Y. Wang, E. Edwards, I. Hopper, N. Clow, P. Grant *J Appl Phys A*, **120**, 609, (2015).
9. H. Marsh, E. Heintz, F. Rodrigues-Reinoso, (eds.) *Introduction to Carbon Technologies*, University of Alicante, Alicante, 1997.
10. L.J. Gurvich, *Zh Russ Fiz-Khim Obschestva Chem*, **47**, 805, (1915).
11. E.P. Barrett, L.G. Joyner, P.P. Halenda, *J Am Chem Soc*, **73**, 373, (1951).
12. S. Lowell, J. E. Shields, M. A. Thomas, M. Thommes, *Particle Technology Series*, **16**, 129, (2004).
13. R.G Parr, W. Yang, *Density-Functional Theory of Atoms and Molecules*, Oxford University Press, New York, 1989.
14. L. F. Chen, C. K. Ong, C. P. Neo, V. V. Varadan, Vijay K. Varadan, *Microwave electronics: Measurement and materials characterization*. First ed., Chichester: John Wiley & Sons, Ltd., 2004.
15. J. Sheen, *Elsevier Measurement*, **42**, 57, (2009).
16. A. Verna, D. C. Dube, *IEEE Trans on Industrial Measurement*, **54**, 2120, (2005).
17. M. Lin, Y. Wang, M. N. Afsar, 30th Intl. Conf. on Infrared and Millimeter Waves & 13th Intl. Conf. on Terahertz Electronics, 2005, p. 62.
18. Donnet, J.-B. and E. Custodero, in: *The Science and Technology of Rubber*, J.E. Mark, B. Erman, C.M. Roland, (eds.), Academic Press: Boston. 2013, p. 383.

19. B. Rodgers, W. Waddell, in: The Science and Technology of Rubber, J.E. Mark, B. Erman, C.M. Roland, (eds.), Academic Press: Boston., 2013, p. 417.
20. D. Sirdeshmukh, L. Sirdeshmukh, K.G. Subhadra, C.S. Sunandana, Electrical, Electronic and Magnetic Properties of Solids, Springer, 2014.
21. A. Kaynak, A. Polat, U. Yilmazer, *Mater Res Bull*, **31**, 1195, (1996).
22. R.M. Cornell, U. Schwertmann, *The iron oxides*. VCH Press, Weinheim, Germany, 1996.
23. L. Blaney, *The Lihigh Review* **15-2007**, Paper 5, (2007).
24. R.W. Collins, A. S. Ferlauto, G. M. Ferreira, Chi Chen, J. Koh, R. J. Koval, *Solar Energy Materials and Solar Cells*, **78**, 143, (2003).
25. N.N. Song, H.T. Yang, H. L. Liu, X. Ren, H. F. Ding, X. Q. Zhang, A. H. Cheng, *Sci Rep-UK*, **3**, 3161, (2013).
26. A. A. Al-Ghamdi, O. A. Al-Hartomy, F. R. Al-Solamy, N.T. Dishovsky, N. T. Atanasov, G. L. Atanasova, *Int J Electron Communications*, **72**, 184, (2017).

СРАВНЕНИЕ НА СВОЙСТВАТА НА КОМПОЗИТИ НА БАЗАТА НА ЕСТЕСТВЕН КАУЧУК С ХИБРИДНИ ПЪЛНИТЕЛИ СЪДЪРЖАЩИ РАЗЛИЧНА МОДИФИЦИРАЩА ФАЗА И ТЯХНАТА ПРИЛОЖИМОСТ В ГЪВКАВИ АНТЕНИ

А.Г. Ал-Сехеми^{1, 2}, А. Ал-Гамди³, Н.Т. Дишовски^{4*}, П.А. Малинова⁴, Н.Т. Атанасов^{5,6}, Г.Л. Атанасова^{5,6}

¹Изследователски център по материалознание на нови материали, Университет „Крал Халид“, 61413 Абха, Саудитска Арабия

²Департамент по химия, Колеж за наука, Университет „Крал Халид“, 61413 Абха, Саудитска Арабия

³Департамент по физика, Научен факултет, Университет „Крал Абдул Азис“, Джеда, Саудитска Арабия

⁴Департамент по полимерно инженерство, Химико-технологичен и металургичен университет, 1756 София, България

⁵Департамент по телекомуникации, Факултет по телекомуникации и управление, Висше училище по телекомуникации и пощи, 1700 София, България

⁶Департамент по комуникации и компютърно инженерство, Инженерен факултет, Юго-западен университет “Неофит Рилски“, 2400 Благоевград, България

Постъпила на 19 октомври, 2017 г.; коригирана на 4 април, 2018 г.

(Резюме)

Статията представя сравнение на ефекта, който химичната природа и структурните особености на модифициращата оксидна фаза имат върху диелектричните и магнитни свойства на композити на базата на естествен каучук. Използваните пълнители са получени чрез импрегниране на проводящи въглеродни сажди с модифициращите оксиди, SiO₂ и Fe₃O₄. Изследвана е приложимостта на композитите като подложки за малки гъвкави носими антени. Установено е, че химичната и кристалографска природа на модифициращата оксидна фаза са решаващите фактори, определящи реалните части на диелектричната и магнитна проникваемост и тангенса от ъгъла на загубите на композитите, съдържащи хибридни пълнители. Всички разработени композити отговарят на изискванията към материалите за каучукови подложки на антени. Когато се изискват по-добри характеристики на антената, за предпочитане е подложката на антената да бъде от композит, съдържащ хибриден пълнител с модифицираща фаза от силициев диоксид. Когато фокусът е върху минитюаризацията на антената, за предпочитане е да се използва хибриден пълнител с магнетитна модифицираща фаза.

Preparation of Fe₃O₄/TiO₂ composite and its application in photocatalysis of organic pollutants

Y.M. Li, W.M. Ni*, M.Q. Chen, Z. Zhou, Y. Q. Yang

College of Science and Technology, Zhejiang International Studies University, Hangzhou 310023, China

Received May 10, 2017, Accepted March 2, 2018

Titanium iron ore is used as a raw material to prepare titanium dioxide and ferrous chloride by hydrochloric acid leaching method, and the titanium dioxide is coated on the magnetic Fe₃O₄ to form Fe₃O₄/TiO₂ composite. Through the design of a single variable test (temperature, added dose of Fe₃O₄ colloidal solution), eight Fe₃O₄/TiO₂ composites were prepared under different conditions. The different photocatalytic performances of the prepared Fe₃O₄/TiO₂ composites were investigated, and the effect of phosphotungstic acid addition on the performance of Fe₃O₄/TiO₂ composite was also examined. X-ray diffraction (XRD), X-ray energy dispersive spectrometry (EDX), scanning electron microscopy (SEM), Fourier transform infrared spectroscopy (FT-IR) and titration were used for characterization of the composites. In addition, recycling of the catalyst was explored. The results showed that the optimal conditions for preparation of Fe₃O₄/TiO₂ composite were: temperature below 80 °C, addition of 4 mL Fe₃O₄ colloidal solution. The prepared Fe₃O₄/TiO₂ composite had the highest removal efficiency of RhB. The photocatalysis under ultraviolet (UV) light is better than under sun light, with the highest removal rate of 98.3% and apparent rate constant *k* of 1.1 h⁻¹. TiO₂ was successfully coated on the Fe₃O₄ surface, as confirmed by EDX, SEM and FT-IR, and the Fe₃O₄/TiO₂ composite was of high purity. The addition of phosphotungstic acid did not improve the performance of the Fe₃O₄/TiO₂ composite, further study is needed.

Keywords: Ilmenite, Fe₃O₄/TiO₂ composite, Photocatalysis

INTRODUCTION

Research on nano-magnetic particles is being developed for over 30 years, owing to their advantages such as small size, strong surface plasticity and magnetism at room temperature [1-3]. The use of nano-magnetic particles coated on inorganic materials with photo-catalytic activity, such as titanium dioxide, etc., has become the focus in recent research [4-6]. Photocatalyst TiO₂ is nontoxic, harmless, less corrosive to the equipment, but the recycling process is difficult to conduct, so that preparation of Fe₃O₄/TiO₂ composite photocatalyst easy for recycling is important for the treatment of sewage [7-9]. However, there are several factors that may affect the catalytic ability of the nano-magnetic particles [10-12]. In order to degrade methyl orange, Yoon *et al.* [13] utilized TiO₂ which was surface-modified by phosphotungstic acid (H₃PW₁₂O₄₀, HPW) aqueous solution. It was found that the catalytic activity of the system was significantly improved and the improvement was attributed to the results of HPW and TiO₂ composite photoexcitation. Otherwise, Ozer *et al.* [14] reported that the HPW-modified TiO₂ has a very high degradation activity for dichlorobenzene and they attributed the increase in activity to the synergistic effect between polyoxometalates (POM) and TiO₂.

Ilmenite (FeTiO₃) is widely distributed in large amounts in China, and is mainly used for the production of titanium dioxide and artificial rutile, iron has not been well used. Thus, developing a new technology to make comprehensive utilization of the various elements in minerals has become an inevitable trend of mineral use.

In order to improve the utilization rate of ilmenite, Fe₃O₄ was prepared by the extraction of FeCl₂ and TiO₂ from ilmenite, and TiO₂ was coated on the magnetic Fe₃O₄ particles under the optimal conditions to prepare Fe₃O₄/TiO₂ composite photocatalyst. The effect of Fe₃O₄/TiO₂ composite photocatalyst on the degradation of rhodamine was studied. The photocatalytic activity of Fe₃O₄/TiO₂ composite modified by phosphotungstic acid was investigated and compared with that of the not modified composite; the recovery of the catalyst was also investigated.

EXPERIMENTAL DETAILS

Experimental apparatus and reagents

X-ray powder diffractometer (XRD, Bruker, D8-ADVANCE, Germany), scanning electron microscope (SEM, Quanta FEG 250, USA), X-ray energy dispersive spectrometer (EDX, Quanta FEG 250, USA), ultraviolet spectrophotometer (Shimadzu UV-2550PC, Japan), infrared spectrometer (Thermo Nicolet IS10, USA)

* To whom all correspondence should be sent:
nwm1225@gmail.com

Ilmenite (provided by Zhejiang Normal University, the chemical composition is shown in Table 1), Rhodamine B (analytical grade, Shanghai San Aisi Reagent Co., Ltd.)

Table 1. Chemical composition of the ilmenite (mass ratio %)

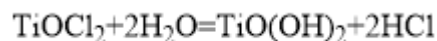
Material composition	TiO ₂	FeTiO ₃	Al ₂ O ₃	SiO ₂
Content	10.76	76.25	3.14	9.85

Preparation of catalyst

Extraction of FeCl₂ from ilmenite. Add 30 g of ilmenite and pour 90 g of concentrated hydrochloric acid (1:3 (m/m) of ilmenite and concentrated hydrochloric acid) into a 250 mL three-necked flask. The mixture was stirred in an oil bath at 80°C for 4 h to obtain a brown substance. The resulting ilmenite acid solution (filtrate) was filtered while hot and allowed to stay at room temperature for a period of time and then cooled in an ice-salt bath at -18°C for 12 h. FeCl₂ • 4H₂O crystals would precipitate. FeCl₂ • 4H₂O crystals and filtrate were separated by filtration. The main reaction equation is as follows:



Extraction of TiO₂ from ilmenite. The filtrate obtained as described above was stirred at 105°C for 5 h, poured into a beaker, cooled at room temperature for a period of time, then filtered to obtain white solid metatitanic acid. 3.0M hydrochloric acid was added to the metatitanic acid, and incubated in a water bath at 60°C for 2 h. The mixture was suction-filtered, washed with 1.0M sodium hydroxide solution, then twice with 1.0M hydrochloric acid, and finally washed three times with distilled water. The washed metatitanic acid was put into a muffle furnace at 500°C for 3 h to remove water, then TiO₂ solid was obtained. The main reaction equations are as follows:



Preparation of Fe₃O₄. Add 30 mL of distilled water to a mixture of 5.96 g of FeCl₂ • 4H₂O and 16.22 g of FeCl₃ • 6H₂O (n(Fe²⁺)/n(Fe³⁺)=1:2), heat in a water bath at 50°C, and stir to dissolve it. Then drop ammonia, quickly at first, and slowly at the end, adjust the pH of the reaction solution to 11, allow aging after the reaction, and finally wash, centrifugate the resulting product several times, and separate to get pure Fe₃O₄ colloidal solution.

Preparation and optimization of Fe₃O₄/TiO₂. A 10% TiO₂ solution was prepared and an appropriate amount of Fe₃O₄ colloidal solution was added to the solution. The reaction mixture was stirred for 2 h at a certain temperature in an oil bath. After completion of the reaction, the solid was filtered and washed with ethanol and distilled water and dried in a vacuum oven at 50°C for 3 h [11].

Four temperatures (40 °C, 60 °C, 80 °C and 100 °C) and different amounts of Fe₃O₄ colloidal solution (4 mL, 6 mL and 8 mL), modified or not by phosphotungstic acid, were selected to explore the optimal preparation conditions of the composite. Fe₃O₄/TiO₂ composites were labeled as catalysts No. 1-8 according to the different preparation conditions (see Table 2).

Table 2. Preparation of Fe₃O₄/TiO₂ composite under different conditions

No.	Reaction temperature (°C)	Amount of Fe ₃ O ₄ colloidal solution (mL)
1#	60	4
2#	40	4
3#	80	4
4#	100	4
5#	80	4
6#	80	6
7#	80	8
8# (+HPW)	80	4

Characterization of Fe₃O₄/TiO₂ composite

X-ray diffraction (XRD) analysis. The experimental conditions for XRD were: copper target, tube voltage 40 kV, tube current 40 mA, scanning step size 0.02 degrees, scanning angle 10-80°.

Fourier transform infrared spectroscopy (FT-IR). In this experiment, the sample preparation method for FT-IR was: mix the sample evenly with KBr of spectral purity in a ratio of 1: 100 before test.

Scanning electron microscopy (SEM) analysis. The conditions for this experiment were as follows: measured voltage of 15 kV, the sample should be tested after drying treatment.

X-ray energy dispersive spectrometry (EDX) analysis. Each element has its own X-ray characteristic wavelength, the magnitude of the characteristic wavelength depends on the energy released during the energy level transition energy ΔE. In this experiment, EDX was combined with SEM for analysis of the surface composition of the sample.

Photocatalytic properties of Fe₃O₄/TiO₂ composite

Photocatalytic properties. Add 50 mL of the 1×10⁻⁵M rhodamine B solution (shown in Figure 1)

Y.M. Li et al.: Preparation of Fe₃O₄/TiO₂ composite and its application in photo-catalysis of organic pollutants

to 50, 100, 150 and 200 mg of the prepared catalyst, respectively, use ultrasound dispersion, allow adsorption equilibrium to be reached in a dark room for 30 min, exposed to ultraviolet light or solar light, respectively. The samples were taken every half hour and the supernatant was analysed after centrifugation. The absorbance was measured at 554 nm by an ultraviolet-visible spectrophotometer, and the changes in RhB concentration were observed. The photodegradation rate (Y) was calculated by the following formula:

$$Y = \frac{A_0 - A}{A_0} \times 100\% = \frac{C_0 - C}{C_0} \times 100\%$$

where C₀ is the initial concentration of RhB, C is the concentration of RhB at a certain point in the course of catalytic reaction, A₀ is the absorbance of RhB with concentration of C₀, and A is the absorbance of RhB of concentration C.

Dynamics of the photocatalytic degradation of rhodamine by Fe₃O₄/TiO₂ composite was studied and the photocatalytic activity of the catalyst was evaluated by the apparent rate constant k. According to the results, the effect of catalyst dosage on the degradation of rhodamine B was compared, the optimal dosage was selected and the effects of ultraviolet light (254 nm) and sunlight on photocatalytic degradation of rhodamine were compared.

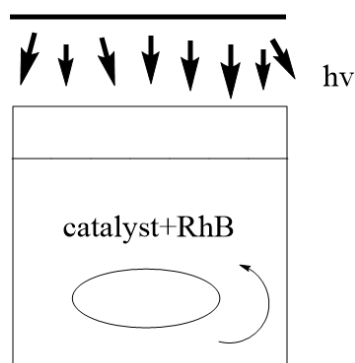


Fig. 1. Schematic diagram of photocatalytic reaction

Catalyst recovery application

The Fe₃O₄/TiO₂ composite in the rhodamine B solution was allowed to settle down by a permanent magnet base, and the upper layer solution was removed. The remaining Fe₃O₄/TiO₂ composite was washed with acetone and deionized water and vacuum-dried for recovery.

RESULTS AND DISCUSSION

Preparation and characterization of Fe₃O₄/TiO₂ composite photocatalyst

In this paper, the preparation of Fe₃O₄/TiO₂ composite was based on the extraction of FeCl₂ and

TiO₂ from ilmenite. XRD, FT-IR, SEM and EXD were used to characterize the structure, surface functional groups, composition and morphology of the photocatalyst.

The 1# and 3# Fe₃O₄/TiO₂ composites displayed better photocatalytic properties. The XRD spectrum is shown in Figure 2.

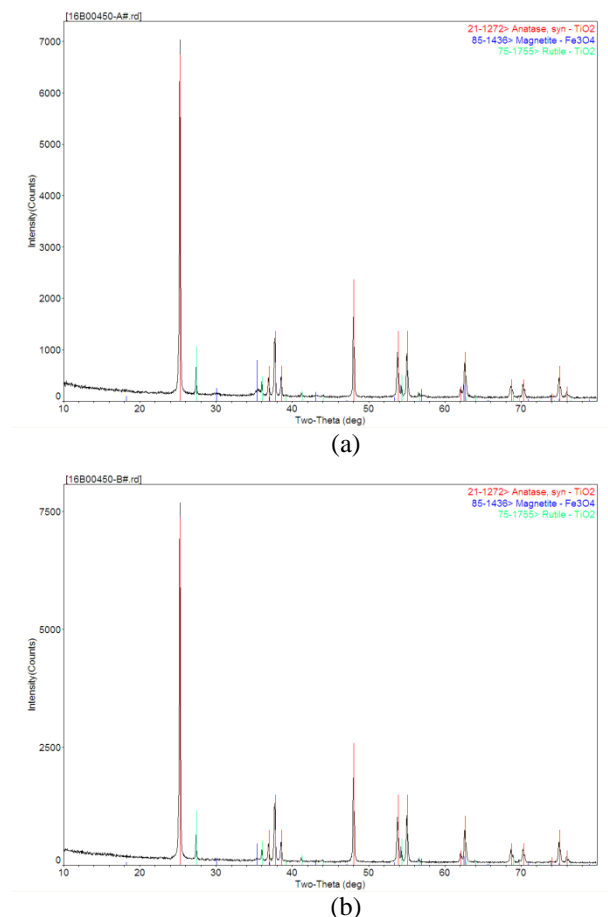


Fig. 2. XRD spectrum of 1# (a) and 3# (b) of Fe₃O₄/TiO₂ composite

Several main diffraction peaks marked by red lines correspond to (101), (004), (200), (105), (211), (116) crystal surfaces of TiO₂. The characteristic peak values agree well with the data of the standard card (JCPDS) NO.21-1272. Strong diffraction of TiO₂ corresponding to (101), (004) and (200) appeared, which confirmed that the of 1# and 3# catalysts include anatase-TiO₂. There are several diffractive peaks at 2θ=30.3°, 35.7°, 53.8°, 57.2° and 62.9° corresponding to the characteristics of FCC (face centered-cubic) Fe₃O₄ crystal (220), (311), (400), (422), (511) and (400). It means that both 1# and 3# catalysts contain Fe₃O₄ particles belonging to cubic crystal. There is no other impurity peak in the picture, which shows that the product is pure. There are several sharp diffractive peaks at 2θ=27.4°, 36.2°, 41.4° and 54.3°. They correspond to (101), (004), (200), (105), (211), (116) crystal surfaces of TiO₂. The characteristic

peak values agree well with the data of the standard card (JCPDS) NO.75-1755., which confirmed that the 1# and 3# catalysts both include rutile-TiO₂. The results showed that the 1# and 3# catalysts are composed of face-centered cubic Fe₃O₄, rutile-TiO₂ and anatase-TiO₂.

The infrared spectrum of Fe₃O₄/TiO₂ composite is shown in Figure 3. The position of the characteristic absorption peak is basically consistent with the report [15,16]. The absorption peak at 3416 cm⁻¹ corresponds to the stretching vibration peak of a hydroxyl group on the surface of the Fe₃O₄ particles. The peak at 1637 cm⁻¹ is the bending vibration between the H-O-H bonds. This was attributed to the absorption of water molecules on the surface of Fe₃O₄/TiO₂ magnetic composite, which was related to the small amount of adsorbed water in the composite. The absorption peak near 638 cm⁻¹ is caused by the stretching vibration of crystal TiO₂ and the Ti-O bond on the surface.

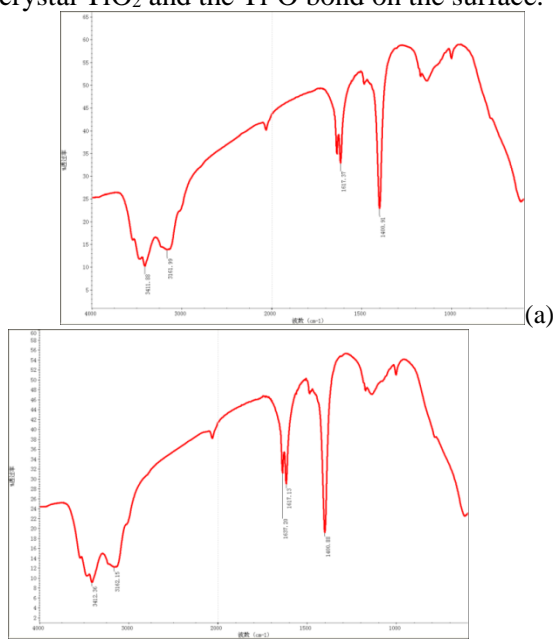


Fig. 3. FT-IR spectra of 1# (a) and 3# (b) of Fe₃O₄/TiO₂ composite

Figure 4 shows the SEM spectra of Fe₃O₄/TiO₂ composite at different magnifications. The SEM spectrum of 1# of Fe₃O₄/TiO₂ composite is presented in Figs. 4(a)-(d). The conditions for preparation of 1# were: 60°C with addition of 4 mL of Fe₃O₄ colloidal solution and reaction time 2 h. In Figs. 4(e)-(h) the SEM spectrum of 3# of Fe₃O₄/TiO₂ composite is shown. The conditions for preparation of 3# were: 80°C with addition of 4 mL of Fe₃O₄ colloidal solution and reaction time 2 h. Figure 4 shows that the prepared 1# and 3# of Fe₃O₄/TiO₂ composite have cluster structure. The magnetic properties of Fe₃O₄ make the Fe₃O₄/TiO₂ composite agglomerate together. The particle

diameters of the composite are about 50-120 nm. There are small particles on the surface, which should be of TiO₂ coated on the surface of Fe₃O₄. The particle diameters of Fe₃O₄ are about 25-40 nm, and of the TiO₂ nanoparticles - about 5 nm. Judging from the particle size, there are 1-3 layers of nano-TiO₂ coated on the surface of the magnetic Fe₃O₄[1]. The surface composition of the sample was analyzed by both EDX (Figure 5) and SEM.

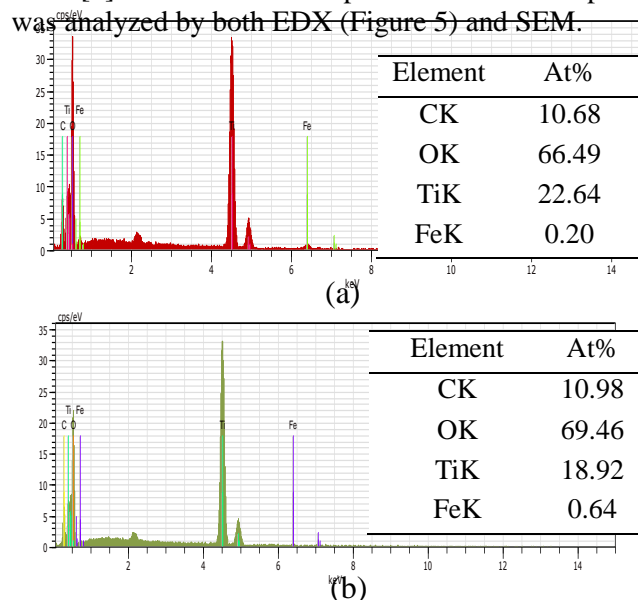


Fig. 5. EDX spectrum of 1# (a) and 3# (b) of Fe₃O₄/TiO₂ composite

Figure 5 shows the composition of both 1#(a) and 3#(b) catalysts. The major components of the surface of both catalysts are O, Ti and Fe. Among them, C is graphite during sample analysis and the content of Ti atoms is much higher than of Fe, which indicated that TiO₂ in 1# and 3# is situated on the Fe₃O₄ surface.

Effect of Fe₃O₄/TiO₂ addition on removal efficiency of RhB

Samples of 50, 100, 150 and 200 mg of the prepared catalyst were added to 50 mL of RhB solution of initial concentration of 1×10⁻⁵M and were subjected to photocatalytic experiments under sunlight. The results are shown in Figure 6.

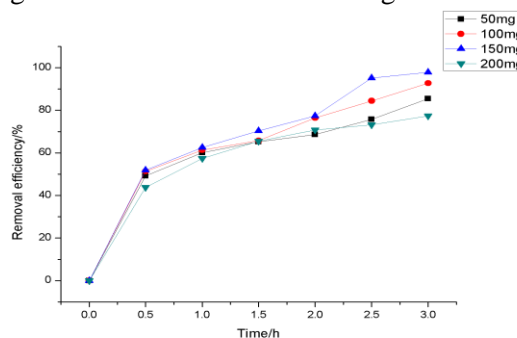


Fig. 6. Effect of Fe₃O₄/TiO₂ composite addition on removal efficiency of RhB.

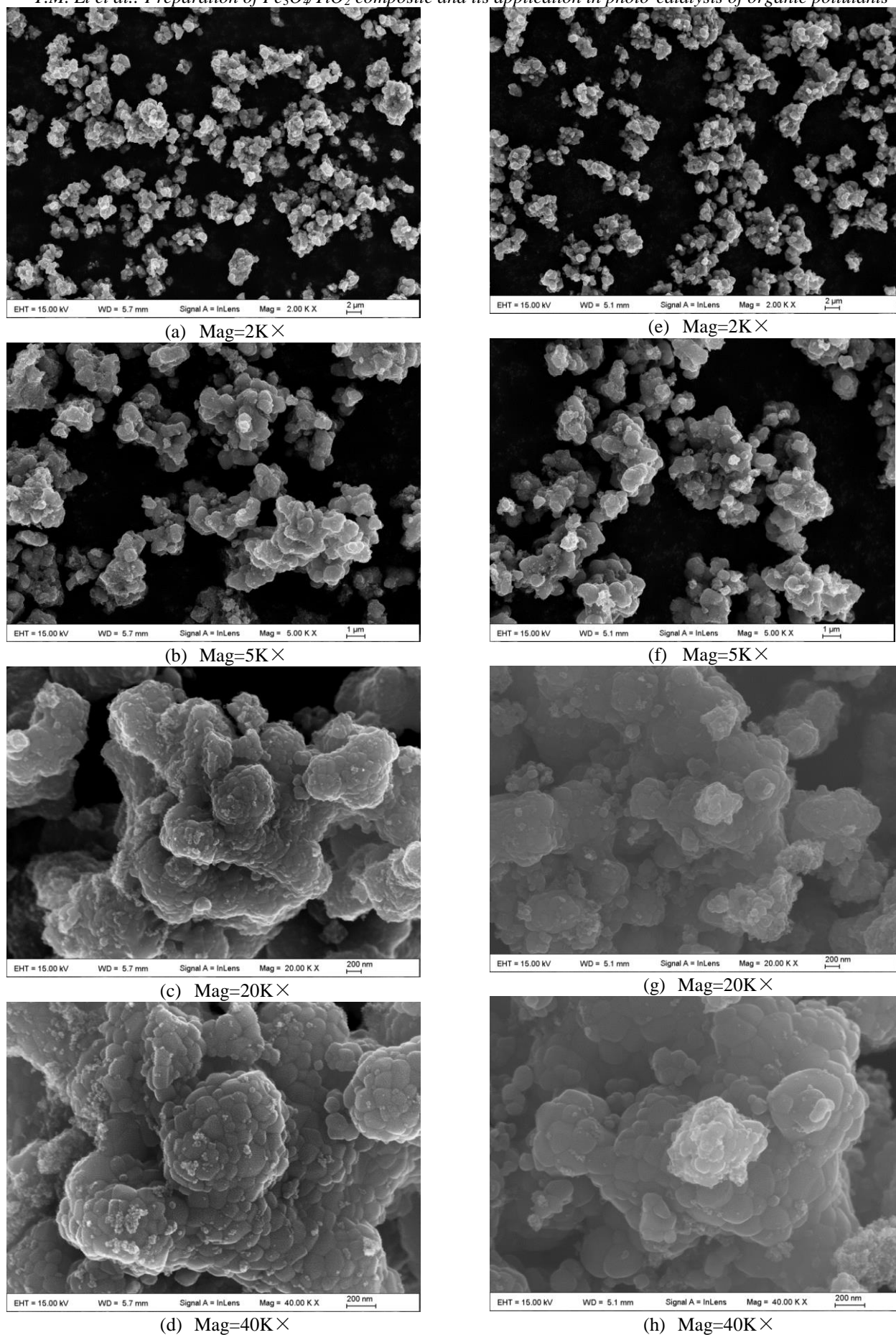


Fig. 4. SEM spectrum of 1# (a-d) and 3# (e-h) of Fe_3O_4/TiO_2 composite

The best addition of catalyst is 150 mg. After 3 h of photocatalytic reaction, the removal efficiency of RhB was 98.1% by adding 150 mg of catalyst. The removal efficiency of RhB was 75.9% and 85.6% with 200 mg and 50 mg of catalyst, respectively.

Effect of preparation temperature for Fe_3O_4/TiO_2 on removal efficiency of RhB

The effects of different preparation temperatures (40°C, 60°C, 80°C and 100°C) of the Fe_3O_4/TiO_2 catalysts on the removal efficiency of RhB were investigated under UV and sunlight. The results are shown in Figure 7. The results showed that the highest degradation efficiency of Fe_3O_4/TiO_2 catalyst prepared at 80°C is 92.2% and 89.0%, under UV light and sunlight, respectively. The degradation efficiency of Fe_3O_4/TiO_2 catalyst

prepared at 100°C was 75.9% and 72.8%, respectively.

Effect of Fe_3O_4 addition for Fe_3O_4/TiO_2 composite on removal efficiency of RhB

The effect of Fe_3O_4 colloidal solution (4 mL, 6 mL and 8 mL) for Fe_3O_4/TiO_2 catalyst on the removal efficiency of RhB was also investigated under UV and sunlight. The results are shown in Figure 8. The highest degradation efficiency of RhB by the Fe_3O_4/TiO_2 catalyst was achieved by adding 4 mL of Fe_3O_4 colloidal solution, with 98.1% and 98.3%, respectively, under UV light and sunlight. The degradation efficiency of the Fe_3O_4/TiO_2 catalyst prepared by adding 8 mL of Fe_3O_4 colloidal solution was 80.8% and 76.9%, respectively. Therefore, addition of 4 mL of Fe_3O_4 colloidal solution was considered as optimal.

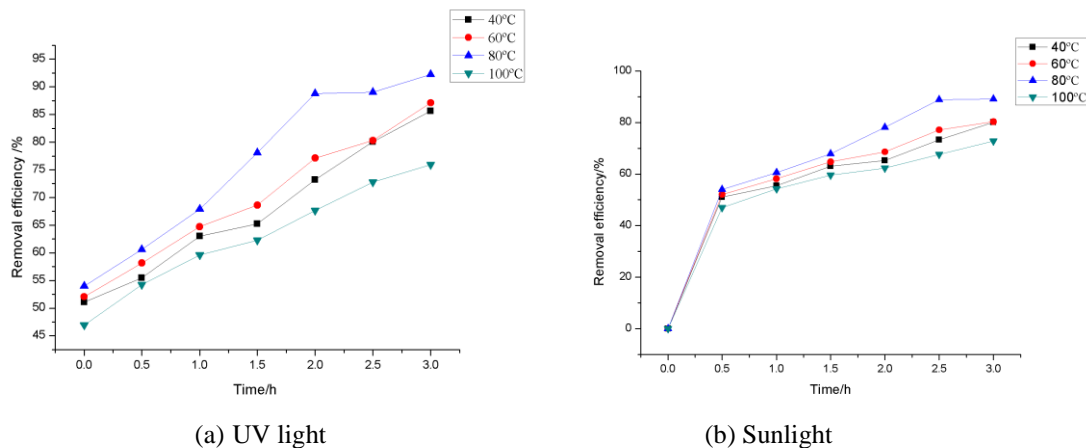


Fig. 7. Effects of preparation temperature of Fe_3O_4/TiO_2 composite on removal efficiency of RhB under (a) UV light and (b) sunlight

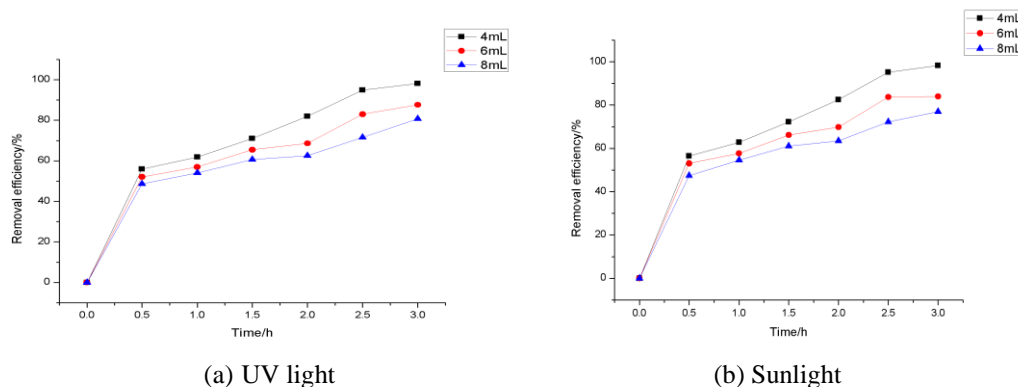


Fig. 8. Effects of Fe_3O_4 addition for Fe_3O_4/TiO_2 composite on removal efficiency of RhB under (a) UV light and (b) sunlight

Effect of light source for Fe_3O_4/TiO_2 composite on removal efficiency of RhB

The effects of ultraviolet light and sunlight for Fe_3O_4/TiO_2 catalyst on the removal efficiency of RhB were compared. Fe_3O_4/TiO_2 catalyst was

prepared by the optimal conditions. The average of the degradation efficiency is shown in Figure 9. The photocatalysis under ultraviolet (UV) is better than under sun light, 95.1% and 93.7%, respectively, with the highest removal rate of 98.1% and 98.3%, respectively.

The effect of HPW-modified catalyst on the removal efficiency of RhB was investigated by using HPW impregnation method to improve Fe₃O₄/TiO₂ composite photocatalyst. The results are shown in Figure 10. The degradation efficiency of Fe₃O₄/TiO₂ catalyst prepared by adding HPW did not improve the performance of the Fe₃O₄/TiO₂ composite, which was 26.5% and 23.8%, respectively, much lower than those under the optimal conditions. Further study is needed to reveal the mechanism.

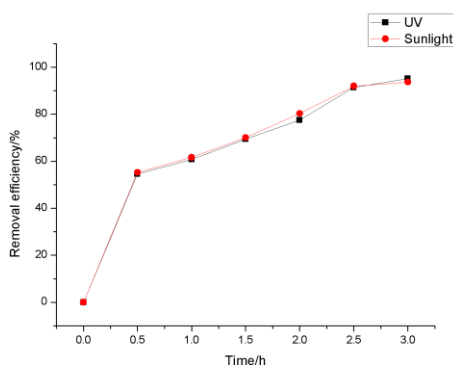


Fig. 9. Effects of light source on removal efficiency of RhB by Fe₃O₄/TiO₂ composite under UV light and sunlight

Photocatalytic degradation of RhB by Fe₃O₄/TiO₂

Ozer *et al.* [16] reported that for the POM composite photocatalyst, the photocatalytic oxidation reaction follows the Langmuir-Hinshelwood (L-H) kinetic equation:

$$r = -\frac{dC}{dt} = \frac{k_r K_a C_0}{1 + K_a C_t}$$

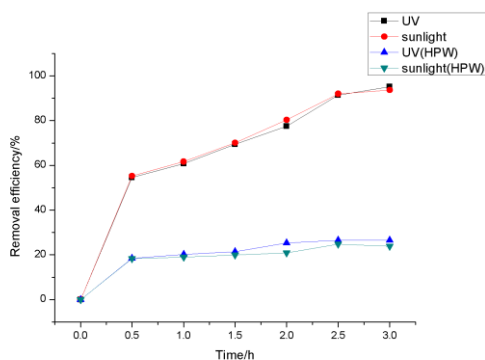


Fig. 10. Effects of phosphotungstic acid addition to Fe₃O₄/TiO₂ composite on removal efficiency of RhB under UV light and sunlight

In the equation, r is the initial apparent reaction rate ($\text{mg}\cdot\text{L}^{-1}\cdot\text{h}^{-1}$), C_t is the concentration of reactants at time t ($\text{mg}\cdot\text{L}^{-1}$), C_0 is the initial concentration of the reactants ($\text{mg}\cdot\text{L}^{-1}$), K_a is the L-H equilibrium adsorption constant ($\text{L}\cdot\text{mg}^{-1}$), K_r is the reaction rate

constant ($\text{mg}\cdot\text{L}^{-1}\cdot\text{h}^{-1}$). The degradation reaction was of first order and when $KC_0 \ll 1$, the kinetic equation can be simplified as follows:

$$\ln \frac{C_0}{C} = k_r K_a t = kt$$

In the equation, K (h^{-1}) is the apparent first-order reaction rate constant.

In this experiment, 150 mg addition of Fe₃O₄/TiO₂ catalyst was used to study the reaction kinetics as a function of reactant concentration. The activity difference of the catalyst prepared under different conditions was compared by calculating the apparent rate constant k . The results are shown in Table 3. Six different concentrations of RhB standard solution were prepared. The standard curve was as shown in Figure 11, the correlation coefficient was 0.9982.

The data in Table 3 show that the apparent rate constants of the 3 # catalyst on the photodegradation process of RhB are the largest ones, 1.0646 and 1.0851 h^{-1} , respectively, whether under ultraviolet light or sunlight. 3 # catalyst was prepared at 80 °C, by adding 4mL of Fe₃O₄ colloidal solution, consistent with the best conditions.

Table 3. Comparison of apparent rate constants (k) for Fe₃O₄/TiO₂ composite under different light source

	1#	2#	3#	4#
UV light	0.5369	0.5019	1.0646	0.3900
Sunlight	0.3036	0.4344	1.0851	0.3026
	5#	6#	7#	8#
UV light	0.7256	0.5908	0.4373	0.0710
Sunlight	0.6619	0.5448	0.4081	0.3053

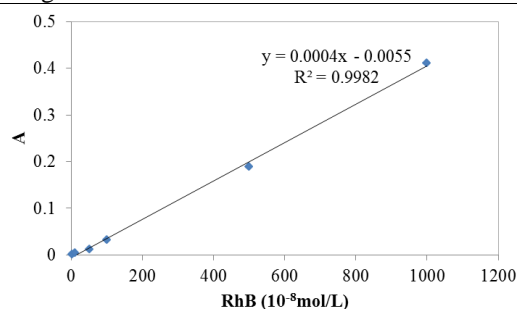


Fig. 11. Standard curve for RhB

Table 4. Effects of Fe₃O₄/TiO₂ composite recycling on removal efficiency of RhB

	First recycling	Second recycling	Third recycling
Removal efficiency	90%	81%	75%

Recovery of Fe₃O₄/TiO₂ composite catalyst

The effect of Fe₃O₄/TiO₂ composite recycling on removal efficiency was also investigated. It was found that the removal efficiency decreased from

98% to 75% after 3 cycles of recovery (Table 4). The best recycling strategy should include 2 cycles.

CONCLUSIONS

The average efficiency of degradation of RhB by Fe₃O₄/TiO₂ composite prepared from ilmenite under UV light is better than under sunlight, and the apparent rate constant *k* of 1.1 h⁻¹. The amount of catalyst, the preparation temperature of the catalyst and the amount of Fe₃O₄ colloidal solution for the preparation of the catalyst, all have effects on the photodegradability. The optimal conditions for preparation of Fe₃O₄/TiO₂ composite are: 80°C, with addition of 4 mL of Fe₃O₄ colloidal solution. The addition of phosphotungstic acid did not improve the performance of the Fe₃O₄/TiO₂ composite.

TiO₂ was successfully coated on the Fe₃O₄ surface as confirmed by EDX, SEM and FT-IR, and the Fe₃O₄/TiO₂ composite was of high purity. It is easy to use the magnetic property to recycle, the best recycling strategy should be 2 cycles, with degradation efficiency up to 81%.

Acknowledgements: This research was funded by National Natural Science Foundation of China (41503082). The authors would also like to extend thanks to anonymous reviewers for the improvement of this paper.

REFERENCES

1. W. S. Tung, W. A. Daoud, *Appl. Mater. Interfaces*, **1**, 2453 (2009).

2. J.Y. Jing, Y. Zhang, J. Y. Liang, *J. Nanoparticle Res.*, **14**, 827 (2012).
3. J. S. Xie, Q. S. Wu, D. F. Zhao, *Carbon*, **50**, 800 (2012).
4. T. H. Xie, X. Y. Sun, J. Lin, *J. Phys. Chem. C*, **112**, 9753 (2008).
5. D. Beydoun, R. Amal, *Mater. Sci. Eng.*, **B94**, 71 (2002).
6. A. Nishimura G. Mitsui, K. Nakamura, M. Hirota, E. Hu, *Inte. J. Photoenergy*, 184169 (2012).
7. M. Shahid, A. MacDonagh, J. H. Kim, H. K. Shon, *Desalination & Water Treatment*, **54**, 979 (2015).
8. X. H. Feng, H. J. Guo, K. Patel, H. Zhang, X. Lou, *Chem. Eng. J.*, **244**, 327 (2014).
9. J. Y. Jing, J. Li, J. Feng, W. Li, W. W. Yu, *Chem. Eng. J.*, **219**, 355 (2013).
10. L. Yan, Y. F. Wang, J. Li, S. B. Yang, *J. Mater. Sci.-Mater. Electronics*, **27**, 10616 (2016).
11. L. Zhang, Z. Wu, L. W. Chen, L. J. Zhang, X. L. Li, H. F. Xu, H. Y. Wang, G. Zhu, *Solid State Sci.*, **52**, 42 (2016).
12. Y. H. Chang, C. C. Ou, H. W. Yeh, C. S. Yang, *J. Mol. Catalysis A- Chemical*, **412**, 67 (2016).
13. M. Yoon, J. A. Chang, Y. Kim, J. R. Choi, K. Kim, S. J. Lee, *J. Phy. Chem. B*, **105**, 2539 (2001).
14. R. R. Ozer, J. L. Ferry, Investigation of the photocatalytic activity of TiO₂-polyoxometalate systems, *Environ. Sci. Technol.*, **5**, 3242 (2001).
15. G. A. He, H. Liu, R. Chen, *J. Nanomaterials*, 856387 (2013).
16. S. Sivakumar, P. K. Pillai, P. Mukundan, K. G. K. Warrier, *Mater. Lett.*, **57**, 330 (2002).
17. R. R. Ozer, J. L. Ferry, *J. Phys. Chem. B*, **104**, 9444 (2000).

Получаване на Fe₃O₄/TiO₂ композит и приложението му за фотокатализ на органични замърсители

И.М. Ли, У.М. Ни*, М.К. Чен, З. Жоу, И.К. Янг

Колеж по наука и технология, Университет за международни изследвания на Жейнг, Хангжоу, 310023, Китай

Постъпила на 10 май, 2017 г.; приета на 2 март, 2018 г.

(Резюме)

Титаново-желязна руда е използвана като суровина за получаване на титанов диоксид и железен (II) оксид чрез излужване със солна киселина. Титановият диоксид е нанесен върху магнитния Fe₃O₄ с образуване на Fe₃O₄/TiO₂ композит. Осем Fe₃O₄/TiO₂ композита са получени при различна температура и количество на колоидния разтвор на Fe₃O₄. Изследвани са фотокаталитичните свойства на композитите, както и влиянието на добавка от фосфофолфрамова киселина. Композитите са охарактеризирани чрез рентгенова дифракция (XRD), енергийно дисперсивна рентгенова спектрометрия (EDX), сканираща електронна микроскопия (SEM), Fourier трансформираща инфрачервена спектроскопия (FT-IR) и титруване. Изследвани са възможностите за рециклиране на катализатора. Оптималните условия за получаване на Fe₃O₄/TiO₂ композит са: температура под 80°C и добавка от 4 mL Fe₃O₄ колоиден разтвор. Така полученият Fe₃O₄/TiO₂ композит има най-висока ефективност за отстраняване на родамин В. Фотокатализът е по-ефективен при облъчване с UV светлина, отколкото със слънчева светлина. Максималната степен на извличане е 98.3%, а привидната скоростна константа *k* е 1.1 h⁻¹. TiO₂ е нанесен успешно на повърхността на Fe₃O₄, което е потвърдено чрез EDX, SEM и FT-IR, като Fe₃O₄/TiO₂ композитът е с висока чистота. Добавянето на фосфофолфрамова киселина не води до подобряване на неговите свойства.

Analytical characteristics of wild and cultivated strawberries (spring & autumn harvests) of Southern Bulgaria & Northern Greece

S. I. Papanov^{1*}, Ek. G. Petkova², K. V. Ivanov¹, St. D. Ivanova¹, V. V. Grudeva³

¹Medical University Plovdiv, Faculty of Pharmacy, 15A V. Aprilov Bul., 4000 Plovdiv, Bulgaria

²Medical University Plovdiv, Medical College, 120 Br. Bakston Str., 4004 Plovdiv, Bulgaria

³Hospital Sveta Ekaterina, 52A Pencho Slaveykov Bul., 1431 Sofia, Bulgaria

Submitted February, 16, 2018; Revised April 18, 2018

Strawberries with their aroma and sweet taste are the most popular fruit in the world. There are more than 600 sorts of strawberries that differ in taste, size and texture. An analysis of pH, total phenols, antioxidant activity (radical trapping activity) total anthocyanin of wild growing and cultivated varieties of strawberries with origin North Greece and South Bulgaria. A methodology has been developed for determining of common phenols, antioxidant activity, common anthocyanins. The average value of pH index ranges from 3.26 for strawberry samples from northern Greece to 3.34 and 3.55 for strawberry samples from southern Bulgaria. Total phenols: 4.58±0.02 mg GAE/g fresh weight for Wild Strawberries; 1.34±0.02 mg GAE/g fresh weight for strawberry sample from Northern Greece; 1.36±0.03 mg GAE/g fresh weight and 1.41±0.01 mg GAE/g fresh weight strawberry sample from southern Bulgaria. Total anthocyanins: 0.34±0.01 mg/g fresh weight for strawberry sample from Northern Greece; 0.21±0.01 mg/g fresh weight and 0.22±0.01 mg/g fresh weight for strawberry sample from southern Bulgaria. Antioxidant activity: Wild strawberries - 41,38±0,20 m.mol TE/g fresh weight; 7,35±0,30 m.mol TE/g fresh weight for strawberry sample from Northern Greece; 8,99±0,20 m. mol TE/g fresh weight and 10,20±0,20 m.mol TE/g fresh weight for strawberries from southern Bulgaria. There is a direct correlation between antioxidant activity and total phenols. There is an inverse relationship between antioxidant activity / phenols and anthocyanins.

Keywords: strawberries; antioxidant; phenols; anthocyanins.

INTRODUCTION

The strawberry is a genus of plants of the *Rosaceae* family.

Strawberries with their aroma and sweet flavor are the most popular fruit in the world. There are more than 600 varieties of strawberries that differ in taste, size and texture [1-5]. Strawberries are rich in both mineral substances and vitamin C, carotene, vitamin E and vitamins of group B. Vitamin C is predominant with 58,80 mg. per 100 grams of strawberries - the recommended daily dose [1, 4-8]. About 90% of mature strawberry is water but contains sugars, about 80% of which are glucose and fructose.

The color of strawberries is due to anthocyanins, mainly to peargonidin-3-glucoside. Anthocyanins are water-soluble pigments found in plant cells. In addition, anthocyanins can be used as pH indicators- they are pink in acidic, purple in neutral and yellow in alkaline solutions [9].

According to a study published in Journal of Nutritional Biochemistry, strawberries help lower total cholesterol (by 8,78%), bad cholesterol (13,72%), and triglycerides (by 20,8%).

Studies suggest that consumption of

strawberries, may have beneficial effects against oxidative stress mediated diseases such as cancer. Berries contain multiple phenolic compounds, which are thought to contribute to their biological properties [10].

Flavonoids in strawberries have excellent antioxidant and anti-cancer properties [1, 11].

Important phenolic acids in strawberries are the ellagitannins and ellagic acid glucosides, which break down to pure ellagic acid, also present in the fruit [12].

Ellagic acid is valuable to human health because it is antimutagenic and has anticarcinogenic activity against chemical-induced cancers [13].

Ellagitannins in strawberries are primarily located in the achenes [14].

Scope: Determination and analysis of pH, total phenols, antioxidant activity (radical trapping activity) total anthocyanin of wild growing and cultivated varieties of strawberries.

MATERIAL AND METHODS

Object of the study was the antioxidant characteristics of wild growing and cultivated varieties of strawberries grown at different altitudes:

Wild strawberries (Velingrad, Bulgaria) - 755m. altitude.

* To whom all correspondence should be sent:
stoyan.papanov@abv.bg

Caparoso variety, (Northern Greece) - 115m altitude.

Zeenger variety (Belomorski-Plovdiv, Bulgaria) - 164m altitude.

Asia variety (Byaga village, Bulgaria) - 374m altitude.

Temptation variety (Gotse Delchev, Bulgaria) - 540m altitude.

Albion variety (Sofia, Bulgaria) - 598m altitude.

The study was conducted from May to September 2017 in laboratories of the University of Food Technologies Plovdiv and Laboratory of Pharmaceutical Analysis of the Medical University of Plovdiv.

The following research methods were used for the study:

- Systematic approach and critical analysis of the available scientific periodicals;
- Spectrophotometric method for determination of adsorption and standard Gallic acid;
- DPPH method for determining the antioxidant activity (radical trapping activity).

The study was carried out using the following apparatus:

1. Analytical scale KERN ABJ 220-4M;
2. Spectrophotometer Camspec M107, UK; pH-determiner;
3. Standardized pH determiner with pH 4,0 and 7,0 standard buffer solutions (WTW inoLab pH 7110, Germany);
4. Standardized pH meter with pH 4,0 and 7,0 standard buffer solutions, pH meter Denver Instrument Ultra Basic.

For the purposes of the study, the following reagents and solutions were used.

- To determine common phenols:

7,5% Na₂CO₃ (weighing 7,5 g Na₂CO₃ and dissolving in 100 ml dH₂O) and Folin-Ciocalteus phenol reagent (Sigma) - a 5 times diluted reagent is used (1 ml + 4 ml dH₂O)

- To determine antioxidant activity by DPPH method:

0,1 M DPPH reagent: 10 mg.DPPH (2,2-Diphenyl-1-picrylhydrazil) dilutes in 250 ml methanol

- To determine common anthocyanins:

Buffer with pH 1.0 (potassium chloride, 0,025 M)

Buffer with pH 4.5 (sodium acetate, 0,4 M) HCl (to adjust pH)

All reagents and solutions are of analytical purity.

Samples of fresh strawberries were cut into pieces and then homogenized with a blender to a homogeneous mass. Weighed 8 grams (analytical scale KERN ABJ 220-4M) from the sample and quantitatively transfer it into a 50 ml volumetric flask with ethanol and volume is brought to the mark. The sample was homogenized and stored at room temperature for 15 minutes.

Analysis path to determine common phenols

We placed 0,2 ml of sample solution in a cuvette then we placed 1,0 ml of Folin-Ciocalteus phenol reagent (diluted 5 times) and 0,8 ml 7,5% solution of Na₂CO₃. For control sample, the same reagents were prepared, but instead of 0,2 ml sample there were placed 0,2 ml solvent. The samples thus prepared were allowed to stand for 20 minutes at room temperature [15-18]. Adsorption of the sample was measured spectrophotometrically against a control with wavelength $\lambda=765$ nm (Camspec M107, UK). The amount of common phenols was reported according to a pre-set standard gallon acid right: $Y=12,557x - 0,0871$.

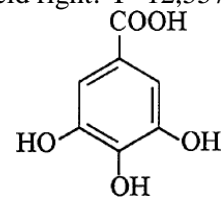


Fig. 1. Gallic acid

Calculations:

$$\text{mg GAE/g f.s} = (V \times C) / M \quad (1)$$

where:

GAE – gallic acid equivalent

f.s – fresh substance, g

V – volume of the extract, ml

C - concentration of phenols in the extract read by standard straight, mg/ml

M - weight of extracted plant material, g

Path of the method for determining the antioxidant activity (radical trapping activity) using DPPH method [19-22].

We placed in a cuvette 2,85 ml of 0,1 M DPPH after that we placed 0,15 ml of sample. For the control, the same reagents were prepared but a solvent was placed instead of sample. Thus, prepared samples are kept 15 min at 37°C. Adsorption of the sample was measured spectrophotometrically against a control (solvent methanol) at a wavelength of $\lambda=517$ nm (Camspec M107, UK). Antioxidant activity was reported according to a pre - established standard straight Trolox ® (Sigma).

Calculation:

$$I, \% = \frac{A \text{ control sample} - A \text{ sample}}{A \text{ sample}} * 100 \quad (2)$$

$$C, \text{ m.mol TE/ml} = 102.06. I\% + 0,7954 \quad (3)$$

$$\text{m.mol TE/g. fresh weight} = (V \times C) / M \quad (4)$$

where:

- C- concentration, **mM TE-TROLOX** equivalents
- I – percentage inhibition
- A – Absorption
- M – Weight of the sample, g
- V – Volume of the sample, (100 ml)

Path of the analysis to determine common anthocyanins

Buffer with pH 1.0 (potassium chloride, 0,025 M). – was weighed 1,86 g KCl in a cup and add distilled water around 980 ml. We measured pH and corrected pH to 1.0 ($\pm 0,05$) with HCl (approximately 6,3 ml). We transferred to a 1 liter volumetric flask and dilute to the mark with distilled water;

Buffer with pH 4.5 (sodium acetate, 0.4 M). – was weighed 54.43 g $\text{CH}_3\text{CO}_2\text{Na} \times 3\text{H}_2\text{O}$ in a cup and add distilled water up to 960 ml. We measured pH and corrected pH to 4.5 ($\pm 0,05$) with HCl (approximately 20 ml). We transferred to a 1 liter volumetric flask.

Determine the absorbance of the sample diluted with pH 1.0 (6 times) with buffer, (A) and buffer (B) pH 4,5, as well with 520 nm, as with 700 nm.

Diluted test samples were scored against a blank sample filled with distilled water [22-26].

Calculation of the concentration of anthocyanin pigments is expressed as cyanidin-3-glucosidic equivalents as follows:

$$\text{Anthocyanin pigments (mg/L)} = A \times \text{MW} \times \text{DF} \times 10^3/\epsilon \quad (5)$$

where:

- A = (A520 nm - A700 nm) pH 1.0 - (A520nm - A700nm) pH 4.5;
- MW (molecular weight) = 449,2 g/mol for cyanidin-3-glucosidic;
- DF = dilution factor
- $\epsilon = 26900$ molar extinction coefficient in $\text{L} \times \text{mol}^{-1}$ and cm^{-1}
- 10^3 = conversion factor from g in mg [27-31].

RESULTS AND DISCUSSION

The results presented are the arithmetic mean of at least three parallel studies.

Important phenolic acids in strawberries are the ellagitannins and ellagic acid glucosides, which break down to pure ellagic acid, also present in the fruit [11].

Information on the content of the total phenols in the samples tested is given in Table 1. The values of the total phenols ranged from 4,58 to 1,34.

Table1: Common phenols of wild growing and cultivated varieties of strawberries with origin Northern Greece and South Bulgaria.

Variety	Common phenols(mg GAE/g fresh weight)
Wild Strawberries, (Velingrad, Bulgaria)	4,58 \pm 0,02
Caparoso variety, (Northern Greece)	1,34 \pm 0,02
Zeenger variety, (Belomorski, Plovdiv, Bulgaria)	1,36 \pm 0,03
Asia variety, (Byaga village, Bulgaria)	1,41 \pm 0,01
Albion variety, (Sofia, Bulgaria)	1,71 \pm 0,01
Temptation variety (Gotse Delchev, Bulgaria)	2,16 \pm 0,02

The highest content of common phenols is observed in wild strawberries 4,58 mg GAE/g fresh weight, followed by a variety of Temptation – 2,16 mg GAE/g fresh weight, Albion variety – 1,71 mg GAE/g fresh weight, Asia variety – 1,41 mg GAE/g fresh weight, Zhenger variety – 1,36 mg GAE/g fresh weight and Caparoso variety – 1,34 mg GAE/g fresh weight.

The anthocyanins are a group of flavonoids with exceptionally good scavenging activities. Pelargonidin-based anthocyanins such as pelargonidin 3-glucoside, pelargonidin 3-rutinoside, and pelargonidin 3-glucoside–succinate are the

predominant anthocyanins in cultivated strawberry fruit [29].

The common anthocyanins of the samples we studied are within the range from 0,35 to 0,19 mg/g of fresh weight are presented in Table 2.

The conducted study of anthocyanins gives us reason to arrange the varieties we examine as follows: Temptation variety, 0,35 mg/g fresh weight, Caparoso variety 0,34 mg/g fresh weight, Albion variety 0,25 mg/g fresh weight, Asia variety 0,22 mg/g fresh weight, Zeenger variety 0,21 mg/g fresh weight.

Table 2: Common anthocyanins of wild growing and cultivated varieties of strawberries with origin Northern Greece and South Bulgaria.

Variety	Common anthocyanins (mg/g fresh weight)
Wild Strawberries, (Velingrad, Bulgaria)	0,19 ± 0,01
Caparoso variety, (Northern Greece)	0,34 ± 0,01
Zeenger variety, (Belomorski, Plovdiv, Bulgaria)	0,21 ± 0,01
Asia variety, (Byaga village, Bulgaria)	0,22 ± 0,01
Albion variety, (Sofia, Bulgaria)	0,25 ± 0,01
Temptation variety, (Gotse Delchev, Bulgaria)	0,35 ± 0,01

The DPPH method for determining the antioxidant activity of strawberries is also used by and the results obtained are highly accurate [30].

The results for the antioxidant activity of our samples, determined by the DPPH method is shown in Table 3.

Table 3. Antioxidant activity of wild growing and cultivated varieties of strawberries with origin Northern Greece and South Bulgaria.

Variety	Antioxidant activity (m mol TE/g fresh weight)
Wild strawberries, (Velingrad, Bulgaria)	41,38 ± 0,20
Caparoso variety, (Northern Greece)	7,35 ± 0,30
Zeenger variety, (Belomorski, Plovdiv, Bulgaria)	8,99 ± 0,20
Asia variety, (Byaga village, Bulgaria)	10,20 ± 0,20
Albion variety, (Sofia, Bulgaria)	19,32 ± 0,20
Temptation variety, (Gotse Delchev, Bulgaria)	22,48 ± 0,20

Antioxidant activity ranges from 41,38 to 7,35 m mols TE/g fresh weight.

It is greatest with Wild Strawberries next in place we could put Temptation variety with 22,48 m mols TE/g fresh weight and Albion variety with 19,32 m mols TE/g fresh weight.

Grouped based on the antioxidant activity indicator, we can place Azia variety, sort Zeenger

and sort Caparoso, respectively, with 10,20; 8,99; 7,35 m mols TE/g fresh weight.

www.truehealth.ru for the ph indicator, of different strawberry varieties gives values in the range of 3 to 3.9. The results obtained by us for ph of the varieties under consideration are presented in Table 4.

Table 4. pH of wild growing and cultivated varieties of strawberries with origin North Greece and South Bulgaria.

Variety	Ph
Wild strawberries, (Velingrad, Bulgaria)	3,55
Caparoso variety, (Northern Greece)	3,32
Zeenger variety, (Belomorski, Plovdiv, Bulgaria)	3,34
Asia variety, (Byaga village, Bulgaria)	3,55
Albion variety, (Sofia, Bulgaria)	3,74
Temptation variety, (Gotse Delchev, Bulgaria)	3,85

As can be seen from Table 4, the values we obtained for ph are in the range of 3.32 to 3.85, which confirms the objectivity of the methodology used by us.

CONCLUSIONS

1. An absolute favorite in the varieties studied by us on the indicator common phenols are Wild Strawberries followed by Temptation variety. Approximately the same indicator is for Zeenger variety and Caparoso variety.

2. The highest anthocyanin value is seen in Temptation variety and Caparoso variety.

In wild strawberries, the lowest anthocyanin value is observed. This can be explained by approximately the same soil composition.

3. The antioxidant activity of Wild Strawberries is approximately twice as high as that of the Temptation variety and Albion variety strains

and three times bigger than that of Asia variety and Zeenger variety and six times greater than that of Caparoso variety.

4. There is a direct correlation between antioxidant activity and total phenols.

5. There is an inverse relationship between antioxidant activity/phenols and anthocyanin.

REFERENCES

1. <http://www.bb-team.org/articles/>.
2. F. Chinnici, A. Bendini, A. Gaiani, C. Riponi, *J. Agric. Food Chem.*, **52**, 46 (2004).
3. A. Addie, M. Dekker, R. Verkerk, W. Jongen, *J. Agric. Food Chem.*, **48**, 4120, (2000).
4. G. Wu, F. Bazer, T. Cudd, C. Meininger, T. Spencer, *J. Nutr.*, **134**, 2171 (2004).
5. A. D'Ercole, *Acta Paediatr. (Suppl.)*, **428**, 32 (1999).
6. K. Aaby, G. Skrede, E. Wrolstad, *J. Agric. Food Chem.*, **53**, 4033 (2005).

7. Y. Amakura, M. Okada, S. Tsuji, Y. Tonogai, *J. Chromatogr. A*, **896**, 90 (2000).
8. B. Ancos, E. Gonzáles, M. Cano, *J. Agric. Food Chem.*, **48**, 4568 (2000).
9. eic.res.org/feature/whats-in-your.
10. Y. Zhang, N.P. Seeram, R. Lee, L. Feng, D. Heber, *J. Agric. Food Chem.*, **56**: 670 (2008).
11. M. Cho, R. Howard, L. Prior, R. Clark, *J. Agric. Food Chem.* **85**, 2152 (2005).
12. B. Cerda', F.A. Toma's-Barbera'n, J.C. Espin, *J. Agr. Food Chem.*, **53**, 227 (2005).
13. T.Okuda, T. Yoshida, T. Hatano, *Planta Med.*, **55**, 117 (1989).
14. J. Maas, S. Wang, G. Galletta, The strawberry into the 21st century. Timber Press, Portland, OR, pp.115-117, (1991).
15. B. Cordenunsi, M. Genovese, R. João, N. Hassimotto, R. Santos, F. Lajolo, *Food Chem.*, **91**, 117 (2005).
16. U. Justesen, P. Knuthsen, T. Leth, *J. Chromatogr. A*, **799**, 105 (1998).
17. K. Meyers, C. Watkins, M. Pritts, R. Liu, *J Agric Food Chem.*, **51**, 6887 (2003).
18. A. Proteggente, A. Pannala, G. Pagana, L. Van Buren, E. Wagner, S. Wiseman, F. Van De Put, C. Dacombe, C.A. Rice-Evans, *Free Radic. Res.*, **36**: 217 (2002).
19. M. Olsson, J. Ekvall, K. Gustavsson, J. Nilsson, D. Pillai, *J. Agric. Food Chem.*, **52**, 2493 (2004).
20. S. Tulipani, B. Mezzetti, F. Capocasa, S. Bompadre, J. Beekwilder, C. Ric de Vos, *J. Agric. Food Chem.*, **56**, 698 (2008).
21. C. Pallavi, K. Pankaj, K. Prabhakar, M. Nitin, A. Aniket, *Scientia Horticulturae*, **172**,:124 (2014),.
22. S. Tulipani, G. Marzban, A. Herndl, M. Laimer, B. Mezzetti, M. Battino, *Food Chem.*, **124**, 906 (2011).
23. L. Ribeiro, D. Salvadori, *Mutation Res.*, **544**, 197 (2003).
24. J. Frank, R. Xiao, S. Yu, M. Ferguson, L. Hennings, P. Simpson, M. Ronis, N. Fang, T. Badger, F. Simmen, *Nutrit. Res.*, **26**, 141 (2006).
25. B. Fromenty, M. Robin, A. Igoudjil, A. Mansouri, D. Pessayre, *Diabetes Metab.*, **30**, 122 (2004).
26. J. Folch, M. Lees, G. Sloane Stanley, *J. Biol. Chem.*, **226**, 490 (1957).
27. M. Schaalán, H. El-Abhar, M. Barakat, E. El-Denshary, *J. Diabetes Complication.*, **23**, 202 (2009).
28. G. Block, M. Dietrich, E. Norkus, *Epidemiol.*, **17**, 404 (2006).
29. F. Tomas-Barberan, M. Clifford, *J. Sci. Food Agric.*, **80**, 1074 (2000).
30. M. Krokida, Z. Maroulis, *Drying Technol.*, **15**, 2444 (1997).
31. M. Janković, *A Publication of the Faculty of Agriculture*, **38**, 129 (1993).

АНАЛИТИЧНИ ХАРАКТЕРИСТИКИ НА ДИВИ И КУЛТИВИРАНИ ЯГОДИ (ЛЯТНА И ЕСЕННА РЕКОЛТА) В ЮЖНА БЪЛГАРИЯ И СЕВЕРНА ГЪРЦИЯ

Ст.И. Пъпанов^{1*}, Ек.Г. Петкова², К.В. Иванов¹, Ст.Д. Иванова¹, В.В. Грудева³

¹Медицински университет в Пловдив, Факултет по фармация, 4000 Пловдив, България

² Медицински университет в Пловдив, Медицински колеж, 4004 Пловдив, България

³Болница „Св. Екатерина“, 1431 София, България

Постъпила на 16 февруари, 2018 г.; коригирана на 18 април, 2018 г.

(Резюме)

Ягодите със своя аромат и сладък вкус са най-популярният плод на света. Съществуват повече от 600 разновидности ягоди, които се различават по вкус, размер и текстура. Целта на проучването е анализ на рН, общи феноли, антиоксидантна активност (радикал улавяща активност) и общи антоциани на диворастящи и култивирани сортове ягоди с произход Северна Гърция и Южна България. Разработена е методология за определяне на общи феноли, антиоксидантна активност и общи антоциани. Средната стойност на показателя рН е в границите от 3,26 за проба ягоди от Северна Гърция до 3,34 и 3,55 за проба ягоди от Южна България. Общи феноли: $4,58 \pm 0,02$ мг GAE/г свежо тегло при Диворастящи ягоди; $1,34 \pm 0,02$ мг GAE/г свежо тегло за проба ягоди от Северна Гърция; $1,36 \pm 0,03$ мг GAE/свежо тегло и $1,41 \pm 0,01$ мг GAE/г свежо тегло проба ягоди от Южна България. Общи антоциани: $0,34 \pm 0,01$ мг /г свежо тегло за проба ягоди от Северна Гърция; $0,21 \pm 0,01$ мг /г свежо тегло и $0,22 \pm 0,01$ мг/г свежо тегло за проба ягоди от Южна България. Антиоксидантна активност: Диворастящи ягоди – $41,38 \pm 0,20$ м мол ТЕ/г свежо тегло; $7,35 \pm 0,30$ м мол ТЕ/г свежо тегло за проба ягоди от Северна Гърция; $8,99 \pm 0,20$ м мол ТЕ/г свежо тегло и $10,20 \pm 0,20$ м мол ТЕ/г свежо тегло за проба ягоди от Южна България. Наблюдава се правопрпорционална зависимост между антиоксидантната активност и общите феноли и обратнопрпорционална зависимост между антиоксидантна активност/ феноли и антоциани.

Instructions about Preparation of Manuscripts

General remarks: Manuscripts are submitted in English by e-mail. The text must be typed on A4 format paper using Times New Roman font size 11, normal character spacing. The manuscript should not exceed 15 pages (about 3500 words), including photographs, tables, drawings, formulae, etc. Authors are requested to use margins of 2 cm on all sides.

Manuscripts should be subdivided into labelled sections, e.g. **Introduction, Experimental, Results and Discussion, etc.** The **title page** comprises headline, author's names and affiliations, abstract and key words. Attention is drawn to the following:

a) **The title** of the manuscript should reflect concisely the purpose and findings of the work. Abbreviations, symbols, chemical formulas, references and footnotes should be avoided. If indispensable, abbreviations and formulas should be given in parentheses immediately after the respective full form.

b) **The author's** first and middle name initials and family name in full should be given, followed by the address (or addresses) of the contributing laboratory (laboratories). **The affiliation** of the author(s) should be listed in detail by numbers (no abbreviations!). The author to whom correspondence and/or inquiries should be sent should be indicated by asterisk (*) with e-mail address.

The abstract should be self-explanatory and intelligible without any references to the text and containing not more than 250 words. It should be followed by key words (not more than six).

References should be numbered sequentially in the order, in which they are cited in the text. The numbers in the text should be enclosed in brackets [2], [5, 6], [9–12], etc., set on the text line. References are to be listed in numerical order on a separate sheet. All references are to be given in Latin letters. The names of the authors are given without inversion. Titles of journals must be abbreviated according to Chemical Abstracts and given in italics, the volume is typed in bold, the initial page is given and the year in parentheses. Attention is drawn to the following conventions: a) The names of all authors of a certain publication should be given. The use of "*et al.*" in the list of references is not acceptable. b) Only the initials of the first and middle names should be given. In the manuscripts, the reference to author(s) of cited works should be made without giving initials, e.g. "Bush and Smith [7] pioneered...". If the reference carries the names of three or more authors it should be quoted as "Bush *et al.* [7]", if Bush is the first author, or as "Bush and co-workers [7]", if Bush is the senior author.

Footnotes should be reduced to a minimum. Each footnote should be typed double-spaced at the bottom of the page, on which its subject is first mentioned. **Tables** are numbered with Arabic numerals on the left-hand top. Each table should be referred to in the text. Column headings should be as short as possible but they must define units unambiguously. The units are to be separated from the preceding symbols by a comma or brackets. Note: The following format should be used when figures, equations, etc. are referred to the text (followed by the respective numbers): Fig., Eqns., Table, Scheme.

Schemes and figures. Each manuscript should contain or be accompanied by the respective illustrative material as well as by the respective figure captions in a separate file (sheet). As far as presentation of units is concerned, SI units are to be used. However, some non-SI units are also acceptable, such as °C, ml, l, etc. The author(s) name(s), the title of the manuscript, the number of drawings, photographs, diagrams, etc., should be written in black pencil on the back of the illustrative material (hard copies) in accordance with the list enclosed. Avoid using more than 6 (12 for reviews, respectively) figures in the manuscript. Since most of the illustrative materials are to be presented as 8-cm wide pictures, attention should be paid that all axis titles, numerals, legend(s) and texts are legible.

The authors are required to submit the text with a list of three individuals and their e-mail addresses that can be considered by the Editors as potential reviewers. Please, note that the reviewers should be outside the authors' own institution or organization. The Editorial Board of the journal is not obliged to accept these proposals.

The authors are asked to submit **the final text** (after the manuscript has been accepted for publication) in electronic form by e-mail. The main text, list of references, tables and figure captions should be saved in separate files (as *.rtf or *.doc) with clearly identifiable file names. It is essential that the name and version of the word-processing program and the format of the text files is clearly indicated. It is recommended that the pictures are presented in *.tif, *.jpg, *.cdr or *.bmp format.

The equations are written using “Equation Editor” and chemical reaction schemes are written using ISIS Draw or ChemDraw programme.

EXAMPLES FOR PRESENTATION OF REFERENCES

REFERENCES

1. D. S. Newsome, *Catal. Rev.–Sci. Eng.*, **21**, 275 (1980).
2. C.-H. Lin, C.-Y. Hsu, *J. Chem. Soc. Chem. Commun.*, 1479 (1992).
3. R. G. Parr, W. Yang, *Density Functional Theory of Atoms and Molecules*, Oxford Univ. Press, New York, 1989.
4. V. Ponec, G. C. Bond, *Catalysis by Metals and Alloys (Stud. Surf. Sci. Catal., vol. 95)*, Elsevier, Amsterdam, 1995.
5. G. Kadinov, S. Todorova, A. Palazov, in: *New Frontiers in Catalysis (Proc. 10th Int. Congr. Catal., Budapest, (1992), L. Guzzi, F. Solymosi, P. Tetenyi (eds.), Akademiai Kiado, Budapest, 1993, Part C, p. 2817.*
6. G. L. C. Maire, F. Garin, in: *Catalysis. Science and Technology*, J. R. Anderson, M. Boudart (eds), vol. 6, SpringerVerlag, Berlin, 1984, p. 161.
7. D. Pocknell, *GB Patent 2 207 355* (1949).
8. G. Angelov, PhD Thesis, UCTM, Sofia, 2001, pp. 121-126.
- 9 JCPDS International Center for Diffraction Data, Power Diffraction File, Swarthmore, PA, 1991.
10. CA **127**, 184 762q (1998).
11. P. Hou, H. Wise, *J. Catal.*, in press.
12. M. Sinev, private communication.
13. <http://www.chemweb.com/alchem/articles/1051611477211.html>.

Texts with references which do not match these requirements will not be considered for publication!!!

CONTENTS

A. M. Naglah, A. S. Al-Wasidi, N. M. Al-Jafshar, J. S. Al-Otifi, M. S. Refat, W. N. Hozzein, Synthesis, characterization and antioxidant measurements of selenium (IV) complexes with some amino acids – binuclear complexes.....	351
D. Pedda Kasim, P. Suneetha, M. S. R. Krishna, B. Dinesh, R. Sri Deepthi, U. Lakshmi Sahitya, Identification of volatile compounds from maize aeral parts infested by <i>Chilo partellus</i> (swine hoe) using GC-MS analysis	363
M. Ishaque, Y. Bibi, A. Qayyum, M. Khalid Rafiq, M. Arshad, S. M. Saqlan Naqvi, S. Nisa, M. A. Jenks, Antioxidant potential, total phenolic and flavonoid contents of three culinary medicinal plant species of Lesser Hamalya, Pakistan	368
S. Bakhshi, H. Abbaspour, S. Saeidisar, Study of phytochemical changes, enzymatic and antioxidant activity of two halophyte plants: <i>Salsola dendroides</i> Pall and <i>Limonium reniforme</i> (Girard) Lincz in different seasons	374
N. Vaseghi, M. Bayat, A.C. Nosrati, M. Ghorannevis, S. Hashemi, Evaluation of the plasma jet effects on the citrinin and ochratoxin A producing species of the genus <i>Penicillium</i>	383
M. Răcuciu, S. Oancea, Impact of 50 Hz magnetic field on the content of polyphenolic compounds from blackberries.....	393
H. S. Sayiner, T. Bakir, F. Kandemirli, Voltammetric and theoretical study of the interaction of ceftriaxone with phenylalanine.....	398
T.M. Popova, St.A. Ivanova, M.V. Dimitrov, Characterization and drug release from extended-release matrix pellets with montelukast sodium.....	405
I.A. Avramova, T.Hr. Radoykova, I.V. Valchev, D.R. Mehandjiev, X-ray photoelectron spectroscopy investigations of lignocellulosic materials.....	411
Ts. Voyslavov, S. Tsakovski, V. Simeonov, S. Arpadjan, The effect of iron and manganese oxyhydroxide soil fraction on occurrence of Cr(VI).....	417
L.H. Borisova, D.S. Kiryakova, A.N. Atanassov, Transformation from α - to β -phase in vinylidene fluoride–hexafluoropropylene copolymer nanocomposites prepared by co-precipitation method.....	423
M. Afqir, A. Tachafine, D. Fasquelle, M. Elaatmani, J-C. Carru, A. Zegzouti, M. Daoud, Sol-gel hydrothermal preparation of $\text{Bi}_4\text{Ti}_3\text{O}_{12}$ ceramic	429
H. L. Bai, D. J. Zhang, F. L. Meng, Y. Fan, P. Zhang, A metal-organic framework of Co(II): synthesis and supercapacitive	433
M. Kumar, G. Rattan, R. Prasad, Promotional effect of Au on γ - Al_2O_3 supported cobalt based catalyst for total oxidation of methane	437
Z. Gokmen, N. G. Deniz, M. E. Onan, C. Sayil, Synthesis and spectral properties of new piperazine derivatives and a structural study	445
Zh. Velkov, D. Tsekova, V. Karadjova, L. Vezenkov, Molecular modeling of galanthamine derivatives comprising peptide moiety: methods, targets and accuracy of results	452
S.P. Hristoskova, L.D. Yocheva, D.S. Yankov, S.T. Danova, Newly characterized butyrate producing <i>Clostridium</i> sp. strain 4a1, isolated from chickpea beans (<i>Cicer arietinum</i> L.)	459
M. Talih, S.N. Dirim, Determination of the drying characteristics of cherry laurel (<i>Laurocerasus officinalis</i> Roem.) puree in a freeze-dryer	467
E. Aslan, Ö.K. Kürkçü, Edge harmonic index of carbon nanocones and an algorithm	478
A.G. Al-Sehemi, A. Al-Ghamdi, N.T. Dishovsky, P. A. Malinova, N.T. Atanasov, G. L. Atanasova Comparison of properties of natural rubber composites with hybrid fillers containing different modifying phase and their applicability in flexible antennas.....	484
Y.M. Li, W.M. Ni, M.Q. Chen, Z. Zhou, Y. Q. Yang, Preparation of $\text{Fe}_3\text{O}_4/\text{TiO}_2$ composite and its application in photocatalysis of organic pollutants.....	494
S. I. Papanov, Ek. G. Petkova, K. V. Ivanov, St. D. Ivanova, V. V. Grudeva, Analytical characteristics of wild and cultivated strawberries (spring & autumn harvests) of Southern Bulgaria & Northern Greece.....	502
INSTRUCTIONS TO THE AUTHORS	507

СЪДЪРЖАНИЕ

А.М. Наглах, А.С. Ал-Васиди, Н.М. Ал-Джафшар, Дж.С. Ал-Отифи, М.С. Рефат, У.Н. Хоцеин, Синтез, охарактеризиране и антиоксидантна активност на комплекси на селен (IV) с някои аминокиселини – бинуклеарни комплекси	362
Д. Педа Касим, П. Сунета, М.С.Р. Кришна, Б. Динеш, Р. Шри Дефти, У. Лакшми Сахитиа, Идентифициране на летливите съединения от надземните части на царевица, инфектирани с <i>Chilo partellus</i> , с помощта на GC-MS анализ	367
М. Ишак, Я. Биби, А. Кайум, М. Халид-Рафик, М. Аршад, С. М. Саклан Накви, С. Низа, М.А. Дженкс, Антиоксидантен потенциал, общо съдържание на феноли и флавоноиди в три вида кулинарни растения в Лесер Хамалия, Пакистан	373
С. Бакши, Х. Абаспур, С. Саедисар, Изследване на фитохимичните промени, ензимната и антиоксидантната активност на две халофитни растения - <i>Salsola dendroides Pall.</i> и <i>Limonium reniforme (Girard) Lincz</i> през различните сезони	382
Н. Вазеги, М. Баят, А.Х. Носрати, М. Гораневис, С. Хашеми, Влияние на плазмените реактивни ефекти върху Цитринин- и Охратоксин А-произвеждащите форми на <i>Penicillium</i>	392
М. Ракучу, С. Оанча, Влияние на 50 Hz магнитно поле върху съдържанието на полифенолни съединения в къпини	397
АХ.С. Сайнер, Т. Бакир, Ф. Кандемирли, Волтаперометрично и теоретично изследване на взаимодействието между цефтриаксон и фенилаланин.....	404
Т.М. Попова, Ст.А. Иванова, М.В. Димитров, Охарактеризиране и лекарствено освобождаване от матрични пелети с удължено освобождаване на монтелукаст натрий	410
И.А. Аврамова, Т.Хр. Радойкова, И.В. Вълчев, Д.Р. Механджиев, Изследване на лигно-целулозни материали посредством рентгенова фотоелектронна спектроскопия	416
Ц. Воиславов, С. Цаковски, В. Симеонов, С. Арпаджан, Влияние на почвената фракция, съдържаща железни и манганови оксихидроксида, върху наличието на Cr(VI)	422
Л.Х. Борисова, Д.С. Кирякова, А.Н. Атанасов, Трансформация на α - в β - фаза при винилиденфлуорид-хексафлуоропропиленови съполимерни композити, получени по метода на съутаяването.....	428
М. Афкир, А. Ташафин, Д. Фаскел, М. Елатмани, Ж.-С. Карю, А. Зегзути, М. Дауд, Зол-гел хидротермално получаване на $\text{Bi}_4\text{Ti}_3\text{O}_{12}$ керамика	432
М. Кумар, Г. Ратан, Р. Прасад, Промоционален ефект на Au върху γ - Al_2O_3 нанесен катализатор на базата на кобалт за пълно окисление на метан	444
З. Гокмен, Н.Г. Дениз, М.Е. Онан, Ц. Саил, Синтез и спектрални свойства на нови пиперазинови производни и структурен анализ	451
Ж. Велков, Д. Цекова, В. Караджова, Л. Везенков, Молекулно моделиране на производни на галантамин, съдържащи пептидна част	458
С.П. Христоскова, Л.Д. Йочева, Д.С. Янков, С.Т. Данова, Новоохарактеризиран щам <i>Clostridium sp.</i> 4A1, изолиран от зърна нахут (<i>Cicer arietinum L.</i>), произвеждащ бутират	466
М. Талих, С.Н. Дирим, Определяне на характеристиките на сушене на пюре от лаврова череша (<i>Laurocerasus officinalis Roem.</i>) в сушилни-фризер.....	477
Е. Аслан, Й.К. Кюркчю, РЪБОВ хармоничен индекс на въглеродни наноконуси и алгоритъм	483
А.Г. Ал-Сехеми, А. Ал-Гамди, Н.Т. Дишовски, П.А. Малинова, Н.Т. Атанасов, Г.Л. Атанасова, Сравнение на свойствата на композити на базата на естествен каучук с хибридни пълнители съдържащи различна модифицираща фаза и тяхната приложимост в гъвкави антени.....	493
И.М. Ли, У.М. Ни, М.К. Чен, З. Жоу, И.К. Янг, Получаване на $\text{Fe}_3\text{O}_4/\text{TiO}_2$ композит и приложението му за фотокатализ на органични замърсители.....	501
Ст.И. Пъпанов, Ек.Г. Петкова, К.В. Иванов, Ст.Д. Иванова, В.В. Грудева, Аналитични характеристики на диви и култивирани ягоди (лятна и есенна реколта) в Южна България и Северна Гърция.....	506
ИНСТРУКЦИЯ ЗА АВТОРИТЕ	507